technische universität
dortmund

Dissertation
zur Erlangung des akademischen Grades
Dr. rer. nat. im Fach Physik

Exploring the Interplay between Flavor and High-p_T Observables in the SMEFT Framework

Lara Nollen
geboren in Dortmund

Dortmund, Juni 2025

Lehrstuhl für theoretische Physik IV
Fakultät Physik
Technische Universität Dortmund

Gutachter der Dissertation:
Prof. Dr. Gudrun Hiller und Prof. Dr. Emmanuel Stamou

Datum der Abgabe:
03. Juni 2025

Vorsitzender des Prüfungsausschusses:
Prof. Dr. Götz Uhrig

Datum der mündlichen Prüfung:
10. Juli 2025

Kurzfassung

Diese Arbeit präsentiert eine globale Analyse zur Suche nach Physik jenseits des Standardmodells im Rahmen der Standardmodell-Effektiven Feldtheorie (SMEFT). Hierzu werden Hochenergie-Daten von Teilchenbeschleunigern mit Präzisionsmessungen aus dem Flavor-Sektor kombiniert, um weitgehend modellunabhängige Schranken auf mögliche neue Wechselwirkungen zu setzen, welche durch Wilson-Koeffizienten parametrisiert sind.

Trotz der Erfolge des Standardmodells bei der Beschreibung fundamentaler Wechselwirkungen bleiben zentrale Fragen, wie etwa die Entstehung von Neutrinomassen, die Natur dunkler Materie und die beobachtete Baryonenasymmetrie, unbeantwortet und deuten somit auf die Existenz neuer Physik hin. Angesichts der Herausforderungen direkter Suche nach neuen Teilchen bieten effektive Feldtheorien einen komplementären Ansatz, um diese Phänomene indirekt zu untersuchen. Im Mittelpunkt unserer Analyse stehen die Synergien verschiedener Observablen, die uns erlauben unter Anwendung bayesischer Statistik gleichzeitig Schranken für zahlreiche Wilson-Koeffizienten zu setzen und unbeschränkte Richtungen im Parameterraum aufzulösen. Ein besonderer Schwerpunkt liegt zudem auf der Untersuchung von Flavor-Strukturen. Dazu verwenden wir den Ansatz der Minimalen Flavorverletzung im Quarksektor sowie lepton-flavorspezifische Szenarien. Unsere Ergebnisse testen Skalen bis zu 1000 TeV, bieten indirekte Informationen über mögliche Flavorstrukturen und eröffnen Perspektiven für zukünftige Forschung.

Abstract

This thesis presents a global analysis aiming to constrain physics beyond the Standard Model within the framework of the Standard Model Effective Field Theory. We combine high-p_T collider measurements and precision flavor observables to set largely model-independent bounds on potential new interactions parameterized by the Wilson coefficients.

Despite its successes in describing a wide range of processes, the Standard Model of Particle Physics does not account for fundamental phenomena such as neutrino mass generation, dark matter existence, and baryon asymmetry, thus hinting at the existence of physics beyond the Standard Model. Given the current challenges in the direct detection of new particles, effective field theories offer a complementary approach to probe these phenomena indirectly. Central to our analysis is the systematic exploration of synergies between high-energy collider data and precision flavor observables using a Bayesian statistical framework. A particular emphasis is further placed on the flavor structure, examining the Minimal Flavor Violation approach in the quark sector and lepton-flavor-specific scenarios. Our results probe energy scales up to 1000 TeV, offer indirect insights into potential flavor structures, and outline directions for future research.

List of Publications

This thesis is based on the following publications and proceedings:

- C. Grunwald, G. Hiller, K. Kröninger and L. Nollen,
  More synergies from beauty, top, Z and Drell-Yan measurements in SMEFT [1],
  In: *JHEP* **11** (2023) 110,
  DOI: 10.1007/JHEP11(2023)110,
  arXiv: 2304.12837

- G. Hiller, L. Nollen, and D. Wendler,
  Total Drell-Yan in the flavorful SMEFT [2],
  In: *Eur. Phys. J. C* **85** (2025) 6, 657,
  DOI: 10.1140/epjc/s10052-025-14349-w,
  arXiv: 2502.12250.

- C. Grunwald, G. Hiller, K. Kröninger and L. Nollen,
  Beyond Universality: Global Fits of lepton-flavor-specific SMEFT Operators [3],
  In preparation

- C. Grunwald, G. Hiller, K. Kröninger and L. Nollen,
  Synergies of Drell-Yan, top and beauty in global SMEFT fits [4],
  Contribution to: [15th International Workshop on Top Quark Physics (TOP2022)]
  Speaker: L. Nollen,
  arXiv: [2211.12261]

- C. Grunwald, G. Hiller, K. Kröninger and L. Nollen,
  Synergies of Drell-Yan, beauty, top, and Z observables in MFV-SMEFT [5],
  Contribution to: 21st Conference on Flavor Physics and CP Violation (FPCP 2023)
  Speaker: L. Nollen,
  In: *PoS* FPCP 2023 058, DOI: 10.22323/1.445.0058, arXiv: 2307.06150

- C. Grunwald, G. Hiller, K. Kröninger and L. Nollen,
  Predicting $B(B \to K^{(*)}\nu\bar{\nu})$ within the MFV-SMEFT using B, Top, Z and Drell-Yan data [6],
  Contribution to: 2023 European Physical Society Conference on High Energy Physics (EPS-HEP2023)
  Speaker: C. Grunwald,
  In: *PoS* EPS-HEP2023 (2024) 298, DOI: 10.22323/1.449.0298

- G. Hiller, L. Nollen and D. Wendler,
  Teaming up MET plus jet with Drell-Yan in the SMEFT [7],
  Contribution to: 9th Symposium on Prospects in the Physics of Discrete Symmetries (Discrete 2024)
  Speaker: D. Wendler,
  In: *PoS* DISCRETE2024 (2025) 002, DOI: 10.22323/1.481.0002

Contents

Chapter 1

Introduction

What are the fundamental laws of nature? For centuries, this question has inspired relentless curiosity and led to countless discoveries that have shaped our understanding of the universe. From the early formulation of quantum field theory [8–11] to the discovery of the Higgs boson [12, 13], the quest to uncover the underlying principles of nature has been one of the most enduring endeavors in science. Among the most outstanding results of this continuous search for answers is the Standard Model of Particle Physics (SM) [14–16], a theoretical framework to describe the fundamental particles and their interactions in terms of quantum fields and gauge invariance, thereby forming the foundation of modern particle physics. During decades of testing and probing for inconsistencies, its predictions have been confirmed in various experiments to an extraordinary degree of accuracy (see e.g. [17, 18]), consolidating its predictive power and robustness.

Despite its successes, the SM remains incomplete as it fails to account for several phenomena that have been observed, for example, in cosmology. Many questions remain unanswered and exciting discoveries still lie ahead. Gravity has yet to be incorporated in a quantum field theoretic framework, and the SM does also not provide a viable candidate for dark matter or dark energy. Furthermore, we do not have an explanation for the observed matter-antimatter asymmetry in the universe or the masses of neutrinos. These unresolved issues suggest the existence of physics beyond the Standard Model (BSM) that still awaits discovery.

The search for BSM physics is one of the central goal of modern experimental particle physics. High-energy colliders like the Large Hadron Collider (LHC) at CERN [19] probe nature on unprecedentedly small scales by colliding protons at energies of several TeV, striving to produce new particles and detect them via their decay products. However, the high energies required to produce such heavy particles as well as the large background in hadron collisions makes these attempts of direct detection of BSM physics challenging, leading to a growing focus on indirect searches (e.g. [20–22]). These aim to uncover subtle effects of new particles and interactions at lower energies through precision measurements, searching for small yet significant deviations from the SM predictions.

A powerful tool for these indirect searches is the use of effective field theories (EFTs). EFTs provide a systematic framework to study the low-energy imprints of high-energy physics without detailed knowledge of the underlying theory, thus allowing to test BSM physics in a largely model-independent manner. In particular, the Standard Model Effective Theory (SMEFT) [23] has emerged as a framework to study the effects that heavy new particles induce on observables below the electroweak scale. While numerous SMEFT studies have been performed across various physics sectors (see e.g. [24–33]), the large number of free parameters in the theory makes it challenging to extract meaningful constraints on BSM physics without additional assumptions. Especially flat directions in parameter space, i.e. directions along which the likelihood is constant, can lead to degeneracies and complicate the interpretation of the data.

While a single sector may not be sufficient to fully constrain the relevant parameter space, combining information from multiple sectors can help improve the bounds. In particular, pairing the precision of flavor observables with the energy-enhanced reach of collider observables can lead to synergies in constraining BSM physics [33–40], which is a main objective of this thesis. By combining data from different sectors, we aim to develop a more comprehensive picture of potential new physics and to identify promising directions for future searches.

Another central element of this work is the role of flavor in the SMEFT. In the SM, the flavor structure is characterized by pronounced hierarchies of the fermion masses as well as in the quark mixing matrix, hinting at an underlying organizing principle. To obtain indirect insights into the flavor structure of BSM physics and test for additional sources of flavor violation, we employ a Minimal Flavor Violation (MFV) [41] ansatz in the quark sector, building on the framework developed in Ref. [1]. The MFV pattern further allows us to connect different flavor components within the SMEFT and to investigate possible correlations among various processes.

Motivated by the persistent tensions in muon-related observables, such as the anomalies in the angular observables of $B \to K^* \mu\mu$ decays [42] or the anomalous magnetic moment [43], we place a particular emphasis on the lepton flavor by performing lepton-flavor specific fits that allow for non-universal couplings. Although recent measurements of the ratio $R_K^{(*)}$ [44, 45] support lepton flavor universality among the first two generations, ample room remains for non-universal effects in the third generation or in different operator structures.

Furthermore, lepton-flavor violating processes are of great interest as they are highly suppressed in the SM but can be enhanced in BSM scenarios, thus providing clean, low-background tests of the SM and sensitive probes of new physics. We therefore consider lepton-flavor violating (LFV) processes, investigating the possibility of LFV contributions to processes involving charged leptons as well as neutrinos. As the neutrino flavor is not measured directly, they probe the incoherent sum over all possible flavor combinations, which can lead to interesting interferences and novel effects in the SMEFT.

In summary, we provide a comprehensive, lepton-flavor specific analysis that bridges collider and flavor observables within the SMEFT framework. By highlighting the synergies among the different observables, our global approach not only tightens the bounds on potential BSM physics but also provides insights into the flavor structure of the SMEFT and possible BSM scenarios.

This thesis is organized as follows. In Chapter 2, we review the mathematical formulation of the SM in order to introduce the fundamental concepts and notations used throughout this work, and we discuss its limitations to motivate the need for BSM physics. In Chapter 3, we introduce the concepts of EFTs, focusing on the SMEFT and the Low Energy Effective Theory (LEFT). We further describe our statistical approach and fitting procedure in Chapter 4, where we also present some illustratory toy model analyses.

Chapter 5 explores the collider phenomenology in the SMEFT. We describe our simulation procedure and examine the Drell-Yan process, Z and W boson decays, and top quark observables, discussing the sensitivity of these observables to the SMEFT Wilson coefficients and the synergies that arise from their combination. This chapter also details the datasets used and addresses various caveats encountered when fitting collider observables. In Chapter 6, we turn to the flavor sector and study lepton and meson decays as well as the anomalous magnetic moments of leptons. We present the relevant observables and data, exploring their dependence on the LEFT Wilson coefficients.

The results of the combined analysis are presented in Chapter 7, where we highlight the complementarities between the collider and flavor sectors and discuss the implications for BSM scenarios. In particular, we perform lepton-flavor specific analyses and investigate the impact of lepton-flavor universal patterns. Finally, Chapter 8 summarizes our findings, outlines possible future directions and prospects, and concludes the thesis.

Chapter 2

The Standard Model of Particle Physics and Beyond

We begin by reviewing the theoretical foundations of the Standard Model (SM) of Particle Physics, which forms the cornerstone of our current understanding of fundamental interactions. Sec. 2.1 provides a concise overview of the key aspects of the SM based on Refs. [46–49]. We focus on its mathematical formulation and fundamental features, such as the electroweak symmetry breaking mechanism and the CKM mixing matrix. Sec. 2.2 explores the perturbative techniques used to calculate physical processes in quantum field theory, addressing the challenges of ultraviolet divergences and introducing the concept of renormalization, which leads to the running of couplings. Finally, in Sec. 2.3, we discuss the limitations of the SM and highlight the unresolved questions and theoretical issues that motivate the search for BSM physics.

2.1. Foundations of the Standard Model

The SM is a quantum field theory built on the principles of quantum mechanics, special relativity and local gauge invariance. It describes the fundamental particles and their interactions via the exchange of gauge bosons and is based on the gauge group $SU(3)_C \times SU(2)_L \times U(1)_Y$. The $SU(3)_C$ component describes the strong interaction, also denoted as Quantum Chromodynamics (QCD) [50–53], while $SU(2)_L \times U(1)_Y$ represents the gauge group of the electroweak (EW) interaction [14–16].

The particle content of the SM is divided into fermions and bosons. Bosons in the SM are either spin-0 (scalar) fields, for instance the Higgs boson, or spin-1 (vector) fields, namely the gauge bosons that mediate the fundamental forces. Fermions, on the other hand, are spin 1/2 fields that obey the Pauli exclusion principle [54] and are further divided into quarks and leptons. Quarks carry color charge and thus interact via the strong force, whereas leptons, including charged leptons as well as neutrinos, are color neutral and therefore only subject to the electroweak interaction.

Furthermore, fermions are organized into three generations that only differ with regard to their mass and their mixing with other fermions. In addition, fermions are chiral, i.e. they are decomposed into left-handed and right-handed components via the projection operators $P_{L,R} = (1 \mp \gamma^5)/2$, with $\gamma_5 = i\gamma^0\gamma^1\gamma^2\gamma^3$ and the Dirac matrices γ^μ. In the SM, the weak interaction couples only to left-handed fermions and right-handed antifermions, which is referred to as the V–A structure of the weak interaction [55, 56]. Thus, left-handed fermions (with negative chirality) form the $SU(2)_L$ doublets Q and L for quarks and leptons, respectively, whereas right-handed fermions (with positive chirality) are $SU(2)_L$ singlets, where E is the charged lepton and $U(D)$ the up(down)-type quark singlets. Tab. 2.1 summarizes the fermionic fields

along with their associated quantum numbers, which dictate their transformation properties under the gauge group.

Field	Particles	$SU(3)_C$	$SU(2)_L$	Y	T_3	Q
Q	$\begin{pmatrix} u_L \\ d_L \end{pmatrix}, \begin{pmatrix} c_L \\ s_L \end{pmatrix}, \begin{pmatrix} t_L \\ b_L \end{pmatrix}$	**3**	**2**	1/6	$1/2$ $-1/2$	$2/3$ $-1/3$
U	u_R, c_R, t_R	**3**	**1**	2/3	0	2/3
D	d_R, s_R, b_R	**3**	**1**	-1/3	0	-1/3
L	$\begin{pmatrix} \nu_e \\ e_L \end{pmatrix}, \begin{pmatrix} \nu_\mu \\ \mu_L \end{pmatrix}, \begin{pmatrix} \nu_\tau \\ \tau_L \end{pmatrix}$	**1**	**2**	-1/2	$1/2$ $-1/2$	0 -1
E	e_R, μ_R, τ_R	**1**	**1**	-1	0	-1

Table 2.1: Fermionic fields in the SM and their quantum numbers under the SM gauge group. Here, Y denotes the hypercharge, which is related to the electric charge Q and the third component of the weak isospin T^3 by the Gell-Mann-Nishijima relation, $Y = 2(Q - T^3)$ [57].

The SM Lagrangian can be compactly written as

$$\begin{aligned}\mathcal{L}_{\text{SM}} = &-\frac{1}{4}\left(B_{\mu\nu}B^{\mu\nu} + W^a_{\mu\nu}W^{\mu\nu}_a + G^a_{\mu\nu}G^{\mu\nu}_a\right) \\ &+ i\bar{L}_i \not{D} L_i + i\bar{E}_i \not{D} E_i + i\bar{Q}_i \not{D} Q_i + i\bar{U}_i \not{D} U_i \\ &+ |D_\mu\varphi|^2 + \mu^2|\varphi|^2 - \lambda|\varphi|^4 \\ &- \bar{Q}_i Y^u_{ij} U_j \tilde{\varphi} - \bar{Q}_i Y^d_{ij} D_j \varphi - \bar{L}_i Y^e_{ij} E_j \varphi + \text{h.c.}\,,\end{aligned} \tag{2.1}$$

neglecting ghost and gauge fixing terms. $\not{D} = \gamma^\mu D_\mu$ and $B_{\mu\nu}$, $W^a_{\mu\nu}$, and $G^a_{\mu\nu}$ are the field strength tensors for the $U(1)_Y$, $SU(2)_L$, and $SU(3)_C$ gauge fields, respectively. They are defined as

$$F^a_{\mu\nu} = \partial_\mu F^a_\nu - \partial_\nu F^a_\mu + igf^{abc}F^b_\mu F^c_\nu\,, \tag{2.2}$$

where F^a_μ are the gauge fields, g is respective the gauge coupling, and f^{abc} are the structure constants of the gauge group, which vanish for the abelian $U(1)_Y$ group. We denote the gauge couplings by g_s, g, and g' for the $SU(3)_C$, $SU(2)_L$, and $U(1)_Y$, respectively.

The covariant derivative D_μ, acting on the fermion fields and the Higgs doublet φ, is defined as

$$D_\mu = \partial_\mu - ig_s G^a_\mu T^a - igW^I_\mu T^I - ig'B_\mu Y\,, \tag{2.3}$$

with T representing the generators of the gauge group, given by the Pauli matrices $\sigma^I/2$ for $SU(2)_L$ and the Gell-Mann matrices λ^a for $SU(3)_C$ [58].

The first line the SM Lagrangian 2.1 comprises the kinetic terms for the gauge fields, including the self-interactions characteristic of non-abelian groups. The second line contains the kinetic terms for the fermions, which further encode the interactions of the fermions with the gauge

fields, dictated by the covariant derivative defined in Eq. 2.3. The index $i = 1, 2, 3$ denote the generation of fermions, and the sum over repeated indices is implied.

The third line describes the Higgs field φ, which is a color-neutral complex doublet under $SU(2)_L$ with hypercharge $Y = 1/2$. The Higgs potential $\mu^2|\varphi|^2 - \lambda|\varphi|^4$ is the most general renormalizable scalar potential, characterized by the mass parameter μ^2 and the self-coupling λ. When $\mu^2 < 0$, the potential acquires a non-zero minimum, causing the Higgs field to develop a vacuum expectation value (VEV)

$$\langle\varphi\rangle = \frac{1}{\sqrt{2}}\begin{pmatrix}0\\ v\end{pmatrix}, \tag{2.4}$$

which spontaneously breaks the electroweak symmetry $SU(2)_L \times U(1)_Y$ to the subgroup $U(1)_{\text{EM}}$, a process denoted as Electroweak Symmetry Breaking (EWSB) [59–63]. In this broken phase, the Higgs field can be expressed as

$$\varphi = \frac{1}{\sqrt{2}}\begin{pmatrix}0\\ v + h(x)\end{pmatrix}, \tag{2.5}$$

where $h(x)$ is the physical Higgs boson field, and $v \approx 246\,\text{GeV}$ is the VEV of the Higgs field.

A direct consequence of the EWSB is the generation of masses for the fermions and the gauge bosons. While an explicit gauge boson mass term of the form $m^2 F_\mu F^\mu$ would break the gauge invariance of the theory, the kinetic term $|D_\mu\varphi|^2$ contains interactions between the Higgs field and the gauge bosons, which, after expanding φ around its VEV yield

$$|D_\mu\varphi|^2 = \frac{1}{2}(\partial_\mu h)^2 + \frac{1}{8}v^2\left(g^2 + g'^2\right)\left(W_\mu^+ W^{-\mu} + \frac{1}{\cos\theta_W^2} Z_\mu Z^\mu\right), \tag{2.6}$$

where h is the physical Higgs boson. The gauge bosons $W^\pm$ and Z are given by the linear combinations

$$W_\mu^\pm = \frac{1}{\sqrt{2}}\left(W_\mu^1 \mp i W_\mu^2\right), \qquad Z_\mu = -\sin\theta_W W_\mu^3 + \cos\theta_W B_\mu, \tag{2.7}$$

with $\sin\theta_W = g'/\sqrt{g^2 + g'^2}$ and $\cos\theta_W = g/\sqrt{g^2 + g'^2}$ denoting the sine and cosine of the weak mixing angle θ_W, respectively. The masses of the gauge bosons are given by

$$m_W = \frac{1}{2}vg, \qquad m_Z = \frac{1}{2}v\sqrt{g^2 + g'^2}, \tag{2.8}$$

following from the kinetic term in Eq. (2.6). The photon field

$$A_\mu = \cos\theta_W W_\mu^3 + \sin\theta_W B_\mu \tag{2.9}$$

remains massless, as it is associated with the unbroken $U(1)_{\text{EM}}$ symmetry.

The remaining terms of Eq. (2.1) comprise the Yukawa interactions [64] between the fermions and the Higgs field. The Yukawa matrices Y_{ij}^u, Y_{ij}^d, and Y_{ij}^e are responsible for generating the masses of the up-type quarks, down-type quarks, and charged leptons, respectively, after the EWSB. In general, the Yukawa matrices are complex and non-diagonal. They can be diagonalized via bi-unitary transformations

$$Y_u^{\text{diag}} = {S_L^u}^\dagger Y_u S_R^u, \qquad Y_d^{\text{diag}} = {S_L^d}^\dagger Y_d S_R^d, \qquad Y_e^{\text{diag}} = {S_L^e}^\dagger Y_e S_R^e, \tag{2.10}$$

where $S_{L,R}^{u,d,e}$ are unitary matrices. The diagonalized Yukawa matrices are related to the fermion masses m_i via

$$\begin{aligned} Y_u^{\text{diag}} &= \sqrt{2}/v\,\text{diag}\,(m_u, m_c, m_t)\ , \qquad Y_d^{\text{diag}} = \sqrt{2}/v\,\text{diag}\,(m_d, m_s, m_b)\ , \\ Y_e^{\text{diag}} &= \sqrt{2}/v\,\text{diag}\,(m_e, m_\mu, m_\tau)\ . \end{aligned} \tag{2.11}$$

The rotation matrices $S_{L,R}^{u,d,l}$ transform the fermion fields from the gauge basis into the mass basis, where the mass terms become diagonal. This step is essential to obtain physical particles with well-defined masses, as observed experimentally. In practice, the rotated fields are defined as

$$u'_{L,R} = S^u_{L,R} u_{L,R}\,, \qquad d'_{L,R} = S^d_{L,R} d_{L,R}\,, \qquad e'_{L,R} = S^e_{L,R} e_{L,R}\,, \tag{2.12}$$

where the primed fields correspond to the mass eigenstates.

While most terms in the SM Lagrangian remain invariant under these redefinitions, the charged current interactions between the $W^\pm$ bosons and the fermions do not. In the gauge basis, the charged current Lagrangian is given by

$$\mathcal{L}_{\text{CC}} = -\frac{g}{\sqrt{2}} \left(\bar{u}_L \gamma^\mu d_L + \bar{\nu}_L \gamma^\mu e_L\right) W^-_\mu + \text{h.c.}\,, \tag{2.13}$$

which after rotating to the mass basis becomes

$$\mathcal{L}_{\text{CC}} = -\frac{g}{\sqrt{2}} \left(\bar{u}'_L \gamma^\mu V_{\text{CKM}} d'_L + \bar{\nu}'_L \gamma^\mu V_{\text{PMNS}} e'_L\right) W^-_\mu + \text{h.c.}\,, \tag{2.14}$$

where the Cabibbo-Kobayashi-Maskawa (CKM) [65, 66] and Pontecorvo-Maki-Nakagawa-Sakata (PMNS) [67–69] matrices are defined as

$$V_{\text{CKM}} = (S^u_L)^\dagger S^d_L\,, \qquad V_{\text{PMNS}} = (S^\nu_L)^\dagger S^e_L\,. \tag{2.15}$$

These unitary matrices encode the mixing among quark and neutrino flavors, respectively, and carry rich phenomenological implications.

For three generations of fermions, both the CKM and the PMNS matrix can be parameterized by three mixing angles and one CP-violating phase[1]. Another common representation of the CKM matrix is the Wolfenstein parameterization [71], which expands the matrix elements in powers of $\lambda \approx 0.2$, where $\lambda = \sin\theta_C$ with θ_C denoting the Cabibbo angle [65]. In terms of the Wolfenstein parameters λ, A, ρ, and η, the CKM matrix is given by

$$V_{\text{CKM}} = \begin{pmatrix} 1 - \frac{\lambda^2}{2} - \frac{\lambda^4}{8} & \lambda & A\lambda^3\left(1 + \frac{\lambda^2}{2}\right)(\rho - i\eta) \\ -\lambda + A^2\lambda^5\left(\frac{1}{2} - \rho - i\eta\right) & 1 - \frac{\lambda^2}{2} - \frac{\lambda^4}{8}\left(1 + 4A^2\right) & A\lambda^2 \\ A\lambda^3\left(1 - \rho - i\eta\right) & -A\lambda^2 + A\lambda^4\left(\frac{1}{2} - \rho - i\eta\right) & 1 - \frac{\lambda^4}{2}A^2 \end{pmatrix}, \tag{2.16}$$

up to order $\mathcal{O}(\lambda^5)$. This parameterization reflects the strong hierarchies in the CKM matrix, where the off-diagonal elements are suppressed by powers of λ compared to the diagonal elements, which are of order one.

[1] If neutrinos are Majorana particles [70], i.e. their own antiparticles, the PMNS matrix contains two additional Majorana phases, which do however not affect neutrino oscillations.

In contrast, the PMNS matrix is responsible for neutrino oscillations, a phenomenon first observed by the Super-Kamiokande experiment in 1998 [72]. The relatively large mixing angles in the PMNS matrix, compared to the small off-diagonal elements in the CKM matrix, indicate that neutrinos undergo significant flavor mixing. This discovery not only provided the first evidence of physics beyond the minimal Standard Model, since neutrinos must be massive to oscillate, but also has important implications for astrophysics and cosmology.

An important phenomenological consequence of the hierarchical structure of the CKM matrix is the strong suppression of flavor-changing neutral currents (FCNCs) in the SM. These processes are forbidden at tree level since the flavor rotations cancel in the Z and γ vertices with fermions. Thus, FCNCs occur only at loop level, as depicted for example in Fig. 2.1, showing a one-loop contribution to the $t \to c\gamma$ transition.

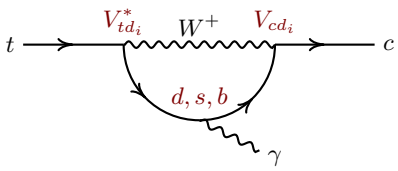

Figure 2.1: SM Feynman diagram contributing to the flavor-changing neutral current (FCNC) process $t \to c\gamma$ at one-loop level. The vertices scale with the CKM matrix elements $V^*_{td_i}$ and V_{cd_i}, where $i = d, s, b$ denotes the down-type quark in the loop.

In the loop, all possible down-type quarks contribute, each with a different CKM factor. The resulting amplitude is a sum of all contributions

$$\mathcal{A} = \sum_{i=d,s,b} V_{ti} V^*_{ci} \mathcal{A}_i \,, \tag{2.17}$$

where $\mathcal{A}_i$ is the partial amplitudes for the $t \to c\gamma$ transition mediated by the i-th quark that are a function of the loop momentum and the ratios $m^2_{d_i}/m^2_w$, with the internal quark masses m_{d_i}. Due to the unitarity of the CKM matrix, there is a strong cancellation between the different contributions, which is only broken by the mass differences of the quarks in the loop.

This mass difference is, however, small since $m^2_{d_i}/m^2_w \sim 0$ for all down-type quarks. As the amplitudes A_i are proportional to these mass ratios, the contributions are strongly suppressed, leading to a very small branching ratio for FCNC processes. This suppression, also known as the Glashow-Iliopoulos-Maiani (GIM) mechanism [73], implies that FCNCs are an excellent test of physics beyond the SM, as new particles can strongly enhance these processes which is a clear sign of new physics against the small SM background. In the case of identical masses, the FCNC amplitude would vanish, as $\sum_{i=d,s,b} V_{ti} V^*_{ci} = 0$ due to the unitarity of the CKM matrix. Since the mass difference in the up-quark sector is much larger than in the down-quark sector because $m^2_t/m^2_W \sim \mathcal{O}(1)$ while $m^2_{u_i}/m^2_W \sim 0$ for the up- and charm-quark, down-type FCNCs are significantly less suppressed than up-type FCNCs.

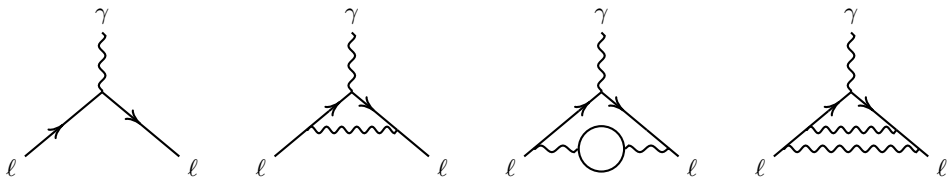

Figure 2.2: Feynman diagrams contributing to the anomalous magnetic moment of the lepton. The diagrams show the tree level contribution (left), the one-loop vertex correction (center left) and two examples of two-loop contributions (center right and right).

2.2. Perturbation Theory, Renormalization and the Running of Couplings

In order to test a theory against experimental data, the ability to compute precise, testable predictions is paramount. The classical scattering process is reflected by the tree-level amplitude, while quantum corrections are encapsulated in loop diagrams, which represent the emission and reabsorption of virtual particles. In the context of the SM, physical processes are computed using perturbation theory, where observables are expanded in a series of terms ordered by increasing powers of the coupling constant. This perturbative approach is justified when the coupling is sufficiently small, ensuring that each successive term in the series is suppressed relative to the preceding one, thereby allowing the series to be truncated at finite order while maintaining a sufficient level of precision.

To systematically organize these perturbative expansions, we can employ Feynman diagrams, which provide a pictorial representation of the underlying processes. In these diagrams, vertices represent interactions as dictated by the Lagrangian, propagators correspond to the transmission of particles between interaction points, and external lines represent the incoming and outgoing states. Each element of the diagram is associated with a corresponding Feynman rule that, taken together, allows us to compute the amplitude of the process. From the sum of all relevant amplitudes, we obtain the cross section or decay rate, a measure of the probability of the process occurring, by squaring the amplitude, applying the appropriate phase space factors, and summing over the final states.

Although virtual higher-order corrections cannot be observed directly, their impact can be measured in precision observables. This also allows to test particles heavier than the energy scales directly accessible in experiments, since virtual particles do not have to be produced on-shell. As an example, in Fig. 2.2 we show some Feynman diagrams for the anomalous magnetic moment of the lepton, which we will discuss again in the context of the LEFT in Sec. 6.1.1.

Evaluating these diagrams involves integrating over all possible momenta circulating in the loop, which often leads to ultraviolet (UV) divergences as the contributions from high-momentum modes become unbounded. If not properly regulated, these divergences render the computed observables infinite and thereby compromise the predictive power of the theory. To eliminate these divergences, a systematic renormalization procedure is employed, where the infinities that emerge from loop integrals are absorbed into redefinitions of the parameters of the theory, such as masses, coupling constants and fields.

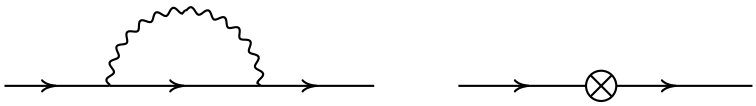

Figure 2.3: One-loop self-energy correction to the fermion propagator (left) and the corresponding counterterm (right). The internal loop represents a virtual particle that contributes to the renormalization of the mass.

In practice, the original (bare) Lagrangian is split into a renormalized part and into counterterms that cancel the divergences. As an illustrative example, we consider the one-loop self-energy correction to the fermion propagator, depicted in Fig. 2.3. This diagram arises from the emission and subsequent reabsorption of a virtual boson like a photon, which modifies the propagator and consequently the mass of the fermion. In dimensional regularization [74, 75], where the spacetime dimension d is analytically continued to $d = 4 - \epsilon$ in order to control the UV divergences, this diagram yields a divergence proportional to $1/\epsilon$. The counterterm δm is then adjusted to cancel this divergence, rendering the renormalized propagator finite.

Similarly, vertex corrections, represented by loop diagrams affecting the interaction vertices, introduce divergences that are canceled by the corresponding counterterms in the interaction Lagrangian. In Quantum Electrodynamics (QED), for instance, the vertex correction arising from the loop diagrams depicted on the center-left to right in Fig. 2.2 modifies the electron-photon interaction, leading to a renormalization of the electromagnetic coupling constant α_{em}.

The renormalization process not only restores finiteness and predictability, but also reveals a scale dependence of the parameters, reflected in the running of the couplings constants. This is quantified via the renormalization group equations (RGEs), which describe how the renormalized couplings evolve with the energy scale μ. Central to this concept are the beta functions, defined for a given coupling α as

$$\beta(\alpha) = \mu \frac{d\alpha}{d\mu} \,. \tag{2.18}$$

These beta functions are computed order by order in perturbation theory by evaluating loop corrections and extracting the associated logarithmic divergences. Their sign indicates whether a coupling increases or decreases with the energy scale, thereby providing information on the behavior of theory in the high energy (UV) and low energy (IR) regimes. For example, a negative beta function implies that the coupling decreases with increasing energy, a property known as asymptotic freedom [51, 52], while a positive beta function indicates that the coupling grows with the energy scale and may eventually become non-perturbative, signaling the presence of a Landau pole [76] or a strongly coupled regime.

As a concrete example, we consider the strong coupling constant $\alpha_s = g_s^2/4\pi$. Its one-loop beta function is given by

$$\beta_0(\alpha_s) = -\frac{b_0}{2\pi}\alpha_s^2 \,, \tag{2.19}$$

with $b_0 = 11 - 2/3 n_f$. For $n_f = 6$ quark flavors, the beta function is negative, indicating that QCD is asymptotically free at high energies in the SM. At low energies, however, the coupling becomes non-perturbative, leading to the phenomenon of confinement [77, 78], where quarks and gluons are not observed as free particles, but only within bound, color-neutral states such

as mesons and baryons. At one-loop, the RGE can be solved analytically and the running of the strong coupling constant can be expressed as

$$\alpha_s(\mu) = \frac{\alpha_s(\mu_0)}{1 + \frac{b_0}{2\pi}\alpha_s(\mu_0)\ln(\frac{\mu}{\mu_0})}\,, \tag{2.20}$$

where μ_0 is the reference scale at which the coupling is defined. The running of the coupling is a key feature of the SM and has been tested extensively in experiments, providing a quantitative verification of the theory.

The boundary condition for the RGE is set by the value $\alpha_s(\mu_0)$ of the couplings at a reference scale. At higher orders, the RGEs are solved numerically to predict the values of the parameters at other energy scales required for theoretical calculations of other observables. In this work, we implement the five-loop RGEs for the strong coupling [79, 80] as well as for the electroweak couplings [80] to compute the running of the SM parameters.

2.3. Limitations of the Standard Model and the Motivation for New Physics

While the SM successfully describes a wide range of phenomena, it is generally regarded as an incomplete theory. Both experimental findings and theoretical considerations indicate that the SM serves only as an effective description applicable up to a certain energy threshold, beyond which a more fundamental framework is required.

A major shortcoming of the SM is its inability to incorporate gravity. As a quantum field theory based on the principle of gauge invariance, the SM successfully accounts for the electroweak and strong interactions, but it does not include gravitational interactions. The consistent quantization of gravity remains one of the most pressing challenges in modern theoretical physics (see e.g. [81–83]).

Another challenge emerged with the observation of neutrino oscillations in 1998 [72]. The discovery provided the first evidence for non-zero neutrino masses, in contrast to the SM prediction of massless neutrinos. Various extensions of the SM have been proposed to account for neutrino masses, such as the seesaw mechanism, which introduces heavy right-handed neutrinos to generate small neutrino masses [84–87] or radiative models where neutrino masses are generated through loop corrections [88, 89]. However, the exact mechanism responsible for neutrino masses remains unknown.

Furthermore, astrophysical and cosmological observations provide strong evidence that roughly a fourth of the energy content of the universe is composed of dark matter and two thirds of dark energy [90–95]. The SM does not provide a viable dark matter candidate nor does it incorporate dark energy. Numerous theoretical models have been proposed to address these shortcomings, including supersymmetry (e.g. [96–99]), extra dimensions (e.g. [100–105]), sterile neutrinos (e.g. [84–86]) and axion-like particles (e.g. [106–109]). To date, however, no direct evidence for new particles or interactions has been found.

Another long-standing puzzle is the observed asymmetry between matter and antimatter in the universe [95, 110]. Although the SM incorporates CP violation through the CKM matrix, the

amount is insufficient to account for the observed baryon asymmetry, implying the existence of new sources of CP violation beyond the SM.

In addition, the very formulation of the SM itself raises questions. For instance, the Higgs mechanism, responsible for the generation of masses of the fermions and weak gauge bosons, is introduced as a phenomenological parameterization rather than emerging from a deeper principle. The parameters of the Higgs potential, μ^2 and λ, are not predicted by the theory but are instead fixed by experimental inputs. The lack of a fundamental quantum or dynamical origin of the potential suggests that the Higgs sector might be only an effective description of a more underlying theory. Alternative approaches, such as composite Higgs models (see e.g. [111–115]), Little Higgs Models [114] or Technicolor [116], offer different perspectives on electroweak symmetry breaking. These models propose, for example, that the Higgs boson emerges as a composite state, that additional symmetries and dynamics are involved, or they eliminate the need of a fundamental scalar field altogether.

The Yukawa sector also presents intriguing characteristics that hint at an underlying structure. Both the CKM matrix and the masses of the fermions exhibit strong hierarchies, as reflected, for example, by the Wolfenstein parameterization (2.16), whose origin remains unexplained. Proposals such as the Froggatt-Nielsen mechanism [117] attempt to explain the observed pattern of fermion masses and mixing by invoking additional symmetries and fields, suggesting that this so-called flavor puzzle might provide hints towards an underlying dynamic.

Furthermore, the emergence of Landau poles in certain couplings, such as the gauge coupling g' of the $U(1)_Y$ group, underscores the need for a new theoretical framework. A variety of extensions, ranging from supersymmetry and extra dimensions to grand unified theories (e.g. [118–120]) have been proposed to address these issues by modifying the ultraviolet behavior of the theory. To date, however, no direct evidence for new particles or interactions predicted by these theories has been found.

In summary, while the SM provides a remarkably successful framework for describing the known particles and their interactions, its limitations collectively motivate the search for new physics beyond the SM. The discovery of the Higgs boson at the LHC in 2012 [12, 13] marked a major milestone in particle physics, yet the LHC has not provided any direct evidence for new particles or interactions so far. The question of what lies beyond remains one of the most pressing challenges in modern physics, with profound implications for both theoretical and experimental research.

Although future collider proposals, such as the FCC-ee [121–125], the FCC-hh [126, 127] or the CLIC [128–131] aim to explore the high energy frontier and search for direct signals of new particles, the construction and commissioning of such experiments represents a long-term endeavor that may span decades. In the meantime, the focus is increasingly shifting towards indirect probes, such as precision measurements and the study of rare decays, which can reveal small but telling deviations from the SM predictions. A powerful tool in these searches are effective field theories, which we explore in detail in the following chapter.

Chapter 3

Effective Field Theories

This chapter provides an introduction to the framework of effective field theories (EFTs), which serve as powerful tools for describing the low-energy phenomenology of physical systems. In the first part of this chapter, Sec. 3.1, we introduce the foundational concepts of EFTs, including the construction methodology, matching and renormalization procedures, as well as the renormalization group evolution of Wilson coefficients. Sections 3.2 and 3.3 provide a more detailed discussion of the Standard Model Effective Field Theory (SMEFT)[23] and the Low-Energy Effective Field Theory (LEFT)[132], respectively. We focus on fermionic operators, the implementation of the Minimal Flavor Violation (MFV) framework [41] in the quark sector, and the resulting phenomenological implications.

3.1. Fundamental Principles of Effective Field Theories

EFTs are constructed around the core idea of the separation of energy scales, allowing us to construct an effective Lagrangian that captures the relevant physics at a given energy range. In many cases, the EFT follows from the decoupling of heavy degrees of freedom, which is formalized by the Appelquist–Carazzone decoupling theorem [133]. In essence, it states that in a renormalizable quantum field theory, the effects of heavy particles on low-energy observables are suppressed by powers of the energy scale over the heavy mass and thus effectively decouple at low energies. Their influence can then be absorbed into the parameters of the effective low-energy theory, denoted as Wilson coefficients [134], which are determined either by matching to the full theory or by fitting to experimental data.

This approach offers several significant advantages. First of all, it simplifies theoretical calculations by allowing us to focus exclusively on the dynamics of the relevant degrees of freedom. Moreover, EFTs are especially useful when the underlying high-energy theory is either unknown or non-perturbative, as they provide a systematic, model-independent framework for parameterizing the effects of high-energy dynamics through higher-dimensional operators and effective coefficients. In this way, EFTs serve as a practical tool to facilitate the study of observable phenomena without requiring detailed knowledge about the underlying fundamental theory.

There are two main approaches to constructing an EFT, commonly referred to as top-down and bottom-up. In the top-down approach, the heavy degrees of freedom are systematically integrated out from the existing full theory. The Wilson coefficients are computed order-by-order in perturbation theory through a process called matching, ensuring that the EFT reproduces the full theory at the corresponding matching scale. This approach is particularly useful for performing simplified calculations with finite and controllable uncertainties in the low-energy regime, where the complexity of the full theory is unnecessary. For example, in many cases, a detailed computation using general relativity is highly complex, while the significantly simpler approximation of Newtonian gravity is sufficient to achieve the required precision.

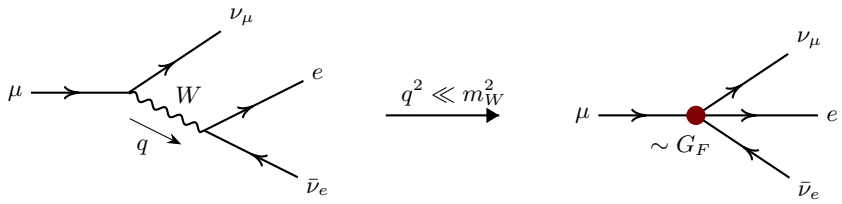

Figure 3.1: Feynman diagram illustrating the Fermi theory of beta decays. On the left, we show the full diagram in the SM with the exchange of a W boson. On the right, the diagram in the effective theory is shown, where the W boson has been integrated out, giving rise to a local four-fermion interaction with a coupling strength G_F.

When the full theory is unknown or not well understood, an EFT can be constructed based on symmetry principles or observed low-energy behavior. In this bottom-up approach, the effective Lagrangian is built from a set of operators that respect the symmetries, ordered by their mass dimension. The corresponding Wilson coefficients are fitted to experimental data, thereby providing indirect insight into the underlying high-energy dynamics. An illustrative example of this approach is Fermi's theory of weak decays [135]. Initially constructed to describe beta decays, it was later understood to be the low-energy limit of the electroweak theory that was developed decades later.

The effective Lagrangian of the four-fermion interaction is given by

$$\mathcal{L}_{\text{Fermi}} = -\frac{G_F}{\sqrt{2}} \left(\bar{\psi}_1 \gamma^\mu (1-\gamma^5)\psi_2\right) \left(\bar{\psi}_3 \gamma_\mu (1-\gamma^5)\psi_4\right) , \tag{3.1}$$

where the Fermi coupling G_F is determined by matching to experimental data. The left handed structure of the interaction was originally motivated by experimental findings [136] and only later understood in the context of the electroweak theory [55]. Starting from the SM Lagrangian, the effective operator is obtained by integrating out the massive W boson, giving rise to a local four-fermion interaction as illustrated in Fig. 3.1. This procedure is justified by the fact that the W boson is much heavier than the energy scale involved in beta decays, so that it is effectively decoupled from the low-energy dynamics. Through the matching procedure, the Wilson coefficient of the Fermi interaction is determined to be $G_F = \sqrt{2}g^2/(8m_W^2)$, with g denoting the weak coupling constant and m_W the W boson mass.

In general, EFTs are organized as a series of effective operators, ordered by a power counting parameter that reflects the suppression of higher-order contributions. This power counting is crucial for determining the relative importance of different operators and to estimate the uncertainties associated with neglected higher-order corrections. In the Fermi theory, for instance, the relevant power counting parameter is p^2/m_W^2, where p represents the momentum transferred by the W boson. For low-energy processes like beta decays, this parameter is sufficiently small to justify the truncation of the operator expansion and the omission of higher-order terms.

Although EFT operators are typically of higher mass dimensions and appear non-renormalizable in the traditional sense, the EFT framework remains predictive through a systematic renormalization process. In an EFT, divergences that arise at a given order in the power counting expansion are absorbed by the counterterms associated with operators of the same or lower

dimension. This renormalization procedure ensures that predictions remain finite and that the EFT expansion is well behaved order by order.

Similar to the running couplings of the SM[1], the Wilson coefficients of the EFT are not constant parameters but evolve with the energy scale according to the renormalization group equations (RGEs). These equations are derived by imposing that the effective action is independent of the renormalization scale μ. In practice, this leads to the condition

$$\mu \frac{d}{d\mu} \langle O \rangle \, C(\mu) = 0 \,, \tag{3.2}$$

where $\langle O \rangle$ denotes the matrix element of an effective operator O and $C(\mu)$ is its corresponding Wilson coefficient.

More explicitly, the RGEs take the form

$$\mu \frac{d}{d\mu} C_i(\mu) = \gamma_{ij} C_j(\mu) \,, \tag{3.3}$$

where the anomalous dimension matrix γ_{ij} encodes the mixing among different operators under renormalization. This mixing is a key feature of EFTs, as operators that are independent at one scale can become correlated at another due to quantum corrections.

The RGEs serve several important purposes in the EFT framework. First, they ensure that physical observables remain independent of the renormalization scale, providing a consistent framework for comparing theoretical predictions with experimental data. Moreover, they allow for the resummation of large logarithms. These logarithms of the form $\log(\mu/\Lambda)$ arise from loop corrections and can spoil the convergence of the perturbative expansion, especially if there is a significant separation between the energy scale μ and the cutoff scale Λ. By solving the RGEs, these logarithms are resummed to all orders, improving the convergence of the EFT expansion.

Finally, the RGEs bridge the gap between the high-energy scale encoded in the Wilson coefficients and the low-energy scale of the observable processes. By evolving the Wilson coefficients from the high-energy scale at which they are matched to the full UV theory down to the low-energy scale at which measurements are performed, the RGEs provide a systematic framework for connecting the UV and IR physics. Thus, renormalization via the RGEs is not only essential for maintaining the consistency and predictability of the EFT, but to ensure that the predictions remain reliable over a wide range of energy scales.

In summary, EFTs provide a systematic framework for connecting high-energy theories to low-energy phenomena. By organizing the effective Lagrangian through operator expansion and power counting, and by systematically matching and employing the RGE running the Wilson coefficients, low-energy observables can be reliably predicted without detailed knowledge of the underlying UV theory. One of the most prominent applications of EFTs is the search for new physics beyond the Standard Model, where they offer a largely model-independent framework to parameterize the effects of unknown high-energy dynamics. In the following section, we explore this application in more detail in the context of the Standard Model Effective Field Theory (SMEFT).

[1] Not to be confused with the team 'running couplings' of the TU Dortmund Campusrun.

3.2. The Standard Model Effective Field Theory

The Standard Model Effective Field Theory (SMEFT) [23] is a theoretical framework that extends the SM by incorporating potential effects of heavy BSM physics above the electroweak (EW) scale. By parameterizing the effects of unknown high-energy dynamics in terms of higher-dimensional operators and Wilson coefficients, the SMEFT provides a systematic and largely model-independent approach to capture the indirect impact of new physics at energy scales of colliders. In this section, we introduce the theoretical foundation of the SMEFT[2], outline the flavor assumptions adopted in our analysis and present the relevant subset of operators.

3.2.1. Theoretical Foundations of the SMEFT

The SMEFT provides a natural extension of the SM within the broader framework of EFTs. In this approach, the SM is considered to be the low-energy limit of a more fundamental theory, where the effects of unknown UV dynamics are systematically encoded as small deviations from the SM predictions.

The SMEFT Lagrangian is organized as an expansion in higher-dimensional operators $O_i^{(d)}$

$$\mathcal{L}_{\text{SMEFT}} = \mathcal{L}_{\text{SM}} + \sum_{d>4} \sum_i \frac{C_i^{(d)}}{\Lambda^{d-4}} O_i^{(d)} \,, \tag{3.4}$$

where d denotes the mass dimension of the operator, Λ represents the scale of NP, and the Wilson coefficients $C_i^{(d)}$ encode the strength of BSM effects. The sum runs over all dimensions $d > 4$ and all operators $O_i^{(d)}$ constructed from the SM fields and their derivatives that are invariant under the SM gauge group $SU(3)_C \times SU(2)_L \times U(1)_Y$. The suppression by Λ^{d-4} ensures that the SMEFT Lagrangian reduces to the SM Lagrangian in the low energy limit ($E^2 \ll \Lambda^2$), where E is the characteristic energy of the process. This structure represents a perturbative expansion in terms of v^2/Λ^2 or E^2/Λ^2, depending on the process and operators under consideration. Consequently, the validity of the SMEFT relies on a sufficient separation of scales $\Lambda \gg v, E$.

Besides the necessary scale separation, the SMEFT requires NP to be weakly coupled, i.e. that the Wilson coefficients $C_i^{(d)}$ are sufficiently small so that $C_i^{(d)}/\Lambda^{d-4} \ll 1$. This ensures perturbativity of the SMEFT expansion and that NP effects can be treated as small corrections to the SM. Moreover, the SMEFT framework implies a linear realization of electroweak symmetry breaking, where the physical Higgs boson is embedded in an $SU(2)_L$ doublet with hypercharge $Y = 1/2$ as postulated in the SM [59–63] (see Sec. 2.1). In contrast, some BSM models predict a non-linear realization, in which the Higgs boson arises, for example, as a composite Nambu Goldstone boson of a new strong interaction (see e.g. [113, 138, 139]). In such cases, the SMEFT can be extended to include non-linear realizations of the electroweak symmetry breaking, as exemplified by the Higgs Effective Field Theory (HEFT) [140, 141]. Given the experimental evidence [142, 143] that the dominantly $J^P = 0^+$ scalar boson discovered at the LHC in 2012 [12, 13] is indeed the fundamental particle predicted by the Brout–Englert–Higgs mechanism of the SM [59, 61], we focus on the linear realization in this work.

Apart from these caveats, the SMEFT provides a largely model-independent framework for parameterizing NP effects. Since they encode the effects of unknown BSM physics, the Wilson

[2] For a recent review, see also e.g. [137]

coefficients $C_i^{(d)}$ are the parameters of interest that can provide crucial insights into the underlying UV dynamics. By fitting the SMEFT to experimental data, we can constrain these coefficients and infer information about the nature of the underlying NP. In order to probe a concrete BSM model, the SMEFT is matched to the corresponding theory at the scale Λ, which fixes the Wilson coefficients in terms of the parameters of the full theory[3].

At dimension $d = 5$, the SMEFT features only one gauge-invariant operator known as the Weinberg operator $O_W = (\tilde{\varphi}^\dagger L)^T C(\tilde{\varphi}^\dagger L)$, where C denotes the charge conjugation operator, and $\tilde{\varphi}_i = \epsilon_{ij}(\varphi_j)^*$, with ϵ_{ij} representing the totally antisymmetric epsilon-tensor with $\epsilon_{12} = +1$. The Weinberg operator violates lepton number conservation and gives rise to neutrino masses after EWSB. Given that lepton number violation is tightly constrained by experimental data, the corresponding NP scale Λ is bounded to be above $\sim 10^{14}$ GeV [150, 151]. More generally, all operators at odd dimensions induce lepton or baryon number violation and are therefore subject to strong experimental constraints [152–155]. As our analysis focuses on observables that conserve these quantum numbers, we restrict our attention to operators of even dimensions.

With increasing mass dimension, the number of operators grows rapidly [156–158]. For instance, the SMEFT Lagrangian at dimension $d = 6$ comprises 76 baryon-number-conserving operators, whereas this number increases to 895 at dimension $d = 8$ [158]. Given the vast number of operators, we restrict our analysis to dimension-six operators. This choice is further motivated by the fact that dimension-six operators are the leading lepton-number-conserving contributions in the SMEFT expansion and are expected to dominate the effects of NP at the EW scale, while higher-dimensional operators are suppressed by additional powers of v^2/Λ^2 and are consequently subdominant.

Possible dimension-eight effects

An important caveat is that the terms arising from the squared amplitude of dimension-six contributions are formally of the same order in $1/\Lambda^2$ as the interference terms from dimension-eight operators with the SM, as we illustrate in the following. In general, the amplitude for a lepton and baryon number conserving process can be written as

$$\mathcal{A} = \mathcal{A}_{\text{SM}} + \sum_i \frac{C_i^{(6)}}{\Lambda^2}\mathcal{A}_i^{6,\text{lin}} + \sum_i \frac{C_i^{(8)}}{\Lambda^4}\mathcal{A}_i^{8,\text{lin}} + \mathcal{O}\left(\frac{1}{\Lambda^6}\right) , \tag{3.5}$$

where $\mathcal{A}_{\text{SM}}$ is the SM amplitude, the term $\mathcal{A}_i^{6,\text{lin}}$ is the linear contributions from dimension-six operators, and $\mathcal{A}_i^{8,\text{lin}}$ denotes the contributions from dimension-eight operators[4]. Since physical observables are typically proportional to the cross section depending on the square of the amplitude, we have

$$\begin{aligned}\sigma \sim & |\bar{\mathcal{A}}_{\text{SM}}|^2 + \frac{1}{\Lambda^2}\sum_i C_i^{(6)} 2\text{Re}\left[\mathcal{A}_{\text{SM}}\mathcal{A}_i^{6,\text{lin}}\right] \\ & + \frac{1}{\Lambda^4}\sum_{i,j} C_i^{(6)} C_j^{(6)} \left(\mathcal{A}_i^{6,\text{lin}}\right)^\dagger \mathcal{A}_j^{6,\text{lin}} + \frac{1}{\Lambda^4}\sum_i C_i^{(8)} 2\text{Re}\left[\mathcal{A}_{\text{SM}}\mathcal{A}_i^{8,\text{lin}}\right] + \mathcal{O}\left(\frac{1}{\Lambda^6}\right) ,\end{aligned} \tag{3.6}$$

where the first line contains the SM contribution and the interference terms from dimension-six operators, while the second line contains the term quadratic in the dimension-six Wilson

[3] Various methods and automated tools have been developed in the literature, see e.g. [144–149]

[4] In the LEFT, additional terms from double insertions of dimension-six terms arise (see Fig. (3.25)), which only contribute via interference at order $1/\Lambda^4$.

coefficients and the interference terms from dimension-eight operators. Notice that both the terms quadratic in the dimension-six Wilson coefficients ($\sim C_i^6 C_j^6$) and the interference terms from dimension-eight operators ($\sim C_i^8$) are of order $1/\Lambda^4$.

We include the quadratic terms of the dimension-six Wilson coefficients in our analysis to constrain several operators that do not interfere with the SM, such as the dipole operators and the LFV operators. They further help the convergence of the fit and allow us to break otherwise flat directions in the parameter space. We do, however, not consider the interference terms from dimension-eight operators. As dimension-eight operators are less constrained by symmetry arguments [159], the number of Wilson coefficients $C_i^{(8)}$ at this dimension is significantly larger than the number of dimension-six operators $C_i^{(6)}$, making it challenging to extract meaningful information from experimental data. For this reason, a systematic inclusion of dimension-eight operators lies beyond the scope of this work and is left for future studies.

Moreover, the effects of dimension-eight operators are typically subleading, since new physics effects in many BSM models are predominantly mediated by dimension-six operators. In these cases, the associated Wilson coefficients are expected to be larger or more directly linked to the leading new physics effects, while the contributions from dimension-8 operators are comparatively suppressed by additional powers of the high energy scale Λ. Consequently, including the squared dimension-6 terms is an effective approximation to capture the leading $1/\Lambda^4$ corrections, with the understanding that the neglected dimension-8 contributions are subdominant within the energy regime and precision of many current analyses.

Important exceptions are processes that receive contributions only at the dimension-eight due to symmetry or kinematic constraints that forbid dimension-six terms [159, 160]. For example, in the Drell-Yan process, while the dominant new physics contributions often arise from dimension-six four-fermion interactions, specific dimension-8 operators can generate additional momentum-dependent corrections that affect the tails of kinematic distributions [161, 162]. Similarly, in the electroweak sector, anomalous quartic gauge couplings appear first at dimension-8, offering new Lorentz structures that can modify multi-boson scattering amplitudes [163].

In the flavor sector, there are cases where four-fermion operators relevant for neutral meson mixing or rare decay processes emerge at dimension-8 when the corresponding dimension-6 contributions are absent or suppressed [164]. Although current experimental data typically do not require the inclusion of these operators to achieve a good fit, they represent an important source of systematic uncertainty. Moreover, certain BSM models do not induce dimension-six operators, so that the dimension-eight operators become the leading contributions [159, 165]. For instance in some composite Higgs models, a non-linearly realized symmetry can protect the Higgs from acquiring large corrections at dimension six, so that leading deviations from the Standard Model may then first appear at dimension-eight [165].

Several recent studies (e.g. [159, 161, 165–168]) have investigated the impact of dimension-eight operators on phenomenology. These works have demonstrated that with current data, the impact of dimension-eight operators is typically at the $\mathcal{O}(1\%)$ level, which is negligible compared to the uncertainties associated with the dimension-six operators. However, as experimental and theoretical precision improves, especially at high-energy colliders or in high-statistics flavor measurements, the contributions from dimension-eight operators may become more relevant and warrant further investigation.

Operator basis

At a given mass dimension d, the set of possible operators $O_i^{(d)}$ is not unique because different operators can be related by field redefinitions or integration by parts. Such relations introduce redundancies unless a basis of linearly independent operators is chosen. For dimension-six operators, the first complete, non-redundant basis was constructed by Grzadkowski et al. [169] and is commonly known to as the Warsaw basis. Other operator bases include the strongly-interacting light Higgs (SILH) basis[170, 171], which is tailored to UV-complete composite Higgs models, and the Hagiwara-Ishihara-Szalapski-Zeppenfeld (HISZ) basis [172], which is often employed in electroweak precision studies[5]. In this work, we adopt the Warsaw basis because it minimizes the number of derivatives by making use of the equations of motion, a feature particularly advantageous for our focus on fermionic observables.

To further reduce the number of free parameters, we select a subset of operators most relevant to our observables and our focus on flavor and fermionic NP. In particular, we restrict our analysis to dipole operators, Higgs-current operators, and leptonic as well as semileptonic four-fermion operators. We do not consider four-quark operators, since they are already strongly constrained by dijet production [25, 38]. Similarly, we neglect Yukawa operators because their impact on our observables is subdominant. For simplicity, we assume that the Wilson coefficients are real-valued, implying no additional CP violation in the SMEFT. In order to ensure the validity of the SMEFT approach across all observables considered in this work, we assume $\Lambda = 10\,\text{TeV}$ in our numerical analyses. We employ the one-loop RGEs [173–175] to evolve the SMEFT Wilson coefficients from the high NP scale Λ down to the relevant energy scales of the observables, which are detailed in the corresponding sections. For the numerical integration of the RGEs we employ the python package `Wilson` [176].

Input parameters

In the SMEFT framework, the extraction of the Lagrangian parameters from experimental data can be affected by the presence of higher-dimensional operators. In practice, this implies that the Wilson coefficients can shift the numerical values of the input parameters that are determined via precision observables [137, 175, 177–181]. In the electroweak sector, for instance, SMEFT corrections can modify the relationships between Lagrangian parameters that are interrelated by the electroweak theory. As an example, the Fermi coupling G_F, typically extracted from the muon lifetime, may receive contributions from four-lepton operators or leptonic current operators that alter the muon decay width.

To minimize these effects, we adopt the $\{\alpha_{\text{em}}, m_W, m_Z\}$ input scheme. This choice is motivated by the fact that, for the subset of operators considered in this work, the relations among these parameters remain unaffected. More details, including the numerical values of the input parameters, are provided in Appendix A .

From these input values, we can derive other quantities, such as the weak mixing angle $\sin^2\theta_W$ and the Higgs vacuum expectation value v. The weak mixing angle is determined from the relation

$$\sin^2\theta_W = 1 - \frac{m_W^2}{m_Z^2}\,, \tag{3.7}$$

[5] Note that both the SILH and HISZ bases are not complete, that is, they do not encompass all possible dimension-six operators.

at tree-level. Due to higher order corrections and the running of the SM parameters, the effective mixing angle used for phenomenological applications is shifted by a factor of $(1 + \delta \sin^2 \theta_W) = 1.0349(3)$ [18]. For the Z-pole observables, many additional higher order contribution must be included, which gives another factor of $\kappa_b = 1.0068$ for b-quark observables and a factor $\kappa_f = 1.0014$ for the couplings to the Z boson to other fermions [18].

The Fermi constant G_F is at tree-level related to the input parameters as

$$G_F = \frac{\pi \alpha_{\text{em}} m_Z^2}{\sqrt{2} m_W^2 (m_Z^2 - m_W^2)} \,. \tag{3.8}$$

The numerical value of G_F is modified by higher order corrections, which give rise to a factor of $1 + \delta_R$ with $\delta_R = 0.03686(21)$ [18]. The Higgs vacuum expectation value is defined as

$$v = \frac{1}{\sqrt{\sqrt{2} G_F}} \,. \tag{3.9}$$

Another set of parameters that may be significantly impacted by SMEFT corrections are the CKM matrix elements, which are primarily determined from precision flavor observables such as meson mixing and leptonic meson decays. The SMEFT introduces corrections to these processes, which can be parameterized in terms of the Wilson coefficients [182]. In order to account for possible SMEFT contributions in the extraction of the CKM matrix elements, we treat the Wolfenstein parameters in Eq. 2.16 as free parameters in the global fit.

3.2.2. MFV in the SMEFT

In full generality, the SMEFT comprises 2499 free parameters at dimension $d = 6$ when generation indices are fully accounted for, the majority of which originate from four-fermion operators. This extensive parameter space poses significant challenges for constraining the SMEFT with experimental data in full generality. However, by imposing well-motivated flavor patterns, the number of free parameters can be strongly reduced[6]. Common flavor assumptions include a $U(3)^5$ symmetry, corresponding to the maximal flavor symmetry of the SM among the quarks and leptons, and a $U(2)^3$ symmetry, which singles out the third generation of quarks while treating the first two generations as identical [183–187]. Such assumptions not only simplify the analysis, but also enable us to connect different sectors and study correlations and systematic deviations across various processes. In this work, we adopt the Minimal Flavor Violation (MFV) hypothesis [41] in the quark sector following Ref. [1][7].

The MFV hypothesis is a well-motivated framework rooted in the observation that the SM is largely invariant under the flavor symmetry $\mathcal{G}_f = U(3)_Q \times U(3)_U \times U(3)_D$ regarding the quark fields, with the exception of the Yukawa sector [41][8]. Although the Yukawa interactions explicitly break this symmetry, in MFV it is formally restored by promoting the Yukawa couplings to spurions. Spurions are auxiliary fields that are assigned quantum numbers and transformation properties under the symmetry, even though they do not correspond to dynamical degrees of

[6] For dedicated analyses of flavor in the SMEFT, see e.g. [183]

[7] For additional analyses of the SMEFT with MFV, see e.g. [33, 37–39, 183, 188, 189].

[8] This symmetry can be extended to also include the lepton fields. As we perform lepton-flavor specific fits, we only apply MFV in the quark sector.

freedom. In particular, the Yukawa matrices transform under $\mathcal{G}_f$ as

$$Y_u : (\mathbf{3}, \bar{\mathbf{3}}, \mathbf{1}), \qquad Y_d : (\mathbf{3}, \mathbf{1}, \bar{\mathbf{3}}), \tag{3.10}$$

while the SM fields transform as

$$Q : (\mathbf{3}, \mathbf{1}, \mathbf{1}), \qquad U : (\mathbf{1}, \mathbf{3}, \mathbf{1}), \qquad D : (\mathbf{1}, \mathbf{1}, \mathbf{3}). \tag{3.11}$$

With this assignment, the Yukawa terms become invariant under $\mathcal{G}_f$.

Building on this concept, the MFV hypothesis posits that all sources of flavor violation, both within and beyond the SM, originate solely from the Yukawa matrices. As a result, flavor-violating effects are naturally suppressed, especially for the light fermions of the first and second generation, consistent with the strong suppression of FCNCs observed in experimental data. In the SMEFT, this pattern is implemented by expanding the Wilson coefficients in terms of Yukawa spurion insertions, thereby preserving the formal invariance under $\mathcal{G}_f$. For the various quark bilinears, the expansions take the form

$$\begin{aligned}
C_{ij}^{\bar{Q}Q} &= \left(a_1 \mathbb{1} + a_2 Y_u Y_u^\dagger + a_3 Y_d Y_d^\dagger + \dots\right)_{ij}, \\
C_{ij}^{\bar{U}U} &= \left(b_1 \mathbb{1} + b_2 Y_u^\dagger Y_u + \dots\right)_{ij}, \\
C_{ij}^{\bar{D}D} &= \left(c_1 \mathbb{1} + c_2 Y_d^\dagger Y_d + \dots\right)_{ij}, \\
C_{ij}^{\bar{Q}U} &= \left[\left(d_1 \mathbb{1} + d_2 Y_u Y_u^\dagger + d_3 Y_d Y_d^\dagger + \dots\right) Y_u\right]_{ij}, \\
C_{ij}^{\bar{Q}D} &= \left[\left(e_1 \mathbb{1} + e_2 Y_u Y_u^\dagger + e_3 Y_d Y_d^\dagger + \dots\right) Y_d\right]_{ij}, \\
C_{ij}^{\bar{U}D} &= \left[Y_u^\dagger \left(f_1 \mathbb{1} + f_2 Y_u^\dagger Y_u + f_3 Y_d^\dagger Y_d + \dots\right) Y_d\right]_{ij},
\end{aligned} \tag{3.12}$$

where the a_i etc. are dimensionless coefficients, and the ellipses denote higher-order spurion insertions.

For the expansion to be considered natural, the coefficients a_i should display a hierarchy $a_i \gg a_{i+1}$ (for all other coefficients analogously), indicating that the Wilson coefficients are dominated by their leading-order contributions. Note, however, that this hierarchy is not a strict requirement, since the expansion serves rather as a parameterization of the SMEFT flavor structure than as a perturbative expansion. Similar spurion expansions can be constructed for other quark bilinears, ensuring that the MFV structure is reflected in the pattern of the SMEFT Wilson coefficients.

Due to the strong hierarchy in the Yukawa couplings, we assume $Y_d \sim 0$ and $Y_u \sim \text{diag}(0, 0, y_t)$, with the top Yukawa $y_t \sim 1$. This assumption has significant phenomenological implications. In particular, interactions suppressed by the light Yukawas effectively vanish, implying that chirality flipping interactions are only present for the top quark in this setup. Furthermore, no right-handed charged current interactions or right-handed flavor-changing neutral currents (FCNCs) are induced in this framework. These simplifications further reduce the number of relevant operators, as they particularly eliminate down-type dipole and scalar operators. Tab. 3.1 summarizes the set of operators considered in this work, based on the flavor assumptions and simplifications outlined above.

Dipole		
$\mathcal{O}_{\substack{uB\\ij}}$ $(\bar{q}_i\sigma^{\mu\nu}u_j)\tilde{\varphi}B_{\mu\nu}$	$\mathcal{O}_{\substack{uW\\ij}}$ $(\bar{q}_i\sigma^{\mu\nu}u_j)\tau^I\tilde{\varphi}W^I_{\mu\nu}$	$\mathcal{O}_{\substack{uG\\ij}}$ $(\bar{q}_i\sigma^{\mu\nu}T^Au_j)\tilde{\varphi}G^A_{\mu\nu}$
$\mathcal{O}_{\substack{eB\\ij}}$ $(\bar{l}_i\sigma^{\mu\nu}e_j)\varphi B_{\mu\nu}$	$\mathcal{O}_{\substack{eW\\ij}}$ $(\bar{l}_i\sigma^{\mu\nu}e_j)\tau^I\varphi W^I_{\mu\nu}$	
Higgs-Current		
$\mathcal{O}^{(1)}_{\substack{\varphi l\\ij}}$ $(\varphi^\dagger i\overleftrightarrow{D}_\mu\varphi)(\bar{l}_i\gamma^\mu l_j)$	$\mathcal{O}^{(3)}_{\substack{\varphi l\\ij}}$ $(\varphi^\dagger i\overleftrightarrow{D}^I_\mu\varphi)(\bar{l}_i\tau^I\gamma^\mu l_j)$	$\mathcal{O}_{\substack{\varphi e\\ij}}$ $(\varphi^\dagger i\overleftrightarrow{D}_\mu\varphi)(\bar{e}_i\gamma^\mu e_j)$
$\mathcal{O}^{(1)}_{\substack{\varphi q\\ij}}$ $(\varphi^\dagger i\overleftrightarrow{D}_\mu\varphi)(\bar{q}_i\gamma^\mu q_j)$	$\mathcal{O}^{(3)}_{\substack{\varphi q\\ij}}$ $(\varphi^\dagger i\overleftrightarrow{D}^I_\mu\varphi)(\bar{q}_i\tau^I\gamma^\mu q_j)$	$\mathcal{O}_{\substack{\varphi u\\ij}}$ $(\varphi^\dagger i\overleftrightarrow{D}_\mu\varphi)(\bar{u}_i\gamma^\mu u_j)$
$\mathcal{O}_{\substack{\varphi d\\ij}}$ $(\varphi^\dagger i\overleftrightarrow{D}_\mu\varphi)(\bar{d}_i\gamma^\mu d_j)$		
Four-Lepton		
$\mathcal{O}_{\substack{ll\\ijkl}}$ $(\bar{l}_i\gamma_\mu l_j)(\bar{l}_k\gamma^\mu l_l)$	$\mathcal{O}_{\substack{ee\\ijkl}}$ $(\bar{e}_i\gamma_\mu e_j)(\bar{e}_k\gamma^\mu e_l)$	$\mathcal{O}_{\substack{le\\ijkl}}$ $(\bar{l}_i\gamma_\mu l_j)(\bar{e}_k\gamma^\mu e_l)$
Semileptonic Four-Fermion		
$\mathcal{O}^{(1)}_{\substack{lq\\ijkl}}$ $(\bar{l}_i\gamma_\mu l_j)(\bar{q}_k\gamma^\mu q_l)$	$\mathcal{O}^{(3)}_{\substack{lq\\ijkl}}$ $(\bar{l}_i\gamma_\mu\tau^I l_j)(\bar{q}_k\gamma^\mu\tau^I q_l)$	$\mathcal{O}_{\substack{qe\\ijkl}}$ $(\bar{q}_i\gamma_\mu q_j)(\bar{e}_k\gamma^\mu e_l)$
$\mathcal{O}_{\substack{lu\\ijkl}}$ $(\bar{l}_i\gamma_\mu l_j)(\bar{u}_k\gamma^\mu u_l)$	$\mathcal{O}_{\substack{ld\\ijkl}}$ $(\bar{l}_i\gamma_\mu l_j)(\bar{d}_k\gamma^\mu d_l)$	$\mathcal{O}^{(1)}_{\substack{lequ\\ijkl}}$ $(\bar{l}^m_i e_j)\epsilon_{mn}(\bar{q}^n_k u_l)$
$\mathcal{O}_{\substack{eu\\ijkl}}$ $(\bar{e}_i\gamma_\mu e_j)(\bar{u}_k\gamma^\mu u_l)$	$\mathcal{O}_{\substack{ed\\ijkl}}$ $(\bar{e}_i\gamma_\mu e_j)(\bar{d}_k\gamma^\mu d_l)$	$\mathcal{O}^{(3)}_{\substack{lequ\\ijkl}}$ $(\bar{l}^m_i\sigma_{\mu\nu}e_j)\epsilon_{mn}(\bar{q}^n_k\sigma^{\mu\nu}u_l)$

Table 3.1: Dimension-six SMEFT Wilson coefficients considered in this work.

The simplified structure of Y_u further implies that all higher-order insertions of the up-type Yukawa spurion imprint as the same pattern. In practice, because all powers of $Y_u \sim \text{diag}(0,0,y_t)$ effectively only produce a non-zero contribution for the C_{33} coefficient, we can effectively sum all higher-order contributions into one effective parameter

$$a_\epsilon = \sum_{i=1}^{\infty} y_t^{2i}\, a_{1+2i}\,, \tag{3.13}$$

which encapsulates all higher-order insertions of the up-type Yukawa spurion[9]. In this way, the otherwise infinite series of Yukawa insertions is reduced to a small number of effective parameters, thereby significantly streamlining the analysis of the SMEFT flavor structure. The resulting simplified expansion for the Wilson coefficients can be written as

$$C_{ij}^{\bar{Q}Q} = a_1\left(a_1\delta_{ij} + a_\epsilon\delta_{i3}\delta_{j3}\right)\,, \tag{3.14}$$

where the a_ϵ term captures the higher-order insertions of the up-type Yukawa spurion, while the a_1 term represents the leading-order contribution.

In order to confront the SMEFT predictions with experimental data, we rotate the Wilson coefficients into the mass basis introduced in Sec. 2.1, which follows from the diagonalization of the Yukawa terms.

In most cases, the rotations and higher-order terms can be absorbed by redefining the Wilson coefficients. However, they have non-trivial phenomenological consequences for the $\bar{Q}Q$ and

[9] A similar argument can be applied more general using the Cayley-Hamilton theorem [190, 191], effectively stating that only a finite number of powers of the Yukawa spurion are independent.

$\bar{U}U$ bilinears. In particular, rotating the $\bar{Q}Q$ bilinears gives

$$\begin{aligned}\bar{Q}_i Q_j C_{ij}^{\bar{Q}Q} =& \bar{u}_i u_j (a_1 \delta_{ij} + a_\epsilon \delta_{i3}\delta_{j3}) + \bar{d}_i d_j (a_1 \delta_{ij} + a_\epsilon V_{ti}^* V_{tj}) \\ &+ \bar{u}_i d_j V_{ij} (a_1 + a_\epsilon \delta_{i3}) + \bar{d}_i u_j V_{ji}^* (a_1 + a_\epsilon \delta_{j3}) \,,\end{aligned} \tag{3.15}$$

where we see that a_ϵ induces flavor-changing neutral currents (FCNCs) in the down quark sector, suppressed by corresponding CKM factors $V_{ti}V_{tj}^*$. For these CKM factors, we employ fixed values instead of the free parameters in the global fit to improve numerical stability of the fit. This is further motivated because the MFV expansion is used as parameterization rather than a fundamental description of the flavor dynamics in this work. We obtained these fixed values for the CKM matrix following Refs. [182, 188], as described in more detail in Appendix B .

Conversely, the up-quark sector remains flavor-diagonal, since up-type FCNCs would be proportional to the small down-quark Yukawa couplings, which we neglect in this work. For the $\bar{U}U$ bilinears, the higher-order terms yield an additional contribution to the top-quark coupling, effectively mimicking a $U(2)^3$ flavor pattern. Another phenomenological consequence of this pattern is that charged current interactions are suppressed by a CKM factor V_{ij} for a $u_i \to d_j$ transition, similar to the SM. Charged current interactions involving the top quark additionally receive a contribution from the higher-order terms with the same CKM suppression as the leading term.

To further reduce the dependence of our fit results on the NP scale Λ, we rescale the Wilson coefficients by a factor of v^2/Λ^2[10]. For the operators containing bilinears whose rotations and higher-order MFV terms can be absorbed, we define the rescaled Wilson coefficients as

$$\tilde{C} = \frac{v^2}{\Lambda^2}\, a_{\text{MFV}} C \,, \tag{3.16}$$

where a_{MFV} denotes the MFV expansion for the corresponding operator. For the $\bar{Q}Q$ and $\bar{U}U$ bilinears, the higher order spurion insertions cannot be fully absorbed and they thus lead to phenomenological consequences. While the MFV expansion naturally introduces the parameters a_1 and a_ϵ, this parameterization is not optimal to investigate the synergies between the different sectors in the SMEFT. To this end, we introduce the parameters

$$r_L = \frac{a_\epsilon^{\bar{Q}Q}}{a_1^{\bar{Q}Q}} \,, \qquad r_R = \frac{a_\epsilon^{\bar{U}U}}{a_1^{\bar{U}U}} \,, \tag{3.17}$$

which quantify the relative size of the higher-order Yukawa insertions compared to the leading-order term[11]. This allows us to parameterize the Wilson coefficients for the $\bar{Q}Q$ and $\bar{U}U$ bilinears as

$$C_{ij} = \tilde{C}\left(\delta_{ij} + r_{L/R}\delta_{i3}\delta_{j3}\right) \,, \tag{3.18}$$

in the flavor basis, with

$$\tilde{C} = \frac{v^2}{\Lambda^2}\, a_1 C \,. \tag{3.19}$$

[10] With this rescaling, the only effect of Λ arises from the RGE running.
[11] In Ref. [1], these parameters are denoted as γ_a and γ_b, respectively.

The mass basis coefficients are obtained as outlined above. Taken together, this gives the following mass-basis parameterization for the different quark currents:

$$\begin{aligned}
&\bar{u}_{\underset{i}{L}} u_{\underset{j}{L}} \sim \tilde{C}\left(\delta_{ij} + r_L \delta_{i3}\delta_{j3}\right) , && \bar{d}_{\underset{i}{L}} d_{\underset{j}{L}} \sim \tilde{C}\left(\delta_{ij} + r_L V_{ti}^* V_{tj}\right) ,\\
&\bar{u}_{\underset{i}{L}} d_{\underset{j}{L}} \sim \tilde{C} V_{ij}\left(1 + r_L \delta_{i3}\right) , && \bar{d}_{\underset{i}{L}} u_{\underset{j}{L}} \sim \tilde{C} V_{ji}^*\left(1 + r_L \delta_{j3}\right) ,\\
&\bar{u}_{\underset{i}{R}} u_{\underset{j}{R}} \sim \tilde{C}\left(\delta_{ij} + r_R \delta_{i3}\delta_{j3}\right) , && \bar{d}_{\underset{i}{R}} d_{\underset{j}{R}} \sim \tilde{C}\delta_{ij} ,\\
&\bar{u}_{\underset{i}{R}} d_{\underset{j}{R}} = 0 , && \bar{d}_{\underset{i}{R}} u_{\underset{i}{R}} = 0 ,\\
&\bar{u}_{\underset{i}{L}} u_{\underset{j}{R}} \sim \tilde{C}\delta_{i3}\delta_{j3} , && \bar{d}_{\underset{i}{L}} d_{\underset{i}{R}} = 0 ,\\
&\bar{d}_{\underset{i}{L}} u_{\underset{j}{R}} \sim \tilde{C} V_{ji}^* \delta_{j3} , && \bar{u}_{\underset{i}{L}} d_{\underset{i}{R}} = 0 .
\end{aligned} \tag{3.20}$$

The FCNC contributions are directly proportional to the parameter r_L, rendering it particularly sensitive to flavor observables such as $b \to s$ transitions where the CKM suppression is minimal. In contrast, r_R plays a more prominent role in top-quark observables, as higher-order insertions of the up-type Yukawa spurion predominantly affect the top-quark sector. These parameters need not be universal across all operators, so we allow r_L and r_R to vary independently for each coefficient. We also perform fits assuming universal values for r_L and r_R, which corresponds to scenarios in which the flavor structure of all operators originates from the same underlying dynamic.

Regarding lepton flavor, we consider multiple scenarios. First, we perform lepton-flavor-specific fits by treating each Wilson coefficient C_{ij} as an independent parameter for different lepton flavors i, j. This approach allows us to investigate NP with lepton-flavor non-universal couplings, which arise, for example, in many leptoquark models [192] or in models with gauged lepton flavor symmetries [193]. Such an approach enables us to probe deviations in each lepton flavor separately, without imposing a priori assumptions about the flavor structure of BSM physics.

We also examine scenarios with lepton-flavor universal couplings. In the simplest case, we assume a lepton-flavor diagonal coupling $C^{\text{LD}} = \delta_{ij} C_{ij}$, which is motivated, by observations in $b \to s$ transitions, indicating that lepton-flavor non-universal effects are small among electron and muon couplings [44, 45]. Additionally, we consider a lepton-flavor violating scenario C^{LFV}, in which all off-diagonal elements are assumed to have the same magnitude. This pattern can naturally arise in models with inherent LFV interactions, such as seesaw models or models with heavy vector-like leptons. Given that LFV processes are strongly constrained by experimental data [18], the scale associated with these couplings is expected to be significantly higher than the scale of the lepton-flavor diagonal interactions.

3.3. The Low Energy Effective Field Theory

While the SMEFT provides a useful framework for observables at and above the electroweak (EW) scale, many precision flavor observables and other low-energy processes require a dedicated EFT that is valid well below the EW scale. The Low Energy Effective Field Theory (LEFT) provides a systematic EFT description of the interactions among the SM particles at energies where the top quark as well as the W, Z and Higgs boson have been integrated out. In effect, LEFT is a systematic extension of the Fermi theory (discussed in Sec. 3.1) that not only captures all low-energy phenomena but also accommodates possible BSM contributions.

In constructing the LEFT, only the light quarks, the leptons, and the massless gauge bosons are retained as dynamical fields. In this low-energy regime, the full SM gauge group $SU(3)_C \times SU(2)_L \times U(1)_Y$ is broken down to $SU(3)_C \times U(1)_{\text{em}}$. Consequently, the $SU(2)_L$ symmetry that links the left-handed fields in the SMEFT is not manifest in the LEFT, and the left-handed fermions are treated as independent fields. Moreover, the LEFT operators are constructed using the photon field strength $F_{\mu\nu}$ directly rather than the hypercharge or the weak gauge bosons as in the SMEFT.

The LEFT coefficients can be expressed in terms of the SMEFT coefficients by matching the two EFTs at the EW scale. We perform the matching at tree level at the scale $\mu = m_W$, which can be obtained trivially by equating the effective Lagrangians[12]. Tab. 3.2 lists the relevant LEFT operators that match onto the SMEFT operators considered in this work. In order to distinguish the operators and coefficients of the SMEFT and the LEFT, we denote the former as O and C and the latter as $\mathcal{Q}$ and $\mathcal{C}$, respectively. We provide the full analytical matching expressions in App. C .

Dipole					
$\mathcal{Q}_{ij}^{e\gamma}$	$(\bar{\ell}_{L\,i}\sigma^{\mu\nu}\ell_{R\,j})F_{\mu\nu}$				
LL					
$\mathcal{Q}_{ijkm}^{V,LL}$	$(\bar{\ell}_{L\,i}\gamma_\mu\ell_{L\,j})(\bar{\ell}_{L\,k}\gamma^\mu\ell_{L\,l})$	$\mathcal{Q}_{ijkm}^{V,LL}$	$(\bar{\nu}_{L\,i}\gamma_\mu\nu_{L\,j})(\bar{\ell}_{L\,k}\gamma^\mu\ell_{L\,l})$	$\mathcal{Q}_{ijkm}^{V,LL}$	$(\bar{\nu}_{L\,i}\gamma_\mu\nu_{L\,j})(\bar{u}_{L\,k}\gamma^\mu u_{L\,l})$
$\mathcal{Q}_{ijkm}^{V,LL}$	$(\bar{\nu}_{L\,i}\gamma_\mu\nu_{L\,j})(\bar{d}_{L\,k}\gamma^\mu d_{L\,l})$	$\mathcal{Q}_{ijkm}^{V,LL}$	$(\bar{\ell}_{L\,i}\gamma_\mu\ell_{L\,j})(\bar{u}_{L\,k}\gamma^\mu u_{L\,l})$	$\mathcal{Q}_{ijkm}^{V,LL}$	$(\bar{\ell}_{L\,i}\gamma_\mu\ell_{L\,j})(\bar{d}_{L\,k}\gamma^\mu d_{L\,l})$
$\mathcal{Q}_{ijkm}^{V,LL}$	$(\bar{\nu}_{L\,i}\gamma_\mu\ell_{L\,j})(\bar{d}_{L\,k}\gamma^\mu u_{L\,l})$	$\mathcal{Q}_{ijkm}^{V,LL}$	$(\bar{d}_{L\,i}\gamma_\mu d_{L\,j})(\bar{d}_{L\,k}\gamma^\mu d_{L\,l})$		
RR					
$\mathcal{Q}_{ijkm}^{V,RR}$	$(\bar{\ell}_{R\,i}\gamma_\mu\ell_{R\,j})(\bar{\ell}_{R\,k}\gamma^\mu\ell_{R\,l})$	$\mathcal{Q}_{ijkm}^{V,RR}$	$(\bar{\ell}_{R\,i}\gamma_\mu\ell_{R\,j})(\bar{u}_{R\,k}\gamma^\mu u_{R\,l})$	$\mathcal{Q}_{ijkm}^{V,RR}$	$(\bar{\ell}_{R\,i}\gamma_\mu\ell_{R\,j})(\bar{d}_{R\,k}\gamma^\mu d_{R\,l})$
LR					
$\mathcal{Q}_{ijkm}^{V,LR}$	$(\bar{\ell}_{L\,i}\gamma_\mu\ell_{L\,j})(\bar{\ell}_{R\,k}\gamma^\mu\ell_{R\,l})$	$\mathcal{Q}_{ijkm}^{V,LR}$	$(\bar{\nu}_{L\,i}\gamma_\mu\nu_{L\,j})(\bar{\ell}_{R\,k}\gamma^\mu\ell_{R\,l})$	$\mathcal{Q}_{ijkm}^{V,LR}$	$(\bar{\nu}_{L\,i}\gamma_\mu\nu_{L\,j})(\bar{u}_{R\,k}\gamma^\mu u_{R\,l})$
$\mathcal{Q}_{ijkm}^{V,LR}$	$(\bar{\nu}_{L\,i}\gamma_\mu\nu_{L\,j})(\bar{d}_{R\,k}\gamma^\mu d_{R\,l})$	$\mathcal{Q}_{ijkm}^{V,LR}$	$(\bar{\ell}_{L\,i}\gamma_\mu\ell_{L\,j})(\bar{u}_{R\,k}\gamma^\mu u_{R\,l})$	$\mathcal{Q}_{ijkm}^{V,LR}$	$(\bar{\ell}_{L\,i}\gamma_\mu\ell_{L\,j})(\bar{d}_{R\,k}\gamma^\mu d_{R\,l})$
$\mathcal{Q}_{ijkm}^{V,LR}$	$(\bar{u}_{L\,i}\gamma_\mu u_{L\,j})(\bar{\ell}_{R\,k}\gamma^\mu\ell_{R\,l})$	$\mathcal{Q}_{ijkm}^{V,LR}$	$(\bar{d}_{L\,i}\gamma_\mu d_{L\,j})(\bar{\ell}_{R\,k}\gamma^\mu\ell_{R\,l})$		

Table 3.2: LEFT Wilson coefficients induced by the SMEFT operators considered in this work.

In order to connect the LEFT coefficients at the matching scale to the coefficients at the scale of the observables, we employ the one loop RGEs of the LEFT are given in Ref. [195]. We use the python package `Wilson` [176] to evolve the LEFT coefficients from the matching scale down to the energy scale relevant for each observable. Note that, due to the divergence of the QCD coupling α_s at low energies, we do not evolve the coefficients below 2 GeV, which we adopt as the nominal scale for processes at very low energies, such as lepton decays or anomalous magnetic moments.

[12] The one loop matching equations can be found in Ref. [194]. Employing the one loop matching is only necessary when two loop RGEs are available.

In contrast to the SMEFT, the LEFT Wilson coefficients carry explicit mass dimensions, for instance $[\mathcal{C}_{e\gamma}] = -1$ for the dipole operator and $[\mathcal{C}^{V,LL}_{ee}_{ijkm}] = -2$ for the four-fermion operators, since the suppression by the high scales Λ or the Higgs vev v is not factored out. The power counting in the LEFT is determined by the typical energy scales of the processes under consideration and the residual low-energy dynamics.

Another difference between the SMEFT and the LEFT is that the LEFT also receives SM contributions to the Wilson coefficients, while the SMEFT coefficients are all zero in the SM limit. This is because the LEFT is constructed to describe low-energy processes, where the SM contributions are relevant, while the SMEFT is designed to capture the effects of heavy degrees of freedom that are integrated out at high energies. In order to distinguish between the SM and possible BSM contributions, we split the LEFT Wilson coefficients into two parts,

$$\mathcal{C} = \mathcal{C}_{\text{SM}} + \mathcal{C}_{\text{BSM}}\,, \tag{3.21}$$

where $\mathcal{C}_{\text{SM}}$ denotes the SM contributions and $\mathcal{C}_{\text{BSM}}$ the BSM contributions. The SM contributions are obtained by evaluating the LEFT operators in the SM limit, while the BSM contributions arise from the SMEFT operators. In the remainder of this work, we will only refer only to the BSM contributions, unless stated otherwise. The SM contributions are included to compute SM predictions and interference terms.

Matching phenomenology

At tree level, the four-fermion operators in the SMEFT directly match onto the corresponding LEFT operators, preserving the chirality structure. However, because the $SU(2)_L$ symmetry is no longer manifest, the LEFT contains more four-fermion operators than the SMEFT. As a result, the SMEFT imposes correlations among the LEFT operators containing left-handed fields, a feature that can be tested experimentally.

Moreover, the leptonic dipole operators in the SMEFT match onto the LEFT dipole coefficient $\mathcal{C}_{e\gamma}$ as

$$\mathcal{C}^{e\gamma}_{ij} = \frac{1}{\sqrt{2}v}\,\tilde{C}^{e\gamma}_{ij}\,, \tag{3.22}$$

with the linear combination of the SMEFT coefficients

$$\tilde{C}^{e\gamma}_{ij} = \left(\cos\theta_W C^{eB}_{ij} - \sin\theta_W C^{eW}_{ij}\right)\,, \tag{3.23}$$

where $\cos\theta_W$ and $\sin\theta_W$ are the cosine and sine of the weak mixing angle, respectively. The orthogonal combination

$$\tilde{C}^{eZ}_{ij} = \left(\sin\theta_W C^{eB}_{ij} + \cos\theta_W C^{eW}_{ij}\right)\,, \tag{3.24}$$

however, does not match onto the LEFT at tree level. This implies that $\mathcal{C}_{e\gamma}$ in the LEFT results in flat directions in the parameter space of the SMEFT, which can be resolved by a combined fit including SMEFT observables that constrain $\mathcal{C}_{eZ}$.

Within our MFV setup, the only quark dipole contribution induced at tree level in the SMEFT is the top-quark coupling. However, since the top quark is integrated out in the matching to the LEFT, no quark dipole operators are generated at tree level. A similar argument applies to

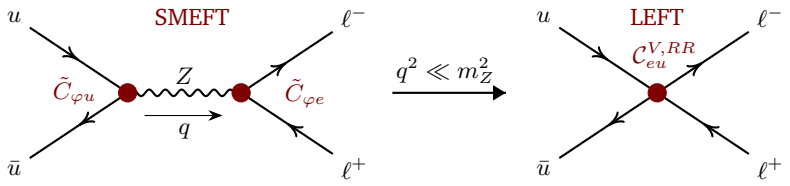

Figure 3.2: Feynman diagrams illustrating the matching of the SMEFT Higgs-current operators to the LEFT four-fermion operators. The left diagram shows the double insertion of the Higgs-current operators, and the right diagram shows the resulting four-fermion LEFT operator after integrating out the Z boson.

the scalar and tensor operators $O_{lequ}^{(1)}$ and $O_{lequ}^{(3)}$, which also do not contribute in the matching procedure. Consequently, the LEFT does not feature scalar or tensor operators in our setup.

The Higgs-current operators in the SMEFT also match onto the LEFT four-fermion operators. In general, the matching also includes double insertions of SMEFT coefficients, for instance

$$\mathcal{C}_{\substack{eu\\ijkl}}^{V,RR} = \frac{1}{v^2}\left(\tilde{C}_{\substack{eu\\ijkl}} - \left(\left(\delta_{ij} 2\mathrm{s}_\theta^2 - \tilde{C}_{\substack{\varphi e\\ij}}\right)\left(-\delta_{kl}\frac{4}{3}\mathrm{s}_\theta^2 - \tilde{C}_{\substack{\varphi u\\ij}}\right)\right)\right), \tag{3.25}$$

as illustrated in Fig. 3.2. In order to maintain a consistent power counting in v/Λ, we distinguish between contributions generated by single insertions (C/Λ^2) and double insertions (C^2/Λ^4) of SMEFT coefficients, so that the double insertions contribute only in the interference terms between the LEFT and SM amplitudes.

The quark Higgs-current operators further induce a four-quark operator in the LEFT, $\mathcal{Q}_{\substack{dd\\ijkl}}^{V,LL}$, even though we do not consider four-quark operators in the SMEFT. This operator is relevant for the mass differences in meson mixing, which we will discuss in Sec. 6.2.1. Other four-quark operators such as those with up-type quarks and different chirality structures are also induced at tree level, but they are not relevant for the observables considered in this work.

Chapter 4

Statistical Methods for EFT Analyses

In modern experimental and theoretical studies alike, the extraction of meaningful results from increasingly complex data sets requires a rigorous and transparent statistical treatment. Accurate quantification and consistent propagation of statistical, systematic, and theoretical uncertainties, including their correlations, are essential for deriving reliable parameter estimates, conducting hypothesis tests, and constructing confidence intervals. Robust uncertainty treatment is particularly crucial when combining multiple measurements or interpreting results within the EFT paradigm.

In this chapter, we present a comprehensive overview of the statistical methods employed in our analysis. We begin by reviewing the fundamentals of statistical inference in Sec. 4.1, comparing frequentist and Bayesian methodologies as outlined in Refs. [196–198]. Sec. 4.2 outlines our fitting procedure, including the treatment of uncertainties and prior selection. Finally, Sec. 4.3 presents toy-model studies to illustrate these concepts, highlighting the impact of marginalization and the choice of priors.

4.1. Statistical Framework

Constraining the Wilson coefficients in the SMEFT Lagrangian demands a robust statistical framework to quantify the agreement between theoretical predictions and experimental data. To this end, a crucial quantity is the likelihood $\mathcal{L}(x\,|\theta)$, which provides a measure of the probability of observing data x given a set of model parameters θ. Maximizing the likelihood allows us to determine the most probable values of the Wilson coefficients, with confidence or credible intervals providing a measure of their uncertainties.

For Gaussian uncertainties, the likelihood of the outcome x_i given the parameters θ can be expressed as

$$\mathcal{L}_i(x_i|\theta) = \frac{1}{\sqrt{(2\pi)\sigma_i^2}} \exp\left(-\frac{(x_i - \mu_i(\theta))^2}{2\sigma_i^2}\right), \tag{4.1}$$

where $\mu_i(\theta)$ is the theoretical prediction as a function of the model parameters θ, and σ_i denotes the total uncertainty. The combined likelihood of a set of statistically independent observables is then given by the product of the likelihoods of all observables

$$\mathcal{L}(x|\theta) = \prod_i \mathcal{L}_i(\theta|x_i)\,, \tag{4.2}$$

allowing for a straightforward combination of various observables in the fit.

In cases where observables are not independent, the likelihood can be extended to account for correlations between observables. This is typically incorporated using the covariance matrix Σ_{ij}

defined as

$$\Sigma_{ij} = \begin{cases} \sigma_i^2 & \text{if } i = j\,, \\ \rho_{ij}\sigma_i\sigma_j & \text{if } i \neq j\,, \end{cases} \tag{4.3}$$

where σ_i and σ_j are the uncertainties of observables i and j, respectively, and ρ_{ij} is the correlation coefficient between them. The likelihood then takes the form

$$\mathcal{L}(x|\theta) = \frac{1}{\sqrt{(2\pi)^n|\Sigma|}} \exp\left(-\frac{1}{2}(x-\mu(\theta))^T\Sigma^{-1}(x-\mu(\theta))\right)\,, \tag{4.4}$$

where n is the number of observables and x is the vector of observables and $|\Sigma|$ is the determinant of the covariance matrix.

In the limit of uncorrelated observables, the covariance matrix becomes diagonal with $\Sigma_{ij} = \sigma_i^2\delta_{ij}$, where σ_i is the uncertainty of observable i. In this case, $|\Sigma| = \prod_i \sigma_i^2$ and the likelihood reduces to the product of the individual likelihoods, as shown in Eq. (4.2).

Following the construction of the likelihood function, statistical inference provides estimates of the model parameters and their uncertainties. There are two main paradigms for statistical inference, which are frequently referred to as the frequentist and Bayesian approaches. While both methods give similar results in many cases, they are based on different philosophical foundations and have distinct implications for the interpretation of results.

Frequentist methods regard parameters as fixed but unknown quantities, interpreting the probability as the long-run frequency of observing the data given the parameters. In practice, the maximum likelihood estimation (MLE) method is a common approach in frequentist statistics to find parameter values that maximize the likelihood function, yielding point estimates of the parameters. Frequentist intervals, known as confidence intervals, reflect ranges within which the true parameter value is expected to fall with a predefined frequency (e.g., 95%) upon repeated experiments. These intervals typically derive from likelihood thresholds, frequently utilizing chi-squared distributions.

Conversely, Bayesian inference treats parameters as random variables with a probability distribution that encodes prior beliefs or information before observing data. Observational data updates these priors through Bayes' theorem [199]

$$\mathcal{P}(\theta|x) = \frac{\mathcal{L}(x|\theta)\pi(\theta)}{\mathcal{Z}}\,, \tag{4.5}$$

where $\pi(\theta)$ is the prior probability distribution of the parameters, and

$$\mathcal{Z} = \int d\theta \mathcal{L}(x|\theta)\pi(\theta)\,, \tag{4.6}$$

is the marginal likelihood, also referred to as the evidence. The resulting posterior distribution $\mathcal{P}(\theta|x)$ then reflects both the prior information and the likelihood of the observed data. This concept is illustrated in Fig. 4.1, which shows a broad Gaussian prior in orange, a Gaussian likelihood in blue and the resulting posterior distribution in red. With sufficient data, posterior distributions typically converge, reducing sensitivity to prior assumptions, a property known as Bayesian consistency.

The posterior distribution serves as a distributional basis from which best-fit values based on the mode, median, or mean can be extracted, as well as credible intervals that provide a measure

of the uncertainties of the parameters [200]. If uniform priors are employed, the results of Bayesian inference align with frequentist MLE outcomes.

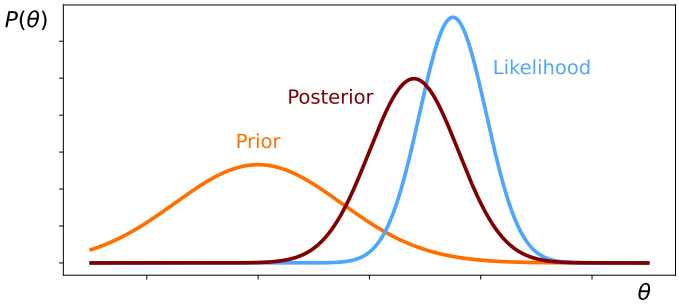

Figure 4.1: Illustration of the Bayesian framework. The prior distribution $\pi(\theta)$ is updated by the likelihood $\mathcal{L}(x|\theta)$ to yield the posterior distribution $\mathcal{P}(\theta|x)$.

Both, the frequentist and Bayesian approaches are commonly used in particle physics. The prerequisites for using a frequentist approach, i.e. repeated measurements of the same observable, are easily met in high-energy physics experiments, where large datasets of particle collisions are collected. The Bayesian approach, on the other hand, is particularly popular in cosmology, where oftentimes only a single measurement of an observable is available, thus making a frequentist approach impractical.

In the context of SMEFT, frequentist methods are, for example, used by Ellis et al. [31], González-García et al. [163, 201], Greljo et al. [35, 39, 202] Hurth et al. [33, 188, 189], Maltoni et al. [203–205] and Westhoff et al. [38, 206], while Bayesian fits are used by e.g the SMEFIT collaboration [32, 207, 208] or de Blas et al [209, 210]. In Ref. [211], an explicit comparison of the two approaches is made, showing that they yield similar results in many cases. The main differences are found for underfluctuated observables, where the Bayesian approach tends to yield tighter constraints on the Wilson coefficients due to volume effects in marginalization.

In this work, we adopt the Bayesian approach, which allows us to incorporate prior information obtained by prefits about the Wilson coefficients and the CKM parameters. This is particularly useful in the context of large global SMEFT fits, where prior knowledge can help to constrain the parameter space and improve the robustness of the results.

4.2. Fitting Procedure

The general objective of the fitting procedure is to obtain credible intervals for the Wilson coefficients $\tilde{C}_i$, thereby quantifying potential BSM effects within the SMEFT framework. Moreover, the posterior distribution of the MFV ratios $r_{L/R}$ defined in Eq. (3.17) is also of interest, as it provides indirect information about the quark-flavor structure of the Wilson coefficients. To this end, we utilize the EFT*fitter* package [212], which is built upon the Bayesian Analysis Toolkit (BAT.jl) [213, 214].

As a first step, the full likelihood function is constructed including statistical, systematic and theory uncertainties. We assume all uncertainties to be Gaussian distributed. In case where

uncertainties are presented as asymmetric, we adopt a conservative approach by symmetrizing them using the larger uncertainty value. Experimental correlations between observables are taken into account as provided by the experimental collaborations. These correlations have been shown to have a significant impact on the SMEFT fits, as demonstrated e.g. in Ref. [215]. Given that we assume BSM effects to be small, we neglect theoretical uncertainties of the SMEFT signal predictions.

To determine optimal priors for the Wilson coefficients, we initially conduct a prefit analysis employing Reactive Nested Sampling through the UltraNest package [216]. For these fits, we utilize flat priors in the ranges $[-10, 10]$. If the posterior distribution extends beyond this range, we expand the priors accordingly until sufficient convergence is achieved. This step identifies critical parameter space regions relevant to our analysis and excludes the possibility of secondary solutions. For the main fit, uniform priors within the ranges established by the prefit analysis are chosen for the Wilson coefficients. Regarding the CKM parameters, we employ Gaussian priors derived from a separate fit neglecting SMEFT effects, as detailed in Appendix B . For the MFV ratios, we adopt flat priors in the ranges $[-10, 10]$ for r_L and r_R.

To ensure an effective sampling of the posterior distribution, we employ the robust adaptive Metropolis–Hastings algorithm [217] for the final fits. This algorithm dynamically adapts the proposal distribution based on the current state of the Markov chain, allowing for an efficient exploration of the parameter space. For each fit, we run $N_{\text{chains}} = 20$ independent chains, each comprising 10^6 steps. The first 30% of these samples are discarded as burn-in. The subsequent samples provide the basis for constructing posterior distributions and credible intervals for the Wilson coefficients.

4.3. Toy Model Studies

In this section, we present toy model analyses designed to illustrate the statistical treatment and highlight the effects of marginalization and prior choices on the determination of Wilson coefficients. We focus on simplified scenarios involving two Wilson coefficients, C_1 and C_2, and dimensionless observables $X_i(C_1, C_2)$.

4.3.1. Comparison of Bayesian and Frequentist Approaches

We first consider a simplified scenario with a single observable

$$X_a(C_1, C_2) = 1 + C_1^2 + 3C_2^2 + 2C_1C_2\,, \tag{4.7}$$

with an assigned theoretical uncertainty of $\sigma_a^{\text{th}} = 0.1$. The dependence of X_a on the Wilson coefficients is quadratic and cannot be fully expressed as a linear combination of the coefficients, allowing us to constrain both coefficients simultaneously.

For our benchmark scenario, we assume a SM-like measurement $X_a^{\text{exp}} = 1.00(0.05)$, giving us a total uncertainty of $\sigma_{\text{tot}} = \sqrt{\sigma_{\text{exp}}^2 + \sigma_{\text{th}}^2} \approx 0.11$. Assuming a Gaussian distribution of the uncertainties, we can write the likelihood function as

$$\mathcal{L}(C_1, C_2) = \frac{1}{\sqrt{2\pi}\sigma_{\text{tot}}} \exp\left(-\frac{(X_a^{\text{exp}} - X_a(C_1, C_2))^2}{2\sigma_{\text{tot}}^2}\right)\,, \tag{4.8}$$

which corresponds to

$$\chi^2(C_1, C_2) = \frac{(X_a^{\text{exp}} - X(C_1, C_2))^2}{\sigma_{\text{tot}}^2} = \frac{(C_1^2 + 3C_2^2 + 2C_1C_2)^2}{0.112^2}\,, \tag{4.9}$$

in a frequentist context.

Minimizing the χ^2 function yields the best-fit values $C_1^{\text{opt}} = 0, C_2^{\text{opt}} = 0$ and $\chi^2_{\text{min}} = 0$. Confidence intervals are determined by $\Delta\chi^2$ thresholds corresponding to specific confidence levels, forming elliptical contours in the C_1–C_2 plane.

Because our toy observable X_a depends on the two Wilson coefficients C_1 and C_2 only through the combination

$$C' = \sqrt{C_1^2 + 3C_2^2 + 2C_1C_2}\,, \tag{4.10}$$

a single measurement of X_a can only constrain the combination C' and thus a single direction in the two-dimensional parameter space. In a frequentist interpretation, Wilks's theorem then postulates that the relevant $\Delta\chi^2$ threshold for a desired confidence level corresponds to one degree of freedom, not two. Thus, for example, the boundary of the 68% confidence level region is $\Delta\chi^2 = 1.0$, while the boundary of the 2σ region is $\Delta\chi^2 = 4.0$.

We show the 1σ, 2σ and 3σ regions as orange contours in Fig. 4.2. We compare these contours to the two-dimensional posterior distribution obtained from a Bayesian analysis, which is shown in blue. The Bayesian credible intervals coincide closely with the frequentist confidence intervals, showing that the two approaches yield similar results in the case of a Gaussian likelihood and flat priors.

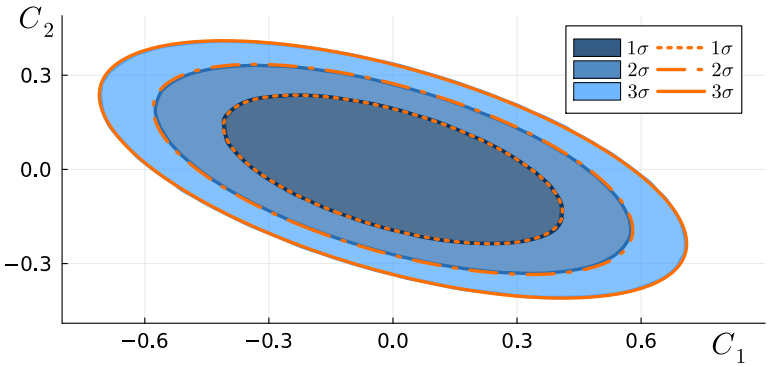

Figure 4.2: Confidence intervals in the C_1–C_2 plane for a toy model analysis with a single observable X_a. We show the results using a frequentist approach in orange and the results from a Bayesian analysis in blue. The contours indicate the 1σ, 2σ and 3σ intervals, corresponding to 68%, 95% and 99.7% confidence levels.

To obtain bounds on the individual Wilson coefficients from the posterior, we marginalize over the second coefficient in the Bayesian framework. In the frequentist approach, conversely, the one-dimensional confidence intervals of C_1 can be obtained by profiling over C_2 and minimizing χ^2 for each fixed value of the coefficient of interest. and then determining the regions in

parameter space that satisfy $\chi^2(C_1, C_2) < \chi^2_{\min} + \Delta\chi^2$. Concretely, we find $C_1 = -3C_2$ in this scenario, yielding

$$\chi^2_{\text{prof}}(C_1) = \frac{4C_1^4}{9\sigma^2_{\text{tot}}}\,, \tag{4.11}$$

which can be solved for the one-dimensional confidence intervals.

We compare the resulting confidence intervals on $|C_1|$ in Tab. 4.1. We show results from the frequentist approach as well as the corresponding credible intervals obtained by a Bayesian analysis. We further compare the results from a two-parameter study to the one-parameter fit with $C_2 = 0$. We see that the bounds from the frequentist approach are slightly larger than those from the Bayesian approach. Moreover, the two-parameter fits broader constraints than the fits with $C_2 = 0$, since the latter do not feature destructive interference in the observable X_a and thus result in tighter bounds.

Fit type	1σ	2σ	3σ
Frequentist (2-parameter)	0.41	0.58	0.71
Bayesian (2-parameter)	0.30	0.49	0.65
Frequentist ($C_2 = 0$)	0.33	0.47	0.58
Bayesian ($C_2 = 0$)	0.27	0.42	0.55

Table 4.1: Bounds on $|C_1|$ for different confidence levels from a toy model analysis with a single observable X_a. We compare the bounds from the frequentist approach with the bounds from the Bayesian approach, using a two-parameter fit as well as a simplified one-parameter analysis with $C_2 = 0$.

4.3.2. Non-SM like Measurements and Impact of Priors

To explore the influence of non-SM-like measurements, we consider a modified benchmark, $X^{\text{exp}} = 1.25 \pm 0.05$, representing a 2.2σ deviation from the SM. This measurement results in an elliptical best-fit contour defined by $C_1^2 + 3C_2^2 + 2C_1C_2 = 0.25$. We further investigate the impact of the prior choice by comparing fits using a flat prior to a fit with a Gaussian prior with a width of 0.5 centered around the SM expectation of $C_i = 0$

$$C_i^{\text{prior}} = \frac{2}{2\pi}\exp\left(-2C_i^2\right)\,. \tag{4.12}$$

Fig. 4.3 shows the resulting two-dimensional posterior distribution as well as the marginalized distributions for the Wilson coefficient C_1. The blue contours correspond to the fit using flat priors, while the orange contours indicate the bounds resulting from a fit with Gaussian priors. The results show a significant difference between the two approaches. The Gaussian priors bias the posterior distribution towards smaller values, reducing the posterior width. This highlights the importance of the choice of priors in the analysis, especially in the case of non-SM-like measurements.

This difference is also reflected in the marginalized posterior distribution for C_1, which is shown in the upper panel of Fig. 4.3. The blue histogram shows the one-marginalized posterior distribution obtained from the fit with flat priors, while the orange histogram shows the marginalized posterior distribution obtained from the fit with Gaussian priors. The vertical lines indicate the 1σ, 2σ and 3σ intervals. We see that the bounds from the fit with Gaussian priors are stronger than those from the fit with flat priors. Moreover, the fit with flat priors exhibits a double-peak structure and slightly disfavors the SM point compared to the best fit points at $|C_1| = 0.5$, whereas the fit with Gaussian priors exhibits a distribution with a broad best-fit plateau in the range $[-0.4, 0.4]$.

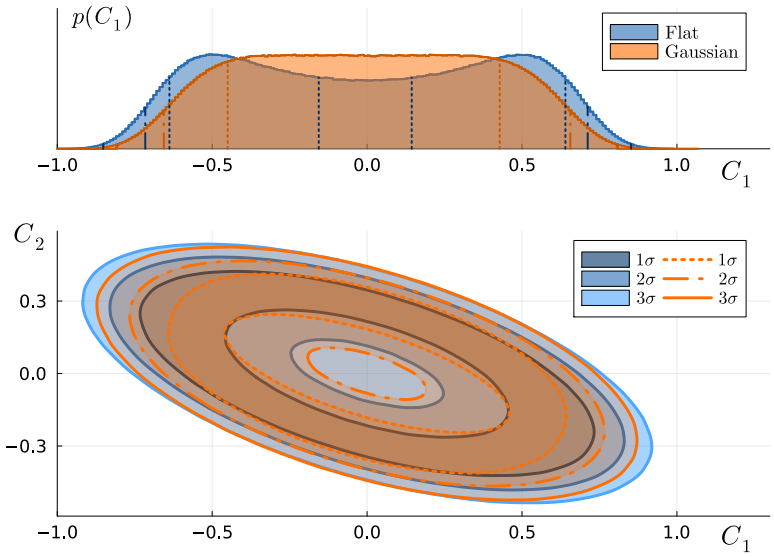

Figure 4.3: Marginalized posterior distribution for the Wilson coefficient C_1 (top) and two-dimensional bounds on the Wilson coefficients C_1 and C_2 (bottom) from a toy model analysis with a single observable X. We show the results from a fit with flat priors in blue and the results from a fit with Gaussian priors in orange. The contours and vertical lines indicate the 1σ, 2σ and 3σ intervals.

This shows that the choice of priors can have a significant impact on the results of the analysis, especially in the case of non-SM-like measurements. While flat priors lead to similar results to the frequentist approach, Gaussian priors can bias the posterior distribution towards certain regions of the parameter space. We thus aim to use flat priors in our analysis, as they are less sensitive to the choice of prior and provide a more robust estimate of the parameter space.

4.3.3. The Impact of Marginalization

To investigate the impact of marginalization on the bounds, we introduce an additional observable

$$X_b(C_2) = C_2, \tag{4.13}$$

with a benchmark measurement $X_b^{\text{exp}} = 0.00 \pm 0.05$ and a theory uncertainty $\sigma_b^{\text{th}} = 0.05$. This observable adds a second constraint on the parameter space and enhances our sensitivity to C_2. Fig. 4.4 shows the results of a combined fit to both observables X_a and X_b.

On the lower left, we show the two-dimensional posterior distribution in the C_1–C_2 plane, which is obtained by combining the likelihood functions from both observables. The contours indicate the 1σ, 2σ and 3σ intervals. We further show the marginalized posterior distributions as well as the posterior distribution from a fit setting $C_j = 0$ on the upper left for $j = 2$ and on the right for $j = 1$.

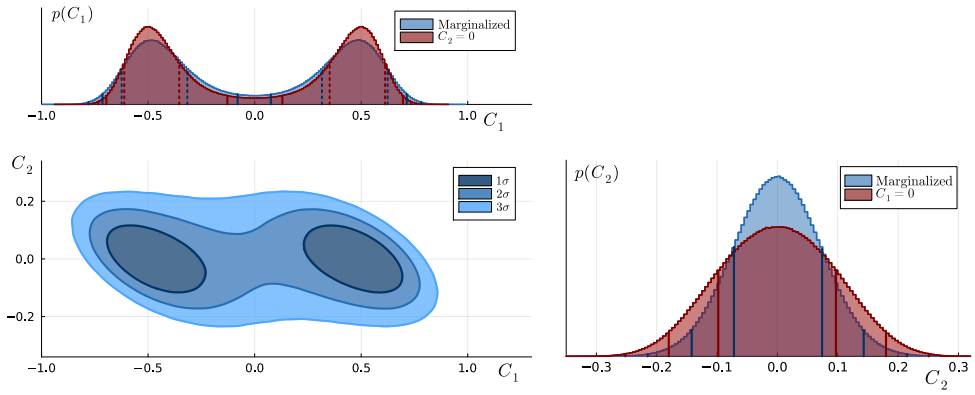

Figure 4.4: Marginalized posterior distributions for the Wilson coefficient C_1 (top), C_2 (right) and two-dimensional credible intervals on the Wilson coefficients C_1 and C_2 (bottom) from a toy model analysis using two observables X_a and X_b. We show the posterior of the two-parameter analysis in blue and the one-parameter fit with $C_j = 0$ in red. The contours and vertical lines indicate the 1σ, 2σ and 3σ intervals.

We see that the marginalized posterior distribution for C_2 is significantly more narrow than the one-dimensional posterior distribution obtained from the fit with $C_1 = 0$, showing that in certain cases, a combined fit can significantly tighten the bounds on the Wilson coefficients compared to single-parameter fits. This is due to volume effects in marginalization, as seen also in e.g. Ref. [211].

In other cases, however, the bounds from the combined fit can be weaker than those from the single-parameter fits, as can be seen for the coefficient C_1. This is due to the fact that setting $C_2 = 0$ in the fit with X_a prevents potential cancellation effects in the observable X_a, which leads to tighter bounds on C_1.

Chapter 5

Collider Observables in the SMEFT

In this chapter, we explore how the SMEFT framework can be used to systematically capture the effects of heavy new physics on collider processes. First, we discuss the methodology for simulating SMEFT contributions to key observables at the LHC in Sec. 5.1. We then study several processes in more detail, including electroweak boson decays (Sec. 5.2), dilepton production at LEP (Sec. 5.3), the Drell–Yan process at the LHC (Sec. 5.4) as well as top quark production and decay (Sec. 5.5). By examining the sensitivity of these processes to the SMEFT Wilson coefficients, we highlight the different directions in parameter space that are probed by the various processes and discuss their complementarity in combined analyses.

5.1. Collider Processes in the SMEFT

Many collider observables can be categorized as either unfolded measurements or raw event counts. Unfolded measurements attempt to correct the data for detector effects to provide observables that are as close as possible to the particle- or parton-level quantities. This unfolding process typically relies on a response matrix derived from simulations and assumes that the migration of events between reconstructed and true kinematic bins is well understood.

While unfolding allows for a more direct comparison between experimental results and theoretical predictions at the parton level, it introduces model-dependent uncertainties and can amplify statistical fluctuations. Moreover, it often relies on bin-by-bin corrections or regularized matrix inversion, which come with trade-offs in terms of bias and variance. In this work, examples of unfolded observables include the measurements of the Z and W boson observables at LEP and the LHC [17, 218–220] as well as dilepton production at LEP [221], which are discussed in Secs. 5.2 and 5.3, respectively.

For these observables, we can directly compare the experimental results to the theoretical predictions of the cross sections, without the need for additional corrections or simulations. We compute the cross sections in the SMEFT at leading order using using MATHEMATICA [222] with the FEYNCALC [223–226] and `SmeftFR` v3.0 [227] packages.

In contrast, some experimental results, such as measurements of DY production [228–232] are presented as raw or background-subtracted event yields, either in inclusive regions or in binned distributions at detector level. These observables are closer to what is actually measured and avoid the uncertainties associated with unfolding, but they pose a challenge for SMEFT interpretations. In order to compare these data to the SMEFT, we require full simulations of the contributions at the detector level, including parton showering, hadronization, acceptance, and efficiency effects. As these include various non-perturbative effects, an analytical treatment of these computations is not feasible. Instead, they are typically computed using Monte Carlo event generators, as we discuss in the following.

Typically, the theoretical description of collider processes is factorized into two main components: the short distance, hard scattering process of the partons, which is computed perturbatively as an expansion in the coupling constants, and the long-distance, non-perturbative effects that are associated with the internal structure of the colliding protons. This separation is formalized by the QCD factorization theorem [233, 234], which ensures that at sufficiently high energies, the hard scattering is independent of the proton's non-perturbative content, up to power-suppressed corrections of order Λ_{QCD}/Q, where Q denotes the momentum transfer and Λ_{QCD} is the QCD scale.

Hard Scattering Process and Flavor Composition

To compute the hard scattering process, we calculate the partonic cross-section $\hat{\sigma}(\hat{s})$ at the scale of the partonic center-of-mass energy $\hat{s}$ at leading order using the Monte Carlo event generator MADGRAPH5_aMC@NLO [235]. For the implementation of the SMEFT Lagrangian, we employ the `SMEFTsim` 3.0 package [180, 236], which provides `FeynRules` [237, 238] source files as well as pre-exported models in the `UFO` format [239] for the dimension-six SMEFT operators in the Warsaw basis [169], which can be directly imported into MADGRAPH5_aMC@NLO .

At hadron colliders such as the LHC, the composition of the colliding protons must also be taken into account. This internal structure is described by parton distribution functions (PDFs), which parameterize the parton content of the colliding protons by quantifying the probability of finding a parton with a given momentum fraction x within the proton. In practice, the PDFs depend on the factorization scale μ_F, which separates the short-distance dynamics of the hard scattering from the non-perturbative long-distance effects. The PDFs are typically determined from global fits to experimental data (see e.g. [240–248]), such as, for example, deep inelastic scattering or Drell-Yan (DY) production, ensuring that they accurately reflect the parton content of the proton at various energy scales.

In this work, we use the leading-order Monte Carlo variant of the NNPDF4.0 PDF sets [248, 249] as implemented in LHAPDF 6 [250]. We choose a dynamical factorization scale $\mu_F = m_T$, where m_T is the transverse mass of the final-state particles. We illustrate the PDFs in Fig. 5.1, showing the quark (solid), antiquark (dashed) and gluon PDFs (orange) at the scales $\mu_F^2 = 10^3\,\text{GeV}^2$ and $\mu_F^2 = 10^6\,\text{GeV}^2$. Note that because of the large top-quark mass, the top-quark contribution to the PDFs is negligible at LHC energies, so that we neglect the top-quark PDFs in our analysis. For the charm and bottom quarks, the PDFs of the quark and antiquark coincide, as they are produced symmetrically through gluon splitting.

At large x, the PDFs are dominated by the valence quarks, which carry most of the proton's momentum. These large momentum fractions are particularly relevant for high-energy processes such as DY production with high-invariant-masses, which typically probes $x \leq 0.1 - 0.5$. At small x, the PDFs are dominated by the gluons, which are scaled by a factor of $1/10$ in Fig. 5.1. Therefore, processes such as $t\bar{t}$ production are typically dominated by gluon-gluon fusion at LHC energies, which allows for a high sensitivity on the gluon dipole operators O_{uG}, as discussed in Sec. 5.5. The DY process, on the other hand, does not receive contributions from the gluon PDFs at leading order, as leptons do not couple to gluons.

Below $x \sim 10^{-2}$, the sea quarks, produced primarily through gluon splitting, begin to contribute significantly to the PDFs. Among the sea quarks, the heavier flavors are suppressed at moderate and high x due to their larger mass. As the factorization scale μ_F increases, this mass effect gradually diminishes and the PDFs approach a more universal form because the quark masses become less relevant compared to the energy scale of the process. This is illustrated in Fig. 5.1,

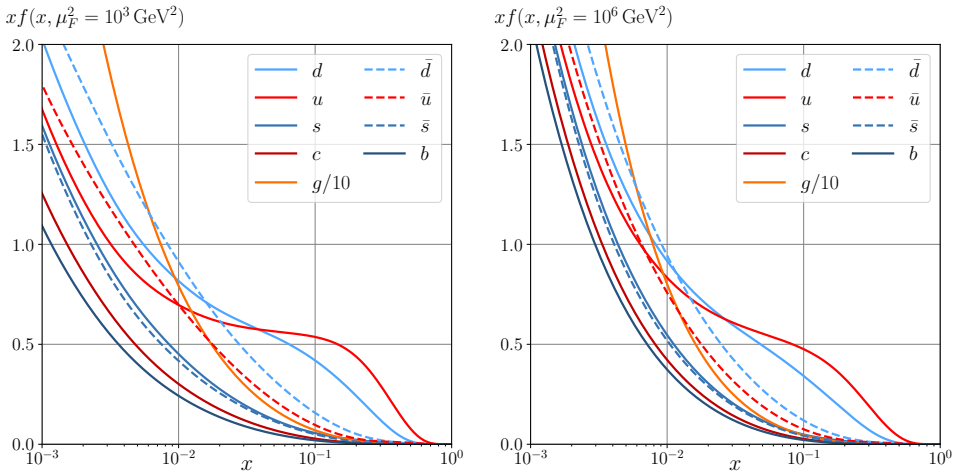

Figure 5.1: NNPDF4.0 PDFs [248, 249] multiplied by x at $\mu_F^2 = 10^3\,\mathrm{GeV}^2$ (left) and $\mu_F^2 = 10^6\,\mathrm{GeV}^2$ (right). The PDFs are shown as a function of the momentum fraction x of the parton within the proton. The solid lines represent quarks, while the dashed lines represent antiquarks. For c and b quarks, the quark and antiquark PDFs are identical. The gluon PDF, scaled by a factor of $1/10$, is shown in orange, up-type quarks are shown red and down-type quarks in blue.

where we see that at $\mu_F^2 = 10^6\,\mathrm{GeV}^2$, the gap between the light and heavy quarks is significantly reduced compared to $\mu_F^2 = 10^3\,\mathrm{GeV}^2$.

For a process based on quark-antiquark annihilation (e.g. DY production), we can further define parton luminosity functions

$$\mathcal{L}_{q_i\bar{q}_j}(\tau) = \tau \int_\tau^1 \frac{\mathrm{d}x}{x} \left[f_{q_i}(x,\mu_F) f_{\bar{q}_j}(\tau/x,\mu_F) + f_{\bar{q}_j}(x,\mu_F) f_{q_i}(\tau/x,\mu_F) \right] , \tag{5.1}$$

where $f_{q_i}(x,\mu_F)$ are the PDFs for a quark q_i evaluated at momentum fraction x and factorization scale μ_F, and $\tau = \hat{s}/s$ is the ratio of the partonic center-of-mass energy squared to the hadronic center-of-mass energy squared. The parton luminosities encapsulate the probability of finding the required quark-antiquark pairs within the protons to initiate the hard scattering process.

The hadronic cross-section is then obtained by convoluting the partonic cross-section, $\hat{\sigma}(\hat{s})$, with the corresponding parton-luminosity functions $\mathcal{L}_{q_i\bar{q}_j}(\tau)$

$$\sigma = \sum_{ij} \int \frac{\mathrm{d}\tau}{\tau}\, \mathcal{L}_{q_i\bar{q}_j}(\tau)\, \hat{\sigma}(\tau s)\,, \tag{5.2}$$

where the sum runs over all relevant quark flavors. Fig. 5.2 illustrates the parton luminosity functions for the flavor diagonal (upper left), FCNC (upper right) and CC (lower panels) quark contributions. We see that the light up and down quarks dominate the parton luminosities, while the heavier quarks, such as the charm and bottom quarks, are significantly suppressed due to the PDFs. This hierarchy reflects the fact that the quark-antiquark collisions at high energies are primarily driven by valence quark interactions. As a result, processes that are

driven by quark-antiquark annihilation at tree-level are especially sensitive to any new physics modifications of the light quarks, while sensitivity to heavier quarks is suppressed.

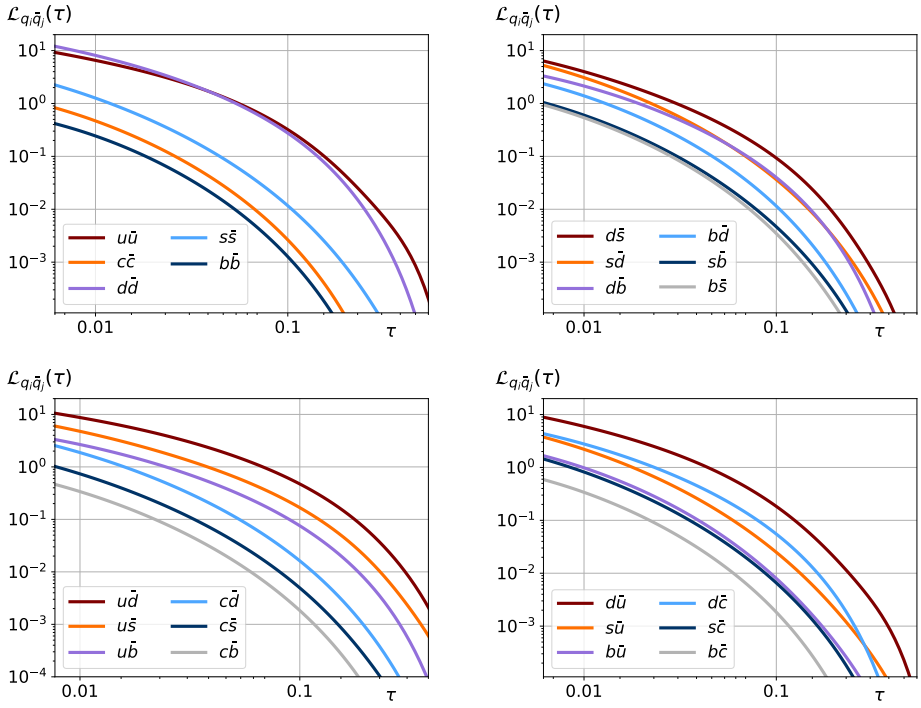

Figure 5.2: Parton luminosity functions for the NNPDF4.0 PDF sets [248, 249]. We show the flavor-diagonal contributions (upper left), FCNC contributions (upper right), and charged-current contributions for $u_i d_j \to W^+$ (lower left) and $u_i \bar{d}_j \to W^+$ (lower right). The luminosities are shown as a function of $\tau = \hat{s}/s$, where $\hat{s}$ is the partonic center-of-mass energy squared and s is the hadronic center-of-mass energy squared.

Furthermore, while neutral-current SM processes are strictly flavor diagonal at tree-level, i.e., only quark-antiquark and dilepton pairs of the same flavor contribute, the SMEFT framework induces additional FCNC and lepton-flavor-violating (LFV) contributions. The FCNC contributions in our MFV framework are, however, strongly suppressed by the CKM factors compared to the flavor-diagonal contributions, as outlined in Sec. 3.2.2

Even though processes at hadron colliders can only be measured inclusively with regard to the initial-state partons, i.e., the hadronic cross section is a sum over all possible partonic configurations, the different contributions do not interfere, so multiple flavor components of the Wilson coefficients can be constrained simultaneously, as long as dimension-six squared terms are included. A similar argument holds for different chiralities of the initial and final state fermions. At high energies, the interference terms between different chirality contributions are suppressed by the smallness of the SM Yukawa couplings, so that the contributions can be treated independently. This is particularly relevant for the four-fermion operators, which typically receive contributions from both left-handed and right-handed fermions.

Hadronization, Parton Showering, and Detector Simulation

After computing the hard scattering process and folding in the PDFs, the parton-level events are further processed using PYTHIA 8.3 [251] to simulate hadronization, parton showering, initial and final state radiation, as well as particle decays. These effects account for the non-perturbative dynamics of QCD and QED, which are important to accurately model the hadronic final state and the decay products of the particles produced in the hard scattering process.

The parameters governing these non-perturbative effects are tuned to experimental data to ensure an accurate phenomenological description. In our simulation, we employ the CMS Tune MonashStar [252] for CMS and the ATLAS A14 central tune with NNPDF2.3LO [253] for ATLAS.

Finally, the detector response is modeled using the parametric simulation tool DELPHES3 [254] with detector cards tailored for the CMS and ATLAS detectors. The detector simulation accounts for the acceptance and efficiency of the detector, as well as the resolution of the measured observables. The resulting events are then binned into histograms or analyzed in terms of differential distributions, depending on the experimental setup and the observable under consideration using the ROOT [255] or the MADANALYSIS 5 [256] framework.

Energy Enhancement of the SMEFT Contributions

An important advantage of collider observables in the SMEFT is that the contribution of some operators grows with the energy of the process, so that the SMEFT contributions are enhanced in the high-energy tails of differential distributions [2, 34, 35, 162, 167, 257–259]. This is particularly relevant for four-fermion operators, for which the amplitudes typically scale as $\hat{s}/\Lambda^2$ in the high-energy limit, with $\hat{s}$ being the center-of-mass energy squared of the process. As the SM cross-section typically falls off as $1/\hat{s}$, the SMEFT contributions can become dominant in the high-energy tails of distributions, thus strongly enhancing the sensitivity to the corresponding Wilson coefficients.

Another type of operators featuring an energy enhancement, although less pronounced, are the dipole operators, which scale as $v\sqrt{\hat{s}}/\Lambda^2$. An exception is the contribution of the gluonic dipole operators O_{uG} and O_{dG} to the process $pp \to \nu\bar{\nu}j$, which receive full energy enhancement $\sim \hat{s}/\Lambda^2$ as they contribute to the longitudinal modes of the Z boson [2, 260]. The Higgs-current operators, on the other hand, do not scale with energy, but rather contribute through a correction of the order v^2/Λ^2 to the amplitude. Hence, they are only subdominant at high energies.

To illustrate the different energy-scaling behavior of the SMEFT operators, Fig. 5.3 shows corresponding examples of SMEFT contributions to the differential event count for the DY process $pp \to e^+e^-$ at CMS [228]. We compare the SM prediction (red) from the CMS collaboration [228] to the contributions of the four-fermion operator $O_{lq}^{(3)}$ (orange), the dipole operator O_{eW} (dark-blue), and the Higgs-current operator $O_{\varphi l}^{(3)}$ (light-blue) computed at leading order following the simulation procedure outlined above.

As expected, the contribution of the semileptonic four-fermion operator $O_{lq}^{(3)}$ features a pronounced rise in the tail of the $m_{e^+e^-}$ distribution, before falling off at the masses above $\sim 1\,\text{TeV}$ due to PDF suppression. By contrast, the dipole contributions from O_{eW} grows more modestly, with a characteristic enhancement proportional to $v\sqrt{\hat{s}}/\Lambda^2$ in the amplitude. The Higgs-current operator $O_{\varphi l}^{(3)}$, conversely, enters purely through a v^2/Λ^2 correction, yielding only a small, energy-independent contribution to the spectrum. Both, the dipole and the Higgs-current operators, however, retain the characteristic Z-pole peak in the differential distribution. This is

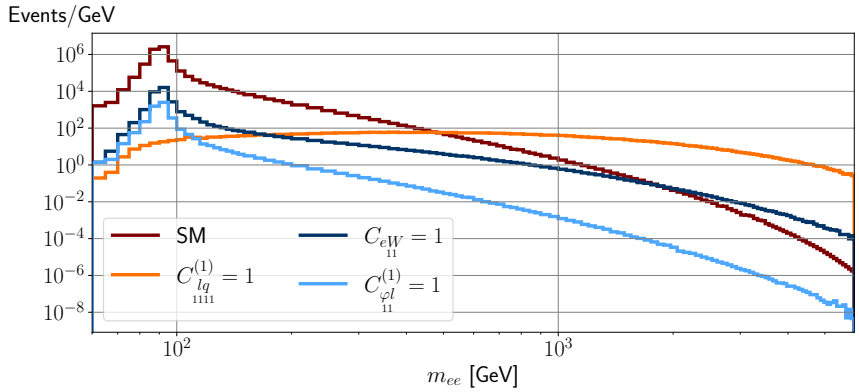

Figure 5.3: Differential event count for the DY process $pp \to e^+e^-$ at CMS. The SM prediction (red) from Ref. [228] is shown together with the simulated contributions of the operators $O_{lq}^{(3)}$ (orange), $O_{\varphi l}^{(3)}$ (light-blue), and O_{eW} (dark-blue).

due to the fact that contribute via modifying the $Z\ell\ell$ vertex, thus scaling proportional to the Z-contribution.

5.2. Z and W Boson Decays

Decays of the massive electroweak gauge bosons, the Z and the W, have long served as precision probes of the electroweak sector of the SM. Within the framework of the SMEFT, higher-dimensional Higgs-current operators can modify the couplings between the gauge bosons and the fermions. Furthermore, electroweak dipole operators introduce chirality-flipping contributions to the decays of the Z and W bosons, which are suppressed in the SM due to the small fermion masses.

In this section, we discuss the key observables and their sensitivities to the SMEFT Wilson coefficients. Our analysis focuses on the Z boson decays into fermion-antifermion pairs, the asymmetries in these decays, and the W boson decays into a lepton-neutrino pair as well as into a quark-antiquark pair. By combining these observables, we obtain complementary constraints on the SMEFT Wilson coefficients and effectively resolve flat directions in the parameter space.

5.2.1. Partial Z Widths

In the SM, the massive Z boson arises a linear combination of the neutral electroweak gauge bosons W^3 and B (see Sec. 2.1). Consequently, its couplings to fermions are determined by both the weak isospin and the hypercharge, as prescribed by the electroweak framework. This leads to gauge couplings with distinct left-handed and right-handed components, which can be expressed as

$$g_{L\,ij}^{f,\mathrm{SM}} = \delta_{ij}\left(T_3^f - Q_f \sin^2\theta_W\right), \qquad g_{R\,ij}^{f,\mathrm{SM}} = -\delta_{ij} Q_f \sin^2\theta_W\,, \tag{5.3}$$

in the SM, where T_3^f is the weak isospin of the fermion f, Q_f is its electric charge, and θ_W is the weak mixing angle. At tree level, the partial decay width of the Z boson into a fermion-antifermion pair is given by[1]

$$\Gamma(Z \to f_i \bar{f}_j) = N_c^f \frac{G_F m_Z^3}{6\pi\sqrt{2}} \left[\left(g_{L\,ij}^f \right)^2 + \left(g_{R\,ij}^f \right)^2 \right] , \tag{5.4}$$

where N_c^f is the number of colors of the fermion f, with $N_c^f = 1$ for leptons and $N_c^f = 3$ for quarks.

The partial widths of the Z boson decaying into fermion–antifermion pairs represent some of the most precisely measured observables in the electroweak sector. Table 5.1 presents the experimental results obtained at LEP [17] alongside the corresponding Standard Model prediction. In our analysis, we incorporate the correlation matrix provided in Tab. 7.1 of Ref. [17] for these measurements. Including these correlations is crucial, as they have been shown to significantly affect the derived bounds [215].

Observable	Measurement	SM Prediction
$\Gamma(Z \to e^+e^-)$	83.92(12) MeV [17]	83.987(68) MeV [17]
$\Gamma(Z \to \mu^+\mu^-)$	83.99(18) MeV [17]	83.986(68) MeV [17]
$\Gamma(Z \to \tau^+\tau^-)$	84.08(22) MeV [17]	83.796(67) MeV [17]
$\Gamma(Z \to \nu\bar{\nu})$	497.4(2.5) MeV [17]	501.435(45) MeV [18]
$\Gamma(Z \to \text{had})$	1745.8(2.7) MeV [17]	1742.3(1.6) MeV [17]
$\Gamma(Z \to b\bar{b})$	377.6(1.3) MeV [17]	376.02(0.74) MeV [17]
$\Gamma(Z \to c\bar{c})$	300.5(5.3) MeV [17]	300.10(0.47) MeV [17]

Table 5.1: Measurements of the Z boson decay widths as well as the corresponding SM predictions used in this analysis.

While the Z boson couplings to fermions are flavor diagonal in the SM, the SMEFT operators can induce LFV couplings. Such contributions can be constrained by measurements of the Z boson branching fractions into LFV final states, such as $\mathcal{B}(Z \to e\mu)$. Tab. 5.2 summarizes the current 95% CL limits on these branching fractions as measured by the ATLAS collaboration [218, 219].

Moreover, the dineutrino channel, which is measured inclusively with regard to the neutrino flavor, can also receive LFV contributions, thereby offering additional constraints. Similarly, within the SMEFT framework, FCNC operators may contribute to the total hadronic width of the Z boson, which can be constrained by the measurements of the total hadronic width presented in Tab. 5.1.

In the presence of higher-dimensional operators in the SMEFT, the couplings in Eq. (5.3) and, consequently, the Z boson partial widths, receive additional contributions. In this framework,

[1] Note that while this expression is derived at tree level, the SM predictions in Tab. 5.1 incorporate QED and QCD final state corrections as well as contributions from non-factorizable complex corrections [17]. For the computation of the SMEFT contributions, these corrections are neglected.

	$\mathcal{B}(Z \to e\mu)$	$\mathcal{B}(Z \to e\mu)$	$\mathcal{B}(Z \to e\mu)$
95% CL limit	$2.62 \cdot 10^{-7}$ [218]	$5.0 \cdot 10^{-6}$ [219]	$6.5 \cdot 10^{-6}$ [219]

Table 5.2: 95% CL limits on the Z boson branching fractions with LFV final states measured by the ATLAS collaboration.

the modified couplings of the Z boson to fermions are given by

$$g_{L\,ij}^{\nu} = \frac{1}{2}\delta_{ij} - \frac{1}{2}\tilde{C}_{\varphi l\,ij}^{-}\,, \qquad g_{R\,ij}^{\nu} = 0\,, \tag{5.5}$$

$$g_{L\,ij}^{e} = \delta_{ij}\left(\sin^2\theta_W - \frac{1}{2}\right) - \frac{1}{2}\tilde{C}_{\varphi l\,ij}^{+}\,, \qquad g_{R\,ij}^{e} = \delta_{ij}\sin^2\theta_W - \frac{1}{2}\tilde{C}_{\varphi e\,ij}\,, \tag{5.6}$$

$$g_{L\,ij}^{u} = \delta_{ij}\left(\frac{1}{2} - \frac{2}{3}\sin^2\theta_W\right) - \frac{1}{2}\tilde{C}_{\varphi q\,ij}^{-}\,, \qquad g_{R\,ij}^{u} = -\frac{2}{3}\delta_{ij}\sin^2\theta_W - \frac{1}{2}\tilde{C}_{\varphi u\,ij}\,, \tag{5.7}$$

$$g_{L\,ij}^{d} = \delta_{ij}\left(-\frac{1}{2} + \frac{1}{3}\sin^2\theta_W\right) - \frac{1}{2}\tilde{C}_{\varphi q\,ij}^{+}\,, \qquad g_{R\,ij}^{d} = \frac{1}{3}\delta_{ij}\sin^2\theta_W - \frac{1}{2}\tilde{C}_{\varphi d\,ij}\,, \tag{5.8}$$

where the linear combinations of Wilson coefficients are defined as

$$\tilde{C}_{\varphi l}^{\pm} = \tilde{C}_{\varphi l}^{(1)} \pm \tilde{C}_{\varphi l}^{(3)}\,, \qquad \tilde{C}_{\varphi q}^{\pm} = \tilde{C}_{\varphi q}^{(1)} \pm \tilde{C}_{\varphi q}^{(3)}\,. \tag{5.9}$$

In addition to these vector-coupling contributions, the SMEFT framework also induces dipole couplings via electromagnetic dipole operators. As the decay $Z \to t\bar{t}$ is kinematically not allowed and the all other quark-dipole operators vanish in our MFV SMEFT framework, only the leptonic dipole operators contribute.

The resulting dipole contribution to the partial Z boson decay width is given by

$$\Gamma_{\text{Dipole}}(Z \to \ell_i \ell_j) = N_c^f \frac{G_F m_Z^3}{24\pi\sqrt{2}}\left(\tilde{C}_{eZ\,ij}^2 + \tilde{C}_{eZ\,ji}^2\right)\,, \tag{5.10}$$

with the effective dipole coefficient $\tilde{C}_{eZ}$ defined in Eq. (3.24). Since $m_f \ll m_Z$, the SM dipole contributions, scaling as m_f^2/m_Z^2, are negligible.

Different observables in the SMEFT framework offer complementary sensitivity to various combinations of Wilson coefficients. Taken individually, many of the observables exhibit flat directions in the parameter space and do thus not allow to constrain individual coefficients, whereas a combined fit can resolve these degeneracies. As an example, we consider the charged lepton width sensitive to $\tilde{C}_{\varphi l}^{+}$ and the dineutrino channel probing the orthogonal combination $\tilde{C}_{\varphi l}^{-}$. By analyzing both observables simultaneously, we can separately constrain $\tilde{C}_{\varphi l}^{1}$ and $\tilde{C}_{\varphi l}^{3}$. In the left panel of Fig. 5.4, we show the 95% CL posterior regions for a two-dimensional fit neglecting RGE effects and mixing in the $e\mu$ sector. The posterior regions for the charged-lepton and dineutrino channels are shown in orange and blue, respectively, while the red contour illustrates how their combination yields tight, non-degenerate bounds on both $\tilde{C}_{\varphi \ell}^{1}$ and $\tilde{C}_{\varphi \ell}^{3}$.

An analogous synergy occurs in hadronic decays, with up-type quark final states probing the combination $\tilde{C}_{\varphi q}^{-}$ and down-type states probing $\tilde{C}_{\varphi q}^{+}$. Each quark channel, however, features

interference between the SMEFT and the SM, producing two distinct preferred regions in the fit. As a result, the combined quark analysis admits four disconnected allowed regions in the $(\tilde{C}^1_{\varphi q}, \tilde{C}^3_{\varphi q})$ plane, as shown in the right panel of Fig. 5.4. We show the bounds from the $Z \to c\bar{c}$ channel in orange, $Z \to b\bar{b}$ in blue and the combined fits in red. Including additional observables, such as hadronic W decays or flavor observables, provides independent bounds in these parameter planes, fully lifting the remaining degeneracies and significantly strengthening the overall constraints on the SMEFT Wilson coefficients.

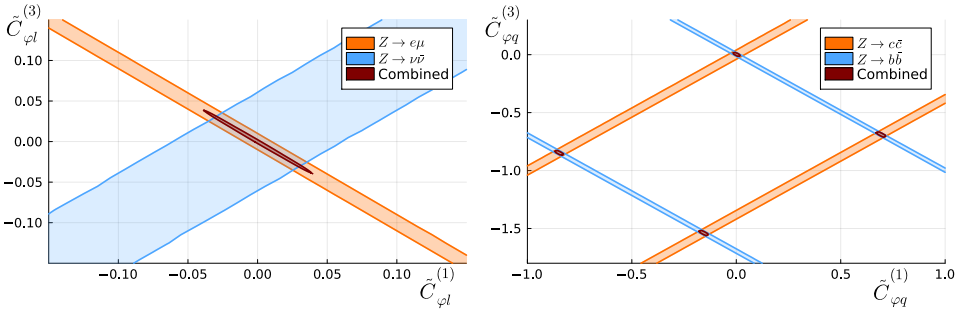

Figure 5.4: Synergies between the Z boson decay channels in the $\tilde{C}^1_{\varphi l}$–$\tilde{C}^3_{\varphi l}$ plane (left) and the $\tilde{C}^1_{\varphi q}$–$\tilde{C}^3_{\varphi q}$ plane (right). The colored regions correspond to the 90% credible regions of the posterior probability distributions. We show the individual fits to $Z \to e\mu$ ($Z \to c\bar{c}$) in orange, $Z \to \nu\bar{\nu}$ ($Z \to b\bar{b}$) in blue and the combined fit in red.

5.2.2. Z Asymmetries

In addition to partial width measurements, asymmetry observables of the Z boson offer further constraints on the SMEFT Wilson coefficients [261]. A key observable is the forward-backward asymmetry, defined as

$$A^f_{\rm FB} = \frac{\sigma^f_{\rm F} - \sigma^f_{\rm B}}{\sigma^f_{\rm F} + \sigma^f_{\rm B}}\,, \tag{5.11}$$

where the forward and backward cross sections are given by

$$\sigma^f_{\rm F} = \int_0^1 d\cos\theta \frac{d\sigma(e^+e^- \to f^+f^-)}{d\cos\theta}\,, \quad \sigma^f_{\rm B} = \int_{-1}^0 d\cos\theta \frac{d\sigma(e^+e^- \to f^+f^-)}{d\cos\theta}\,. \tag{5.12}$$

These asymmetries benefit from the cancellation of many systematic uncertainties in the measurements, such as those related to the luminosity and detector effects, making them highly precise probes of the Z boson couplings. Furthermore, the forward-backward asymmetry is sensitive to the differences between left-handed and right-handed couplings, thereby providing additional information and helping to disentangle the contributions from different Wilson coefficients.

At tree level, the differential cross section for the process $(e^+e^- \to f^+f^-)$ is given by [17]

$$\frac{d\sigma(e^+e^- \to f^+f^-)}{d\cos\theta} = \frac{3}{8}\sigma^{\rm tot}_{ff}\left[(1+\cos^2\theta)(1-\mathcal{P}_e\mathcal{A}_f) + 2(1-\mathcal{A}_e-\mathcal{P}_e\mathcal{A}_f)\cos\theta\right] \tag{5.13}$$

where $\mathcal{P}_e$ denotes the electron beam polarization and $\mathcal{A}_f$ is the asymmetry parameter defined by

$$\mathcal{A}_f = \frac{(g_L^f)^2 - (g_R^f)^2}{(g_L^f)^2 + (g_R^f)^2} \,. \tag{5.14}$$

Integrating Eq. (5.12) over the forward and backward regions as in Eq. (5.11) shows that the forward-backward asymmetry is proportional to $\mathcal{A}_e\mathcal{A}_f$, thus provides a direct probe of the chiral structure of the couplings.

The experimental measurements of the forward-backward asymmetries are corrected for radiative effects and photon-exchange contributions, yielding the pole asymmetries denoted as $A_{\rm FB}^{0,f}$. These are directly related to the asymmetry parameters as

$$A_{\rm FB}^{0,f} = \frac{3}{4}\mathcal{A}_e\mathcal{A}_f \,, \tag{5.15}$$

which allows for their direct computation within the SMEFT framework given the modified couplings in Eq. (5.8).

An important caveat is that the forward-backward asymmetry is defined as a ratio, where both the numerator and the denominator depend on the SMEFT Wilson coefficients. To maintain a consistent expansion in powers of Λ^{-2}, we expand the asymmetries up to order Λ^{-4}. Further details on this procedure can be found in Appendix D .

Moreover, additional contributions arise from contact four-fermion interactions. For charged leptons, this contribution is given by

$$A_{\rm FB,\,4f}^{0,\ell} = \frac{3(\tilde{C}^2_{\substack{ee\\ee\ell\ell}} + \tilde{C}^2_{\substack{ll\\ee\ell\ell}} - \tilde{C}^2_{\substack{le\\ee\ell\ell}} - \tilde{C}^2_{\substack{le\\\ell\ell ee}})}{4(\tilde{C}^2_{\substack{ee\\ee\ell\ell}} + \tilde{C}^2_{\substack{ll\\ee\ell\ell}} + \tilde{C}^2_{\substack{le\\ee\ell\ell}} + \tilde{C}^2_{\substack{le\\\ell\ell ee}})} \,, \tag{5.16}$$

and for quarks by

$$A_{\rm FB,\,4f}^{0,u/d} = \frac{3(\tilde{C}^2_{\substack{eu/d\\eeqq}} + (\tilde{C}^{\mp}_{\substack{lq\\eeqq}})^2 - \tilde{C}^2_{\substack{lu/d\\eeqq}} - \tilde{C}^2_{\substack{qe\\qqee}})}{4(\tilde{C}^2_{\substack{eu/d\\eeqq}} + (\tilde{C}^{\mp}_{\substack{lq\\eeqq}})^2 + \tilde{C}^2_{\substack{lu/d\\eeqq}} + \tilde{C}^2_{\substack{qe\\qqee}})} \,, \tag{5.17}$$

which we expand up to Λ^{-4}. These additional four-fermion contributions must be taken into account when comparing SMEFT predictions with experimental measurements of the Z boson forward-backward asymmetry.

Tab. 5.3 summarizes the experimental measurements of the Z boson forward-backward asymmetries at LEP [17]. We further include the correlations of the data given in Tabs. 2.13 and 5.11 of Ref. [17] in our fit.

5.2.3. W Decays

Decays of the W boson provide additional information on SMEFT Wilson coefficients by probing charged current interactions, complementary to the neutral current interactions accessed via Z boson decays. The W boson can decays either into a charged-lepton-neutrino pair ($W \to \ell\nu$) or into a quark-antiquark pair ($W \to q\bar{q}'$). Partial width measurements from colliders such as

Observable	Measurement [17]	SM Prediction [17]
$A_{\text{FB}}^{0,e}$	0.0145(25)	0.01627(27)
$A_{\text{FB}}^{0,\mu}$	0.0169(13)	0.01627(27)
$A_{\text{FB}}^{0,\tau}$	0.0188(17)	0.01627(27)
$A_{\text{FB}}^{0,b}$	0.0992(16)	0.10324(88)
$A_{\text{FB}}^{0,c}$	0.0707(35)	0.07378(68)

Table 5.3: Measurements of the Z boson forward-backward asymmetries at LEP [17], alongside the corresponding SM predictions [17].

LEP [262–265], the Tevatron [266, 267] and the LHC [220] provide stringent test on the SM predictions dictated by the EW theory.

SMEFT contributions modify the partial decay widths of the W boson decays by introducing corrections from higher-dimensional operators. At tree level, the partial width for the decay $W \to \ell_i \nu_j$ in the SMEFT is given by

$$\Gamma(W \to \ell_i \nu_j) = \frac{m_W^3}{12\pi v^2} \left(\left(\delta_{ij} + \tilde{C}^{(3)}_{\substack{\varphi l \\ ij}} \right)^2 + \tilde{C}^2_{\substack{eW \\ ij}} \right) , \tag{5.18}$$

which is sensitive to the triplet Higgs-current coefficient $\tilde{C}^{(3)}_{\varphi l}$ and the electroweak dipole coefficient $\tilde{C}_{eW}$.

Within the SM, only lepton-flavor-diagonal couplings ($i = j$) contribute to the decay $W \to \ell_i \nu_j$. However, the SMEFT framework can introduce additional lepton-flavor-violating (LFV) couplings, where $i \neq j$. Since experimental measurements do not distinguish the neutrino flavor, all neutrino species contribute incoherently. As a result, the partial width for $\Gamma(W \to \ell_i \nu)$ is given by the incoherent sum over all neutrino flavors

$$\Gamma(W \to \ell_i \nu) = \sum_j \Gamma(W \to \ell_i \nu_j) \, . \tag{5.19}$$

The W decay width thus simultaneously probes both, lepton-flavor-diagonal and LFV couplings.

Notably, the sensitivity of the W boson decay to the dipole coefficient $\tilde{C}_{eW}$ offers an opportunity to disentangle the contributions from the electroweak dipole coefficients in the Z boson decays, which only probe to the linear combination $\tilde{C}_{eZ}$. By combining information from both W and Z processes, it is possible to separately constrain the individual contributions from $\tilde{C}_{eW}$ and $\tilde{C}_{eB}$, thereby lifting the degeneracies of the individual observables in the parameter space.

Fig. 5.5 illustrates this interplay for the $e\mu$ coefficients by showing individual and combined two-dimensional fits of $\tilde{C}_{eW}$ and $\tilde{C}_{eB}$, neglecting RGE running and mixing. The blue region shows the 95% posterior region from the $W \to e\nu$ fit, which is relatively broad owing to large SM backgrounds and experimental challenges associated with the neutrino in the final state. The orange region shows the 95% contour from the bound on $\mathcal{B}(Z \to e\mu)$, which is narrow

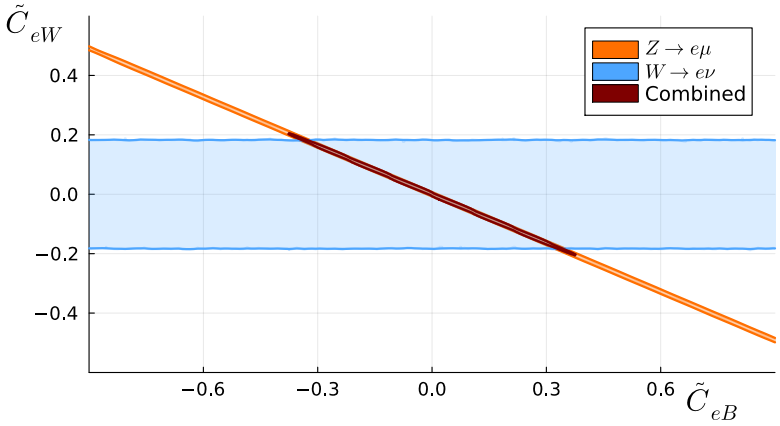

Figure 5.5: Synergies between the W and Z boson decay channels in the $\tilde{C}_{eW}$–$\tilde{C}_{eB}$ plane for the $e\mu$ coefficients. The colored regions correspond to the 90% credible regions of the posterior probability distribution. We show the individual fits to the W decay measurement in blue, the Z decay width in orange, and the combined fit in red.

along the $\tilde{C}_{eZ}$ direction but insensitive to the orthogonal combination. The red contour shows the combined fit, which strongly reduces the allowed region by lifting the flat direction and constraining both coefficients individually.

In addition to the leptonic channels discussed above, the hadronic decays of the W boson provides additional information by probing the triplet Higgs-current operator $\tilde{C}^{(3)}_{\varphi q}$. At tree level, the partial decay width for the W boson decaying into a quark-antiquark pair is given by

$$\Gamma(W \to u_i \bar{d}_j) = \frac{m_W^3 N_c}{12\pi v^2} \left(V_{ij} + \tilde{C}^{(3)}_{\substack{\varphi q \\ ij}} \right)^2 , \tag{5.20}$$

where $N_c = 3$ is the number of colors and V_{ij} denotes the corresponding CKM matrix element. In our MFV SMEFT framework, no dipole contributions are induced as the decay to a top quark is kinematically forbidden. The total hadronic width typically measured by experiments is given by the sum over all accessible final states

$$\Gamma(W_{\text{had}}) = \sum_{i,j} \Gamma(W \to u_i \bar{d}_j) , \tag{5.21}$$

where the sum extends over all quark flavors except for the top quark.

Tab. 5.4 summarizes the experimental data we employ in our fit, obtained from the W boson branching fraction measurements from by CMS collaboration [220]. By multiplying the measured branching fractions with the total W boson width [18], we obtain the partial widths that can be directly compared with SMEFT predictions. Branching fractions, in contrast, need to be expanded in powers of Λ^2 to keep a consistent SMEFT expansion, significantly complicating the computations as a myriad of different channels and Wilson coefficients contribute to the total decay width. We also incorporate the correlation matrix presented in Fig. 8 of Ref. [220].

$\Gamma(W \to e\nu)$	$\Gamma(W \to \mu\nu)$	$\Gamma(W \to \tau\nu)$	$\Gamma(W_{\text{had}})$
0.226(5) GeV	0.228(5) GeV	0.225(6) GeV	1.407(29) GeV

Table 5.4: Measurements of the W boson branching fractions by the CMS collaboration [220].

The SM predictions for the partial decay width $W \to \ell_i \nu_i$ are $0.22629(4)$ GeV [18], assuming $m_\ell/m_W \approx 0$. For the decay into a quark-antiquark final state $u_i \bar{d}_j$, the SM prediction is given by $|V_{ij}|^2 0.7053(4)$ GeV [18] where the prediction includes the effects of final state QED and QCD corrections [268, 269].

5.3. Dilepton Production at LEP

Beyond the Z-pole observables discussed in the previous section, measurements of off-peak dilepton production $e^+e^- \to \ell^+\ell^-$ with $\ell = e, \mu, \tau$ at LEP provide additional constraints on the SMEFT parameter space. In particular the four-lepton operators O_{ee}, O_{ll} and O_{le} induce contact interactions scaling as s/Λ^2 at high energies, which dominate the SMEFT contributions at energies well above the Z resonance. Additionally, leptonic Higgs-current and electroweak dipole operators induce chirality-dependent modifications to the $Z\ell^+\ell^-$ and $\gamma\ell^+\ell^-$ vertices, altering both the overall rate and the angular distributions of the final-state leptons. The clean environment at LEP thus allows for precise measurements and stringent constraints on lepton-flavor specific new physics.

We compute the SMEFT contributions to this process at tree level using MATHEMATICA [222] in combination with the FEYNCALC [223–226] and `SmeftFR` v3.0 [227] packages. In general, the differential cross section for the process $e^+e^- \to \ell^+\ell^-$ with $\ell \neq e$ within the SMEFT framework can be factorized into contributions corresponding to the Mandelstam variables t and u. Contributions proportional to s can always be rewritten in terms of u and t employing the relation $s + t + u = \sum m_i \approx 0$ which allows us to substitute $s = -(t + u)$, assuming $m_\ell \ll \sqrt{s}$. Each of these contributions gives rise to a distinct angular dependence of the outgoing leptons, so that the differential cross section can be expressed as

$$\frac{d\sigma}{d\cos\theta} = \frac{1}{16\pi^2 s}\left[\eta_{u^2}(1-\cos\theta)^2 + \eta_{t^2}(1+\cos\theta)^2 + \eta_{ut}\,(1-\cos^2\theta)\right], \tag{5.22}$$

where θ is the scattering angle of the outgoing lepton in the center-of-mass frame. The coefficients η_{u^2}, η_{t^2} and η_{ut} encode the dependence on the SMEFT Wilson coefficients.

The terms proportional to $(1-\cos\theta)^2$ contributing to η_{u^2} are generated by interactions in which the incoming and outgoing leptons share the same chirality (i.e. both left-handed or both right-handed). Consequently, this contribution receives corrections from operators such as O_{ee} or O_{ll}.

In contrast, the terms contributing to η_{t^2} that give rise to a $(1+\cos\theta)^2$ dependence arise from interactions where the incoming and outgoing leptons have opposite chiralities. For instance, left-handed incoming leptons converting into right-handed outgoing leptons, or vice versa. This structure is typically induced by operators like O_{le}, which couples left-handed leptons to right-handed ones. Vertex corrections arising from the Higgs-current operators modify both

of these terms by introducing interference effects with the SM amplitude or among different SMEFT contributions.

The terms proportional to $(1 - \cos\theta^2)$, contributing to η_{ut} originate from vertex structures with mixed chiralities, involving both left-handed and right-handed leptons on the incoming and outgoing sides. In the limit of massless leptons, such contributions vanish in the SM. Within SMEFT, however, these terms are generated by the dipole operators, offering a unique angular structure.

Analogous arguments apply to the $e^+e^- \to e^+e^-$ process. The computation of the differential cross section is, however, more involved due to additional t-channel contributions from photon and Z boson exchange that must be taken into account. Therefore, we rely on the numerical evaluation of the cross sections using MATHEMATICA for this process.

We employ the differential cross-section measurements at $\sqrt{s} = 207\,\text{GeV}$ from the DELPHI collaboration [221] as experimental input. We only use the highest energy bin, since the energy-enhancement of the SMEFT operator is most pronounced in this region and employing only one bin reduces the impact of unknown correlations if the data. Fig. 5.6 illustrates the data and the different chirality structures contributing in the SM and the SMEFT. We show the different angular distributions in Eq. (5.22) together with the SM predictions and the data on $e^+e^- \to \mu^+\mu^-$ from Ref. [221].

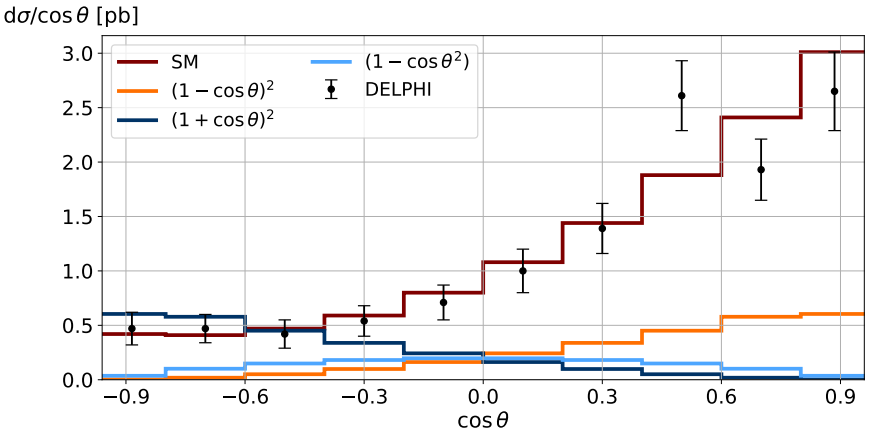

Figure 5.6: Differential cross section for the process $e^+e^- \to \mu^+\mu^-$ at $\sqrt{s} = 207\,\text{GeV}$ as a function of $\cos\theta$. The data from Ref. [221] is indicated by the black dots, while the SM prediction presented in Ref. [221] is shown in red. The contributions of the different chirality structures are shown in blue and orange.

5.4. The Drell-Yan Process in the SMEFT

The Drell-Yan (DY) process, denoting the production of a lepton-antilepton pair at a hadron collider, is a key process for probing semileptonic new physics (see e.g. [2, 162, 201, 260, 270–273]). In the SMEFT, it receives contributions from several operator classes, most notably semileptonic four-fermion interactions. These operators induce contact terms, which yield

strong constraints in the high-invariant mass tails of the dilepton spectrum due to the s/Λ^2 scaling of the amplitudes.

In addition to the four-fermion coefficients, DY observables further test the Higgs-current and the leptonic electroweak-dipole operators, for which the amplitudes scale as v^2/Λ^2 and $v\sqrt{\hat{s}}/\Lambda^2$, respectively [34, 162]. The interplay of these operators not only shifts the total rate, but also affects the shape of the differential cross sections, allowing us to set competitive bounds on numerous coefficients simultaneously. We compute the corresponding contributions following the simulation process outlined in Sec. 5.1. In the following, we present the theoretical description of the DY process in the SMEFT, discuss the experimental setup, and summarize the sensitivity of the DY channels to the various Wilson coefficients.

5.4.1. Neutral-Current Drell-Yan Process

In the SM, the neutral-current Drell-Yan process is primarily mediated by the exchange of a photon or a Z boson between an initial-state quark-antiquark pair, where the partonic cross section is known up to N^3 order in QCD [274]. Experimentally, the differential distributions of neutral current DY processes are typically presented in terms of the invariant mass of the dilepton system, $m_{\ell\ell}$. An exception is the $\tau^+\tau^-$ channel, where the transverse mass m_T^{tot} is used because the rapid decays of the τ leptons into final states with neutrinos prevent a full reconstruction of the event.

The experimental data depend sensitively on the kinematic cuts that are optimized for each analysis. We account for these effects by recasting the original analyses using ROOT [255], and we validate our simulation setup by reproducing the SM predictions for the DY process. We achieve a good agreement with the results reported by the experimental collaborations, typically with a deviation of less than 20%.

As the distinct chirality structures of the DY amplitude can be treated as independent fields in the high-energy limit, we can simultaneously constrain multiple linear combinations of Wilson coefficients. However, owing to the interference between the photon and the Z boson contributions, the different contributions are non-trivially correlated, leading to a complex interplay among the various operators. Of particular importance for the neutral current DY process are the linear combinations

$$\tilde{C}_{lq}^{\pm} = \tilde{C}_{lq}^{(1)} \pm \tilde{C}_{lq}^{(3)}\,, \qquad \tilde{C}_{\varphi l}^{\pm} = \tilde{C}_{\varphi l}^{(1)} \pm \tilde{C}_{\varphi l}^{(3)}\,, \qquad \tilde{C}_{\varphi q}^{\pm} = \tilde{C}_{\varphi q}^{(1)} \pm \tilde{C}_{\varphi q}^{(3)}\,, \tag{5.23}$$

which arise from the left-handed lepton and quark currents. The various combinations can be probed by distinct initial and final state configurations, leading to a rich phenomenology.

Tab. 5.5 summarizes the contributions of the different linear combinations to the partonic processes. It is evident that by analyzing only a single channel at a time, we encounter flat directions in the parameter space along which the likelihood remains constant. Combining the channels accessible by the composite structure of the proton allows us to largely break theses degeneracies. The only exception is the operator $O_{\varphi l}^{-}$, which is only probed by dineutrino final states. Although studies of the dineutrino DY process within the SMEFT exist [2, 260], they do not yet include the Higgs-current operators, so we do not consider this process here. Instead, we can resolve this flat direction by combining DY data with measurements of the $Z \to$ invisible decay width (see Sec. 5.2.1) or with the charged current DY process, described in the following subsection.

Operator	Processes	Operator	Processes
O_{lq}^{+}	$d_L\bar{d}_L \to \ell^+\ell^-$, $u_L\bar{u}_L \to \nu\bar{\nu}$	O_{lq}^{-}	$u_L\bar{u}_L \to \ell^+\ell^-$, $d_L\bar{d}_L \to \nu\bar{\nu}$
$O_{\varphi l}^{+}$	$pp \to \ell^+\ell^-$	$O_{\varphi l}^{-}$	$pp \to \nu\bar{\nu}$
$O_{\varphi q}^{+}$	$d_L\bar{d}_L \to ll$	$O_{\varphi q}^{-}$	$u_L\bar{u}_L \to ll$

Table 5.5: Contributions of the linear combinations $O_{lq}^{\pm}$, $O_{\varphi l}^{\pm}$ and $O_{\varphi q}^{\pm}$ of SMEFT operators to the neutral-current DY process.

The experimental data on the DY process that we employ to constrain the Wilson coefficients are summarized in Tab. 5.6. We include measurements of the DY process for the e^+e^-, $\mu^+\mu^-$, and $\tau^+\tau^-$ channels as well as for the LFV processes $e^+\mu^-$, $e^+\tau^-$, and $\mu^+\tau^-$.

Process	Observable	Integrated Luminosity	# Bins	Experiment	Reference
$pp \to ee$	$\frac{\mathrm{d}\sigma}{\mathrm{d}m_{ee}}$	137 fb^{-1}	117	CMS	[228]
$pp \to \mu\mu$	$\frac{\mathrm{d}\sigma}{\mathrm{d}m_{\mu\mu}}$	140 fb^{-1}	48	CMS	[228]
$pp \to \tau\tau$	$\frac{\mathrm{d}\sigma}{\mathrm{d}m_T^{\mathrm{tot}}}$	139 fb^{-1}	4	ATLAS	[229]
$pp \to e\mu$	$\frac{\mathrm{d}\sigma}{\mathrm{d}m_{e\mu}}$	139 fb^{-1}	4	ATLAS	[230]
$pp \to e\tau$	$\frac{\mathrm{d}\sigma}{\mathrm{d}m_{e\tau}}$	139 fb^{-1}	4	ATLAS	[230]
$pp \to \mu\tau$	$\frac{\mathrm{d}\sigma}{\mathrm{d}m_{\mu\tau}}$	139 fb^{-1}	4	ATLAS	[230]

Table 5.6: Measurements of the neutral current Drell-Yan process considered in this work. We list the process, the differential observable, the integrated luminosity, number of bins, the experimental collaboration as well as the reference.

There are, however, important caveats to consider when interpreting DY data within the SMEFT framework. One significant challenge is the potential masking of BSM effects in the PDFs, as the PDFs are in part extracted from DY data. Consequently, any new physics deviations might be inadvertently absorbed into the PDF fits, thereby diluting the sensitivity of the analysis. A possible solution is to perform a simultaneous fit of both the PDFs and the SMEFT parameters, as demonstrated, for example, in Ref. [202], but such an approach is beyond the scope of this work.

Another simplification employed in our analysis is the neglect of SMEFT effects on background processes. Although the background contributions for electron and muon channels are typically small, significant backgrounds arise in processes involving τ leptons due to misidentifications and other experimental challenges. Ideally, these background contributions should be modeled consistently within the SMEFT framework. However, this level of detail is deferred to future work.

Finally, it is crucial to ensure the validity of the EFT expansion. The DY data extend to bins with invariant masses up to several TeV, necessitating that the new physics scale Λ remains

sufficiently well separated to ensure a good convergence of the EFT expansion. To this end, we assume a benchmark value of $\Lambda = 10\,\text{TeV}$ throughout our analysis.

5.4.2. Charged-Current Drell-Yan Process

While the neutral current DY process is mainly mediated by the Z boson and the photon in the SM, the charged current process arises from W boson exchange. In the SMEFT, this process is predominantly sensitive to the triplet operators $O_{\varphi q}^{(3)}$, $O_{\varphi l}^{(3)}$, and $O_{lq}^{(3)}$, as well as to the electroweak dipole operator O_{eW}. These operators modify the W boson couplings to quarks and leptons and give rise to addition four-fermion contact interactions. An important feature of the charged current channel is that the neutrino flavor is not determined experimentally. As a consequence, the total cross section is obtained as a sum over the cross sections for the individual neutrino flavors,

$$\sigma(pp \to \ell_i \nu) = \sum_j \sigma(pp \to \ell_i \nu_j)\,, \tag{5.24}$$

where the sum runs over the three neutrino flavors. This summation inherently incorporates both lepton-flavor-diagonal (LFD) and lepton-flavor-violating (LFV) contributions, which contribute incoherently and can therefore be constrained simultaneously.

Experimentally, the charged current DY process is typically analyzed in terms of the transverse mass m_{T}, which is defined as

$$m_{\text{T}} = \sqrt{2 p_T^{\ell} p_T^{\text{miss}} \left(1 - \cos(\Delta\phi)\right)}\,, \tag{5.25}$$

where p_T^{ℓ} is the transverse momentum of the charged lepton, p_T^{miss} is the missing transverse momentum, and $\Delta\phi$ is the azimuthal angle between the charged lepton and the missing transverse momentum. Deviations in the shape and normalization of the m_T, distributions can signal the presence of new physics effects in charged currents, which would imprint in the triplet SMEFT coefficients.

We simulate the SMEFT contributions following the process outlined in Sec. 5.1. Tab. 5.7, summarizes the data used to constrain the Wilson coefficients in our analysis. We include measurements of the charged current DY process for the $e\nu$, $\mu\nu$, and $\tau\nu$ channels.

Process	Observable	Integrated Luminosity	# Bins	Experiment	Reference
$pp \to e\nu$	$\frac{\mathrm{d}\sigma}{\mathrm{d}m_T}$	139 fb^{-1}	65	ATLAS	[231]
$pp \to \mu\nu$	$\frac{\mathrm{d}\sigma}{\mathrm{d}m_T}$	139 fb^{-1}	54	ATLAS	[231]
$pp \to \tau\nu$	$\frac{\mathrm{d}\sigma}{\mathrm{d}m_T}$	138 fb^{-1}	18	CMS	[232]

Table 5.7: Measurements of the charged current Drell-Yan process considered in this work. We list the process, the differential observable, the integrated luminosity, number of bins, the experimental collaboration as well as the reference.

A key benefit of the charged-current process is that it helps to disentangle the different linear combinations of Wilson coefficients presented in Eq. 5.23. In particular, the charged current adds

a linearly independent direction in the parameter space by constraining only the $\tilde{C}_{lq}^{(3)}$ directions. Fig. 5.7 illustrates this synergy by showing the 95% credible regions of the two-dimensional fits in the $\tilde{C}_{lq}^{(1)}$-$\tilde{C}_{lq}^{(3)}$ plane for the $e\mu$ coefficients. We show the bounds from a fit to charged-current process $pp \to e\nu$ in orange, a fit to the neutral current process with up(down)-type quarks in the initial state in light blue (medium blue), a fit to the combined neutral current process in dark blue and the combined fit to the neutral and charged current processes in red. We see how the combination of the various channels leads to a significant reduction in the allowed parameter space, lifting degeneracies and tightening the bounds on the Wilson coefficients. This demonstrates the power of combining different channels to extract more information from the data and improve our understanding of the underlying physics.

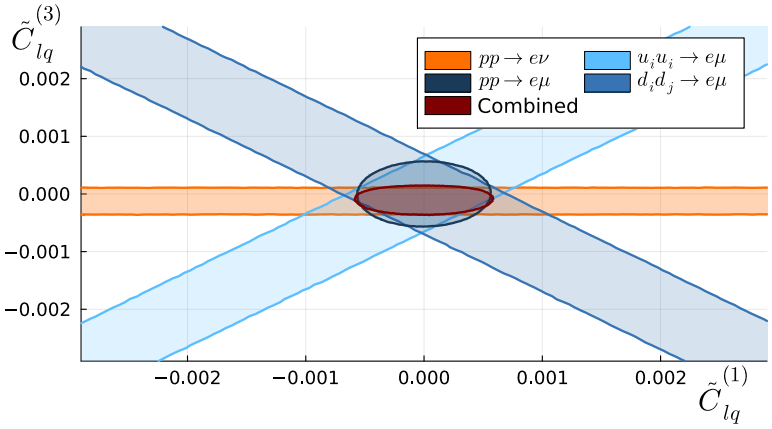

Figure 5.7: Synergy between the neutral current and charged current Drell-Yan processes in the $\tilde{C}_{lq}^{(1)}$-$\tilde{C}_{lq}^{(3)}$ plane. The 95% credible regions are shown for the $pp \to e\nu$ process in orange, the neutral current process with up(down)-type quarks in the initial state in light blue (medium blue), the combined neutral current process in dark blue, and the combined fit to the neutral and charged-current processes in red.

5.5. Top-Quark Observables

In many extensions of the SM, new dynamics and particles are expected to preferentially affect the third generation of fermions. In particular, the top quark plays a unique role in the SM and the search for new physics, as it is the heaviest known elementary particle and the only quark that decays before hadronizing. This special role is also reflected within the MFV framework discussed in Sec. 3.2.2, where the top quark receives the strongest corrections from higher-order spurion insertions. Therefore, the top-quark sector is expected to be particularly sensitive to the effects of flavor-symmetry breaking.

Furthermore, the top quark observables provide a complementary probe of the flavor structure that is not accessible by the DY process discussed in Sec. 5.4. While DY observables are predominantly sensitive to the light quarks due to the structure of the PDFs, the top quark, and to a lesser extent the bottom quark, are strongly PDF suppressed (see Fig. 5.1). Consequently,

the third generation is only weakly constrained by DY measurements, making direct probes of top quark observables a crucial part of global analysis in the SMEFT.

Precision measurements of top quark properties, such as decay widths, helicity fractions, and various production channels, therefore offer valuable probes of both the SMEFT modifications and the MFV parameterization (see e.g.Refs. [26, 29–31, 37, 38, 275]). In the following section, we explore the observables associated with top-quark decay as well as top-quark pair production and discuss their sensitivity to SMEFT Wilson coefficients.

5.5.1. Top-Quark Decay Observables

In the SM, the top quark decays almost exclusively into a W boson and a b quark. Although decays into an s or d quark are in principle possible, they are strongly suppressed by small CKM elements, V_{ts} and V_{td}, respectively, entering the decay amplitude. FCNC decays such as $t \to c\gamma$ are even further suppressed by the GIM mechanism introduced in Sec. 2.1, making these channels negligibly small in the SM[2].

In contrast to the decays of light fermions, the W boson is produced on-shell in the decay of the top quark, leading to a rapid decay process. The top quark therefore decays before it can hadronize, allowing for a direct measurement of its intrinsic characteristics, such as spin and polarization. Within the SMEFT framework, higher-dimensional operators can modify both the total decay width and the angular distribution of the decay products, measured via the helicity fractions of the W boson.

Decay Width

The total top-quark decay width is a fundamental observable that reflects the strength of the charged-current interactions of the third generation, making it sensitive to modifications in the W coupling to fermions. The SMEFT operators can modify the decay width by altering the coupling strength of the tWd_i vertex, with $d_i = d, s, b$. At tree-level, the top quark decay width in the SMEFT is given by

$$\begin{aligned}\Gamma_t = \sum_{i=d,s,b} \frac{m_t^3}{16\pi v^2}\left(1-\frac{m_W^2}{m_t^2}\right)^2 \Bigg[\left(1+2\frac{m_W^2}{m_t^2}\right)(V_{ti}+\tilde{C}^{(3)}_{\substack{\varphi q\\ i3}})^2 \\ + 2\left(2+\frac{m_W^2}{m_t^2}\right)\tilde{C}^2_{\substack{uW\\ i3}} - 6\sqrt{2}\frac{m_W}{m_t}(V_{ti}+\tilde{C}^{(3)}_{\substack{\varphi q\\ i3}})\tilde{C}_{\substack{uW\\ i3}}\Bigg]\end{aligned} \tag{5.26}$$

where the first line corresponds to the contribution of the Higgs-current operator $O^{(3)}_{\varphi q}$, and the terms in the second line represent the contribution of the dipole operator O_{uW} as well as the interference between the two, respectively. To incorporate higher-order QCD corrections, the tree-level width is multiplied by a factor $1 - 2\alpha_s/3\pi(2\pi^2/3 - 5/2) \sim 0.91$[276], resulting in a SM prediction of $1.343(8)$ GeV. The value is in good agreement with the current experimental average of $\Gamma_t = 1.42(19)$ GeV [18].

[2] In the MFV framework, no up-type FCNC are induced that might otherwise potentially contribute to FCNC top-quark decays.

Helicity Fractions

The helicity fractions of the W boson, denoted as the left-handed ($\mathcal{F}_L$), right-handed ($\mathcal{F}_R$), and longitudinal ($\mathcal{F}_0$) components, provide a sensitive probe of the structure of the weak interaction and the nature of the tWb vertex. In the SM, the V-A structure of the weak interaction implies that the longitudinal component is dominant, accompanied by a sizable left-handed fraction, while the right-handed fraction is strongly suppressed. In the SMEFT framework, higher-dimensional operators can alter this pattern by introducing new Lorentz structures or by interfering with the SM amplitude, thereby altering the relative size of the helicity fractions. Detailed angular analyses of the decay products can therefore provide a powerful tool to constrain the SMEFT parameter space.

We compute the SMEFT contributions to the helicity fractions at tree level using the FeynCalc [223–226] and `SmeftFR` v3.0 [227] packages in Mathematica [222]. The resulting partial widths read

$$\begin{aligned}
\Gamma_0 &= \sum_{i=d,s,b} \frac{m_t^3}{16\pi v^2}\left(1-\frac{m_W^2}{m_t^2}\right)^2\left[(V_{ti}+\tilde{C}^{(3)}_{\substack{\varphi q\\ i3}})^2 - 2\sqrt{2}\frac{m_W}{m_t}(V_{ti}+\tilde{C}^{(3)}_{\substack{\varphi q\\ i3}})\tilde{C}_{\substack{uW\\ i3}} + 2\frac{m_W^2}{m_t^2}\tilde{C}^2_{\substack{uW\\ i3}}\right],\\
\Gamma_L &= \sum_{i=d,s,b} \frac{m_t^3}{8\pi v^2}\left(1-\frac{m_W^2}{m_t^2}\right)^2\left[\frac{m_W^2}{m_t^2}(V_{ti}+\tilde{C}^{(3)}_{\substack{\varphi q\\ i3}})^2 - 2\sqrt{2}\frac{m_W}{m_t}(V_{ti}+\tilde{C}^{(3)}_{\substack{\varphi q\\ i3}})\tilde{C}_{\substack{uW\\ i3}} + 2\tilde{C}^2_{\substack{uW\\ i3}}\right],\\
\Gamma_R &= 0\,,
\end{aligned} \tag{5.27}$$

where we neglect the b quark mass since $m_b \ll m_t, m_W$. The helicity fractions are defined as the ratios

$$F_i = \frac{\Gamma_i}{\Gamma}\,, \tag{5.28}$$

with $i = 0, L, R$. To maintain a consistent expansion in powers of Λ^{-2}, we expand the helicity fractions up to order $\mathcal{O}(1/\Lambda^4)$ as described in Appendix D .

Since we neglect m_b and our MFV setup does not induce any right-handed charged current operators at tree level, the right-handed helicity fraction receives no SMEFT contribution. Consequently, any observation of a significant right-handed component would signal new physics beyond the MFV ansatz.

As experimental input, we employ the measurements of the helicity fractions from the ATLAS collaboration [277] at $\sqrt{s} = 13\,\text{TeV}$ using $139\,\text{fb}^{-1}$ of data. We also incorporate the correlation matrix given in Tab. 2 of Ref. [277] in the analysis. For the SM predictions, we rely on the results from Ref. [278] computed at NNNLO QCD and NLO EW accuracy. Tab. 5.8 summarizes the numerical values of both the experimental data and the SM predictions.

5.5.2. Top-Quark Pair Production

Top-quark pair production is an extensively studied process at hadron colliders that helps to test the SM and to probe potential BSM effects in the third generation of quarks. In addition to the inclusive differential pair-production cross section measurements [279], several analyses have extended the investigation to top-quark pair production in association with additional

Observable	Measurement [277]	SM Prediction [278]
$\mathcal{F}_0$	0.684(15)	0.686(3)
$\mathcal{F}_L$	0.318(9)	0.312(2)
$\mathcal{F}_R$	-0.002(14)	0.00157(2)

Table 5.8: Experimental data on the helicity fractions of the top quark decay products by the ATLAS collaboration at $\sqrt{s} = 13\,\text{TeV}$ using $139\,\text{fb}^{-1}$ of data [277], as well as the corresponding SM predictions [278].

particles, such as an additional Z boson [280] or W boson [281], an additional photon [282], or a Higgs boson [283], to probe modified couplings of the top quark. These associated production channels are sensitive to different combinations of Wilson coefficients, and therefore provide a complementary window into the SMEFT parameter space.

In the SMEFT framework, higher-dimensional operators can induce deviations not only in the overall cross section but also in the detailed kinematic distributions, such as the invariant mass of the top quark pair or the transverse momentum distributions of the extra particles. We simulate the SMEFT contributions at tree-level using MADGRAPH5_aMC@NLO [235] in conjunction with the `SMEFTsim` 3.0 package [180, 236]. The generated events are binned and analyzed with MADANALYSIS 5 [256], following the binning and selections reported in the corresponding experimental studies.

Given that the gluon-fusion channel dominates top quark pair production at the LHC, the largest SMEFT contributions typically arise from the O_{uG} operator, which modifies the top-gluon coupling. Meanwhile, operators such as O_{uW}, O_{uB} and $O_{\varphi q}^{-}$ affect the subleading contributions mediated by the Z boson and photon exchange. Notably, the associated production processes enhance our sensitivity to these operators. For example, the O_{uW} operator is predominantly constrained by $t\bar{t}W$ production. Similarly, the linear combinations

$$\tilde{C}_{uZ} = -\sin\theta_W \tilde{C}_{uB} + \cos\theta_W \tilde{C}_{uW}\,, \qquad \tilde{C}_{u\gamma} = \cos\theta_W \tilde{C}_{uB} + \sin\theta_W \tilde{C}_{uW}\,, \tag{5.29}$$

are primarily probed by $t\bar{t}Z$ and $t\bar{t}\gamma$ production, respectively.

Tab. 5.9 summarizes the top quark pair production observables used in our SMEFT fit, listing the processes, observables, number of bins, and the references for the experimental data and the corresponding SM predictions.

In addition, we incorporate constraints from top-quark pair production in association with leptons, $pp \to t\bar{t}\ell^+\ell^-$. For quark-current and -dipole operators affecting the top-quark pair production, we use the results reported by the CMS collaboration in Ref. [288][3]. For constraints on semileptonic four-fermion operators, we employ the lepton-flavor-specific analysis from the ATLAS collaboration, as presented in Ref. [289]. This analysis is performed lepton-flavor specific, aligning closely with our objective, but does not include contributions from dipole and Higgs-current operators.

[3]This analysis also includes the $pp \to t\bar{t}\ell\nu$ process.

Process	Observable	Number of Bins	Reference	SM Reference
$pp \to t\bar{t}$	$\frac{\mathrm{d}\sigma}{\mathrm{d}m_{t\bar{t}}}$	15	[279]	[279]
$pp \to t\bar{t}Z$	$\frac{\mathrm{d}\sigma}{\mathrm{d}p_{\mathrm{T}}(Z)}$	7	[280]	[284]
$pp \to t\bar{t}\gamma$	$\frac{\mathrm{d}\sigma}{\mathrm{d}p_{\mathrm{T}}(\gamma)}$	11	[282]	[285]
$pp \to t\bar{t}W$	$\sigma(t\bar{t}W)$	1	[281]	[286]
$pp \to t\bar{t}H$	$\sigma(t\bar{t}H)$	1	[283]	[287]

Table 5.9: Top quark pair production observables considered in the global SMEFT fit. We list the processes, observables, number of bins used in the analysis, as well as the references for the experimental data and the SM predictions.

The $t\bar{t}\ell\ell$ channel is particularly valuable, as it uniquely probes semileptonic coefficients involving right-handed top-quarks. It thus directly constrains the MFV ratio r_R, defined in Eq. (3.17). While operators involving left-handed quark doublets are indirectly constrained via $SU(2)L$ relations to b-quark observables, they remain weakly constrained in the DY process due to PDF suppression. Consequently, the $t\bar{t}\ell\ell$ process provides essential additional sensitivity. Furthermore, this channel uniquely tests scalar and tensor coefficients $\tilde{C}^{(1)}_{lequ}$ and $\tilde{C}^{(3)}_{lequ}$, which are otherwise not directly accessible in collider observables within the MFV framework.

For our analysis, we directly utilize the $\Delta \ln L$ values provided by the experimental collaborations. To evaluate the likelihood across the parameter space, we perform a two-dimensional interpolation of the provided binned likelihood functions using a radial basis function (RBF) method. We randomly sample 100 points across the parameter space, applying a weighting factor proportional to $1/r$, where r is the distance from the parameter space center. This approach ensures denser sampling in regions with higher likelihood, while adequately covering the entire parameter space. The resulting likelihood distribution is subsequently approximated by a multivariate Gaussian function.

Coefficient	90% CI	Coefficient	90% CI
$\tilde{C}^{-}_{lq}$	$[-0.027, 0.065]$	$\tilde{C}_{qe}$	$[-0.048, 0.048]$
$\tilde{C}_{lu}$	$[-0.041, 0.052]$	$\tilde{C}_{eu}$	$[-0.034, 0.056]$
$\tilde{C}^{(1)}_{lequ}$	$[-0.11, 0.11]$	$\tilde{C}^{(3)}_{lequ}$	$[-0.020, 0.020]$

Table 5.10: 90% credible intervals (CI) for the semileptonic four-fermion Wilson coefficients obtained from $t\bar{t}\ell\ell$ production.

To assess the impact of the inclusion of the $tt\ell\ell$ channel as well as the updated measurements of $t\bar{t}W$ and $t\bar{t}H$ production compared to the previous global fit in Ref. [1], we compare the results of a fit to the top quark observables using the observables and measurements outlined above (2025) with the previous results of Refs. [1] (2023) and [36] (2021) in Tab. 5.11.

Analysis	$\tilde{C}_{uB}$	$\tilde{C}_{uG}$	$\tilde{C}_{uW}$
2021 [36]	[-0.0215, 0.0245]	[-0.0214, 0.0032]	[-0.0058, 0.0018]
2023 [1]	[-0.000, 0.0224]	[-0.0017, 0.0003]	[-0.0010, 0.0032]
2025	[-0.0006, 0.023]	[-0.0014, 6.0e-5]	[-0.0009, 0.0005]
Analysis	$\tilde{C}_{\varphi q}^{(1)}$	$\tilde{C}_{\varphi q}^{(3)}$	$\tilde{C}_{\varphi u}$
2021 [36]	[-0.19, 0.99]	[-0.081, 0.025]	[-0.80, 0.63]
2023 [1]	[-0.08, 0.83]	[-0.113, 0.017]	[-0.68, 0.30]
2025	[-0.16, 0.25]	[-0.023, 0.0095]	[-0.37, 0.29]

Table 5.11: 90% credible intervals of the top-quark sector fits from Ref. [36] (2021) and Ref. [1] (2023), compared with the fit results using the updated data included in this work (2025).

We see significant improvements with regard to the analysis in Ref. [1], particularly for $\tilde{C}_{\varphi q}^{(3)}$ and $\tilde{C}_{uW}$. This stems mainly from the new data on $t\bar{t}W$, while the inclusion of the $t\bar{t}\ell\ell$ channel helps to better constrain $\tilde{C}_{\varphi u}$. In addition, $tt\ell\ell$ provides additional sensitivity to the semileptonic operators that were unconstrained by the tree-level top-quark observables in Ref. [1]. The corresponding 90% credible intervals for the Wilson coefficients are summarized in Tab. 5.10.

Chapter 6

Flavor Observables in the LEFT

Given the current lack of direct hints for BSM physics, increasing focus has been placed on indirect probes of new dynamics in precision flavor measurements. The high experimental accuracy of these observables allows to set strong bounds on new physics, in particular in the context of flavor-changing neutral currents (FCNCs) and lepton-flavor-violating (LFV) processes. Due to the GIM mechanism and the small neutrino masses, these processes are highly suppressed in the SM, making them ideal probes of BSM physics due to small experimental backgrounds.

We systematically analyze both, leptonic and mesonic observables to obtain a comprehensive picture of flavor physics in the SMEFT and place limits on a wide range of coefficients. By utilizing the LEFT framework, we aim to obtain a largely model-independent picture of BSM effects at low energies that can be directly mapped onto the SMEFT. Notably, different observables probe complementary combinations of Wilson coefficients, which helps break degeneracies in the parameter space and tighten the constraints.

In the leptonic sector, we concentrate on the anomalous magnetic moments of charged leptons as well as different lepton decay channels, including lepton-flavor violating decays, charged current processes and semileptonic channels. We further explore the mesonic sector through mass splittings in neutral meson mixing and leptonic as well as semileptonic meson decays, focusing in particular on FCNC transitions.

6.1. Leptonic Observables

Leptonic processes benefit from precise experimental measurements and are largely free from the hadronic uncertainties that complicate quark-based probes like meson decays, making them sensitive probes of potential new physics. LFV processes, in particular, are tightly constrained, since the SM background is effectively negligible. While the LEFT features a multitude of unrelated leptonic coefficients, the SMEFT framework dictates a link among left-handed currents, thus connecting neutrino and charged lepton observables and allowing for a comprehensive analysis of the underlying dynamics.

In the LEFT, leptonic transitions are described by the four-fermion contact interactions and the electromagnetic dipole operator $\mathcal{Q}_{e\gamma}$. The latter contributes strongly to the magnetic moments of charged leptons, which are measured with high precision. The off-diagonal, LFV components of the same operator, on the other hand, induce radiative lepton decays, such as $\mu \to e\gamma$, which are effectively background-free and therefore very sensitive to BSM effects.

Four-lepton operators, by contrast, are best probed by three-body lepton decays, including both lepton-flavor violating decays $\ell_i \to \ell_j \ell_k \ell_l$ and flavor-conserving modes with neutrinos in the final state, such as $\ell_i \to \ell_j \nu_i \bar{\nu}_j$. In addition, semileptonic four-fermion operators are probed by semileptonic tau decays $\tau \to \ell_i M$ and $\tau \to \nu_i M$, offering further tests of charged- as well as

neutral-current interactions. By combining measurements across these various channels, we can simultaneously probe multiple flavor structures and set limits on wide range of LEFT Wilson coefficients.

6.1.1. Anomalous Magnetic Moments

The anomalous magnetic moment of a charged lepton is defined as

$$a_\ell = \frac{g_\ell - 2}{2}\,, \tag{6.1}$$

where g_ℓ denotes the gyromagnetic factor. It encapsulates the quantum corrections to the magnetic moment of the leptons, hence serving as a high-precision test of the SM and its potential extensions. While the Dirac equation predicts $g_\ell^{\text{tree}} = 2$ at tree level, higher-order corrections induce a significant shift of this value, leading to a non-zero SM prediction for a_ℓ. Since the anomalous magnetic moment essentially captures the cumulative effect of all quantum corrections, it is highly sensitive to virtual new particles contributing to the loops, which might not be directly accessible at colliders. The leading SM contributions arise from one-loop QED corrections, which are well understood and accurately predicted [18, 43, 290].

For the electron, a_e is predicted up to five-loop order [291], matching the high experimental accuracy that features a precision of 12 significant digits [18]. Notably, the muon anomalous magnetic moment, a_μ, exhibits a persistent 5σ tension with the SM prediction [43, 290], known as the muon $g-2$ anomaly [1]. This discrepancy is one of the few potential signals of BSM physics at present experimental facilities. By contrast, the short lifetime of the tau lepton, $\tau_\tau \sim 2.9 \cdot 10^{-13}$s [18], limits the precision of its anomalous magnetic moment measurement, so that currently only a 95% credible interval on a_τ is available [293]. Tab. 6.1 summarizes the experimental measurements of the anomalous magnetic moments of the charged leptons alongside their corresponding SM predictions.

Observable	Measurement	SM Prediction
a_e	$1159.65218062(12) \cdot 10^{-6}$ [18]	$1159.652181606(23) \cdot 10^{-6}$ [291]
a_μ	$1165.92059(22) \cdot 10^{-6}$ [43]	$1165.91810(43) \cdot 10^{-6}$ [290]
a_τ	$0.057 < a_\tau < 0.024$ (95%CL) [293]	$0.01532279(5)$ [294]

Table 6.1: Experimental measurements of the anomalous magnetic moments of the charged leptons together with the corresponding SM predictions.

In the LEFT, the dominant contribution to a_ℓ arises from the electromagnetic dipole operator

$$a_\ell = \frac{2\,m_\ell}{\sqrt{\pi\alpha_{\text{em}}}}\mathcal{C}_{e\gamma}^{\ell\ell}\,, \tag{6.2}$$

[1] During the finalization of this thesis, a new SM prediction was published in Ref. [292], showing no tension between the SM and experimental values.

where the Wilson coefficient $\mathcal{C}_{e\gamma}$ is evaluated at the scale $\mu = 2\,\text{GeV}$[2]. Since $\mathcal{Q}_{e\gamma}$ features a chirality-flip, its effect scales with the lepton mass, m_ℓ enhancing sensitivity for the muon and tau compared to that of the electron.

When matching from the SMEFT to the LEFT, $\mathcal{C}_{e\gamma}$ receives tree-level contributions from the SMEFT coefficients $\tilde{C}_{eB}$ and $\tilde{C}_{eW}$. The coefficient $\mathcal{C}_{e\gamma}$ thus defines a flat direction in the SMEFT parameter space, as it is not uniquely determined by the SMEFT coefficients. In addition, renormalization-group (RG) mixing links the dipole terms to the scalar and tensor operators $\tilde{C}^{(1)}_{lequ}$ and $\tilde{C}^{(3)}_{lequ}$ as illustrated by the Feynman diagrams in Fig. 6.1, further complicating the interpretation of the bounds on $\mathcal{C}_{e\gamma}$ within the SMEFT. Consequently, robust constraints on BSM scenarios require combining limits from a_ℓ with complementary probes, like Z-pole observables sensitive to $\tilde{C}_{eZ}$ and high-p_T processes (e.g. $pp \to t\bar{t}\ell\ell$) that test scalar and tensor interactions.

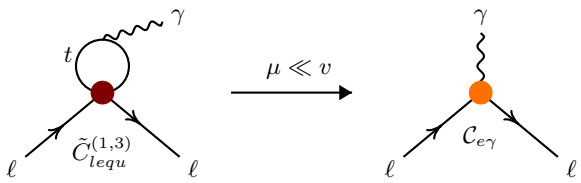

Figure 6.1: Feynman diagrams illustrating the operator mixing of the electromagnetic dipole operator with the scalar and tensor operators in the SMEFT. The red dot indicates the SMEFT operator insertion, while the orange dot represents the LEFT operator contribution.

6.1.2. Lepton-Flavor-Violating Decays

Lepton-flavor-violating (LFV) decays are essentially null-tests in the SM, suppressed both by the GIM mechanism and the smallness of neutrino masses. Within the LEFT, LFV processes arise from the off-diagonal entries of the electromagnetic dipole operator $\mathcal{C}_{e\gamma}$, as well as from the four-lepton contact terms. We consider three classes of LFV decays, namely radiative decays $\ell_i \to \ell_j\gamma$, three-body decays $\ell_i \to \ell_j\ell_k\ell_l$, and semileptonic tau decays $\tau \to \ell_i M$, each probing distinct combinations of Wilson coefficients.

Radiative Decays

Radiative decays, $\ell_i \to \ell_j\gamma$, directly test the off-diagonal entries of the electromagnetic dipole coefficient $\mathcal{C}_{e\gamma}$ in the LEFT, complementing the information obtained on the diagonal components from the anomalous magnetic moments. At tree-level, the partial width for a radiative decay lepton decay in the LEFT is given by

$$\Gamma(\ell_i \to \ell_j\gamma) = \frac{m^3_{\ell_i}}{4\pi}\left(|\mathcal{C}_{e\gamma}|^2_{ij} + |\mathcal{C}_{e\gamma}|^2_{ji}\right) . \tag{6.3}$$

The chirality flip of the transition implies a suppression by the third power of the lepton mass, $m^3_{\ell_i}$, effectively enhancing the contribution for heavier leptons.

[2]This scale is selected instead of the natural choice $\mu \sim m_{\ell_i}$, in order to avoid potential QCD-induced divergences in the RGE running.

The current experimental limits are very tight, due to the clean signature and effective background suppression. Especially the decay $\mu \to e\gamma$ has been measured with outstanding precision, thanks to the comparatively long lifetime of the muon and the excellent experimental sensitivity. Tab. 6.2 summarizes the current experimental limits on the branching ratios of the radiative decays. The most stringent bounds are obtained from the MEG II experiment, which has recently set a limit on the branching ratio of $\mu \to e\gamma$ at $2.2 \cdot 10^{-13}$ [295]. Other decays are less accessible due to the short lifetime of the τ, but still provide valuable information on LFV interactions.

$\mathcal{B}(\mu \to e\gamma)$	$\mathcal{B}(\tau \to e\gamma)$	$\mathcal{B}(\tau \to \mu\gamma)$
$< 2.2 \cdot 10^{-13}$ [295]	$< 3.3 \cdot 10^{-8}$ [296]	$< 4.2 \cdot 10^{-8}$ [297]

Table 6.2: Current experimental limits on the branching fractions of LFV radiative decays at 90% CL.

To illustrate the reach of the data on anomalous magnetic moments and radiative LFV decays in constraining the electromagnetic dipole operator, we perform a simplified single-coefficient fit neglecting RGE effects. Using the relation

$$\tilde{C} = \frac{v^2}{\Lambda^2} C \,, \tag{6.4}$$

we can translate limits on $|\mathcal{C}^{ij}_{e\gamma}|$ into lower bounds on the new-physics scale $\Lambda/\sqrt{C}$. The resulting sensitivities are displayed in Fig. 6.2. Our findings show that radiative decays provide stronger constraints than anomalous magnetic moments by orders of magnitude, owing to the background-free searches in LFV analyses. In particular, the current limit on the $e\mu$ dipole coefficient implies $\Lambda \gtrsim 7 \cdot 10^5$ TeV for a unit Wilson coefficient, marking one of the most stringent bounds in the SMEFT framework.

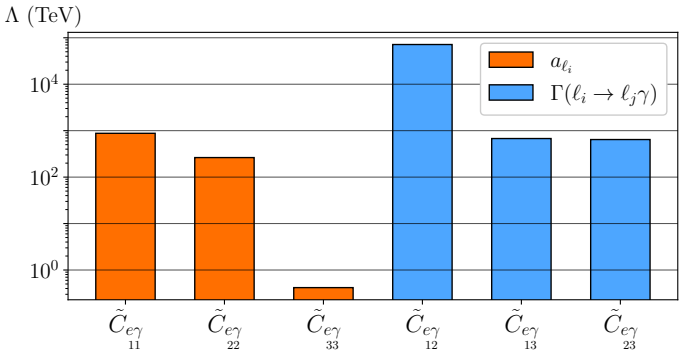

Figure 6.2: Lower bounds at the 90% credible level on $\Lambda/\sqrt{C}$ for the dipole coefficient $\mathcal{C}_{\substack{e\gamma \\ ij}}$, obtained from fits to the anomalous magnetic moment of charged leptons (orange) and to branching fractions of radiative LFV decays (blue).

Three-Body Decays

LFV three-body lepton decays, $\ell_i \to \ell_j \ell_k \ell_l$, provide highly sensitive probes of LFV four-lepton coefficients $\mathcal{C}_{ee}^{V,XY} = (\bar{\ell}_X \gamma^\mu \ell_X)(\bar{\ell}_Y \gamma_\mu \ell_Y)$ with $X, Y = L, R$, as well as dipole mediated photon penguins for final state containing an opposite-sign same-flavor pair. If the final state consists of three leptons of the same flavor ($j = k = l$), the partial width can be expressed as [298–300]

$$\begin{aligned}\Gamma(\ell_i \to \ell_j \bar{\ell}_j \ell_j) =& \frac{m_{\ell_i}^5}{1536\pi^3}\left(2\big(\mathcal{C}^{V,LL}_{\substack{ee\\jijj}}\big)^2 + 2\big(\mathcal{C}^{V,RR}_{\substack{ee\\jijj}}\big)^2 + \big(\mathcal{C}^{V,LR}_{\substack{ee\\jijj}}\big)^2 + \big(\mathcal{C}^{V,LR}_{\substack{ee\\jjji}}\big)^2\right) \\ &+ \frac{m_{\ell_i}^3 \alpha_{\text{em}}}{12\pi^2 \Gamma_{\ell_i}}\left(\log\frac{m_{\ell_i}^2}{m_{\ell_j}^2} - \frac{11}{4}\right)\left(|\mathcal{C}_{\substack{e\gamma\\ij}}|^2 + |\mathcal{C}_{\substack{e\gamma\\ji}}|^2\right) \\ &- \frac{m_{\ell_i}^4 \sqrt{\alpha_{\text{em}}\pi}}{96\pi^3 \Gamma_{\ell_i}}\left((2\mathcal{C}^{V,LL}_{\substack{ee\\jijj}} + \mathcal{C}^{V,LR}_{\substack{ee\\jijj}})\mathcal{C}_{\substack{e\gamma\\ji}} + (2\mathcal{C}^{V,RR}_{\substack{ee\\jijj}} + \mathcal{C}^{V,LR}_{\substack{ee\\jjji}})\mathcal{C}_{\substack{e\gamma\\ij}}\right),\end{aligned} \tag{6.5}$$

where the first line corresponds to pure four-lepton contributions, the second line accounts for the electromagnetic dipole operator, and the third line describes the interference between the two. The logarithmic term arises from the phase space integration and is a consequence of the chirality flip induced by the dipole operator. The different chirality structures contribute incoherently, allowing us to constrain several Wilson coefficients simultaneously. Notably, the decay rate scales with the fifth power of the lepton mass, which strongly enhances the sensitivity to heavier lepton flavors.

For a final state consisting of an opposite-sign same-flavor lepton pair $\bar{\ell}_k \ell_k$ together with a lepton of different flavor ℓ_j, the partial width is given by [298–300]

$$\begin{aligned}\Gamma(\ell_i \to \ell_j \bar{\ell}_k \ell_k) =& \frac{m_{\ell_i}^5}{1536\pi^3}\left(\big(\mathcal{C}^{V,LL}_{\substack{ee\\jikk}}\big)^2 + \big(\mathcal{C}^{V,RR}_{\substack{ee\\jikk}}\big)^2 + \big(\mathcal{C}^{V,LR}_{\substack{ee\\jikk}}\big)^2 + \big(\mathcal{C}^{V,LR}_{\substack{ee\\kkji}}\big)^2\right) \\ &+ \frac{m_{\ell_i}^3 \alpha_{\text{em}}}{12\pi^2 \Gamma_{\ell_i}}\left(\log\frac{m_{\ell_i}^2}{m_{\ell_k}^2} - 3\right)\left(|\mathcal{C}_{\substack{e\gamma\\ij}}|^2 + |\mathcal{C}_{\substack{e\gamma\\ji}}|^2\right) \\ &- \frac{m_{\ell_i}^4 \sqrt{\alpha_{\text{em}}\pi}}{96\pi^3 \Gamma_{\ell_i}}\left((\mathcal{C}^{V,LL}_{\substack{ee\\jikk}} + \mathcal{C}^{V,LR}_{\substack{ee\\jikk}})\mathcal{C}_{\substack{e\gamma\\ji}} + (\mathcal{C}^{V,RR}_{\substack{ee\\jikk}} + \mathcal{C}^{V,LR}_{\substack{ee\\kkji}})\mathcal{C}_{\substack{e\gamma\\ij}}\right),\end{aligned} \tag{6.6}$$

where the prefactors differ slightly compared to Eq. (6.5), as the leptons are now distinguishable. The overall structure is, however, analogous.

A final state with two identical same-sign leptons ℓ_j, on the other hand, implies lepton flavor violation by two units, in contrast to the decays in Eqs. (6.5) and (6.6). Here, the dipole operator does not contribute, since two LEFT insertions are required which are of order Λ^{-8} after squaring the amplitude. Hence, only the four-lepton operators contribute and the partial width is given by [298–300]

$$\Gamma(\ell_i \to \ell_j \bar{\ell}_k \ell_j) = \frac{m_{\ell_i}^5}{1536\pi^3}\left(2\big(\mathcal{C}^{V,LL}_{\substack{ee\\jijk}}\big)^2 + 2\big(\mathcal{C}^{V,RR}_{\substack{ee\\jijk}}\big)^2 + \big(\mathcal{C}^{V,LR}_{\substack{ee\\jijk}}\big)^2 + \big(\mathcal{C}^{V,LR}_{\substack{ee\\jkji}}\big)^2\right). \tag{6.7}$$

Tab. 6.3 lists current 90% CL experimental limits. The limit $\mathcal{B}(\mu^- \to e^- e^+ e^-) < 10^{-12}$ [301] currently provides the most stringent constraints on LFV four-lepton interactions, while decays involving the tau lepton are experimentally less accessible.

Observable	Limit	Observable	Limit
$\mathcal{B}(\tau^- \to e^- e^+ e^-)$	$2.7 \cdot 10^{-8}$ [302]	$\mathcal{B}(\tau^- \to \mu^- \mu^+ \mu^-)$	$2.1 \cdot 10^{-8}$ [302]
$\mathcal{B}(\tau^- \to e^- \mu^+ \mu^-)$	$2.7 \cdot 10^{-8}$ [302]	$\mathcal{B}(\tau^- \to e^+ \mu^- \mu^-)$	$1.7 \cdot 10^{-8}$ [302]
$\mathcal{B}(\tau^- \to \mu^- e^+ e^-)$	$1.8 \cdot 10^{-8}$ [302]	$\mathcal{B}(\tau^- \to \mu^+ e^- e^-)$	$1.5 \cdot 10^{-8}$ [302]
$\mathcal{B}(\mu^- \to e^- e^+ e^-)$	$1.0 \cdot 10^{-12}$ [301]		

Table 6.3: Current experimental limits on the branching fractions of LFV three-body lepton decay, all at 90% CL.

Semileptonic Tau Decays

Semileptonic decays of the τ provide a valuable and complementary handle on LFV interactions. They probe semileptonic four-fermion operators, in contrast to the four-lepton operators probed by the LFV three-body decays. While the purely leptonic channels yield exceptionally clean observables, semileptonic modes necessarily include hadronic matrix elements, carrying inherent non-perturbative uncertainties. These matrix elements are encoded in decay constants and form factors, computed, for example, using lattice QCD.

Depending on whether the hadronic final state is a pseudoscalar meson or a vector meson, distinct linear combinations of LEFT Wilson coefficients are probed, providing the opportunity to disentangle different chirality combinations. For decays into pseudoscalar mesons P, such as π, K, or η, the amplitude can be expressed in terms of the effective coefficients $\mathcal{C}^P_{VA/AA}$, which are defined as

$$\mathcal{C}^P_{\substack{VA/AA \\ ij}} = \sum_{q,km} \kappa^{P,q}_{km} \left(\mathcal{C}^{VRR}_{\substack{eq \\ ijkm}} - \mathcal{C}^{VLR}_{\substack{qe \\ kmij}} \mp \left(\mathcal{C}^{VLL}_{\substack{eq \\ ijkm}} - \mathcal{C}^{VLR}_{\substack{eq \\ ijkm}} \right) \right) , \tag{6.8}$$

with the flavor factors $\kappa^{P,q}_{km}$. These factors encode the quark content of the meson as well as the corresponding hadronic decay constant f_P. As numerical values for f_P, we employ results obtained by lattice QCD computations, to avoid potential SMEFT effects that might arise in experimental determinations. We list the definition of the factors $\kappa^{P,q}_{km}$ and the numerical values of the decay constants f_P in Appendix E in Tabs. 7 and 5, respectively. The partial width for the decay $\tau \to \ell_i P$ is then given by

$$\Gamma(\tau \to \ell_i P) = \frac{m_\tau^3}{256\pi} \left(1 - \frac{m_P^2}{m_\tau^2}\right)^2 \left(|\mathcal{C}^P_{\substack{VA \\ i3}}|^2 + |\mathcal{C}^P_{\substack{AA \\ i3}}|^2 \right) . \tag{6.9}$$

For decays into vector mesons V, such as ρ, ω, K^*, or ϕ, additional contributions arise from the LFV components of the electromagnetic dipole operator, mediated by photon exchange. The relevant combinations of LEFT Wilson coefficients can be defined as

$$\begin{aligned} \mathcal{C}^V_{\substack{VV/AV \\ ij}} &= \sum_{q,km} \kappa^{V,q}_{km} \left(\mathcal{C}^{VRR}_{\substack{eq \\ ijkm}} + \mathcal{C}^{VLR}_{\substack{qe \\ kmij}} \pm \left(\mathcal{C}^{VLL}_{\substack{eq \\ ijkm}} + \mathcal{C}^{VLR}_{\substack{eq \\ ijkm}} \right) - 4\delta_{ij} \frac{e^2 Q_q}{m_V} \right) , \\ \mathcal{C}^V_{\substack{T/T_5 \\ ij}} &= - \sum_{q,km} \frac{eQ_q}{m_V} \delta_{km} \kappa^{V,q}_{km} (\mathcal{C}_{\substack{e\gamma \\ ij}} \pm \mathcal{C}_{\substack{e\gamma \\ ji}}) , \end{aligned} \tag{6.10}$$

where Q_q denotes the electric charge of the quark q. The prefactors $\kappa_{km}^{V,q}$ are defined analogously to the pseudoscalar factors in Eq. (6.8). We list the definition of the factors $\kappa_{km}^{V,q}$ in Appendix E in Tab. 8, and the numerical values of the decay constants f_V in Tab. 5. The resulting expression for the partial width of the decay $\tau \to \ell_i V$ is given by

$$\begin{aligned}\Gamma(\tau \to \ell_i V) =& \frac{m_\tau^3}{256\pi}\left(1-\frac{m_V^2}{m_\tau^2}\right)^2 \left(\left(1+\frac{2m_V^2}{m_\tau^2}\right)\left(|\mathcal{C}_{VV\,i3}^V|^2+|\mathcal{C}_{AV\,i3}^V|^2\right)\right. \\ &\left. + 32\left(1+\frac{m_V^2}{2m_\tau^2}\right)\left(|\mathcal{C}_{T\,i3}^V|^2+|\mathcal{C}_{T_5\,i3}^V|^2\right) + \frac{24 m_V}{m_\tau}\left(\mathcal{C}_{T\,i3}^V \mathcal{C}_{VV\,i3}^V + \mathcal{C}_{T_5\,i3}^V \mathcal{C}_{AV\,i3}^V\right)\right),\end{aligned} \tag{6.11}$$

where the first term corresponds to the four-lepton contributions, the second term accounts for the dipole operators and the third term describes the interference between the two.

Tab. 6.4 summarizes the current experimental limits on the branching fractions of LFV semileptonic τ decays. The most strongest limits are obtained from the Belle II experiment, which has set bounds on the branching ratios of $\tau \to \ell V$ decays at the level of 10^{-8} [303].

Observable	Limit	Observable	Limit
$\mathcal{B}(\tau^- \to e^-\pi^0)$	$8.0 \cdot 10^{-8}$ [304]	$\mathcal{B}(\tau^- \to \mu^-\pi^0)$	$1.1 \cdot 10^{-7}$ [304]
$\mathcal{B}(\tau^- \to e^-\eta)$	$9.2 \cdot 10^{-8}$ [305]	$\mathcal{B}(\tau^- \to \mu^-\eta)$	$6.5 \cdot 10^{-8}$ [304]
$\mathcal{B}(\tau^- \to e^-\eta')$	$1.6 \cdot 10^{-7}$ [304]	$\mathcal{B}(\tau^- \to \mu^-\eta')$	$1.3 \cdot 10^{-7}$ [304]
$\mathcal{B}(\tau^- \to e^-\rho^0)$	$2.2 \cdot 10^{-8}$ [303]	$\mathcal{B}(\tau^- \to \mu^-\rho^0)$	$1.7 \cdot 10^{-8}$ [303]
$\mathcal{B}(\tau^- \to e^-\omega)$	$2.4 \cdot 10^{-8}$ [303]	$\mathcal{B}(\tau^- \to \mu^-\omega)$	$3.9 \cdot 10^{-8}$ [303]
$\mathcal{B}(\tau^- \to e^-K^*)$	$1.9 \cdot 10^{-8}$ [303]	$\mathcal{B}(\tau^- \to \mu^-K^*)$	$2.9 \cdot 10^{-8}$ [303]
$\mathcal{B}(\tau^- \to e^-\bar{K}^*)$	$1.7 \cdot 10^{-8}$ [303]	$\mathcal{B}(\tau^- \to \mu^-\bar{K}^*)$	$4.3 \cdot 10^{-8}$ [303]
$\mathcal{B}(\tau^- \to e^-\phi)$	$2.0 \cdot 10^{-8}$ [303]	$\mathcal{B}(\tau^- \to \mu^-\phi)$	$2.3 \cdot 10^{-8}$ [303]

Table 6.4: Current experimental limits on the branching fractions of LFV semileptonic tau decays, all at 90% CL.

6.1.3. Charged-Current Lepton Decays

In the SM, charged-current lepton decays, both the purely leptonic mode $\ell_i \to \ell_j \nu\bar{\nu}$ and the semileptonic decay $\tau \to M\nu$, are mediated by the exchange of a W boson, governed by the V-A structure of the weak interaction. At energies far below the W mass, the heavy gauge bosons can be integrated out, leading to an effective theory described by local four-fermion operators. These decays thus provide a cross-check of the collider probes of charged-currents, provided by the W boson decay widths and the charged current DY production.

A distinctive feature of these decays is that the neutrinos in the final state escape detection, and their individual flavors are not resolved. Experimental and theoretical rates are therefore summed over all neutrino species, rendering the decay widths inclusive with regard to neutrino flavors. This inclusivity causes lepton-flavor–diagonal (LFD) and lepton-flavor–violating (LFV) contributions to enter incoherently, allowing both to be constrained simultaneously. In this

sense, charged-current lepton decays probe new interactions complementary to purely leptonic or flavor-changing neutral–current observables.

Charged-Current Three Body Decays

The decays $\ell_i \to \ell_j \nu_k \bar{\nu}_m$ are among the most precisely measured processes in particle physics, free from hadronic uncertainties and calculated to very high accuracy in the SM. Tab. 6.5 summarizes the current experimental measurements of the leptonic decay widths, alongside the corresponding SM predictions. We compute the SM predictions following Ref. [306], including electroweak radiative corrections.

Observable	Measurement	SM Prediction
$\Gamma(\mu^- \to e^- \nu \bar{\nu})$	$2.995984(3) \cdot 10^{-19}$ GeV [307]	$2.994(5) \cdot 10^{-19}$ GeV
$\Gamma(\tau^- \to e^- \nu \bar{\nu})$	$4.045(11) \cdot 10^{-13}$ GeV [307]	$4.028(7) \cdot 10^{-13}$ GeV
$\Gamma(\tau^- \to \mu^- \nu \bar{\nu})$	$3.936(11) \cdot 10^{-13}$ GeV [307]	$3.918(7) \cdot 10^{-13}$ GeV

Table 6.5: Experimental values of the partial decay widths of the charged-current leptonic decay of charged leptons, compared to the SM predictions computed following Ref. [306].

The partial width within the LEFT is given by

$$\Gamma(\ell_i \to \ell_j \nu_k \bar{\nu}_m) = \sum_{k,m} \frac{m_{\ell_i}^5 |\mathcal{C}^{V,LL}_{\substack{\nu e \\ kmij}}|^2}{1536\pi^3}\,, \tag{6.12}$$

neglecting the mass of the final state lepton and the neutrinos. Since the width scales with the fifth power of the lepton mass, contributions to τ decay are enhanced by a factor of $(m_\tau/m_\mu)^5 \sim 10^6$ compared to the muon decay. The latter are, however, measured to a much higher precision.

Semileptonic Charged-Current Tau Decays

Semileptonic modes of the tau lepton, $\tau \to P\nu$ with $P = \pi, K$, provide an additional handle on charged current interactions coupling lepton to quark currents. Non-perturbative effects in the hadronic matrix elements are encoded in the decay constants f_P, which we list in Appendix E in Tab. 5.

In the LEFT, the partial width for the decay $\tau \to \nu_i P$ is given by

$$\Gamma(\tau \to \nu_i P) = \frac{m_\tau^3}{128\pi} f_P^2 \left(1 - \frac{m_P^2}{m_\tau^2}\right)^2 |\mathcal{C}^{V,LL}_{\substack{\nu edu \\ i3kl}}|^2\,. \tag{6.13}$$

Tab. 6.6 summarizes the experimental partial widths and the corresponding SM predictions for τ decays into the lightest pseudoscalar mesons π and K. For the computation of the SM predictions, we include electroweak radiative corrections, following Ref. [308].

Observable	Measurement	SM Prediction
$\Gamma(\tau^- \to \pi^- \bar{\nu})$	$2.453(12) \cdot 10^{-13}$ GeV [307]	$2.451(33) \cdot 10^{-13}$ GeV
$\Gamma(\tau^- \to K^- \bar{\nu})$	$1.578(23) \cdot 10^{-14}$ GeV [307]	$1.618(13) \cdot 10^{-14}$ GeV

Table 6.6: Experimental values of the partial decay widths of semileptonic τ decays including neutrinos, together with the corresponding SM predictions computed following Ref. [308].

6.2. Meson Decays

Meson decays offer a wealth of observables via various different decay channels. In particular, FCNC transitions are highly suppressed in the SM by the GIM mechanism, making them very sensitive to possible new physics contributions. This suppression is even more pronounced for LFV processes, which are forbidden at tree-level and highly suppressed at loop level due to the smallness of neutrino masses, rendering the SM background essentially negligible.

In this section, we explore mass differences in the $B_{(s)}$-$\bar{B}_{(s)}$ meson systems as well as leptonic and semileptonic meson decay modes within the LEFT. The mixing-induced mass splittings $\Delta m_{s/d}$ are governed by four-quark operators and depend sensitively on the CKM matrix elements, thus providing a powerful probe of the flavor structure of the SMEFT. Purely leptonic meson decays, such as $B_{(s)} \to \ell^+\ell^-$ benefit from minimal hadronic uncertainties, as they are encoded in a single decay constant that can be determined with high precision using lattice QCD. Semileptonic decays, such as $B \to K^{(*)}\ell^+\ell^-$, on the other hand, offer extensive kinematic information, enabling discrimination among different Wilson coefficients and sensitivity to various operator structures. By combining multiple decay channels, we can effectively constrain different linear combinations of Wilson coefficients, enhancing the sensitivity of our searches for new physics within the SMEFT.

6.2.1. Mass Differences in Meson Mixing

Neutral B_q-$\bar{B}_q$ mixing proceeds in the SM through box diagrams, in which a meson oscillates into its antiparticle via the exchange of two virtual W bosons and up-type quarks in the loop. The GIM mechanism strongly suppresses these transitions, resulting in small mixing amplitudes in which the top-quark contribution dominates. The resulting mass splitting Δm_q between the heavy and light mass eigenstates depends on short-distance physics, encoded in the LEFT Wilson coefficients, as well as on the CKM matrix element combination $|V_{tq}V_{tb}^*|$. The theoretical prediction of Δm_q also relies on the evaluation of non-perturbative hadronic matrix elements of the four-quark operator, which is determined most reliably through lattice QCD, thereby minimizing hadronic uncertainties.

Extensions of the SM may introduce new heavy particles that enter the mixing loop or generate new contact interactions at tree level, making the mass splitting a sensitive indicator of BSM dynamics. Within the SMEFT, the leading effects on Δm_q arise from double insertions of the operator $O_{\varphi q^+}$, which allows for FCNC couplings to the Z at tree-level. Integrating out the heavy degrees of freedom maps this contribution onto the four-quark LEFT operator $\mathcal{Q}_{dd}^{V,LL}$, which

describes a purely left-handed four-quark contact interaction. Under the MFV assumption, no other chirality structures contribute to the mixing, as they would require right-handed FCNCs.

Fig. 6.3 illustrates the different contributions to the mixing of a B_q meson into its antiparticle $\bar{B}_q$. The left diagram shows an example of the SM process, whereas the diagram in the middle illustrates the contribution that arises from the double insertion of the SMEFT operator $O^+_{\varphi q}$. The diagram on the right shows the corresponding contribution in the LEFT, induced by the operator $\mathcal{Q}^{V,LL}_{dd}$ after integrating out the heavy degrees of freedom.

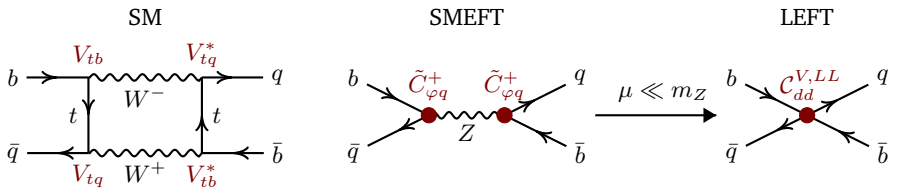

Figure 6.3: Feynman diagrams for B_q-$\bar{B}_q$ mixing. On the left, we show an example for the SM process mediated by the exchange of virtual W bosons and top quarks. The diagram in the middle show the contribution from the SMEFT operator $O^+_{\varphi q}$, which contributes to the mixing through double insertion. The right diagram shows the resulting contribution in the LEFT after integrating out the heavy gauge bosons, described by the operator $\mathcal{Q}^{V,LL}_{dd}$.

The mass difference in the LEFT framework is given by[3] [182, 309–311]:

$$\Delta m_q = \frac{m_{B_q} f_{B_q}^2 \hat{B}_{B_q}}{3} \left(\frac{m_W^2}{4\pi^2 v^4} (V_{tq} V_{tb}^*)^2 S_0(x_t) \eta_{2B} - 8 \mathcal{C}^{V,LL}_{\substack{dd \\ qbqb}} \right) , \tag{6.14}$$

where f_{B_q} is the decay constant of the B_q meson, and $\hat{B}_{B_q}$ is the bag parameter encoding hadronic matrix elements. The function $S_0(x_t)$ represents the Inami-Lim loop function, defined as

$$S_0(x) = \frac{4x - 11x^2 + x^3}{4(1-x)^2} - \frac{3x^3 \log x}{2(1-x)^3} , \tag{6.15}$$

with $x_t = m_t^2/m_W^2$, and η_{2B} denotes short-distance QCD corrections[4].

Note that the computation of the mass difference in Eq.(6.14) differs from that in Ref.[1]. The latter includes loop-level matching, introducing additional contributions from $\tilde{C}_{uW}$, whereas in this work, we consistently employ tree-level matching to remain aligned with the one-loop RGE precision. Additionally, we correct a normalization factor in the definition of the Wilson coefficient $\mathcal{C}^{V,LL}_{\substack{dd \\ qbqb}}$. The factor $|VtqV_{tb}^*|^2$, which was mistakenly included in Ref. [1] in the definition of $C^{\text{mix}}_{V,LL}$ is omitted here. This correction leads to stronger constraints on the Wilson coefficients $\tilde{C}^{(1)}_{\varphi q}$ and $\tilde{C}^{(3)}_{\varphi q}$.

Tab. 6.7 summarizes the SM predictions alongside the current experimental measurements of the mass differences in the $B_{(s)}$ meson systems.

[3] The LEFT operator $\mathcal{Q}^{V,LL}_{dd}$ arises from double insertion of the SMEFT operator $O^+_{\varphi q}$ and thus is of order Λ^{-4}. Contributions $\sim (\mathcal{C}^{V,LL}_{dd})^2$ are hence of order Λ^{-8} and therefore neglected.

[4] Numerical values for these parameters are provided by lattice QCD computations and summarized in Appendix E , Tab. 4.

Observable	Measurement	SM Prediction
Δm_d	$0.5069(19)\,\text{ps}^{-1}$ [307]	$0.504(26)\,\text{ps}^{-1}$
Δm_s	$17.766(6)\,\text{ps}^{-1}$ [307]	$17.68(76)\,\text{ps}^{-1}$

Table 6.7: Experimental measurements and SM predictions of the mass differences in the $B_{(s)}$ meson systems.

6.2.2. Leptonic Meson Decays

Leptonic meson decays offer comparatively clean observables, since all hadronic uncertainties are encoded in a single decay constant that can be determined with percent-level accuracy using lattice QCD computations. In the SM, these decays are helicity suppressed, i.e. they scale with the mass of the final state lepton, leading to small branching ratios especially for the light leptons. This suppression can be advantageous for BSM searches, as it offers a low–background environment in which new scalar or pseudoscalar interactions, such as those mediated by new charged Higgs bosons or by leptoquarks, could lift the suppression and produce significant enhancements.

Leptonic meson decays offer a variety of different channels, depending on the initial state meson and the final state leptons. Each channel probes distinct combinations of Wilson coefficients due to variations in chirality structures and flavor couplings, allowing for a comprehensive exploration of the parameter space and complementary tests of the LEFT and SMEFT. In the following, we discuss the different modes and their implications for BSM physics.

Leptonic Decays of Neutral Pseudoscalar Mesons

In the LEFT, the partial decay width $P \to \ell_i \ell_j$ of a pseudoscalar meson P reads [312]

$$\begin{aligned}\Gamma(P \to \ell_i^- \ell_j^+) = &\frac{\sqrt{\lambda(m_P^2, m_{\ell_i}^2, m_{\ell_j}^2)}}{128\pi m_P^3}\Big(\left(m_P^2 - (m_{\ell_i} + m_{\ell_j})^2\right)(m_{\ell_i} - m_{\ell_j})^2 |C_{\substack{VA\\ij}}^P|^2 \\ &+ \left(m_P^2 - (m_{\ell_i} - m_{\ell_j})^2\right)\left(m_{\ell_i} + m_{\ell_j}\right)^2 |C_{\substack{AA\\ij}}^P|^2\Big)\,,\end{aligned} \tag{6.16}$$

with the Källén function $\lambda(a,b,c) = a^2 + b^2 + c^2 - 2(ab + ac + bc)$. The effective coefficients $C_{\substack{VA\\ij}}^P$ and $C_{\substack{AA\\ij}}^P$ are defined in Eq. (6.8).

For flavor-conserving final states with $i = j$, the expression reduces to

$$\Gamma(P \to \ell_i^- \ell_i^+) = \frac{m_P m_{\ell_i}^2}{32\pi}\sqrt{1 - \frac{4m_{\ell_i}^2}{m_P^2}}|C_{\substack{AA\\ii}}^P|^2\,, \tag{6.17}$$

where only the axial-axial coefficient C_{AA}^P contributes. Here, we focus on the decays of B_0 and B_s mesons, since the decays of light pseudoscalar mesons, such as the π^0 or the η, are dominated by long-distance contributions, which our EFT setup does not reliably account

for[5]. In the case of the B_s meson, we correct the partial width by a factor of $(1 - y_s)$ with $y_s = \Delta\Gamma_s/(2\Gamma_s) \sim 0.064(4)$ [18] to account for the width difference $\Delta\Gamma_s$ of the two neutral-meson mass eigenstates[6].

Tab. 6.8 compiles the current experimental limits and measurements of the leptonic decay width alongside the SM predictions. For most of the decays, only upper limits are available, since the branching ratio is strongly chirality suppressed by the lepton mass and thus challenging to observe, especially for the electron channel. The branching ratios for the decays into tau leptons are larger in the SM, but experimentally much more challenging due to the rapid decay of the τ. The only decay that has been observed to date is the $B_s^0 \to \mu^+\mu^-$ channel [18], which is in good agreement with the SM prediction.

Observable	Measurement	SM prediction
$\Gamma(B^0 \to ee)$	$< 1.1 \cdot 10^{-21}$ [18, 313]	$1.03(6) \cdot 10^{-27}$
$\Gamma(B^0 \to \mu\mu)$	$< 6.5 \cdot 10^{-23}$ [18, 314]	$4.40(0.24) \cdot 10^{-23}$
$\Gamma(B^0 \to \tau\tau)$	$< 9.1 \cdot 10^{-16}$ [315]	$9.2(0.5) \cdot 10^{-21}$
$\Gamma(B_s^0 \to ee)$	$< 4.1 \cdot 10^{-21}$ [18, 313]	$3.36(0.16) \cdot 10^{-26}$
$\Gamma(B_s^0 \to \mu\mu)$	$1.45(12) \cdot 10^{-21}$ [18]	$1.43(7) \cdot 10^{-21}$
$\Gamma(B_s^0 \to \tau\tau)$	$< 3.0 \cdot 10^{-15}$ [18, 315]	$3.04(0.14) \cdot 10^{-19}$

Table 6.8: Current limits and measurements of the leptonic decays of neutral pseudoscalar mesons into a lepton flavor conserving charged lepton pair. All limits are given at 90% CL.

Additionally, there are various experimental searches for LFV leptonic meson decays. In the SM, these processes vanish at tree-level and remain beyond current experimental reach at higher orders, so any nonzero observation would be an unambiguous sign of new physics. Within the LEFT framework, the partial decay width for the LFV decay $P \to \ell_i^+ \ell_j^-$ simplifies to

$$\Gamma(P \to \ell_i^+ \ell_j^-) = \frac{m_P m_{\ell_j}^2}{128\pi} \left(1 - \frac{m_{\ell_j}^2}{m_P^2}\right)^2 \left(|C_{V\,ij}^P|^2 + |C_{A\,ij}^P|^2\right), \tag{6.18}$$

with $i \neq j$ and $m_{\ell_i} \ll m_{\ell_j}$. In contrast to the LFC decays, both the vector and axial vector coefficients contribute to this process. Since no LFV decay has been measured to date, only 90% CL bounds are available, which we list in Tab. 6.9 .

Leptonic Decays of Charged Pseudoscalar Mesons

The purely leptonic decay of a charged pseudoscalar meson, $P^- \to \ell^- \bar{\nu}_\ell$, proceeds in the SM through the tree-level exchange of a W boson, providing a clean probe of charged current

[5] In our MFV setup, no up-type FCNCs and hence no neutral current D meson decays are induced.
[6] For the B_0 meson, the width splitting is $y_d \sim 0.001(10)$ [307] and is thus negligible

Observable	Limit	Observable	Limit
$\mathcal{B}(\pi^0 \to e\mu)$	$3.2 \cdot 10^{-10}$ [316]	$\mathcal{B}(\eta \to e\mu)$	$6.0 \cdot 10^{-6}$ [317]
$\mathcal{B}(\eta' \to e\mu)$	$4.7 \cdot 10^{-4}$ [318]	$\mathcal{B}(K_L \to e\mu)$	$4.7 \cdot 10^{-12}$ [319]
$\mathcal{B}(B^0 \to e\mu)$	$1.0 \cdot 10^{-9}$ [320]	$\mathcal{B}(B_s^0 \to e\mu)$	$5.4 \cdot 10^{-9}$ [320]
$\mathcal{B}(B^0 \to e\tau)$	$1.6 \cdot 10^{-5}$ [321]	$\mathcal{B}(B_s^0 \to e\tau)$	$1.4 \cdot 10^{-3}$ [322]
$\mathcal{B}(B^0 \to \mu\tau)$	$1.4 \cdot 10^{-5}$ [323]	$\mathcal{B}(B_s^0 \to \mu\tau)$	$4.2 \cdot 10^{-5}$ [323]

Table 6.9: Current experimental limits on the branching fractions of LFV decays of neutral pseudoscalar mesons, all at 90% CL.

interactions. In the LEFT, the partial decay width can be expressed as

$$\Gamma(P \to \ell_i \nu_j) = \frac{m_P m_{\ell_i}^2}{64\pi} f_P^2 \left(1 - \frac{m_{\ell_i}^2}{m_P^2}\right)^2 |\mathcal{C}^{V,LL}_{\substack{\nu e u d \\ jikm}}|^2 \,, \tag{6.19}$$

where f_P is the decay constant of the pseudoscalar meson P. The factor $m_{\ell_i}^2$ reflects the helicity suppression of the decay, similar to the leptonic decay of neutral pseudoscalar mesons, which strongly suppresses the decay width for light leptons.

The SM contribution to the coefficient $\mathcal{C}^{V,LL}_{\nu e u d}$ is governed by the CKM matrix and the Higgs vev v

$$\mathcal{C}^{V,LL,\text{SM}}_{\substack{\nu e u d \\ jikm}} = \delta_{ij} \frac{2V_{mk}}{v^2} \,, \tag{6.20}$$

where V_{mk} is the CKM matrix element that enters the u_m-d_k-W vertex. Within the SMEFT framework, the effective operator $\mathcal{Q}^{V,LL}_{\nu e u d}$ receives additional tree-level contributions from the triplet operators $O^{(3)}_{lq}$ and $O^{(3)}_{\varphi q}$. Under the assumption of MFV, only left-handed currents contribute to the charged-current interactions of light quarks, so that $\mathcal{C}^{V,LL}_{\nu e u d}$ is the only coefficient relevant for this process.

Experimentally, the measurements of the decay widths represent the inclusive sum over all kinematically accessible neutrino flavors $\Gamma(P \to \ell_i \nu) = \sum_j \Gamma(P \to \ell_i \nu_j)$, since the neutrino flavors are not directly observable. While only the flavor diagonal combination $i = j$ contributes within the SM, the SMEFT and LEFT also allow for flavor off-diagonal contributions, which can be sizable in the presence of LFV new physics.

Tab. 6.10 summarizes the current experimental determinations and upper limits on these partial widths alongside the SM predictions. For light mesons, the decay widths are measured with high precision and are in good agreement with the SM predictions. In heavier systems such as the D and D_s mesons, the muon and tau modes are observed with uncertainties of a few percent, while the electron channels are beyond the current experimental reach. The branching fraction of the leptonic decay of the B^+ meson is suppressed by the large total B^+ decay width, so that mostly upper limits are available, with the exception of the $B^+ \to \tau^+ \nu$ channel that has been measured with a precision of about 20%. Overall, the measurements are in good agreement with the SM predictions, placing stringent bounds on any BSM contribution to $\mathcal{C}^{V,LL}_{\nu e u d}$.

Observable	Measurement [GeV]	SM prediction [GeV]
$\Gamma(\pi^+ \to e^+\nu)$	$3.110(10) \cdot 10^{-21}$ [18]	$3.17(4) \cdot 10^{-21}$
$\Gamma(\pi^+ \to \mu^+\nu)$	$2.5281(5) \cdot 10^{-17}$ [18]	$2.471(31) \cdot 10^{-17}$
$\Gamma(K^+ \to e^+\nu)$	$8.41(4) \cdot 10^{-22}$ [18]	$8.58(5) \cdot 10^{-22}$
$\Gamma(K^+ \to \mu^+\nu)$	$3.379(8) \cdot 10^{-17}$ [18]	$3.340(20) \cdot 10^{-17}$
$\Gamma(D^+ \to e^+\nu)$	$< 5.6 \cdot 10^{-18}$ [18, 324]	$5.93(9) \cdot 10^{-21}$
$\Gamma(D^+ \to \mu^+\nu)$	$2.38(11) \cdot 10^{-16}$ [18]	$2.52(4) \cdot 10^{-16}$
$\Gamma(D^+ \to \tau^+\nu)$	$7.6(1.7) \cdot 10^{-16}$ [18]	$6.71(10) \cdot 10^{-16}$
$\Gamma(D_s^+ \to e^+\nu)$	$< 1.1 \cdot 10^{-16}$ [18, 325]	$1.616(16) \cdot 10^{-19}$
$\Gamma(D_s^+ \to \mu^+\nu)$	$7.03(16) \cdot 10^{-15}$ [18]	$6.87(7) \cdot 10^{-15}$
$\Gamma(D_s^+ \to \tau^+\nu)$	$7.04(16) \cdot 10^{-14}$ [18]	$6.69(7) \cdot 10^{-14}$
$\Gamma(B^+ \to e^+\nu)$	$< 3.9 \cdot 10^{-19}$ [18, 326]	$4.4(1.1) \cdot 10^{-24}$
$\Gamma(B^+ \to \mu^+\nu)$	$< 3.4 \cdot 10^{-19}$ [18, 327]	$1.9(5) \cdot 10^{-19}$
$\Gamma(B^+ \to \tau^+\nu)$	$4.4(1.0) \cdot 10^{-17}$ [18]	$4.2(1.0) \cdot 10^{-17}$

Table 6.10: Current experimental values and limits on the partial width of leptonic decays of charged pseudoscalar mesons, alongside the corresponding SM predictions computed using Eq. (6.19). All limits are at 90% CL.

Quarkonia Decays

Leptonic decays of quarkonium states offer opportunities for probing complementary chiral structures of quark–lepton interactions and also possible contributions from electromagnetic dipole operators. They also provide the advantage of probing the quark-flavor-diagonal components of the Wilson coefficients, which give the dominant contribution in the MFV approach.

Within the LEFT, the partial decay width of a vector quarkonium state V into a lepton pair can be expressed as [328]

$$\begin{aligned}\Gamma(V \to \ell_i^- \ell_j^+) = \frac{m_V}{32\pi}\lambda^{1/2}(m_V, m_{\ell_i}, m_{\ell_j}) \Bigg[&\frac{1}{12}\left(|\mathcal{C}^V_{VV\,ij}|^2 + |\mathcal{C}^V_{AV\,ij}|^2\right)\left(2 - y_i^2 - y_j^2 - 2\left(y_i^2 - y_j^2\right)^2\right) \\ &+ \frac{4}{3}\left(1 + y_i^2 + y_j^2 - 2\left(y_i^2 - y_j^2\right)^2\right)\left(|\mathcal{C}^V_{T_5\,ij}|^2 + |\mathcal{C}^V_{T\,ij}|^2\right) \\ &+ \frac{y_i\, y_j}{2}\left[\left(|\mathcal{C}^V_{VV\,ij}|^2 - |\mathcal{C}^V_{AV\,ij}|^2\right) + 16\left(|\mathcal{C}^V_{T_5\,ij}|^2 - |\mathcal{C}^V_{T\,ij}|^2\right)\right] \\ &+ 2(y_i + y_j)\left(1 - (y_i - y_j)^2\right)\mathcal{C}^V_{VV\,ij}\mathcal{C}^V_{T_5\,ij} + 2(y_i - y_j)\left(1 - (y_i + y_j)^2\right)\mathcal{C}^V_{AV\,ij}\mathcal{C}^V_{T\,ij}\Bigg],\end{aligned} \tag{6.21}$$

where $y_i = m_{\ell_i}/m_V$. The effective coefficients $\mathcal{C}^V_{VV}$, $\mathcal{C}^V_{AV}$, $\mathcal{C}^V_T$, and $\mathcal{C}^V_{T_5}$ are defined in Eqs. (6.8) and (6.10) in terms of the LEFT coefficients. They provide an orthogonal probe of the LEFT parameter space compared to the pseudoscalar decays $P \to \ell_i \ell_j$, thus allowing for a more comprehensive exploration of the Wilson coefficients.

The first line of Eq.(6.21) describes the pure vector and axial-vector contributions, which dominate for light leptons and heavy quark masses. The tensor and pseudotensor operators in the second line that arise from the dipole operators are suppressed by the quarkonia mass and are thus only relevant if they are significantly enhanced by new physics. Interference terms between different Lorentz structures, shown in the last line of Eq.(6.21), are suppressed by factors of y_i and y_j, rendering them negligible in the limit of light final-state leptons. For vector meson decays, there is no helicity suppression as no chirality flip is required, allowing for sizable branching ratios even for light leptons.

Tab. 6.11 summarizes the current experimental measurements of lepton-flavor diagonal decays, alongside the corresponding SM predictions. The uncertainties in the SM predictions are dominated by the uncertainties in the decay constants, which are determined through lattice QCD computations. The numerical values of these decay constants are listed in Appendix E , Tab. 5.

Observable	Γ_{exp} [GeV]	Γ_{SM} [GeV]
$\Gamma(\Phi \to e^+e^-)$	$1.266(15) \cdot 10^{-6}$ [18]	$1.41(11) \cdot 10^{-6}$
$\Gamma(\Phi \to \mu^+\mu^-)$	$1.21(9) \cdot 10^{-6}$ [18]	$1.37(10) \cdot 10^{-6}$
$\Gamma(J/\psi \to e^+e^-)$	$5.53(11) \cdot 10^{-6}$ [18]	$5.59(24) \cdot 10^{-6}$
$\Gamma(J/\psi \to \mu^+\mu^-)$	$5.52(11) \cdot 10^{-6}$ [18]	$5.57(24) \cdot 10^{-6}$
$\Gamma(\Upsilon \to e^+e^-)$	$1.29(5) \cdot 10^{-6}$ [18]	$1.31(4) \cdot 10^{-6}$
$\Gamma(\Upsilon \to \mu^+\mu^-)$	$1.34(4) \cdot 10^{-6}$ [18]	$1.31(4) \cdot 10^{-6}$
$\Gamma(\Upsilon \to \tau^+\tau^-)$	$1.40(6) \cdot 10^{-6}$ [18]	$1.30(4) \cdot 10^{-6}$

Table 6.11: Current experimental values of the partial widths of lepton-flavor diagonal leptonic quarkonia decay widths, alongside the corresponding SM predictions computed using Eq. (6.21).

Searches for lepton-flavor-violating branching fractions of quarkonia ($V \to \ell_i^+ \ell_j^-$, $i \neq j$) have reached sensitivities down to the order of 10^{-6}. No signal has been observed to date, and the resulting upper limits compiled in Tab. 6.12 constrain the off-diagonal components of the LEFT coefficients. These bounds are complementary to those from the leptonic decays of neutral pseudoscalar mesons, as they probe the orthogonal combinations of LEFT Wilson coefficients.

While pseudoscalar meson decays do not allow for decays into massless final states due to the helicity suppression, quarkonia can decay invisibly via $V \to \nu_i \bar{\nu}_j$ in the SM and beyond. In our MFV setup, only left-handed charged currents contribute, leading to the simplified expression

$$\Gamma(V \to \bar{\nu}_i \nu_j) = \frac{f_V^2 m_V^3}{192\pi} \left(|\mathcal{C}^{VLL}_{\substack{eq \\ ijkk}} + \mathcal{C}^{VLR}_{\substack{eq \\ ijkk}}|^2 \right) , \tag{6.22}$$

V	$\mathcal{B}(V \to e^\pm \mu^\mp)$	$\mathcal{B}(V \to e^\pm \tau^\mp)$	$\mathcal{B}(V \to \mu^\pm \tau^\mp)$
Φ	$< 2.0 \cdot 10^{-6}$ [329]		
J/ψ	$< 1.6 \cdot 10^{-7}$ [330]	$< 7.5 \cdot 10^{-8}$ [331]	$< 2.0 \cdot 10^{-6}$ [332]
Υ	$< 3.9 \cdot 10^{-7}$ [333]	$< 2.7 \cdot 10^{-6}$ [333]	$< 2.7 \cdot 10^{-6}$ [333]

Table 6.12: Current experimental limits on branching fractions of LFV quarkonia decays, all at 90% CL.

following from Eq. (6.21). The total invisible decay width is the incoherent sum over all neutrino flavors, $\Gamma(V \to \nu\bar{\nu}) = \sum_{i,j} \Gamma(V \to \nu_i \bar{\nu}_j)$.

Experimentally, the invisible branching fractions have not yet been observed and the current 90% CL limits exceed the SM predictions by several orders of magnitude. As a result, constraints on the LEFT coefficients from these invisible modes remain comparatively weak, leaving significant room for potential new degrees of freedom contributing to semileptonic operators. Tab. 6.13 summarizes the current experimental limits on the invisible decays of quarkonia, alongside the corresponding SM predictions.

Observable	Limit [GeV]	SM prediction [GeV]
$\Gamma(\Phi \to \nu\bar{\nu})$	$< 7.2 \cdot 10^{-7}$ [334]	$8.0(0.6) \cdot 10^{-14}$
$\Gamma(J/\psi \to \nu\bar{\nu})$	$< 6.1 \cdot 10^{-8}$ [335]	$2.06(9) \cdot 10^{-12}$
$\Gamma(\Upsilon \to \nu\bar{\nu})$	$< 1.6 \cdot 10^{-8}$ [336]	$4.6(0.4) \cdot 10^{-19}$

Table 6.13: Current 90% CL experimental limits on branching fractions of quarkonia decays to a dineutrino pair, together with the corresponding SM predictions computed using Eq. (6.22).

6.2.3. Semileptonic Meson Decays

Semileptonic meson decays yield a plethora of observables including differential decay widths, kinematic distributions and angular observables that go well beyond the simple branching fractions accessible by purely leptonic decays. These allow for stringent tests of lepton-flavor universality, the isolation of specific operator structures in the LEFT, and the discrimination between competing new-physics scenarios. The comparatively large branching ratios of semileptonic channels also allow for high experimental precision, which in turn improves the sensitivity to deviations from the SM predictions.

This comes, however, at the cost of a more intricate theoretical description due to the presence of more complex hadronic matrix elements. A central ingredient are the hadronic form factors, which encapsulate the non-perturbative QCD effects in the $P \to P'$ and $P \to V$ transitions. In contrast to the decay constant that parameterize purely leptonic decays, the form factors are continuous functions depending on the kinematic variable q^2, which denotes the invariant mass

of the lepton pair. The form factors are typically extracted from experimental data, lattice QCD calculations or light-cone sum rules at certain points of q^2. These results are then extrapolated using parameterizations such as the BCL [337] or the BSZ [338] parameterization to obtain a continuous description over the whole kinematic range. In this work, we aim to minimize potential BSM contaminations in these form factors by relying only on lattice QCD computations and light-cone sum rules. Details of the parameterizations and numerical inputs are collected in Appendix E .

Charged-Current Semileptonic Decays

At tree-level, charged current processes, such as $B \to D\ell\nu$ or $D \to K\ell\nu$ are mediated by the exchange of a W boson in the SM, providing direct sensitivity to the corresponding CKM matrix elements. The LEFT framework allows for additional BSM contributions to the decay amplitudes, which can be parameterized in terms of the effective coefficient $\mathcal{C}^{V,LL}_{\nu edu}$, similar to the purely leptonic decay of charged pseudoscalar mesons. The differential decay width for the decay $P \to P'\ell\nu$ can be expressed in the LEFT as [339]

$$\begin{aligned}\frac{d\Gamma}{dq^2}(P \to P'\ell_i\nu_j) = \frac{\eta_{\text{EW}}^2}{192\pi^3}\frac{(q^2-m_\ell^2)^2\sqrt{E_{P'}^2-m_{P'}^2}}{q^4 m_P^2}|\mathcal{C}^{V,LL}_{\substack{\nu edu\\ jikm}}|^2 \\ \times\left(\left(1+\frac{m_\ell^2}{2q^2}\right)m_P^2(E_{P'}^2-m_{P'}^2)|f_+(q^2)|^2+\frac{3m_\ell^2}{8q^2}(m_P^2-m_{P'}^2)^2|f_0(q^2)|^2\right),\end{aligned} \tag{6.23}$$

where q^2 denotes the invariant mass of the lepton-neutrino pair, $f_+(q^2)$ and $f_0(q^2)$ are the vector and scalar form factors, respectively, and

$$E_{P'} = \frac{m_P^2+m_{P'}^2-q^2}{2m_P}, \tag{6.24}$$

is the energy of the final state meson P'. The factor η_{EW}^2 accounts for the leading short-distance electroweak corrections [340], with $\eta_{\text{EW}} = 1.009$ for B meson decays and $\eta_{\text{EW}} = 1.0066$ for D meson decays [339].

The full decay width follows from integrating Eq. (6.23) over the allowed kinematic range $m_{\ell l_i}^2 < q^2 < (m_P - m_{P'})^2$. Since the decay width is the incoherent sum over all neutrino flavors, the total decay width probes lepton-flavor diagonal as well as off-diagonal contributions simultaneously, where only the flavor diagonal contributions are present in the SM. For decays into vector mesons, $P \to V\ell\nu$, the differential decay width can be expressed as [307, 341, 342]

$$\frac{\mathrm{d}\Gamma}{\mathrm{d}q^2}(P \to V\ell_i\nu_j) = \frac{q^2}{1536\pi^3 m_P^3}\lambda^{1/2}(m_P^2,m_V^2,q^2)|\mathcal{C}^{V,LL}_{\substack{\nu eud\\ jikm}}|^2\left[H_+^2(q^2)+H_-^2(q^2)+H_{0,T}^2(q^2)\right], \tag{6.25}$$

with the amplitudes

$$\begin{aligned}H_\pm(q^2) &= (m_P+m_V)A_1(q^2) \mp \frac{\lambda^{1/2}(m_P^2,m_V^2,q^2)}{m_P+m_V}V(q^2), \\ H_{0,T}(q^2) &= \frac{m_P+m_V}{2m_V\sqrt{q^2}}\left[(m_P^2-m_V^2-q^2)A_1(q^2)-\frac{\lambda(m_P^2,m_V^2,q^2)}{(m_P+m_V)^2}A_2(q^2)\right],\end{aligned} \tag{6.26}$$

where A_1, A_2, and V denote the form factors.

Tab. 6.14 summarizes the variety of semileptonic channels that we consider in this analysis. A detailed lists of current experimental measurements and limits as well as the corresponding SM predictions are provided in Appendix E . We find overall consistency between the data and the SM, with no tension above $\sim 1.5\sigma$ among all decays.

Meson	$e\nu$	$\mu\nu$	$\tau\nu$
D^0	K^-, K^{*-}, π^-, ρ^-	K^-, K^{*-}, π^-, ρ^-	
D^+	$\bar{K}^0$, $\bar{K}^{*0}$, π^0, η, ρ, ω	$\bar{K}^0$, $\bar{K}^{*0}$, π^0, η, ρ, ω	
D_s	ϕ, K^{*0}	ϕ	
B^0	D^-, D^{*-}, π^-, ρ^-	D^-, D^{*-}, π^-, ρ^-	D^-, D^{*-}, π^-
B^+	$\bar{D}^0$, D^*, π^0, ρ^0	$\bar{D}^0$, D^*, π^0, ρ^0	$\bar{D}^0$, D^*
B_s		D_s^-, D_s^{*-}, K^-	

Table 6.14: Overview of the semileptonic charged-current decays analyzed in this work. The decay channels are grouped according to the final state lepton flavor. Further details on the experimental measurements and SM predictions of the decay widths can be found in Appendix E .

Neutral-Current Semileptonic Decays

Flavor-changing neutral current (FCNC) decays of B mesons are particularly sensitive to NP effects in semileptonic four-fermion operators since their SM contributions are strongly GIM suppressed. Moreover, they directly test the higher order contributions in the MFV framework, thereby providing indirect probes of the size of flavor-symmetry breaking in the quark sector.

Especially decays into vector mesons, such as $B \to K^* \ell^+ \ell^-$, exhibit a rich experimental signature due to the polarization degrees of freedom of the final state, leading to a variety of angular observables. These detailed angular distributions allow for a multi-dimensional analysis that can disentangle the Lorentz structure of the NP contributions.

The decay $P \to V\ell + \ell^-$ can be fully described by the dilepton invariant mass q^2 as well as three kinematic angles, θ_ℓ, θ_V, and ϕ, denoting the angles between the lepton and the V meson, the V meson and the P meson, and the angle between the decay plane of the lepton pair and the V meson, respectively. By projecting the four-dimensional distribution $\frac{\mathrm{d}^4\Gamma}{\mathrm{d}q^2 \mathrm{d}\cos\theta_\ell \mathrm{d}\cos\theta_V \mathrm{d}\phi}$ onto specific angular functions, the independent contributions of the different helicity amplitudes can be isolated [343].

From these, commonly used observables can be constructed, such as the longitudinal polarization fraction $F_L(q^2)$, which measures the fraction of longitudinally polarized vector mesons in the decay, the forward-backward asymmetry $A_{FB}(q^2)$, which quantifies the asymmetry between the forward and backward directions of the lepton pair, and the normalized angular coefficients $S_i(q^2)$. The decay amplitudes in these processes depend on multiple form factors, including vector, axial-vector, and tensor form factors. We provide details on the form factors and their parameterizations in Appendix E .

To further enhance the sensitivity to the Wilson coefficients, optimized observables can be constructed, which are linear combinations of the angular coefficients that maximize the sensitivity to specific NP contributions and further reduce experimental and theory uncertainties. In particular, the optimized observables $P_i(q^2)$ defined as [344, 345]

$$\begin{aligned} P_1 &= \frac{2S_3}{1-F_L}\,, \qquad P_2 = \frac{2A_{FB}}{1-F_L}\,, \qquad P_3 = -\frac{S_9}{1-F_L}\,, \\ P_i' &= \frac{S_i}{\sqrt{F_L(1-F_L)}}\,, \quad i = 4,5,6,8\,, \end{aligned} \tag{6.27}$$

are experimentally well accessible and theoretically clean at large recoil.

As the computation of semileptonic meson decay observables in the LEFT is highly complex, we rely on the python package `flavio` [346] to compute the LEFT contributions for decays and employ the corresponding SM predictions from the literature[7]

Tabs. 6.15 and 6.16 summarize the observables that we consider for the lepton-flavor diagonal decays into pseudoscalar mesons and vector mesons, respectively. Furthermore, Tab. 6.17 summarizes the current experimental limits on lepton-flavor violating semileptonic decay widths, which are sensitive to the lepton-flavor off-diagonal components of the LEFT coefficients.

Observables	Data	Ref	SM Ref
$\Gamma(B^0 \to \pi^0 e^+ e^-)$	90% CL limit	[347]	[348]
$\Gamma(B^0 \to \pi^0 \mu^+ \mu^-)$	90% CL limit	[347]	[348]
$\Gamma(B^+ \to \pi^+ e^+ e^-)$	90% CL limit	[349]	[348]
$\left\langle \frac{d\sigma}{dq^2} \right\rangle (B^+ \to \pi^+ \mu^+ \mu^-)$	9 bins	[350]	[351, 352]
$\Gamma(B^0 \to K^0 e^+ e^-)$	inclusive	[18]	[353]
$\left\langle \frac{d\sigma}{dq^2} \right\rangle (B^0 \to K^0 \mu^+ \mu^-)$	6 bins	[354]	[353]
$\Gamma(B^+ \to K^+ e^+ e^-)$	inclusive	[18]	[353]
$\left\langle \frac{d\sigma}{dq^2} \right\rangle (B^+ \to K^+ \mu^+ \mu^-)$	11 bins	[354]	[353, 355]
$\Gamma(B^+ \to K^+ \tau^+ \tau^-)$	90% CL limit	[356]	[353]

Table 6.15: Overview of the observables for semileptonic decays into pseudoscalar mesons ($P \to P' \ell^+ \ell^-$) considered in this work.

Semileptonic decays to invisible final states, most notably $B \to K \nu \bar{\nu}$, offer an additional handle to probe semileptonic operators. These decays are particularly interesting as they are sensitive to the presence of new physics in the form of additional light degrees of freedom, such as dark photons or dark scalars, which can escape detection in collider experiments. Experimentally, the branching ratio is reported inclusively over all neutrino flavors, potentially allowing for the presence of LFV interactions. Recently, the decay $B^+ \to K^+ \nu \bar{\nu}$ has been observed by the Belle II collaboration with a branching ration of $\mathcal{B}(B^+ \to K^+ \nu \bar{\nu}) = 2.3(0.7) \cdot 10^{-5}$ [372], which is $2.7\,\sigma$ above the SM prediction $\mathcal{B}_{\text{SM}}(B^+ \to K^+ \nu \bar{\nu}) = 5.58(0.37) \cdot 10^{-6}$ [353], sparking great

[7] Analytical expressions can be found in e.g. Refs. [300, 312].

Process	Observables	Ref	SM Ref
$B^0 \to K^{*0} e^+ e^-$	F_L, $P_i^{(\prime)}$ (1 bin)	[357]	[358]
$B^0 \to K^{*0} \mu^+ \mu^-$	F_L, $P_i^{(\prime)}$ (8 bins)	[42]	[346, 358]
$B^0 \to K^{*0} \tau^+ \tau^-$	90% CL limit on $\mathcal{B}$	[359]	[346]
$B^+ \to K^{*+} e^+ e^-$	$\Gamma(B^+ \to K^{*+} e^+ e^-)$	[18]	[346]
$B^+ \to K^{*+} \mu^+ \mu^-$	F_L, $P_i^{(\prime)}$ (8 bins)	[360]	[346, 358]
$B_s \to \phi e^+ e^-$	F_L, S_3 (3 bins)	[361]	[346]
$B_s \to \phi \mu^+ \mu^-$	F_L, S_3, S_4, S_7 (5 bins)	[362]	[346]
$B_s \to K^* \mu^+ \mu^-$	$\Gamma(B_s \to K^* \mu^+ \mu^-)$	[363]	[364]

Table 6.16: Overview of the observables for semileptonic decays of pseudoscalar mesons into vector mesons ($P \to V \ell^+ \ell^-$) considered in this work.

Observable	90% CL limit [GeV]	Observable	90% CL limit [GeV]
$\Gamma(B^0 \to \pi^0 e\mu)$	$6.1 \cdot 10^{-20}$ [365]	$\Gamma(B^0 \to K^0 e\mu)$	$1.6 \cdot 10^{-20}$ [366]
$\Gamma(B^+ \to \pi^+ e\mu)$	$6.8 \cdot 10^{-20}$ [365]	$\Gamma(B^+ \to \pi^+ e\tau)$	$3.0 \cdot 10^{-17}$ [367]
$\Gamma(B^+ \to \pi^+ \mu\tau)$	$2.9 \cdot 10^{-17}$ [367]	$\Gamma(B^+ \to K^+ e\mu)$	$3.7 \cdot 10^{-20}$ [368]
$\Gamma(B^+ \to K^+ e\tau)$	$1.2 \cdot 10^{-17}$ [367]	$\Gamma(B^+ \to K^+ \mu\tau)$	$1.9 \cdot 10^{-17}$ [367]
$\Gamma(B^0 \to K^{*0} e\mu)$	$2.5 \cdot 10^{-21}$ [369]	$\Gamma(B^0 \to K^{*0} e\tau)$	$1.3 \cdot 10^{-17}$ [370]
$\Gamma(B^0 \to K^{*0} \mu\tau)$	$3.6 \cdot 10^{-18}$ [371]	$\Gamma(B^+ \to K^{*+} e\mu)$	$4.0 \cdot 10^{-19}$ [368]
$\Gamma(B_s \to \phi e\mu)$	$6.9 \cdot 10^{-21}$ [369]		

Table 6.17: Current experimental limits on the branching fractions of LFV semileptonic decays of B mesons, all at 90% CL. The upper part of the table lists the decays into pseudoscalar mesons, while the lower part lists the decays into vector mesons.

interest in the particle physics community[8] [374–385]. The decay proceeds via a $b \to s$ FCNC, which is highly suppressed in the SM and thus very sensitive to NP contributions. In our MFV framework, it provides a direct probe of the higher order spurion insertions via the ratio r_L.

[8] For up-type FCNC transitions $c \to u\nu\bar{\nu}$, the BESIII collaboration has set an upper limit of $\mathcal{B}(D^0 \to \pi^0 \nu\bar{\nu}) < 2.1 \cdot 10^{-4}$ [373], which we do not include in this work as no up-type FCNCs are induced in our MFV setup.

In the LEFT, the differential decay width of a B meson to a pseudoscalar meson P and a neutrino pair is given by [386]

$$\frac{\mathrm{d}\Gamma}{\mathrm{d}q^2}(B \to P\nu_i\bar{\nu}_j) = \frac{\lambda^{3/2}(m_B^2, m_P^2, q^2)}{1536\pi^3 m_B^3} |f_+(q^2)|^2 \left(|\mathcal{C}^{V,LL}_{\substack{\nu q \\ ijkl}} + \mathcal{C}^{V,LR}_{\substack{\nu q \\ ijkl}}|^2 \right) . \tag{6.28}$$

For the decay $B^+ \to K^+\nu\bar{\nu}$, we add an additional long distance contribution to the SM prediction following Ref. [353], which arises from the tree-level decay $B^{\to}\tau^+\nu_\tau$ with the subsequent decay $\tau^+ \to K^+\bar{\nu}_\tau$. This contribution is two orders of magnitude larger than the short-distance contribution and thus dominates the partial decay width.

The Kaon decay $K^+ \to \pi^+\nu_i\bar{\nu}_j$ depends on the same sets of Wilson coefficients, but the computation is more involved due to sizable charm-quark contribution. We follow Refs. [387, 388] for the computation of the LEFT decay width and employ the SM prediction given in Ref. [388].

Observable	Measurement [GeV]	SM prediction [GeV]
$\Gamma(K^+ \to \pi^+\nu\bar{\nu})$	$6.1(2.1) \cdot 10^{-27}$ [18]	$4.18(0.32) \cdot 10^{-27}$ [388]
$\Gamma(B^0 \to \pi^0\nu\bar{\nu})$	$< 3.9 \cdot 10^{-18}$ [389]	$2.56(0.55) \cdot 10^{-20}$
$\Gamma(B^0 \to K^0\nu\bar{\nu})$	$< 1.1 \cdot 10^{-17}$ [389]	$1.78(0.10) \cdot 10^{-18}$
$\Gamma(B^+ \to \pi^+\nu\bar{\nu})$	$< 5.6 \cdot 10^{-18}$ [389]	$5.1(1.1) \cdot 10^{-20}$
$\Gamma(B^+ \to K^+\nu\bar{\nu})$	$9.2(2.8) \cdot 10^{-18}$ [372]	$2.08(0.10) \cdot 10^{-18}$
$\Gamma(B^0 \to \rho\nu\bar{\nu})$	$< 1.7 \cdot 10^{-17}$ [389]	$7.4(1.1) \cdot 10^{-20}$
$\Gamma(B^0 \to K^{*0}\nu\bar{\nu})$	$< 7.8 \cdot 10^{-18}$ [389]	$3.95(0.36) \cdot 10^{-18}$
$\Gamma(B^+ \to \rho^+\nu\bar{\nu})$	$< 1.2 \cdot 10^{-17}$ [389]	$1.48(0.21) \cdot 10^{-19}$
$\Gamma(B^+ \to K^{*+}\nu\bar{\nu})$	$< 1.6 \cdot 10^{-17}$ [389]	$3.95(0.36) \cdot 10^{-18}$
$\Gamma(B_s \to \phi\nu\bar{\nu})$	$< 2.3 \cdot 10^{-15}$ [390]	$4.2(0.3) \cdot 10^{-18}$

Table 6.18: Current experimental values and limits on the partial decay width of semileptonic decays to invisible final states, alongside the corresponding SM predictions computed using Eqs. (6.28) and (6.29). All limits are at 90% CL. The upper part presents measurements of the decay with a pseudoscalar meson in the final state, while the lower part lists the decays into a vector meson.

The decay width for the decay of a B meson to a vector meson, $B \to V\nu\bar{\nu}$, is given by [386]

$$\begin{aligned}\frac{\mathrm{d}\Gamma}{\mathrm{d}q^2}(P_i \to V\nu_i\bar{\nu}_j) = &\frac{\lambda^{1/2}(m_{P_i}^2, m_V^2, q^2)\, q^2}{192\pi^3 m_{P_i}^3} \left[\frac{\lambda(m_{P_i}^2, m_V^2, q^2)}{4(m_{P_i} + m_V)^2} |V|^2 |\mathcal{C}^{V,LL}_{\substack{\nu q \\ ijkl}} + \mathcal{C}^{V,LR}_{\substack{\nu q \\ ijkl}}|^2 \right. \\ &\left. + \left(\frac{8 m_{P_i}^2 m_V^2}{q^2} |A_{12}|^2 + \frac{(m_{P_i} + m_V)^2}{4} |A_1|^2 \right) |\mathcal{C}^{V,LL}_{\substack{\nu q \\ ijkl}} - \mathcal{C}^{V,LR}_{\substack{\nu q \\ ijkl}}|^2 \right] ,\end{aligned} \tag{6.29}$$

where V, A_{12}, and A_1 are the vector and axial-vector form factors, respectively. Tab. 6.18 summarizes the current experimental measurements and limits together with the corresponding SM predictions.

Chapter 7

Global Fits of Collider and Flavor Observables

In this chapter, we present the results of our global fits of collider and flavor observables in the SMEFT framework. In Sec. 7.1, we systematically explore the constraints on the SMEFT parameter space and the synergies between different lepton flavors. Sec. 7.2 investigates the flavor structure of the SMEFT by examining the posterior distributions of the MFV ratios r_L^i and r_R^i. We then turn to the CKM matrix fit in Sec. 7.3, where we compare our results to the literature and demonstrate the feasibility of a joint fit of SMEFT and CKM parameters. Finally, we present predictions for dineutrino decay rates in Sec. 7.4.

7.1. Constraints on the Wilson Coefficients

We perform simultaneous fits to the 24 Wilson coefficients listed in 3.1. We further include 8 MFV ratios r_L^i and r_R^i defined in 3.17 as well as the Wolfenstein parameters λ, A, ρ and η as free parameters. Because the dipole operators and the scalar and tensor four-fermion operators are not Hermitian, we include the corresponding coefficients $\tilde{C}_{ij}$ and $\tilde{C}_{ji}$ as independent degrees of freedom in the fit. In total, this gives us 36 free parameters for the lepton-flavor-conserving (LFC) and universal fits, and 42 parameters for the lepton-flavor-violating (LFV) fits due to the additional Wilson coefficients for the non-Hermitian operators.

To offer a clear and systematic presentation of our results, we categorize the Wilson coefficients according to their phenomenological impact. First, we present the results for the Higgs-current operators, followed by the four-lepton operators. We then discuss the dipole operators and finally the semileptonic four-fermion operators. We further provide the 90% credible intervals and lower bounds on $\Lambda/\sqrt{C}$ in Appendix F .

7.1.1. Higgs-Current Operators

As shown in Chapters 5 and 6, the Higgs-current operators contribute to a plethora of observables as they alter the coupling between the heavy gauge bosons and the fermions. We consider the leptonic Higgs-current operators $\tilde{C}_{\varphi l}^{(1)}$, $\tilde{C}_{\varphi l}^{(3)}$, $\tilde{C}_{\varphi e}$, as well as the quark Higgs-current operators $\tilde{C}_{\varphi q}^{(1)}$, $\tilde{C}_{\varphi q}^{(3)}$, $\tilde{C}_{\varphi u}$ and $\tilde{C}_{\varphi d}$ in our analysis. We discuss the leptonic and quark Higgs-current operators separately, as they show different behavior in the global fit results.

Leptonic Higgs-Current Operators

We present the 90% credible intervals for the leptonic Higgs-current operators in Fig. 7.1. LFC couplings are shown in red, LFV couplings in blue and lepton-flavor universal scenarios in orange. The numerical values of the credible intervals are summarized in Appendix F in Tab. 11.

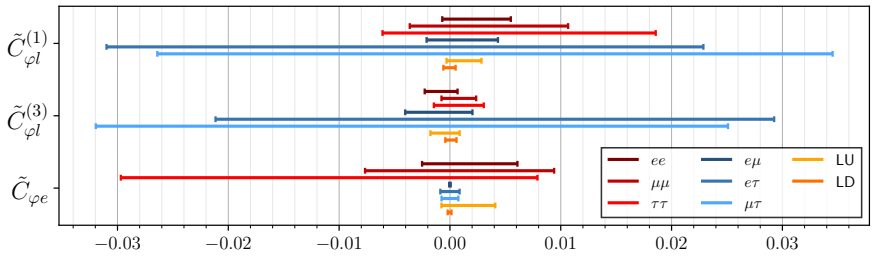

Figure 7.1: 90% credible intervals for the leptonic Higgs-current coefficients. We show the LFC coefficients in red, the LFV coefficients in blue and the lepton-flavor universal scenarios in orange.

We find all Wilson coefficients to be compatible with zero within the 90% credible range, except for the $\tilde{C}_{\varphi l}^{(1)}$ coefficient in the LU scenario, that shows a minor deviation towards positive values. The strongest single-flavor bounds are obtained for the LFV coefficients $\tilde{C}_{\varphi e}$, which are constrained up to about $7 \cdot 10^{-5}$ for the $e\mu$ coupling and about $8 \cdot 10^{-4}$ for the $e\tau$ and $\mu\tau$ coefficients. These tight constraints result from the strong limits on LFV $Z \to \ell_i \ell_j$ decays, which are especially tight for the $e\mu$ with $\mathcal{B}(Z \to e\mu) < 2.62 \cdot 10^{-7}$ [218]. The LFV bounds on $\tilde{C}_{\varphi l}^{(1/3)}$, on the other hand, are about two orders of magnitude weaker, as the linear combination $\tilde{C}_{\varphi l}^{-}$ is only weakly constrained by the $Z \to \nu\bar{\nu}$ decays, thus broadening the credible intervals for both, $\tilde{C}_{\varphi l}^{(1)}$ and $\tilde{C}_{\varphi l}^{(3)}$.

For the LFC coefficients, we find the bounds on $\tilde{C}_{\varphi l}^{(1)}$ and $\tilde{C}_{\varphi e}$ to be of the order of $5 \cdot 10^{-3}$, whereas the bounds on $\tilde{C}_{\varphi l}^{(3)}$ are about a factor of 3 stronger as they receive additional constraints from charged current processes, such as $W \to \ell_i \nu_j$ and $P \to \ell_i \nu_j$ decays. Overall, the constraints on coefficients involving τ leptons are weaker compared to coefficients involving only light leptons, due to the experimental challenges arising from the short lifetime of the τ lepton.

The LU and LD scenarios yield stronger constraints than the fits to individual lepton flavors in most cases. The only exception is the $\tilde{C}_{\varphi e}$ coefficient, with a 90% credible interval of $[-2.0, 1.3] \cdot 10^{-4}$ in the LD scenario compared to $[-6.7, 6.8] \cdot 10^{-5}$ for the $e\mu$ coefficient. This is due to the fact that the best fit points of the LFC couplings are slightly shifted away from zero, thus widening the credible intervals in the combined fit.

Using the upper limits on the Wilson coefficients, we can derive lower bounds on $\Lambda/\sqrt{C}$, thereby providing an estimate of the scale probed by current data. We adopt a conservative approach by taking the endpoint of each credible interval with the larger absolute value. The resulting reaches for the leptonic Higgs-current operators are shown in Fig. 7.2 and summarized in Tab. 12 in Appendix F .

Our results show that the leptonic Higgs-current operators are probed at scales ranging from about 1.4 TeV for the operators $O_{\varphi q}^{(1/3)}$ in the $e\tau$ and $\mu\tau$ fits, to about 30 TeV for the $e\mu$ component of $O_{\varphi e}$. The latter is far beyond the current direct reach of the LHC, demonstrating the power of indirect probes of new physics in the SMEFT framework. For the operators involving left-handed leptons, the reach of the LFC operators is slightly higher than most LFV operators, whereas this is reversed for the right-handed operators due to the strong constraints from LFV $Z \to \ell_i \ell_j$ decays.

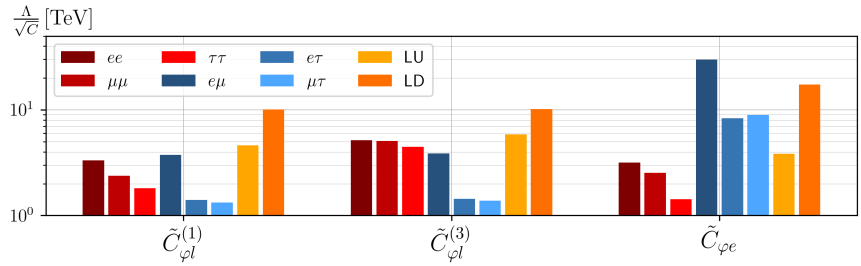

Figure 7.2: Lower bounds on $\Lambda/\sqrt{C}$ for the leptonic Higgs-current coefficients. The scales are derived from the largest absolute value of the 90% credible intervals of the Wilson coefficients presented in Fig. 7.1.

Moreover, the combination of the different lepton flavors in the LU and LD scenarios leads to a significant increase in the reach for the leptonic Higgs-current operators. This is particularly pronounced for $O^{(1)}_{\varphi q}$, where the largest individual flavor reach of about 3.8 TeV for the $e\mu$ coupling is increased to about 15 TeV in the LD scenario, corresponding to a factor of 4. This highlights the power of combined fits in the SMEFT framework, which can significantly enhance the sensitivity to BSM physics.

Quark Higgs-Current Operators

We present the 90% credible intervals for the quark Higgs-current operators in 7.3 and the lower bounds on the $\Lambda/\sqrt{C}$ scale in 7.4. The corresponding numerical values are summarized in Tab. 13 and 14 in Appendix F , respectively.

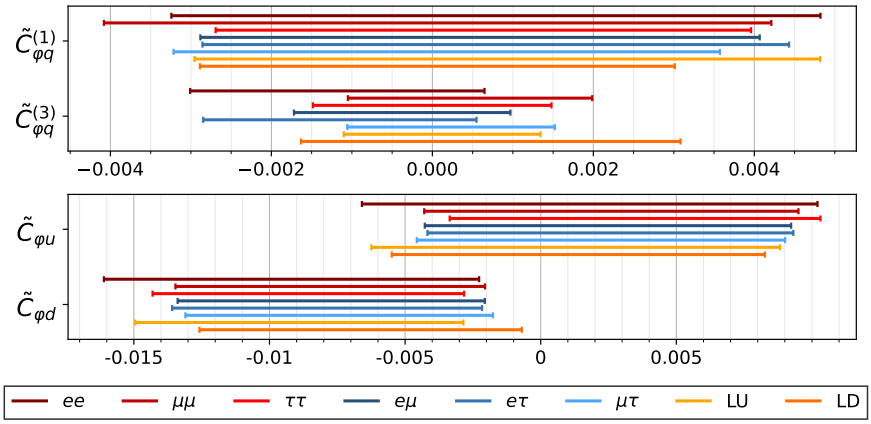

Figure 7.3: 90% credible intervals for the quark Higgs-current coefficients. The upper panel shows the bounds for left-handed operators, while the lower panel shows the bounds for right-handed operators.

We see shifts towards negative values for the coefficients $\tilde{C}_{\varphi d}$ for all lepton flavors, which are mainly driven by the slight deviations in the $Z \to b\bar{b}$ observables. All other coefficients are

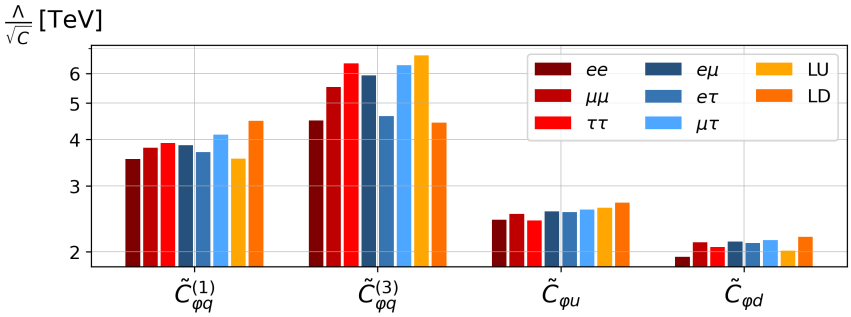

Figure 7.4: Lower bounds on $\Lambda/\sqrt{C}$ at 90% credible level for the quark Higgs-current coefficients. The scales are derived from the largest absolute value of the 90% credible intervals of the Wilson coefficients.

compatible with zero within the 90% credible intervals. As expected, we do not see strong enhancements from the combination of different lepton flavors in the LU and LD scenarios, as the quark Higgs-current operators are lepton-flavor universal by construction. We find the reach to be of similar magnitude as for the single-flavor fits of the leptonic Higgs-current operators, which is of the order of a few TeV.

The dependence on the lepton-flavor scenario is not very pronounced, in particular for the right-handed operators $O_{\varphi u}$ and $O_{\varphi d}$. This is to be expected, as the corresponding coefficients are mainly constrained by the $Z \to b\bar{b}$ and $Z \to c\bar{c}$ decays, which are lepton-flavor universal. For the left-handed operators, on the other hand, the sensitivity of flavor data to the Wilson coefficients is larger, in particular to the triplet coefficients $\tilde{C}^{(3)}_{\varphi q}$ that contribute to the charged-current LEFT coefficient $\mathcal{C}^{V,LL}_{\nu edu}$. As this coefficient features a strong interference between the Higgs-current and the four-fermion operators in these decays, this leads to a larger dependence on limits of the lepton-flavor-specific coefficients and thus on the lepton-flavor scenario.

7.1.2. Four-Lepton Operators

In the lepton-flavor-specific scenarios with LFC couplings, we only consider the coefficients $\tilde{C}_{iiii}$ for the four-lepton coefficients $\tilde{C}_{ll}$, $\tilde{C}_{le}$ and $\tilde{C}_{ee}$. For the LFV coefficients, we consider two different flavor contractions for $\tilde{C}_{ll}$ and $\tilde{C}_{le}$, which are $\tilde{C}_{ijij}$ and $\tilde{C}_{ijji}$ with $i \neq j$. For the right-handed operator O_{ee}, the LFV coefficients are unconstrained by the data because the only bounds on the LFV four-lepton operators arise from decays involving neutrinos. Thus, we do not present bounds on them here. They are nonetheless included in the fits with a flat prior in the range $[-10, 10]$.

We show the resulting 90% credible intervals for the four-lepton operators in Fig. 7.5 and the corresponding lower bounds on $\Lambda/\sqrt{C}$ in Fig. 7.6. The numerical values are summarized in Tab. 15 and 16 in Appendix F . For the LFV coefficients, we show the results for $\tilde{C}_{ijij}$ as striped bars and use solid bars for the $\tilde{C}_{ijji}$ coefficients. While both flavor structures give similar results for the $\tilde{C}_{le}$ coefficients, the $\tilde{C}_{ijij}$ coefficients are significantly less constrained than the $\tilde{C}_{ijji}$ components of the $\tilde{C}_{ll}$ coefficients, as the latter interfere with the SM contribution in the $\ell_i \to \ell_j \nu_i \bar{\nu}_j$ decays, while the former only contribute $\sim \tilde{C}^2$.

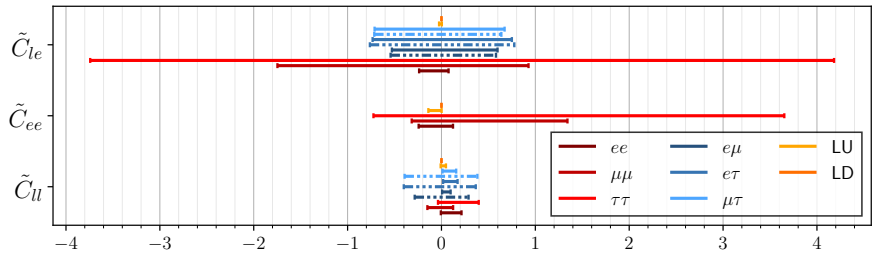

Figure 7.5: 90% credible intervals for the four-lepton coefficients. The dotted lines represent the bounds on the coefficients $\tilde{C}_{ijij}$, while the solid lines show the bounds on the coefficients $\tilde{C}_{ijji}$. The coefficients $\tilde{C}_{ee}$ are not shown, as they are unconstrained by the current data.

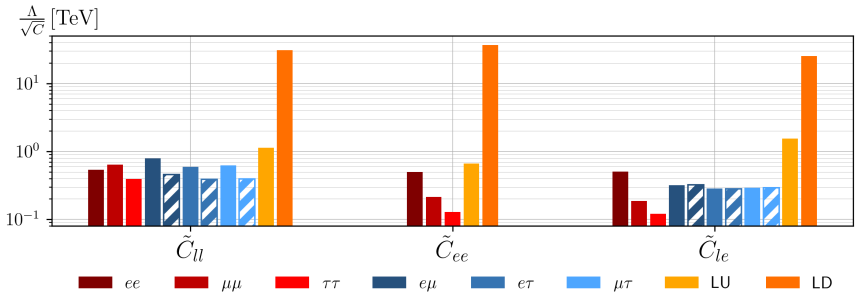

Figure 7.6: Lower bounds on $\Lambda/\sqrt{C}$ for the four-lepton coefficients at the 90% credible level. The scales are derived from the largest absolute value of the 90% credible intervals shown in 7.5. The striped bars represent the bounds on the coefficients $\tilde{C}_{ijij}$, while the solid bars show the bounds on the coefficients $\tilde{C}_{ijji}$. The LFV components of $\tilde{C}_{ee}$ are not shown, as they are unconstrained by the current data.

The reach of the single-flavor constraints is of the order of $\mathcal{O}(0.1\,\text{TeV})$ for all coefficients. The lepton-flavor universal scenarios, on the other hand, yield significantly stronger bounds as they include a multitude of additional flavor combinations. In the LU scenario, the combinations $\tilde{C}_{iijj}$ contribute as well, which are for example tested by dilepton production at LEP, increasing the reach by a factor of about 3 compared to the single-flavor scenarios. In the LD scenario, the enhancement is even larger as all $\tilde{C}_{ijkl}$ coefficients are tested, which are strongly constrained by LFV lepton decays $\ell_i \to \ell_j \ell_k \ell_l$. The resulting lower bounds on the $\Lambda/\sqrt{C}$ scale are of the order of 30 TeV, highlighting again the benefits of combined fits in the SMEFT framework.

Moreover, we see that the 90% credible intervals for the LFV components of $\tilde{C}_{ll}$ with the $\tilde{C}_{ijji}$ flavor structure are slightly shifted away from zero towards negative values. This results from the fact they feature a negative interference term with the SM contribution in the $\ell_i \to \ell_j \nu_i \bar{\nu}_j$ decays, which show some non-significant enhancements compared to the SM predictions. Due to the interference terms, a large part of the posterior is concentrated in the negative region, leading to a shift of the credible intervals towards negative values. The coefficients are, however, still compatible with zero within 3σ.

7.1.3. Dipole Operators

We include leptonic as well as up-type quark dipole operators in the global fit. The leptonic dipole coefficients include $\tilde{C}_{eW}$ and $\tilde{C}_{eB}$, while the up-type quark dipole coefficients comprise $\tilde{C}_{uW}$, $\tilde{C}_{uB}$ and $\tilde{C}_{uG}$, where the latter only contribute to the top-quark coupling in the MFV framework. The down-type quark dipole operators are not included in the fit, as they do not contribute in our MFV setup. We discuss the leptonic and the quark dipole coefficients separately in the following.

Leptonic Dipole Operators

The leptonic dipole operators predominantly contribute via the linear combination $\tilde{C}_{e\gamma}$ and $\tilde{C}_{eZ}$ defined in Eqs. 3.23 and 3.24 to the observables. They are mainly constrained by Z decays and the anomalous magnetic moments of the leptons or radiative lepton decays, respectively. We present the 90% credible intervals for the leptonic dipole operators in Fig. 7.7 and the corresponding lower bounds on $\Lambda/\sqrt{C}$ in Fig. 7.8, while the numerical values are summarized in Tabs. 17, 18 in Appendix F .

Since the leptonic dipole operators are not Hermitian, we include the coefficients $\tilde{C}_{ij}$ and $\tilde{C}_{ji}$ as independent degrees of freedom in the fit. While most observables are sensitive to the combination $\tilde{C}_{ij}^2 + \tilde{C}_{ji}^2$, charged-current processes, such as $W \to \ell_i \nu_j$, are sensitive to only one of the coefficients, leading to slight differences in the corresponding credible intervals.

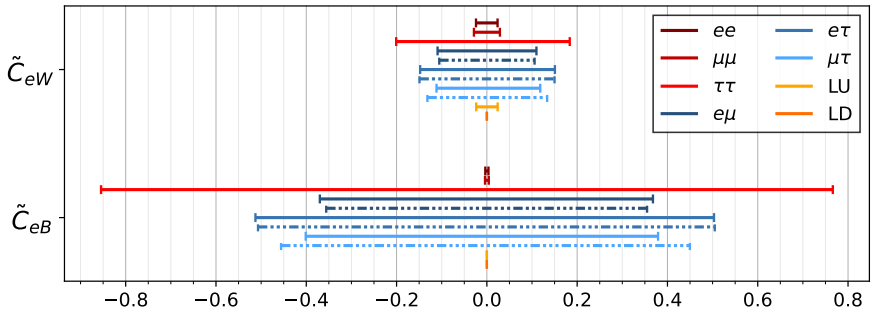

Figure 7.7: 90% credible intervals for the leptonic dipole coefficients. The dotted lines represent the bounds on the coefficients $\tilde{C}_{ji}$, while the solid lines show the bounds on the coefficients $\tilde{C}_{ij}$ with $i < j$.

We find the strongest single-flavor bounds for the $\tilde{C}_{eB}$ coefficient in the ee and $\mu\mu$ fits, with limits of about $4 \cdot 10^{-3}$. These result from the strong constraints on the anomalous magnetic moments of the electron and muon, which are sensitive to the Wilson coefficient $\tilde{C}_{e\gamma}$ that receives the largest contribution from the $\tilde{C}_{eB}$ coefficient. For the $\tau\tau$ coefficient, on the other hand, the anomalous magnetic moment is not constrained as strongly, leading to a 90% credible interval of the order 0.8, which is the weakest bound among the leptonic dipole coefficients.

Although the bounds on the coefficient $\mathcal{C}_{e\gamma}$ from LFV radiative lepton decays, $\ell_i \to \ell_j \gamma$, are stronger than the bounds from the anomalous magnetic moments as shown in Sec. 6.1, the LFV components of $\tilde{C}_{eB}$ are less constrained than the LFC components. This is because the scalar and tensor four-fermion operators $\tilde{C}_{lequ}^{(1/3)}$, which are only very weakly constrained in the LFV

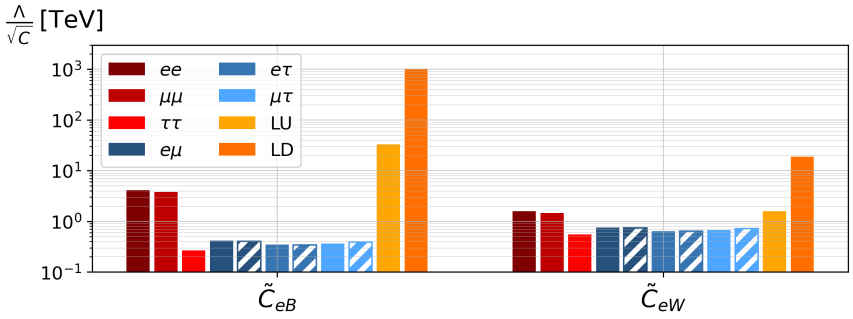

Figure 7.8: Lower bounds on $\Lambda/\sqrt{C}$ for the leptonic dipole coefficients derived from the 90% credible intervals shown in 7.7. The dotted bars represent the bounds on the coefficients $\tilde{C}_{ji}$, while the solid bars show the bounds on the coefficients $\tilde{C}_{ij}$ with $i < j$.

fits, mix strongly with the leptonic dipole operators under RGE and thus broaden the credible intervals for the LFV components of $\tilde{C}_{eB}$ and $\tilde{C}_{eW}$ significantly.

In the ee and $\mu\mu$ fits, on the other hand, the scalar and tensor four-fermion operators are directly constrained by $tt\ell\ell$ production, thus reducing the impact of these operators on the credible intervals of the leptonic dipole coefficients. Nonetheless, the RGE effects still lead to a significant reduction in the reach on $\Lambda/\sqrt{C}$ by approximately 2 orders of magnitude compared to the simplified fits presented in Fig. 6.2 in Sec. 6.1, demonstrating the strong impact of flat directions on the fits.

Notably, we do not see deviations in the 90% credible intervals of the leptonic dipole coefficients from zero, even though the data shows a deviation at the 5σ level in the measurement of the anomalous magnetic moment of the muon, as discussed in Sec. 6.1. This is due to the RGE effects, which dilute the impact of the LEFT coefficient $\mathcal{C}_{e\gamma}$ on the individual SMEFT coefficients $\tilde{C}_{eB}$ and $\tilde{C}_{eW}$. The resulting credible intervals are thus compatible with zero, even though the LEFT fit shows a significant deviation from zero for the $\mathcal{C}_{e\gamma}$ coefficient.

In the $\tau\tau$ and the LFV scenarios, the $\tilde{C}_{eW}$ coefficients are more strongly constrained than the $\tilde{C}_{eB}$ coefficients by a factor of roughly 2-3, as the former additionally contributes to charged current processes and further give the leading contribution to the $\tilde{C}_{eZ}$ coefficients, which are well constrained by Z decays.

Moreover, the results show that the lepton-flavor democratic (LD) scenario yields significantly stronger bounds than the other fits, with a reach of nearly 1000 TeV for the $\tilde{C}_{eB}$ coefficient, compared to bounds of the order of 0.1-1 TeV for the single-flavor scenarios. This strong enhancement arises due to the combination of the tight constraint on the $\tilde{C}_{e\gamma}$ coefficient from the decay $\mu \to e\gamma$ with the bounds on $\tilde{C}^{(1/3)}_{lequ}$ from the $tt\ell\ell$ for ee and $\mu\mu$. The latter lifts the nearly flat direction in the parameter space arising from the RGE effects, thereby significantly tightening the credible intervals for the leptonic dipole coefficients and demonstrating the power of combined fits in the SMEFT framework.

Due to the RGE effects, the limits on the leptonic dipole coefficients would strongly profit from a more precise measurement the $tt\ell\ell$ coupling, which would allow to constrain the scalar and tensor four-fermion operators more tightly. These are currently the limiting factors in the fits,

as they mix strongly with the leptonic dipole operators under RGE running. Moreover, also a better measurement of the $Z \to \ell_i \ell_j$ decays would help to tighten the bounds on the $\tilde{C}_{eZ}$ coefficients, which are comparatively weakly constrained compared to the strong limits on the $\tilde{C}_{e\gamma}$ coefficients from the anomalous magnetic moments and radiative lepton decays.

Both of these measurements could, for example, be performed at the FCC-ee [121–125] or the Compact Linear Collider (CLIC) [128–131], which could help improve the bounds by orders of magnitude. This is particular interesting given the current anomalies in the anomalous magnetic moment of the muon. Constraining the other directions in the parameter space would help to pinpoint potential deviations in the SMEFT, which can currently not be observed due to the weakly constrained directions in the parameter space.

Up-Type Quark Dipole Operators

Fig. 7.9 shows the 90% credible intervals for the up-type quark dipole operators, while 7.10 presents the corresponding lower bounds on $\Lambda/\sqrt{C}$. The up-type quark dipole operators are mainly constrained by the top-quark observables, to which the leptonic operators contribute only subdominantly. Thus, the results for the up-type quark dipole operators depend only weakly on the lepton-flavor scenario.

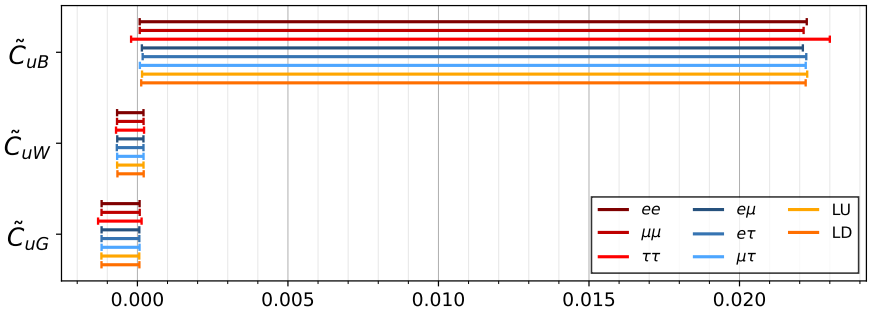

Figure 7.9: 90% credible intervals for the up-type quark dipole coefficients.

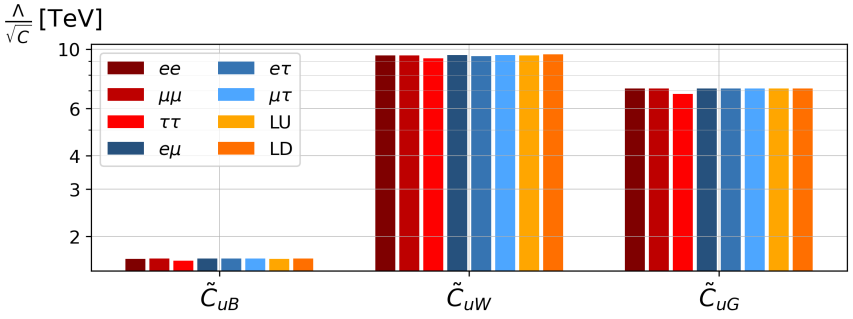

Figure 7.10: Lower bounds on $\Lambda/\sqrt{C}$ at 90% credible level for the up-type quark dipole coefficients. The scales are derived from the largest absolute value of the 90% credible intervals shown in 7.9.

We see a slight shift of the credible intervals of $\tilde{C}_{uB}$ towards positive values. All coefficients are, however, compatible with zero within 2σ. The strongest bounds are obtained for the $\tilde{C}_{uW}$ and $\tilde{C}_{uG}$ coefficients, with limits of the order 10^{-3}, corresponding to a reach on $\Lambda/\sqrt{C}$ of roughly 10 TeV, whereas the $\tilde{C}_{uB}$ coefficient probes scales of 1.7 TeV.

7.1.4. Semileptonic Four-Fermion Operators

The semileptonic four-fermion operators are the largest class of operators in this work and most relevant for many observables. They comprise operators with a vector structure, such as $O_{lq}^{(1/3)}$, as well as the scalar and tensor operators $O_{lequ}^{(1/3)}$. We will discuss the results for the scalar and tensor operators first, followed by the vector operators.

Scalar and Tensor Four-Fermion Operators

The tensor and scalar four-fermion operators do not interfere with the SM contributions and only contribute via the coupling to the top-quark in our MFV framework. As they are not Hermitian, we include the coefficients $\tilde{C}_{ij}$ and $\tilde{C}_{ji}$ as independent degrees of freedom in the fit. We present the resulting 90% credible intervals in Fig. 7.11 and the corresponding lower bounds on $\Lambda/\sqrt{C}$ in Fig. 7.12, where the striped bars represent the bounds on the coefficients $\tilde{C}_{ji}$, while the solid bars show the bounds on the coefficients $\tilde{C}_{ij}$ with $i < j$. The numerical values of the credible intervals and the lower bounds on $\Lambda/\sqrt{C}$ are summarized in Tab. 21 and 22 in Appendix F , respectively.

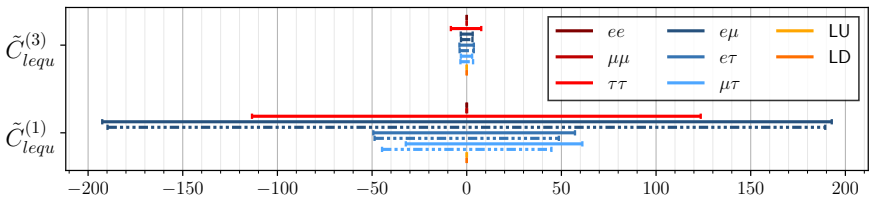

Figure 7.11: 90% credible intervals for the scalar and tensor four-fermion coefficients. The dotted lines represent the bounds on the coefficients $\tilde{C}_{ji}$, while the solid lines show the bounds on the coefficients $\tilde{C}_{ij}$ with $i < j$.

Notably, the only direct collider probe of these operators is $tt\ell\ell$ production, which is sensitive to the ee and $\mu\mu$ coefficients. Apart from that, the coefficients are only constrained via their mixing with the electroweak dipoles under RGE running, resulting in very weak bounds for most coefficients. In particular, the reach of the scalar and tensor four-fermion operators is at the order 1 TeV for the ee and $\mu\mu$ coefficients, while it is roughly 0.1 TeV or below for all other lepton flavors. In general, the tensor operator $\tilde{C}_{lequ}^{(3)}$ features larger RGE mixing with the electroweak dipoles than the scalar operator $\tilde{C}_{lequ}^{(1)}$, leading to stronger bounds on the former by an order of magnitude.

In the LU and LD scenarios, we find a strong enhancement of the reach by a factor of about 10-20 compared to the single-flavor scenarios for the $\tilde{C}_{lequ}^{(3)}$ coefficients, while limits on the $\tilde{C}_{lequ}^{(1)}$ coefficients are of similar magnitude. This is a result of the strong enhancement of the LU and LD $\tilde{C}_{eB}$ coefficients, which directly contribute to the tensor coefficients $\tilde{C}_{lequ}^{(3)}$ via the strong mixing under RGE running. The scalar coefficients, on the other hand, receive less RGE mixing,

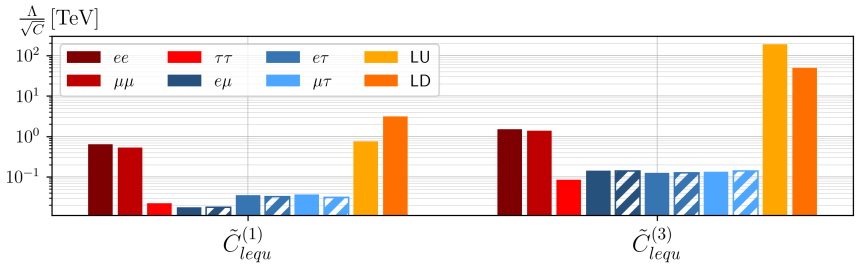

Figure 7.12: Lower bounds on $\Lambda/\sqrt{C}$ for the scalar and tensor four-fermion coefficients at the 90% credible level. The scales are derived from the largest absolute value of the 90% credible intervals shown in 7.11. The striped bars represent the bounds on the coefficients $\tilde{C}_{ji}$, while the solid bars show the bounds on the coefficients $\tilde{C}_{ij}$ with $i < j$.

and are thus mainly constrained by $tt\ell\ell$ production, resulting in a similar reach as the ee and $\mu\mu$ coefficients.

The sensitivity on these operators could be significantly improved by a more precise measurement of the $tt\ell\ell$ coupling. Simultaneously, this would also improve the fit of the leptonic dipoles via their RGE mixing. The prime facilities to perform such measurements would be lepton colliders, such as the FCC-ee [121–125], CLIC [128–131] or a muon collider [391, 392].

Vector Semileptonic Four-Fermion Operators

Fig. 7.13 shows the 90% credible intervals for the vector semileptonic four-fermion operators, while 7.14 presents the corresponding lower bounds on $\Lambda/\sqrt{C}$. The vector operators contribute to a large number of observables, including DY production, $tt\ell\ell$ production, as well as various flavor observables such as meson and semileptonic τ decays.

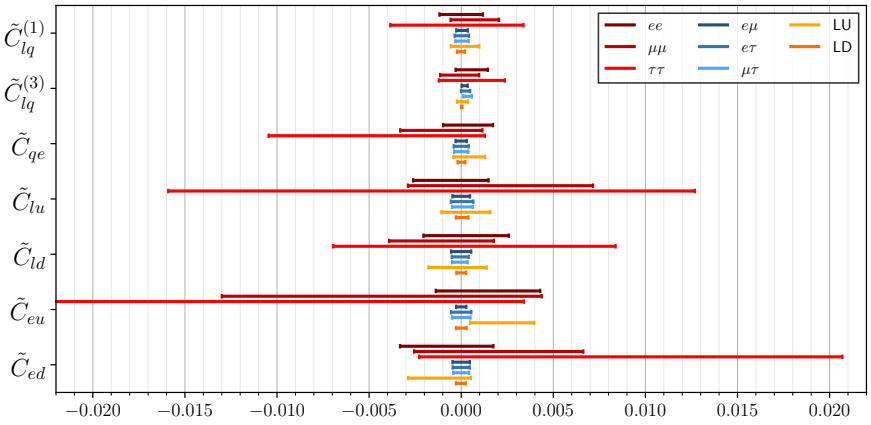

Figure 7.13: 90% credible intervals for the semileptonic four-fermion coefficients with a vector structure.

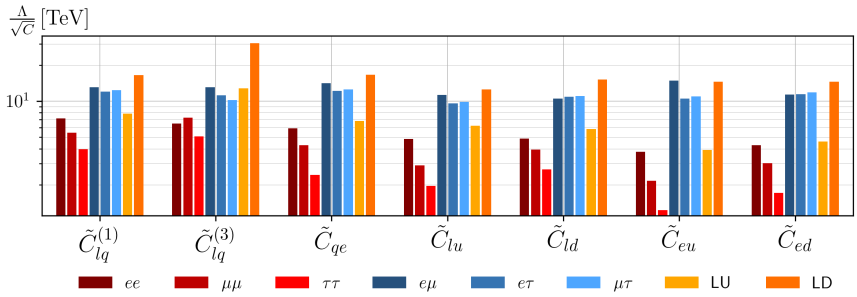

Figure 7.14: 90% credible lower bounds on $\Lambda/\sqrt{C}$ for the semileptonic four-fermion coefficients with a vector structure. The scales are derived from the largest absolute value of the 90% credible intervals shown in 7.13.

The resulting credible intervals are of the order of 10^{-3} for all coefficients except $\tau\tau$ operators including right-handed fermions, which are about an order of magnitude weaker. The corresponding lower on $\Lambda/\sqrt{C}$ range from about 2 TeV for the $\tau\tau$ coefficients to about 30 TeV for the LD $\tilde{C}_{lq}^{(3)}$ coefficient.

We find that the limits in the LFV fits are about a factor 2-4 stronger than the limits in the LFC fits. The reason is that the corresponding observables do not feature a SM contribution, leading to a reduced background and stronger sensitivity on potential BSM contributions.

Furthermore, the bounds on operators with left-handed quark doublets are slightly stronger than the bounds on operators with right-handed quarks, particularly for the LFC coefficients. This is due to the fact that the left-handed operators contribute to FCNC flavor observables, such as $B \to K^{(*)}\ell\ell$, which are well constrained by the data. The right-handed operators, on the other hand, only contribute to lepton-flavor-conserving processes in the MFV framework, such as DY processes and $tt\ell\ell$ production.

Interestingly, we find a small tension in the $\tilde{C}_{eu}$ coefficient in the LU scenario, with a credible interval of $[0.43, 3.2] \cdot 10^{-3}$, whereas similar deviations are absent in fits to the individual lepton flavors. This deviation thus arises solely from the interplay of the different flavors and observables, as well as the overall tightening of the credible intervals in combined fits, showing the significant impact of flavor assumptions on the results.

We further find slight enhancements in the $\tilde{C}_{lq}^{(3)}$ coefficients for $e\mu$ and $\mu\tau$, with 90% credible intervals of $[0.28, 3.7] \cdot 10^{-4}$ and $[0.65, 4.4] \cdot 10^{-4}$, respectively. These are probably driven by slight excesses in some high-p_T bins of the DY process $pp \to \mu\nu$ measured by the ATLAS collaboration [231], to which the $\tilde{C}_{lq}^{(3)}$ coefficients contribute strongly due to the energy-enhancement of the four-fermion operators.

7.1.5. Summary of the Credible Intervals

Overall, we find that the 90% credible intervals for the Wilson coefficients are mostly compatible with zero in all lepton-flavor scenarios. We further see significant differences in the credible intervals for the different classes of operators and the different lepton-flavor scenarios. For, e.g.,

the vector semileptonic four-fermion operators and $\tilde{C}_{\varphi e}$, the LFV couplings are in general more strongly constrained than the LFC couplings. This is due to the fact that the corresponding LFV observables do not receive any SM contributions, making them especially sensitive to the SMEFT coefficients. For the leptonic dipole coefficients, on the other hand, the bounds on ee and $\mu\mu$ components are tighter than the LFV bounds, as the latter are significantly broadened by the RGE mixing with the scalar and tensor four-fermion operators.

We further see strong synergies arising in the combination of different lepton flavors for several coefficients. This is most pronounced for the electroweak dipole coefficients, the four-lepton coefficients and $\tilde{C}^{(3)}_{lequ}$, where the LU and in particular the LD bounds are orders of magnitude stronger than the results of fits to individual lepton flavors.

The strongest constraints are obtained for the dipole coefficient $\tilde{C}_{eB}$ in the LD scenario with a corresponding lower bound on $\Lambda/\sqrt{C}$ of $\sim 1000\,\text{TeV}$. The scalar and tensor operators $\tilde{C}^{(1)}_{lequ}$ and $\tilde{C}^{(3)}_{lequ}$ are currently the least constrained, with the exception of the ee and $\mu\mu$ components. This is because the LFV and $\tau\tau$ coefficients are only indirectly constrained via the RGE mixing with the electroweak dipole operators. Their 90% credible limits are of the order of $2 \cdot 10^2$, leaving ample room for new physics in these operators.

In the future, the fits could be further improved with new data from a high-energy lepton collider such as the FCC-ee [121–125], CLIC [128–131], or a muon collider [391, 392]. These facilities could provide more precise measurements of the $tt\ell\ell$ coupling, thus tightening the constraints on the scalar and tensor four-fermion operators. Simultaneously, this would also improve the constraints on the leptonic dipole coefficients via their RGE mixing. Moreover, better measurements of $Z \to \ell_i \ell_j$ decays would allow more precise probes of $\tilde{C}_{eZ}$ as well as the Higgs-current operators. In addition, dilepton production at lepton colliders would help constrain the four-lepton operators, which are currently only weakly constrained in single-flavor fits.

7.2. Posterior Distributions of the MFV Parameters

In this section, we present the results on the posterior distributions of the MFV ratios r^i_L and r^i_R resulting from our global SMEFT fits. These ratios provide insight into the relative strength of the flavor-diagonal leading term compared to the higher-order spurion insertions in the MFV expansion (3.12).

The ratios r^i_R are defined for right-handed up-type quarks, so that we include such ratios for the operators $O_{\varphi u}$, O_{lu}, and O_{eu}. We show the resulting posterior probability distributions in Fig. 7.15.

We find all posterior distributions to be completely flat, indicating no sensitivity on the structure of right-handed couplings given the data included in this work. This is due to the fact that this ratio solely contributes to the coupling to top-quarks. The corresponding constraints are, however, orders of magnitude weaker than the bounds from DY and flavor observables, which are mostly sensitive to the first two generations of quarks. As a result, the posterior distributions for the ratios r^i_R remain unconstrained.

In the future, the sensitivity could be improved with more data on top-quark couplings, in particular of the $tt\ell\ell$ vertex. As mentioned in Sec. 7.1, the most promising experimental

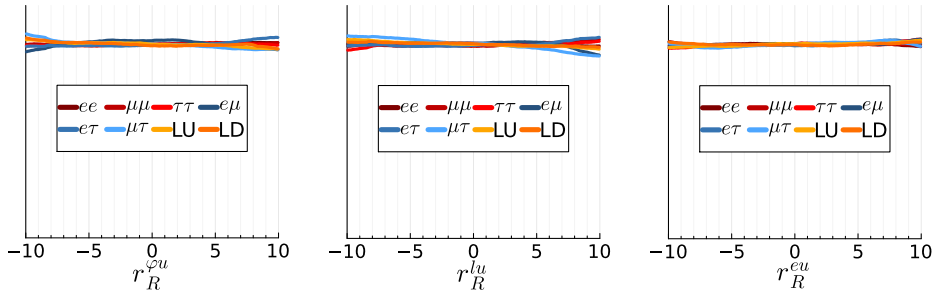

Figure 7.15: Posterior probability distributions for the MFV ratios $r_R^{\varphi u}$ (left), r_R^{lu} (center), and r_R^{eu} (right).

prospects for this are high-energy lepton colliders that operate above the $t\bar{t}$ threshold, such as the FCC-ee [121–125], CLIC [128–131] or a muon collider [391, 392]. These colliders offer a clean environment with high luminosity, which could lead to improved constraints on the MFV ratios r_R^i as well as on the Wilson coefficients in general [208, 393, 394].

For the left-handed operators, we find sensitivity on the ratios r_L^i in all cases, i.e. for $O_{\varphi q}^{(1/3)}$, $O_{lq}^{(1/3)}$, and O_{qe}. The reason is that in addition to the contribution to the top-quark couplings similar to $r_R^{\varphi u}$, these ratios also contribute directly to FCNCs as well as to lepton-flavor-conserving couplings of down-type quarks (see Eq. (3.20)). This results in increased sensitivity on the structure of the MFV expansion, which is reflected in the shape of the posterior for the ratios r_L^i.

For the ratios of the Higgs-current operators, $r_L^{\varphi q^{(1)}}$ and $r_L^{\varphi q^{(3)}}$, we show some examples of the posterior probability distributions in Fig. 7.16. For the sake of clarity, we show the remaining distributions in Appendix F in Fig. 1.

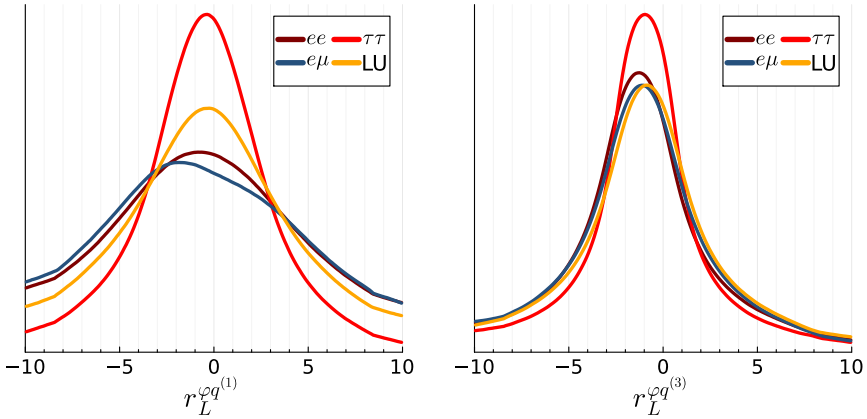

Figure 7.16: Posterior probability distributions for the MFV ratio $r_L^{\varphi q^{(1)}}$ (left) and $r_L^{\varphi q^{(3)}}$ (right) for the ee, $\tau\tau$, $e\mu$ and LU lepton-flavor scenarios. The remaining distributions are shown in Appendix F in Fig. 1.

For $r_L^{\varphi q^{(1)}}$ (left panel of Fig. 7.16), the posterior distributions exhibit distinct shapes across the different lepton-flavor scenarios. They are notably broader than for $r_L^{\varphi q^{(3)}}$, indicating less sensitivity on the MFV structure. Moreover, they exhibit slight asymmetries, particularly in the $e\mu$ scenario. The $\tau\tau$ scenario features the most pronounced peak, which is centered around $r_L^{\varphi q^{(1)}} \sim -0.5$, suggesting that the data may favor a non-zero contribution of higher-order spurion insertions. The ee and $e\mu$ distributions, in contrast, are flatter and more symmetric, indicating less pronounced sensitivity.

In the case of $r_L^{\varphi q^{(3)}}$ (right panel of Fig. 7.16), the distributions are more narrow and very similar across the different lepton-flavor scenarios. The peaks of the $\tau\tau$, $e\mu$ and LU scenarios are centered around $r_L^{\varphi q^{(3)}} \sim -1$, corresponding to a cancellation of the leading MFV term with the higher-order spurion insertion in the top-quark coupling $\sim \tilde{C}(1 + r_L^{\varphi q^{(3)}})$. The ee scenario is shifted further towards negative values, with the peak centered around $r_L^{\varphi q^{(3)}} \sim -1.3$, indicating a slight preference for larger contributions of higher-order spurion insertions.

Furthermore, we show the posterior distributions for the ratios r_L^i of the semileptonic four-fermion operators $O_{lq}^{(1/3)}$ and O_{qe} in Fig. 7.17.

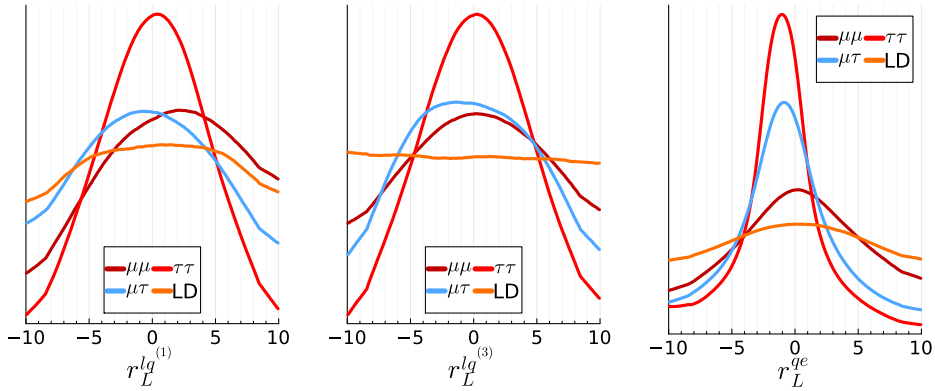

Figure 7.17: Posterior probability distributions for the MFV ratio $r_L^{lq^{(1)}}$ (left), $r_L^{lq^{(3)}}$ (center) and r_L^{qe} (right) for the $\mu\mu$, $\tau\tau$, $\mu\tau$, and LD lepton-flavor scenarios. The remaining distributions are shown in Appendix F in Fig. 2.

For these distributions, the posterior shapes vary substantially across the different lepton-flavor scenarios. Similar to the Higgs-current operators, the distributions for the $\tau\tau$ scenario exhibit the most pronounced peaks, centered around $r_L^i \sim 0$ for $O_{lq}^{(1/3)}$ and around $r_L^i \sim -1$ for O_{qe}, indicating a strong sensitivity to the MFV structure. This may be attributed to the relatively weak collider constraints in the $\tau\tau$ scenario, which in turn allows the flavor observables, sensitive to the product $\tilde{C} \cdot r_L^i$, to impose comparatively stronger bounds.

The other lepton-flavor scenarios, in particular the $\mu\mu$ and $\mu\tau$ scenarios, show broader distributions with some asymmetry, suggesting a mild preference for non-zero higher-order spurion insertions. In contrast, the LD scenario leads to broad, flat distributions with no pronounced peaks, suggesting weak sensitivity. This is likely because the constraints on the Wilson coefficients $\tilde{C}$ are very tight in the LD scenario, so that the product $\tilde{C} \cdot r_L^i$ is constrained to be close to

zero, leading to a flat posterior distribution for r_L^i. The $\mu\mu$ and $\mu\tau$ cases fall in between, with moderate widths and some asymmetry, indicating a mild preference for non-zero higher-order spurion insertions.

We further observe that the posterior distributions for r_L^{qe} are significantly narrower than those for $r_L^{lq^{(1/3)}}$ and $r_L^{lq^{(3)}}$. A reason might be that the operators $O_{lq}^{(1)}$ and $O_{lq}^{(3)}$ also contribute to the $b \to s\nu\bar{\nu}$ decays, which are directly sensitive to the product $\tilde{C} \cdot r_L^i$. Notably, a 3σ deviation from the SM has been reported in the decay $B^+ \to K^+\nu\bar{\nu}$ [372], which prefers large values of $\tilde{C} \cdot r_L^i$. As the Wilson coefficient $\tilde{C}$ are already constrained by other processes to be very small, this broadens the posterior distributions for r_L^i.

In general, all posterior distributions are consistent with $r_L^i = 0$, corresponding to the absence of higher-order spurion contributions in the MFV expansion. This outcome is expected, given the lack of systematic deviations from the SM in the data, which would necessitate sizable flavor-breaking terms to accommodate. However, there is still ample room for large higher-order spurion contributions, as the sensitivity of the data is not sufficient to rule out such contributions.

Our results differ from those of Ref. [1], where a characteristic double-peak structure was found for the posterior distributions of the ratios r_L^i. In that analysis, the MFV ratios were assumed to be universal across all operators involving a given quark bilinear. In our approach, this assumption is relaxed, allowing the MFV ratios to vary independently for each operator, which leads to qualitatively different posterior shapes.

7.3. Fit Results of the CKM Matrix

In this section, we present the results for the CKM matrix elements obtained from the global fits, where we treat the Wolfenstein parameters as nuisance parameters. To ensure sensitivity to these parameters across all lepton-flavor scenarios, we include the observables Δm_d, Δm_s, $\Gamma(B^+ \to \tau^+\bar{\nu})$ and the ratio $\Gamma(K^+ \to \mu^+\nu_\mu)/\Gamma(\pi^+ \to \mu^+\nu_\mu)$ (see Appendix B) in all fits, following Ref. [182]. For scenarios including SMEFT couplings to the muon, we use the partial widths $\Gamma(\pi^+ \to \mu^+\nu_\mu)$ and $\Gamma(K^+ \to \mu^+\nu_\mu)$ instead of their ratio, as SMEFT contributions largely cancel in the latter.

Fig. 7.19 shows the 1σ credible intervals of the Wolfenstein parameters λ, A, ρ, and η obtained from the posterior probability distributions of the Wilson coefficients in the different lepton-flavor scenarios. Black lines indicate the average, while colored bands show the 1σ credible intervals. We compare our results to the current CKMfitter averages [395, 396] shown in gray.

We find our results to be compatible with the CKMfitter averages for all lepton-flavor scenarios. In general, we observe a tendency in our results towards smaller values of A and larger values of ρ compared to the literature, which is, however, within the 1σ uncertainties. Moreover, we see consistency between the different lepton-flavor scenarios.

Furthermore, we extract the CKM matrix elements from the posterior distributions of the Wolfenstein parameters using the parameterization presented in Eq. (2.16). The resulting averages (black) and 1σ credible intervals (colored bands) of the CKM matrix elements are shown in Fig. 7.19. We find that the CKM matrix elements are largely compatible with the current CKMfitter averages [395, 396], shown in gray. We observe a slight deviation for the

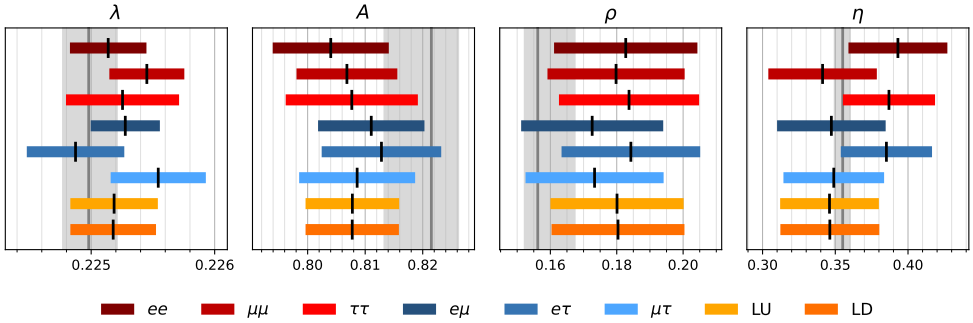

Figure 7.18: 1σ credible intervals of the Wolfenstein parameters λ, A, ρ and η. We show the average in black and the 1σ credible intervals in colored bands. We compare our results to the current CKMfitter averages[395, 396], for which we show the average and the 1σ uncertainties as gray lines and bands, respectively.

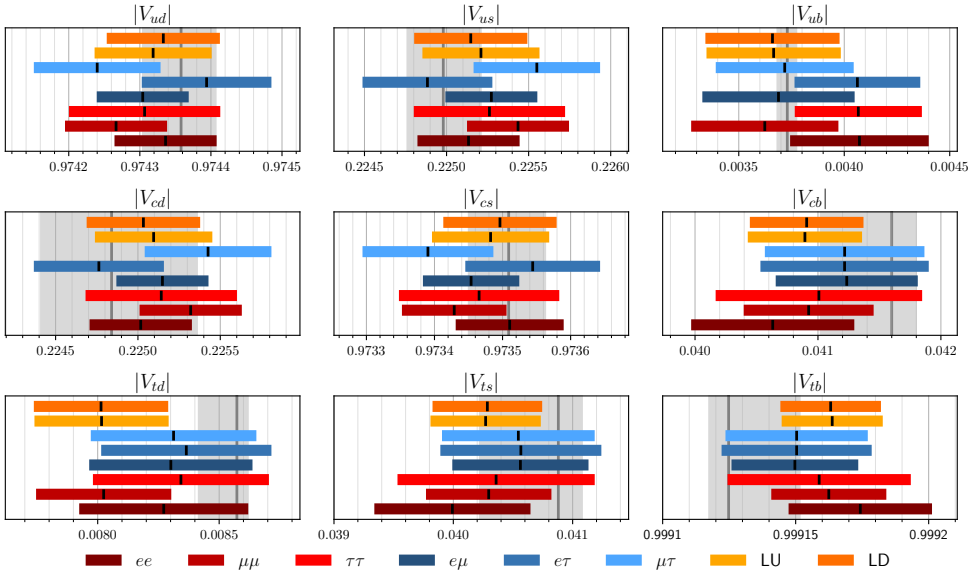

Figure 7.19: 1σ credible intervals of the CKM matrix elements obtained from the posterior distributions of the Wolfenstein parameters. We compare our results to the current CKMfitter averages [395, 396], shown including the 1σ uncertainties in gray.

CKM matrix element V_{td} for the $\mu\mu$, LU and LD scenarios, which are however consistent within 2σ.

The trend we see, for example, in $|V_{cb}|$ towards smaller values is in line with the general trend observed in the literature, where exclusive determinations yield smaller values than inclusive determinations [18, 339]. The comparatively small values for $|V_{td}|$ and $|V_{ts}|$, on the other hand,

are mainly driven by the observables Δm_d and Δm_s, which are sensitive to the CKM matrix elements via the mixing angles in the B_d and B_s systems (see Sec. 6.2.1).

Overall, our uncertainties are larger than the current CKMfitter averages, which is expected given the smaller set of observables in our fit and the additional uncertainties arising from the inclusion of possible BSM contributions via the Wilson coefficients. Nonetheless, the results demonstrate the feasibility of a joint fit of SMEFT and CKM parameters, which is crucial to avoid potential biases arising from the assumption of SM-like CKM parameters in the SMEFT fits. Combined SMEFT and CKM fits were also performed in, e.g., Refs. [182, 188], finding similar results.

7.4. Predictions for Dineutrino Decay Rates

We employ the posterior distributions of the Wilson coefficients obtained from the global fit to derive predictions of the branching fractions of the dineutrino decays $B \to K^{(*)}\nu\bar{\nu}$, $B \to \pi\nu\bar{\nu}$ and $B \to \rho\nu\bar{\nu}$. These decays are particularly interesting given the first measurement and the observed deviation in the branching fraction of the decay $B^+ \to K^+\nu\bar{\nu}$ reported by the Belle II collaboration [372]. They are mediated by $b \to s\nu\bar{\nu}$ and $b \to d\nu\bar{\nu}$ transitions, which are sensitive to potential BSM contributions to FCNC couplings.

We compute the branching ratios based on Eqs. (6.28) and (6.29) for the decay into pseudoscalar and vector mesons, respectively. We show the resulting probability distributions in Fig. 7.20 for the B^0 decays, whereas the posterior distributions of the short-distance contributions to B^+ decays are presented in Appendix F in Fig. 3.

We compare the results using the posterior from our LU fit (blue) to the SM predictions neglecting SMEFT effects (orange), as well as the current experimental bounds (red). We also show the projected sensitivities of the Belle II experiment [397] (dashed purple lines) if available.

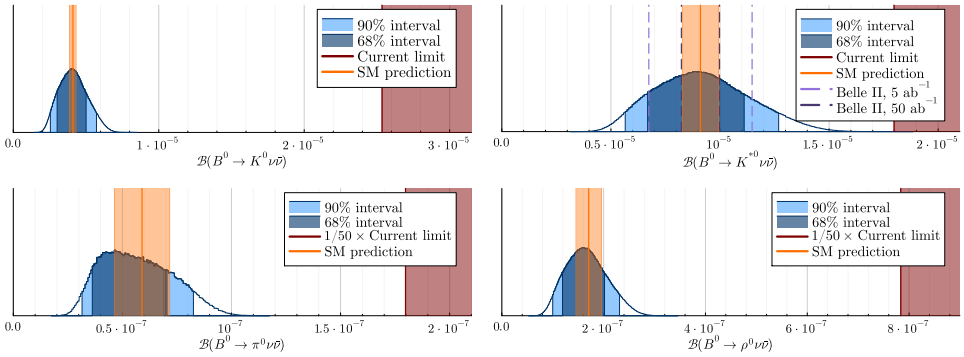

Figure 7.20: Predictions for the dineutrino decays $B^0 \to K^0\nu\bar{\nu}$ (top left), $B^0 \to K^{*0}\nu\bar{\nu}$ (top right), $B^0 \to \pi^0\nu\bar{\nu}$ (bottom left), and $B^0 \to \rho^0\nu\bar{\nu}$ (bottom right) based on the posterior of the LU fit. Colored bands indicate the 68% and 90% credible intervals; the orange band denotes the 1σ SM prediction. Red lines represent current experimental 90% CL bounds, while dashed purple lines show projected sensitivities of the Belle II experiment [397].

For $b \to s$ transitions, our predictions align closely with the SM values. In contrast, the predictions of the branching fractions for $b \to d$ transitions are slightly lower than the SM expectations, reflecting our fit's preference for smaller values of the CKM matrix element $|V_{td}|$. The decays with a $b \to d$ transition are more strongly suppressed in the SM due to the small CKM matrix element V_{td}, so that the experimental bounds are currently orders of magnitude larger than the SM predictions. A signal in these decays would thus be a clear indication of new physics.

In general, the uncertainties of the predictions using our posterior distributions are significantly larger than that of the SM predictions, which is expected given the additional uncertainties arising from the SMEFT contributions. Tabs. 7.1 and 7.2 summarize the predicted short-distance contributions to the branching fractions for $B \to K^{(*)}\nu\bar{\nu}$ and $B \to \pi/\rho\nu\bar{\nu}$, respectively, across different lepton-flavor scenarios. The numbers in parentheses indicate 1σ uncertainties. We see that the predictions are similar across the different flavor scenarios.

Fit	$\mathcal{B}^0 \to K^0\nu\bar{\nu}$	$\mathcal{B}(B^0 \to K^{*0}\nu\bar{\nu})$	$\mathcal{B}(B^+ \to K^{*+}\nu\bar{\nu})$
ee	$4.26(0.94) \times 10^{-6}$	$9.4(2.1) \times 10^{-6}$	$1.02(0.22) \times 10^{-5}$
$\mu\mu$	$4.26(0.86) \times 10^{-6}$	$9.5(1.9) \times 10^{-6}$	$1.02(0.21) \times 10^{-5}$
$\tau\tau$	$4.4(1.0) \times 10^{-6}$	$9.8(2.3) \times 10^{-6}$	$1.06(0.25) \times 10^{-5}$
$e\mu$	$4.32(0.90) \times 10^{-6}$	$9.6(2.0) \times 10^{-6}$	$1.03(0.21) \times 10^{-5}$
$e\tau$	$4.35(0.89) \times 10^{-6}$	$9.7(2.0) \times 10^{-6}$	$1.04(0.21) \times 10^{-5}$
$\mu\tau$	$4.20(0.98) \times 10^{-6}$	$9.3(2.2) \times 10^{-6}$	$1.00(0.23) \times 10^{-5}$
LU	$4.15(0.96) \times 10^{-6}$	$9.2(2.1) \times 10^{-6}$	$9.9(2.3) \times 10^{-6}$
LD	$4.17(0.53) \times 10^{-6}$	$9.3(1.2) \times 10^{-6}$	$1.00(0.13) \times 10^{-5}$

Table 7.1: Predictions for the $B \to K^{(*)}\nu\bar{\nu}$ branching fractions in the various lepton-flavor scenarios. The numbers in parentheses indicate the 1σ uncertainties. For the decay $B^+ \to K^{*+}\nu\bar{\nu}$, there are additional long-distance contributions from $B^+ \to \tau^+(\to K^{*+}\bar{\nu})\nu$ [353, 398], which are not included here.

There are additional long-distance contributions from the decay $B^+ \to \tau^+(\to M^+\bar{\nu})\nu$ for B^+ decays, where M is either a pseudoscalar or vector meson [353, 398], which are not included in Tabs. 7.1 and 7.2. These contributions can in principle also be affected by new physics. In contrast to the short-distance contributions, which are governed by FCNC semileptonic four-fermion operators, the long-distance contributions are captured by the Wilson coefficient $\mathcal{C}^{V,LL}_{\nu edu}$, sensitive to charged-current interactions.

For the decays into pseudoscalar mesons, we can infer predictions for the long-distance contributions from the partial widths of the decays $B^+ \to \tau^+\nu$ and $\tau^+ \to P\bar{\nu}$, using Eqs. (6.19) and (6.13), respectively. Using the posterior of our LU fit, we find

$$\mathcal{B}(B^+ \to K^+\nu\bar{\nu})_{\text{LD}} = 6.2(1.1) \cdot 10^{-7}\,, \tag{7.1}$$

$$\mathcal{B}(B^+ \to \pi^+\nu\bar{\nu})_{\text{LD}} = 9.4(1.6) \cdot 10^{-6}\,. \tag{7.2}$$

Fit	$\mathcal{B}(B^0 \to \pi^0 \nu\bar{\nu})$	$\mathcal{B}(B^+ \to \pi^+ \nu\bar{\nu})$	$\mathcal{B}(B^0 \to \rho^0 \nu\bar{\nu})$	$\mathcal{B}(B^+ \to \rho^+ \nu\bar{\nu})$
ee	$6.2(1.4) \times 10^{-8}$	$1.32(0.29) \times 10^{-7}$	$1.78(0.39) \times 10^{-7}$	$3.83(0.85) \times 10^{-7}$
$\mu\mu$	$5.9(1.2) \times 10^{-8}$	$1.28(0.27) \times 10^{-7}$	$1.71(0.36) \times 10^{-7}$	$3.70(0.77) \times 10^{-7}$
$\tau\tau$	$6.4(1.5) \times 10^{-8}$	$1.37(0.32) \times 10^{-7}$	$1.84(0.44) \times 10^{-7}$	$3.96(0.94) \times 10^{-7}$
$e\mu$	$6.1(1.3) \times 10^{-8}$	$1.32(0.28) \times 10^{-7}$	$1.77(0.38) \times 10^{-7}$	$3.82(0.81) \times 10^{-7}$
$e\tau$	$6.2(1.3) \times 10^{-8}$	$1.34(0.28) \times 10^{-7}$	$1.79(0.37) \times 10^{-7}$	$3.87(0.81) \times 10^{-7}$
$\mu\tau$	$6.0(1.4) \times 10^{-8}$	$1.29(0.30) \times 10^{-7}$	$1.72(0.41) \times 10^{-7}$	$3.72(0.88) \times 10^{-7}$
LU	$5.8(1.4) \times 10^{-8}$	$1.24(0.30) \times 10^{-7}$	$1.67(0.40) \times 10^{-7}$	$3.60(0.86) \times 10^{-7}$
LD	$5.81(0.78) \times 10^{-8}$	$1.24(0.17) \times 10^{-6}$	$1.68(0.23) \times 10^{-7}$	$3.62(0.49) \times 10^{-7}$

Table 7.2: Predictions for the short-distance contributions to the $B \to \pi/\rho\nu\bar{\nu}$ branching fractions in the various lepton-flavor scenarios. The numbers in parentheses indicate the 1σ uncertainties. For the decays of the B^+, there are additional long-distance contributions from $B^+ \to \tau^+(\to M^+\bar{\nu})\nu$ [353, 398], which are not included here.

While the long-distance contributions to the $B^+ \to K^+\nu\bar{\nu}$ amount to about 10% of the total branching fraction, the long-distance contributions to the $B^+ \to \pi^+\nu\bar{\nu}$ are nearly two orders of magnitude larger than the short-distance contributions, thus dominating the total branching fraction.

Testing the MFV Hypothesis

One of the core features of the MFV approach in the SMEFT is the absence of right-handed FCNCs. As a result, the short-distance contributions to dineutrino decays are only sensitive to a single Wilson coefficient, $\mathcal{C}_{\nu d}^{V,LL}$, in the LEFT[1]. Hence, the dependence on the Wilson coefficient cancels in the ratio of the branching fractions, leading to a prediction that is independent of new physics contribution.

Thus, such ratios of branching fractions are fixed to the SM expectation in the MFV hypothesis, which can be tested with future Belle II data. The ratios of the dineutrino branching fractions are only determined by the kinematic factors, form factors, and CKM elements. The kinematic factors can be computed following Eqs. (6.28) and (6.29), while the form factors used in this analysis are listed in Tab. 6 in Appendix E .

To access the ratio of the CKM factors between the $b \to d$ and $b \to s$ transitions, we employ the numerical value $|V_{td}/V_{ts}|^2 = 0.0416(0.0018)$ obtained from the LU fit. We list the resulting predictions for the ratios of the B^0 dineutrino branching fractions in Tab. 7.3.

The ratios of the dineutrino branching fractions of the same transition, either $b \to s$ or $b \to d$, are solely governed by kinematic factors as well as the form factors, which we assumed to be unaffected by new physics. There is, moreover, an additional factor of 1/2 for the decay into a π^0 or ρ^0 meson compared to the decay into Kaons due to isospin. The ratio of a branching

[1] See e.g. Refs [374–376] for a discussion of right-handed currents.

	K^{*0}	K^0	ρ^0	π^0
K^{*0}	1	0.451(38)	0.0181(29)	0.0063(14)
K^0		1	0.0403(58)	0.0139(30)
ρ^0			1	0.346(85)

Table 7.3: Ratios of the dineutrino branching fractions in the MFV hypothesis. Each entry should be read as the ratio of the branching fraction to the column meson to that of the final state with the row meson (i.e., column divided by row). The ratios are fixed to the SM expectation in the MFV hypothesis, which are only determined by kinematic factors, form factors, and CKM factors.

fraction with a $b \to d$ transition to one with a $b \to s$ transition is moreover suppressed by a factor of $|V_{td}/V_{ts}|^2$.

Observing a deviation from these predictions would indicate the presence of new physics beyond the MFV or the SMEFT framework. This could be due to the presence of new right-handed currents, which would induce the Wilson coefficient $\mathcal{C}_{\nu d}^{V,LR}$ and lead to additional contributions to the dineutrino decays that are absent in the MFV hypothesis. Alternatively, it could also indicate the presence of new light degrees of freedom, such as a light dark photon, in which case the SMEFT framework would not be applicable.

Chapter 8

Conclusions and Outlook

In this thesis, we have performed lepton-flavor-specific global fits combining collider and flavor observables in the SMEFT framework. Our analysis systematically explored the synergies between different classes of observables, enabling comprehensive constraints of the 17-dimensional SMEFT parameter space and resolving directions that would otherwise remain unconstrained. In particular, we investigated the flavor structure of the SMEFT by examining the Minimal Flavor Violation approach in the quark sector and assessing the impact of lepton flavor on the global fits.

We have included the largest set of decays in a SMEFT fit to date, covering 163 different lepton and meson decays. The total number of observables is significantly larger, as several decays are measured differentially. We further consider a multitude of collider measurements and additional flavor observables, such as the anomalous magnetic moments of leptons and neutral meson mixing. This extensive dataset allows us to probe a wide range of SMEFT Wilson coefficients across many different flavor combinations, thereby improving the sensitivity to BSM effects.

Most notably, we have found that the combination of different lepton flavors, and thus of distinct observables, can extend the reach on the new physics scale Λ by more than two orders of magnitude relative to single-flavor fits, as illustrated in Fig. 7.7 for $\tilde{C}_{eB}$. This highlights the power of the synergies inherent in global SMEFT fits, which can significantly improve sensitivity to BSM effects. In the lepton-flavor democratic global fit, we were able to test BSM scales of $\Lambda \sim 1000\,\text{TeV}$ for a Wilson coefficient of order $\mathcal{O}(1)$, which is well beyond the direct reach of current collider experiments.

While we found most Wilson coefficients to be consistent with $\tilde{C} = 0$ within the 90% credible intervals, some deviations from the SM were observed. Although they are not statistically significant, with more data and improved uncertainties such hints might someday provide the first indications of new physics in the SMEFT framework. Surprisingly, the largest deviation is found for $\tilde{C}_{eu}$ in the lepton-flavor-universal fit (Tab. 25), despite the absence of such anomalies in the individual lepton-flavor-specific fits. This again highlights the importance of flavor in the SMEFT framework and the potential of global fits to uncover new dynamics.

While this thesis represents a step toward a more comprehensive and consistent search for low-energy imprints of heavy new physics, it also reveals potential for future improvements. Dimension-8 operator contributions, currently omitted from our analysis, could be included in future fits for a more consistent SMEFT expansion and to test BSM models, such as certain composite Higgs models [165], that are not captured by dimension-6 operators. Furthermore, integrating SMEFT fits with PDFs (see e.g. [202, 399, 400]) will be essential, since the impact of future high-energy collider data on the PDF determination is expected to increase. A simultaneous fit of SMEFT coefficients and PDFs will prevent potential new physics effects from being masked by the PDFs, which is particularly important for Drell-Yan production, as it relies heavily on the quark PDFs.

In the coming years, the Belle II experiment promises further progress by delivering extensive new data, particularly on rare decays such as FCNC and lepton-flavor-violating processes [397]. These measurements will sharpen the tests of the SM and might offer further insights into the flavor structure of the SMEFT. In particular, the measurement of dineutrino decay rates will provide new opportunities. Not only will these measurements allow for tests of the MFV hypothesis, but they will also provide lepton-flavor inclusive probes of new dynamics. If the current anomaly in $\mathcal{B}(B \to K\nu\bar{\nu})$ persists, it would provide compelling evidence of BSM physics. In the SMEFT framework, he $SU(2)_L$ symmetry predicts correlated effects in the $b \to s\ell^+\ell^-$ sector, which could be tested in flavor observables as well as in DY production.

At the same time, the high-luminosity phase of the LHC (HL-LHC) and prospective upgrades such as the High-Energy LHC (HE-LHC) are expected to further explore the high-energy frontier, thereby improving the sensitivity to energy-enhanced operators in the SMEFT. The HL-LHC will increase the available data by a factor of 10, while the HE-LHC may double the collision energy to 27 TeV and triple the integrated luminosity. This would boost the sensitivity to the SMEFT coefficients by more than a factor of three compared to current bounds, particularly for the energy-enhanced four-fermion operators [2]. The combination of these improved high-p_T probes with the precision measurements from Belle II offers a promising approach to explore even the most subtle effects of BSM physics and provide guiding directions for future searches.

One of the most significant improvements in SMEFT fits is expected from more precise measurements of the $ttll$ vertex, which is currently only weakly constrained. This could, for example, be realized at a future high-energy lepton collider, which would allow for precise measurements of the $\ell^+\ell^- \to t\bar{t}$ process. Facilities currently under consideration, such as the Future Circular Lepton Collider (FCC-ee) [121–125] or the Compact Linear Collider (CLIC) [128–131], would be particularly well-suited for such measurements. They provide clean collision environments, thus combining the advantages of energy enhancement with high-precision measurements.

The corresponding $t\bar{t}\mu\mu$ vertex, on the other hand, would be best probed at a muon collider, for which the first feasibility studies are currently being conducted [391, 392]. Such a collider would also provide further insights into the recent muon anomalies by testing process such as $\mu\mu \to bs$ [401].

The $tt\ell\ell$ vertex would not only improve the sensitivity to semileptonic four-fermion operators, but also significantly improve the constraints on the leptonic dipole coefficients. The determination of these coefficients is currently limited by the RGE mixing with the scalar and tensor coefficients, which contribute only via the top quark coupling in MFV and are therefore not well constrained by current data. The only direct probe included in this work is $t\bar{t}\ell^+\ell^-$ production, which provides constraints only on the ee and $\mu\mu$ couplings.

Moreover, better determinations of the top-quark couplings would also help to improve the sensitivity to the MFV ratios r_L and r_R, which encode the relative strength of higher-order spurion insertions compared to the leading, flavor-diagonal term in the MFV expansion. These ratios are currently only weakly constrained, in particular for operators with right-handed quark couplings. The reason for this is that the constraints from top-quarks, testing $\tilde{C} \cdot (1 + r_{L/R})$, are significantly weaker than those on the light quark flavors, which predominantly test only $\tilde{C}$.

In addition, a lepton collider would allow for more precise measurements of the Z and W boson decays, which are the main drivers for the constraints on the Higgs-current operators. The $\tilde{C}_{eZ}$ and $\tilde{C}_{eW}$ coefficients would also benefit from such high-precision measurements, thus further improving the bounds on the leptonic dipole coefficients. Moreover, measurements of $\ell\ell \to \ell_i\ell_j$

processes would improve the bounds on the four-lepton coefficients, which are currently among the least constrained coefficients in the single-flavor fits.

Eventually, the most promising avenue for a direct discovery of heavy BSM physics probably remains a high-energy hadron collider. One such potential collider is the FCC-hh [126, 127], intended to operate at energies of up to 1000 TeV. While such a facility remains a long-term prospect, the years leading up to its realization will be crucial for the development of the necessary theoretical tools and the identification of the most promising directions for BSM dynamics. In this quest, EFT methods will play a central role in providing a systematic framework to combine experimental advances with new theoretical insights, thereby guiding the search for new physics.

In conclusion, this thesis demonstrated that global SMEFT fits, combining the energy-enhanced reach of collider observables with the precision of flavor measurements, offer a powerful approach for model-independent BSM searches. Moreover, we find that the fits could be further improved with future data at lepton colliders, such as measurements of $\ell\ell \to t\bar{t}$, $\ell\ell \to \ell_i\ell_j$, and improved determinations of the Z branching fractions. The results presented in this analysis provide a solid foundation for future studies and demonstrate the great potential of the interplay between flavor and high-p_T observables in the SMEFT framework.

Appendix

A Numerical Input Values

In order to compute predictions in the SM or the SMEFT, numerical input values for the parameters of the theory are required. Besides the masses of the particles and the strong coupling constant $\alpha_s(m_Z)$, the electroweak parameters need to be fixed as well. In the SM, the electroweak parameters such as the masses of the W and Z bosons, the Higgs vev, and the electromagnetic coupling constant α_{em} are partially related via the electroweak theory. Thus, only a subset of these parameters is independent and needs to be specified by measurements. Once these parameters are fixed, all other electroweak parameters (e.g. the Fermi constant G_F or the weak mixing angle $\sin^2\theta_W$) can be derived using the relations of the electroweak theory.

Once the SM is extended by dimension-six operators, however, the relationships between a given set of input measurements and the underlying parameters of the Lagrangian can be shifted [137, 175, 177–181]. The measured quantities receive a SMEFT correction due to the potential presence of new physics, which can be parameterized by the Wilson coefficients of the dimension-six operators. As an example, we consider the Fermi constant G_F, for which we can generally denote the relation between the measured value and the underlying parameters as

$$G_F^{\text{meas}} = G_F^{\text{SM}} + \delta G_F \,, \tag{A .1}$$

where G_F^{SM} is the value of the Fermi constant in the SM Lagrangian, G_F^{meas} is the experimental value and δG_F is a shift depending on the Wilson coefficients of the dimension-six operators. In the Warsaw basis, this shift is given by [137, 177]

$$\delta G_F = \frac{1}{v^2 G_F^{\text{meas}}} \left(\frac{\tilde{C}_{ll} + \tilde{C}'_{ll}}{4} - \tilde{C}^{(3)}_{\varphi l} \right) , \tag{A .2}$$

where $\tilde{C}_{ll}$ and $\tilde{C}'_{ll}$ denote the different flavor structures of the dimension-six operator O_{ll}.

This shift in the Fermi constant leads to a changes in the related electroweak parameters. For example, we can express the shifts in vev, the gauge couplings g and g' and the weak mixing angle $\sin^2\theta_W$ in terms of the shift in the Fermi constant as [137]

$$\begin{aligned}
\delta v^2 &= \frac{\delta G_F}{G_F^{\text{meas}}} \,, \\
\delta g^{'} &= \frac{g^{'\text{meas}}}{\sqrt{2}\cos(2\theta_W^{\text{meas}})} \sin^2(\theta_W^{\text{meas}}) \delta G_F \,, \\
\delta g &= \frac{g^{\text{meas}}}{\sqrt{2}\cos(2\theta_W^{\text{meas}})} \sin^2(\theta_W^{\text{meas}}) \delta G_F \,, \\
\delta \sin^2\theta_W &= 2\cos^2(\theta_W^{\text{meas}}) \sin^2(\theta_W^{\text{meas}}) \left(\frac{\delta g^{'}}{g^{'\text{meas}}} - \frac{\delta g}{g^{\text{meas}}} \right) ,
\end{aligned} \tag{A .3}$$

where g and g' are the gauge couplings of the $SU(2)_L$ and $U(1)_Y$ gauge groups, respectively. Similar relations arise for other electroweak input values, such as the masses of the W and Z bosons, and the electromagnetic coupling constant α_{em}.

As a result, different choices of input parameters, also known as input schemes, can lead to different combinations of Wilson coefficient entering a given observable. Although the physical predictions must remain independent of the input scheme, the intermediate mapping from the input parameters to the Wilson coefficients can vary.

In this work, we adopt the $\{\alpha_{\text{em}}, m_W, m_Z\}$ input scheme. In this scheme, the input parameters are only affected by purely bosonic dimension-six operators, which we neglect in our analysis. Thus, the input parameters are not shifted by the presence of new physics, which significantly simplifies the computations. Moreover, since the Fermi constant G_F is not employed as an input parameter, the lepton decays $\ell \to \ell' \nu \bar{\nu}$ do not contribute to our defining relations. Consequently, the associated branching fractions are not fixed by the input scheme and can be treated as free parameters in the fit.

The numerical values used throughout this work are listed in Tab. 1.

Parameter	Value	Parameter	Value
m_W	80.369(13) GeV [18]	m_Z	91.1880(20) GeV [18]
m_h	125.250(11) GeV [18]	m_e	510.99895000(15) keV [18]
m_μ	105.6583755(23) MeV	m_τ	1.77693(9) GeV [18]
m_u	2.16(7) MeV [18]	m_d	4.70(7) MeV [18]
m_c	1.2730(46) GeV [18]	m_s	93.5(8) MeV [18]
m_t	72.57(29) GeV [18]	m_b	4.183(7) GeV [18]
α_{em}	0.0072973525693(11) [18]	$\alpha_s(m_Z)$	0.11830(70) [339]

Table 1: Numerical input parameters extracted from experiment and lattice computations used throughout this work.

B Simplified Fit of the CKM Matrix

In order to obtain fixed values for the CKM matrix elements to use in the MFV parameterization, we follow Ref. [182] and perform a fit of the Wolfenstein parameterization (2.16) using the measurements of $\Gamma(K \to \mu\nu_\mu)/\Gamma(\pi \to \mu\nu_\mu)$, $\Gamma(B \to \tau\nu_\tau)$, ΔM_d, ΔM_s listed in Tab. 2. The computation of these observables is outlined in Sec. 6.2.2 for the leptonic meson decays and in Sec. 6.2.1 the mass differences in the B_d and B_s systems.

Observable	Measurement
$\mathcal{B}\,(B^+ \to \tau^+\bar{\nu}_\tau)$	$1.09(24) \cdot 10^{-4}$ [18]
$\Gamma(K^+ \to \mu^+\nu_\mu)/\Gamma(\pi^+ \to \mu^+\nu_\mu)$	$1.3367(32)$ [18]
ΔM_d	$0.5069(19) \cdot 10^{12}\,\hbar\text{s}^{-1}$ [18]
ΔM_s	$17.765(5) \cdot 10^{12}\,\hbar\text{s}^{-1}$ [18]

Table 2: Input values for the CKM matrix fit.

In contrast to the global fit, we neglect possible SMEFT contributions and perform a fit using only the four Wolfenstein parameters λ, A, ρ, η as degrees of freedom. Employing the Bayesian framework outlined in Sec. 4.2, we get $\{\hat{\lambda}, \hat{A}, \hat{\rho}, \hat{\eta}\} = \{0.22532(47), 0.804(17), 0.184(32), 0.388(52)\}$, corresponding to

$$|V_{\text{CKM}}| = \begin{pmatrix} 0.97429(11) & 0.22532(47) & 0.00405(49) \\ 0.22520(47) & 0.97346(11) & 0.04081(85) \\ 0.00832(21) & 0.04016(87) & 0.999167(35) \end{pmatrix}, \tag{B .4}$$

in agreement with the values obtained in Ref. [182] as well as with the current values of the CKMfitter group [395, 396]. The uncertainties are larger than the current CKMfitter averages, which is expected given the smaller set of observables in the fit.

C Matching the SMEFT onto the LEFT

We match the SMEFT onto the LEFT at tree-level at the scale $\mu = m_W$ following [132]. The matching for the dipole operators is given by

$$\mathcal{C}_{\substack{e\gamma \\ ij}} = \frac{1}{\sqrt{2}v}\left(-\sin\theta_W \tilde{C}_{\substack{eW \\ ij}} + \cos\theta_W \tilde{C}_{\substack{eB \\ ij}}\right). \tag{C .5}$$

The four lepton operators receive matching contributions from the four lepton SMEFT operators as well as from the Higgs-current operators. The matching conditions are given by

$$\begin{aligned}\mathcal{C}^{V,LL}_{\substack{ee \\ ijkl}} = \frac{1}{v^2}\Bigg(&\tilde{C}_{\substack{ll \\ ijkl}} - \frac{1}{4}\Bigg(\left(\delta_{ij}(2\mathrm{s}_\theta^2-1) - \tilde{C}^+_{\substack{\varphi l \\ ij}}\right)\left(\delta_{kl}(2\mathrm{s}_\theta^2-1) - \tilde{C}^+_{\substack{\varphi l \\ kl}}\right) \\ &+ \left(\delta_{il}(2\mathrm{s}_\theta^2-1) - \tilde{C}^+_{\substack{\varphi l \\ il}}\right)\left(\delta_{kj}(2\mathrm{s}_\theta^2-1) - \tilde{C}^+_{\substack{\varphi l \\ kj}}\right)\Bigg)\Bigg),\end{aligned} \tag{C .6}$$

$$\begin{aligned}\mathcal{C}^{V,LL}_{\substack{\nu e \\ ijkl}} = \frac{1}{v^2}\Bigg(&\left(\tilde{C}_{\substack{ll \\ ijkl}} + \tilde{C}_{\substack{ll \\ klij}}\right) - \Bigg(\left(\delta_{ij} - \tilde{C}^-_{\substack{\varphi l \\ ij}}\right)\left(\delta_{kl}(2\mathrm{s}_\theta^2-1) - \tilde{C}^+_{\substack{\varphi l \\ kl}}\right) \\ &- 2\left(\delta_{il} + \tilde{C}^{(3)}_{\substack{\varphi l \\ il}}\right)\left(\delta_{kj} + \tilde{C}^{(3)}_{\substack{\varphi l \\ kj}}\right)\Bigg)\Bigg),\end{aligned} \tag{C .7}$$

$$\mathcal{C}^{V,LR}_{\substack{ee \\ ijkl}} = \frac{1}{v^2}\left(\tilde{C}_{\substack{le \\ ijkl}} - \left(\left(\delta_{ij}(2\mathrm{s}_\theta^2-1) - \tilde{C}^+_{\substack{\varphi l \\ ij}}\right)\left(\delta_{kl}2\mathrm{s}_\theta^2 - \tilde{C}_{\substack{\varphi e \\ kl}}\right)\right)\right), \tag{C .8}$$

$$\mathcal{C}^{V,LR}_{\substack{\nu e \\ ijkl}} = \frac{1}{v^2}\left(\tilde{C}_{\substack{le \\ ijkl}} - \left(\left(\delta_{ij} - \tilde{C}^-_{\substack{\varphi l \\ ij}}\right)\left(\delta_{kl}2\mathrm{s}_\theta^2 - \tilde{C}_{\substack{\varphi e \\ kl}}\right)\right)\right), \tag{C .9}$$

$$\begin{aligned}\mathcal{C}^{V,RR}_{\substack{ee \\ ijkl}} = \frac{1}{v^2}\Bigg(&\tilde{C}_{\substack{ee \\ ijkl}} - \frac{1}{4}\Bigg(\left(\delta_{ij}2\mathrm{s}_\theta^2 - \tilde{C}_{\substack{\varphi e \\ ij}}\right)\left(\delta_{kl}2\mathrm{s}_\theta^2 - \tilde{C}_{\substack{\varphi e \\ kl}}\right) \\ &+ \left(\delta_{il}2\mathrm{s}_\theta^2 - \tilde{C}_{\substack{\varphi e \\ il}}\right)\left(\delta_{kj}2\mathrm{s}_\theta^2 - \tilde{C}_{\substack{\varphi e \\ kj}}\right)\Bigg)\Bigg),\end{aligned} \tag{C .10}$$

(C .11)

The matching conditions for the semileptonic four fermion operators are given by

$$\mathcal{C}^{V,LL}_{\substack{eu\\ijkl}} = \frac{1}{v^2}\left(\tilde{C}^{-}_{\substack{lq\\ijkl}} - \left(\left(\delta_{ij}(2\mathrm{s}_\theta^2-1) - \tilde{C}^{+}_{\substack{\varphi l\\ij}}\right)\left(\delta_{kl}(1-\frac{4}{3}\mathrm{s}_\theta^2) - \tilde{C}^{-}_{\substack{\varphi q\\ij}}\right)\right)\right), \tag{C .12}$$

$$\mathcal{C}^{V,LL}_{\substack{ed\\ijkl}} = \frac{1}{v^2}\left(\tilde{C}^{+}_{\substack{lq\\ijkl}} - \left(\left(\delta_{ij}(2\mathrm{s}_\theta^2-1) - \tilde{C}^{+}_{\substack{\varphi l\\ij}}\right)\left(\delta_{kl}(-1+\frac{2}{3}\mathrm{s}_\theta^2) - \tilde{C}^{+}_{\substack{\varphi q\\ij}}\right)\right)\right), \tag{C .13}$$

$$\mathcal{C}^{V,LL}_{\substack{\nu u\\ijkl}} = \frac{1}{v^2}\left(\tilde{C}^{+}_{\substack{lq\\ijkl}} - \left(\left(\delta_{ij} - \tilde{C}^{-}_{\substack{\varphi l\\ij}}\right)\left(\delta_{kl}(1-\frac{4}{3}\mathrm{s}_\theta^2) - \tilde{C}^{-}_{\substack{\varphi q\\ij}}\right)\right)\right), \tag{C .14}$$

$$\mathcal{C}^{V,LL}_{\substack{\nu d\\ijkl}} = \frac{1}{v^2}\left(\tilde{C}^{-}_{\substack{lq\\ijkl}} - \left(\left(\delta_{ij} - \tilde{C}^{-}_{\substack{\varphi l\\ij}}\right)\left(\delta_{kl}(-1+\frac{2}{3}\mathrm{s}_\theta^2) - \tilde{C}^{+}_{\substack{\varphi q\\ij}}\right)\right)\right), \tag{C .15}$$

$$\mathcal{C}^{V,LL}_{\substack{\nu edu\\ijkl}} + \text{h.c.} = \frac{2}{v^2}\left(\tilde{C}^{(3)}_{\substack{lq\\ijkl}} - \left(\left(\delta_{ij} + \tilde{C}^{(3)}_{\substack{\varphi l\\ij}}\right)\left(V_{lk} + \tilde{C}^{(3)}_{\substack{\varphi q\\ij}}\right)\right)\right), \tag{C .16}$$

$$\mathcal{C}^{V,RR}_{\substack{eu\\ijkl}} = \frac{1}{v^2}\left(\tilde{C}_{\substack{eu\\ijkl}} - \left(\left(\delta_{ij}2\mathrm{s}_\theta^2 - \tilde{C}_{\substack{\varphi e\\ij}}\right)\left(-\delta_{kl}\frac{4}{3}\mathrm{s}_\theta^2 - \tilde{C}_{\substack{\varphi u\\ij}}\right)\right)\right), \tag{C .17}$$

$$\mathcal{C}^{V,RR}_{\substack{ed\\ijkl}} = \frac{1}{v^2}\left(\tilde{C}_{\substack{ed\\ijkl}} - \left(\left(\delta_{ij}2\mathrm{s}_\theta^2 - \tilde{C}_{\substack{\varphi e\\ij}}\right)\left(\delta_{kl}\frac{2}{3}\mathrm{s}_\theta^2 - \tilde{C}_{\substack{\varphi d\\ij}}\right)\right)\right), \tag{C .18}$$

$$\mathcal{C}^{V,LR}_{\substack{eu\\ijkl}} = \frac{1}{v^2}\left(\tilde{C}_{\substack{lu\\ijkl}} - \left(\left(\delta_{ij}(2\mathrm{s}_\theta^2-1) - \tilde{C}^{+}_{\substack{\varphi l\\ij}}\right)\left(-\delta_{kl}\frac{4}{3}\mathrm{s}_\theta^2 - \tilde{C}_{\substack{\varphi u\\ij}}\right)\right)\right), \tag{C .19}$$

$$\mathcal{C}^{V,LR}_{\substack{ed\\ijkl}} = \frac{1}{v^2}\left(\tilde{C}_{\substack{ld\\ijkl}} - \left(\left(\delta_{ij}(2\mathrm{s}_\theta^2-1) - \tilde{C}^{+}_{\substack{\varphi l\\ij}}\right)\left(\delta_{kl}\frac{2}{3}\mathrm{s}_\theta^2 - \tilde{C}_{\substack{\varphi d\\ij}}\right)\right)\right), \tag{C .20}$$

$$\mathcal{C}^{V,LR}_{\substack{ue\\ijkl}} = \frac{1}{v^2}\left(\tilde{C}_{\substack{qe\\ijkl}} - \left(\left(\delta_{ij}(1-\frac{4}{3}\mathrm{s}_\theta^2 - \tilde{C}^{-}_{\substack{\varphi q\\ij}})\right)\left(\delta_{kl}2\mathrm{s}_\theta^2 - \tilde{C}_{\substack{\varphi e\\kl}}\right)\right)\right), \tag{C .21}$$

$$\mathcal{C}^{V,LR}_{\substack{de\\ijkl}} = \frac{1}{v^2}\left(\tilde{C}_{\substack{qe\\ijkl}} - \left(\left(\delta_{ij}(-1+\frac{2}{3}\mathrm{s}_\theta^2 - \tilde{C}^{+}_{\substack{\varphi q\\ij}})\right)\left(\delta_{kl}2\mathrm{s}_\theta^2 - \tilde{C}_{\substack{\varphi e\\kl}}\right)\right)\right). \tag{C .22}$$

$$\mathcal{C}^{V,LR}_{\substack{\nu u\\ijkl}} = \frac{1}{v^2}\left(\tilde{C}_{\substack{lu\\ijkl}} - \left(\left(\delta_{ij} - \tilde{C}^{-}_{\substack{\varphi l\\ij}}\right)\left(-\delta_{kl}\frac{4}{3}\mathrm{s}_\theta^2 - \tilde{C}_{\substack{\varphi u\\ij}}\right)\right)\right), \tag{C .23}$$

$$\mathcal{C}^{V,LR}_{\substack{\nu d\\ijkl}} = \frac{1}{v^2}\left(\tilde{C}_{\substack{ld\\ijkl}} - \left(\left(\delta_{ij} - \tilde{C}^{-}_{\substack{\varphi l\\ij}}\right)\left(\delta_{kl}\frac{2}{3}\mathrm{s}_\theta^2 - \tilde{C}_{\substack{\varphi d\\ij}}\right)\right)\right). \tag{C .24}$$

(C .25)

The matching conditions for the four-quark operators are given by

$$\mathcal{C}^{V,LL}_{\substack{dd\\ijkl}} = \frac{1}{2v^2}\left(\tilde{C}^{+}_{\substack{\varphi q\\ij}}\tilde{C}^{+}_{\substack{\varphi q\\kl}}\right). \tag{C .26}$$

(C .27)

D Expansion of Ratios in the SMEFT

Many observables, e.g. branching fractions and asymmetries, are given as ratios where not only the numerator but also the denominator can be affected by new physics contributions. In order to keep a consistent expansion in $\tilde{C}$, we expand these ratios up to the second order in the Wilson coefficients. As an example, we consider the branching ratio $\mathcal{B}_i$, which is defined as

$$\mathcal{B}_i = \frac{\Gamma_i}{\Gamma_{\text{total}}}\,, \tag{D .28}$$

in terms of the partial decay width Γ_i and the total decay width $\Gamma_{\text{total}} = \sum_j \Gamma_j$. Both, the partial and the total decay width can be affected by NP contributions. We can write the partial decay width Γ_i as a sum of the SM contribution $\Gamma_{i,\text{SM}}$ and the new physics contributions proportional to the Wilson coefficients $\tilde{C}_n$ as

$$\Gamma_i = \Gamma_{i,\text{SM}} + \sum_n a_n^i \tilde{C}_n + \sum_{n,m} b_{nm}^i \tilde{C}_n \tilde{C}_m\,, \tag{D .29}$$

and the total decay width similarly as

$$\Gamma_{\text{total}} = \sum_j \Gamma_j = \Gamma_{\text{SM}} + \sum_{j,n} a_n^j \tilde{C}_n + \sum_{j,n,m} b_{nm}^j \tilde{C}_n \tilde{C}_m\,. \tag{D .30}$$

with

$$\Gamma_{\text{SM}} = \sum_j \Gamma_{j,\text{SM}}\,. \tag{D .31}$$

We can then expand the branching ratio to second order in $\tilde{C}$ as

$$\begin{aligned}\mathcal{B}_i =& \frac{\Gamma_{i,\text{SM}}}{\Gamma_{\text{SM}}} + \sum_n \tilde{C}_n \left(\frac{a_n^i}{\Gamma_{\text{SM}}} - \frac{\Gamma_{i,\text{SM}} \sum_j a_n^j}{\Gamma_{\text{SM}}^2} \right) \\ &+ \sum_{n,m} \tilde{C}_n \tilde{C}_m \left(\frac{b_{nm}^i}{\Gamma_{\text{SM}}} - \frac{a_n^i \sum_j a_m^j + a_m^i \sum_j a_n^j}{\Gamma_{\text{SM}}^2} + \frac{\Gamma_{i,\text{SM}} \left(\sum_j a_n^j\right) \left(\sum_k a_m^k\right)}{\Gamma_{\text{SM}}^3} - \frac{\Gamma_{i,\text{SM}} \sum_j b_{nm}^j}{\Gamma_{\text{SM}}^2} \right)\,.\end{aligned} \tag{D .32}$$

In the case of a vanishing SM contribution $\Gamma_i^{\text{SM}} = 0$, the interference terms a^i vanish as well and the branching ratio is given by

$$\mathcal{B}_i = \sum_{n,m} \frac{b_{nm}^i}{\Gamma^{\text{SM}}} \tilde{C}_n \tilde{C}_m + \mathcal{O}(\tilde{C}^3)\,. \tag{D .33}$$

The same holds for other ratios of observables, such as asymmetry parameters or ratios of decay widths as well.

E Meson Decays in the LEFT

Tab. 3 summarizes the numerical values of the meson masses used throughout this work.

Meson	Mass [GeV]	Meson	Mass [GeV]
π^0	0.1349768(5) [18]	π^+	0.13957039(18) [18]
η	0.547862(17) [18]	η'	0.95778(6) [18]
ρ	0.77526(23) [18]	ρ^+	0.77511(34) [18]
ω	0.78266(13) [18]	ϕ	1.019461(16) [18]
K^0	0.497611(13) [18]	K^+	0.493677(15) [18]
K^{*0}	0.89555(20) [18]	K^{*+}	0.89167(26) [18]
D^0	1.86484(5) [18]	D^+	1.86966(5) [18]
D_s	1.96835(7) [18]	J/Ψ	3.096900(6) [18]
D^{*0}	2.00685(5) [18]	D^{*+}	2.01026(5) [18]
D_s^*	2.1122(4) [18]	$\Upsilon(1S)$	9.46040(10) [18]
B^0	5.27972(8) [18]	B^+	5.27941(7) [18]
B_s	5.36693(10) [18]	B_s^*	5.4154(14) [18]
B^*	5.32475(20) [18]		

Table 3: Numerical input values of the meson masses used in this analysis. The masses are taken from the Particle Data Group [18].

Meson mixing

Tab. 4 lists the numerical values of the input parameters used for the computation of the mass differences in the $B_{d,s}$ systems.

Parameter	Value
$f_{B_d}^2 \hat{B}_{B_d}$	0.2106(55) GeV[402]
$f_{B_s}^2 \hat{B}_{B_s}$	0.2561(57) GeV[402]
η_{2B}	0.5500(75) [403]

Table 4: Numerical values of the input parameters used for the computation of the mass differences in the $B_{d,s}$ systems.

Decay constants

In the study of leptonic and semileptonic decays of mesons, the non-perturbative effects are commonly parameterized in terms of decay constants f_M. The decay constant of a pseudoscalar meson P (e.g. π, K, B) is defined by the matrix element of the axial-vector current between the vacuum state and the meson state

$$\langle 0|\bar{q}_1\gamma^\mu q_2|P(p)\rangle = i f_P\, p^\mu\,, \tag{E .34}$$

where p is the four-momentum of the meson and q_1 and q_2 are the contributing quark fields. It is a non-perturbative quantity that can be computed using lattice QCD or other non-perturbative methods.

Similarly, for a vector meson V (e.g. ρ, K^*, Υ), the vector decay constant f_V is defined by

$$\langle 0|\bar{q}_1\gamma^\mu q_2|V(p,\varepsilon)\rangle = -i f_V\, m_V\, \varepsilon^\mu\,, \tag{E .35}$$

where m_V is the mass of the vector meson and ε^μ is its polarization vector. The broader decay width that is typically associated with vector mesons makes Lattice QCD calculations more challenging, so that the decay constants are often extracted from light-cone sum rules calculations.

Tab. 5 list the numerical values of the decay constants used in this analysis.

f_M	Value [MeV]	f_M	Value [MeV]
f_π	130.2(0.8) [339]	f_η^q	108(3) [404]
f_η^s	-111(6) [404]	$f_{\eta'}^q$	89(3) [404]
$f_{\eta'}^s$	136(6) [404]	$f_{\rho/\omega}$	199(4) [405]
f_ϕ	241(9) [406]	f_K	155.7(0.3) [339]
f_{K^*}	241 [407]	$f_{J/\Psi}$	418(9) [408]
f_D	210.4(1.5) [339]	f_{D_s}	247.7(1.2) [339]
f_Υ	649(31) [409]	f_B	190.0(1.3) [339]
f_{B_s}	230.3(1.3) [339]		

Table 5: Decay constants of the mesons used in this analysis.

Form Factors

In semileptonic decays of heavy mesons, the hadronic matrix elements are no longer simple constants but functions of the momentum transfer q^2 between the initial and final states. These

dependencies are encapsulated in form factors, defined as

$$\langle P'(k)|\bar{q}_1\gamma^\mu q_2|P(p)\rangle = f_+(q^2)\left((p+k)^\mu - \frac{m_P^2 - m_{P'}^2}{q^2}q^\mu\right) + f_0(q^2)\frac{m_P^2 - m_{P'}^2}{q^2}q^\mu\,, \quad \text{(E .36)}$$

$$\langle P'(k)|\bar{q}_1\sigma^{\mu\nu}q_\nu q_2|P(p)\rangle = i\frac{f_T(q^2)}{m_P + m_{P'}}\left(q^2(p+k)^\mu - (m_P^2 - m_{P'}^2)q^\mu\right)\,, \quad \text{(E .37)}$$

for a decay into a pseudoscalar meson P', where p and k are the four-momenta of the initial and final mesons, respectively, and $q = p - k$ is the momentum transfer.

For decays into vector mesons, the matrix element is more complicated due to the presence of the polarization vector ε of the vector meson. The matrix elements can be expressed as

$$\langle V(k,\varepsilon)|\bar{q}_1\gamma^\mu q_2|P(p)\rangle = \epsilon^{\mu\nu\rho\sigma}\varepsilon_\nu^* p_\rho k_\sigma \frac{2V(q^2)}{m_P + m_V}\,, \quad \text{(E .38)}$$

$$\langle V(k,\varepsilon)|\bar{q}_1\gamma^\mu\gamma_5 q_2|P(p)\rangle = i\varepsilon_\nu^*\Big(A_1(q^2)g^{\mu\nu}(m_P + m_V) - A_2(q^2)\frac{(p+k)^\mu q^\nu}{m_P + m_V} - (A_3(q^2) - A_0(q^2))q^\mu q^\nu\frac{2m_V}{q^2}\Big)\,, \quad \text{(E .39)}$$

$$\langle V(k,\varepsilon)|\bar{q}_1\sigma^{\mu\nu}q_\nu q_2|P(p)\rangle = \epsilon^{\mu\nu\rho\sigma}\varepsilon_\nu^* p_\rho k_\sigma 2T_1(q^2)\,, \quad \text{(E .40)}$$

$$\langle V(k,\varepsilon)|\bar{q}_1\sigma^{\mu\nu}q_\nu\gamma_5 q_2|P(p)\rangle = i\varepsilon_\nu^*\Big(T_2(q^2)\left(g^{\mu\nu}(m_P^2 - m_V^2) - (p+k)^\mu q^\nu\right) + T_3(q^2)q^\nu\left(q^\mu - \frac{q^2(p+k)^\mu}{(m_P^2 - m_V^2)}\right)\Big)\,, \quad \text{(E .41)}$$

where $V(q^2)$, $A_1(q^2)$, $A_2(q^2)$, $A_3(q^2)$, $A_0(q^2)$, $T_1(q^2)$, $T_2(q^2)$ and $T_3(q^2)$ denote the form factors depending on the momentum transfer q^2.

To determine the form factors, non-perturbative methods, such as lattice QCD valid at high q^2 or light-cone sum rules describing the low q^2 region are employed to calculate discrete values at specific q^2. The form factors are then interpolated to the full kinematic range of the decay process using suitable parameterizations. Most parameterizations are based on the z expansion, which maps the q^2 plane onto the unit circle using

$$z(q^2;t_0) = \frac{\sqrt{t_+ - q^2} - \sqrt{t_+ - t_0}}{\sqrt{t_+ - q^2} + \sqrt{t_+ - t_0}}\,, \quad \text{(E .42)}$$

where $t_+ = (m_P + m_{P'/V})^2$ and t_0 is a reference point chosen to minimize $|z(q^2)|$ across the physical region. The form factors are then expressed as a series expansion in $z(q^2)$, for which different parameterizations exist.

The most common approaches are the Boyd–Grinstein–Lebed (BGL) parameterization [410]

$$F(q^2) = \frac{1}{P(q^2)\phi(q^2)}\sum_{n=0}^{N} a_n z^n(q^2)\,, \quad \text{(E .43)}$$

with the Blaschke factor

$$P(q^2) = \frac{z(q^2) - z(m_{P^*}^2)}{1 - z(q^2)z(m_{P^*}^2)}\,, \tag{E .44}$$

accounting for sub-threshold poles at $q^2 = m_{P^*}^2$ and the outer function $\phi(q^2)$ encoding the known branch-cut behavior and phase-space factors. The expansion is typically truncated at $N = 3$ or $N = 4$. The expansion coefficients a_n are determined from a fit to the lattice QCD and light-cone sum rules data, with the unitarity constraint

$$\sum_{n=0}^{\infty} a_n \geq 1\,. \tag{E .45}$$

Another frequently used parameterization is the Bourrely–Caprini–Lellouch (BCL) parameterization [337]

$$f_+(q^2) = \frac{1}{1 - q^2/m_{P^*}} \sum_{n=0}^{N-1} b_n \left[z(q^2)^n - (-1)^{n-N} \frac{n}{N} z(q^2)^N \right]\,, \tag{E .46}$$

$$f_0(q^2) = \sum_{n=0}^{N} b_n^0 z(q^2)^n\,, \tag{E .47}$$

where the subtraction term in $f_+(q^2)$ enforces the correct behavior in the limit $q^2 \to t_+$.

A common parameterization for the vector-meson form factors is given by the Bharucha–Straub–Zwicky (BSZ) expansion [338]

$$F(q^2) = \frac{1}{P(q^2)\phi(q^2)} \sum_{n=0}^{N} a_n z^n(q^2)\,, \tag{E .48}$$

following the same analytic structure as the BGL parameterization but computing $\phi(q^2)$ perturbatively. In all three schemes, the combination of analyticity, unitarity and controlled truncation yields a systematically improvable, model-independent description of the form factors across the entire physical q^2 range.

Tab. 6 lists the form factors we use for the SM and LEFT predictions in our analysis. To avoid possible BSM contaminations, we rely purely on Lattice QCD calculations as well as light-cone sum rule results.

Chiral coefficients

We give the definition of the flavor factors and summarize the relevant form factors for the effective chiral coefficients defined in Eqs. (6.8) and (6.10) for the pseudoscalar and vector mesons, respectively. The numerical values of the decay constants f_P and f_V are listed in Tab. 5.

Decay	Reference	Framework	Parameterization
$D \to \pi$	[411]	LQCD	BCL (N=4)
$D \to \eta$	[342]	LCSR	single pole
$D \to \eta'$	[412]	LQCD	single pole
$D \to K$	[339]	LQCD	BCL (N=4)
$B \to \pi$	[339]	LQCD	BCL (N=3)
$B \to K$	[1]	LQCD	BSZ (N=3)
$B \to D$	[339]	LQCD	BCL (N=3)
$B_s \to K$	[339]	LQCD	BCL (N=4)
$B_s \to D_s$	[413]	LQCD	BCL (N=2)
$D \to \rho$	[342]	LCSR	two-parameter pole
$D \to \omega$	[342]	LCSR	two-parameter pole
$D \to K^*$	[342]	LCSR	two-parameter pole
$D_s \to \phi$	[342]	LCSR	two-parameter pole
$D_s \to K^*$	[342]	LCSR	two-parameter pole
$B \to \rho$	[338]	LCSR	BSZ (N=3)
$B \to K^*$	[338]	LCSR	BSZ (N=3)
$B \to D^*$	[414]	LQCD & LCSR	BSZ (N=3)
$B_s \to \phi$	[338]	LCSR	BSZ (N=3)
$B_s \to K^*$	[338]	LCSR	BSZ (N=3)
$B_s \to D_s^*$	[339]	LQCD	BGL (N=3)

Table 6: Form factors used for the semileptonic decays of mesons. The upper part of the table lists the form factors for the decays into pseudoscalar mesons, while the lower part lists the form factors for the decays into vector mesons. The framework used for the calculation is indicated in the third column, while the parameterization used for the form factors is listed in the last column. LQCD stands for Lattice QCD, LCSR for light-cone sum rules, BGL refers to the Boyd–Grinstein–Lebed parameterization [410], BCL to the Bourrely–Caprini–Lellouch parameterization [337] and BSZ to the Bharucha–Straub–Zwicky expansion [338].

P	km	$\kappa_{km}^{P,u}$	$\kappa_{km}^{P,d}$
π^0	11	$f_\pi/\sqrt{2}$	$-f_\pi/\sqrt{2}$
η	11	$f_\eta^q/\sqrt{2}$	$f_\eta^q/\sqrt{2}$
η	22	0	f_η^s
η'	11	$f_{\eta'}^q/\sqrt{2}$	$f_{\eta'}^q/\sqrt{2}$
η'	22	0	$f_{\eta'}^s$
K_L	12	0	f_K
D_0	12	f_D	0
B_0	13	0	f_B
B_s	23	0	f_{B_s}

Table 7: Flavor factors for the pseudoscalar mesons P. The flavor factors are defined in terms of the decay constants f_P and the quark content of the mesons. The indices km refer to the quark content of the meson.

V	km	$\kappa_{km}^{V,u}$	$\kappa_{km}^{V,d}$
ρ	11	$f_\rho/\sqrt{2}$	$-f_\rho/\sqrt{2}$
ω	11	$f_\omega/\sqrt{2}$	$f_\omega/\sqrt{2}$
K^*	21	0	f_{K^*}
$\bar{K}^*$	12	0	f_{K^*}
ϕ	22	0	f_ϕ
J/Ψ	22	$f_{J/\Psi}$	0
Υ	33	0	f_Υ

Table 8: Flavor factors for the vector mesons V. The flavor factors are defined in terms of the decay constants f_V and the quark content of the mesons. The indices km refer to the quark content of the meson.

Decay	Γ_{exp} [GeV]	Γ_{SM} [GeV]
$D^0 \to K^+ e\nu$	$5.69(0.04) \cdot 10^{-14}$ [18]	$5.67(0.08) \cdot 10^{-14}$
$D^0 \to K^+ \mu\nu$	$5.47(0.07) \cdot 10^{-14}$ [18]	$5.54(0.07) \cdot 10^{-14}$
$D^0 \to \pi^+ e\nu$	$4.67(0.07) \cdot 10^{-15}$ [18]	$4.55(0.07) \cdot 10^{-15}$
$D^0 \to \pi^+ \mu\nu$	$4.28(0.19) \cdot 10^{-15}$ [18]	$4.49(0.07) \cdot 10^{-15}$
$D^+ \to \bar{K}^0 e\nu$	$5.56(0.06) \cdot 10^{-14}$ [18]	$5.72(0.08) \cdot 10^{-14}$
$D^+ \to \bar{K}^0 \mu\nu$	$5.58(0.12) \cdot 10^{-14}$ [18]	$5.59(0.07) \cdot 10^{-14}$
$D^+ \to \pi^+ e\nu$	$2.37(0.11) \cdot 10^{-15}$ [18]	$2.33(0.03) \cdot 10^{-15}$
$D^+ \to \pi^+ \mu\nu$	$2.23(0.10) \cdot 10^{-15}$ [18]	$2.30(0.03) \cdot 10^{-15}$
$D^+ \to \eta e\nu$	$7.1(0.4) \cdot 10^{-16}$ [18]	$8.1(1.7) \cdot 10^{-16}$
$D^+ \to \eta \mu\nu$	$6.6(0.4) \cdot 10^{-16}$ [18]	$8.0(1.5) \cdot 10^{-16}$
$B^0 \to D^+ e\nu$	$1.06(0.06) \cdot 10^{-14}$ [415]	$1.00(0.01) \cdot 10^{-14}$
$B^0 \to D^+ \mu\nu$	$1.04(0.06) \cdot 10^{-14}$ [415]	$1.00(0.01) \cdot 10^{-14}$
$B^0 \to D^+ \tau\nu$	$4.3(0.9) \cdot 10^{-15}$ [18]	$2.95(0.13) \cdot 10^{-15}$
$B^0 \to \pi^+ \ell\nu$	$6.33(0.17) \cdot 10^{-17}$ [18]	$6.8(2.2) \cdot 10^{-17}$
$B^+ \to D^0 \ell\nu$	$9.20(0.32) \cdot 10^{-15}$ [18]	$1.01(0.05) \cdot 10^{-14}$
$B^+ \to D^0 \tau\nu$	$3.1(1.0) \cdot 10^{-15}$ [18]	$2.97(0.14) \cdot 10^{-15}$
$B^+ \to \pi^0 \ell\nu$	$3.01(0.12) \cdot 10^{-17}$ [18]	$3.4(1.1) \cdot 10^{-17}$
$B_s \to D_s \mu\nu$	$1.00(0.09) \cdot 10^{-14}$ [416]	$1.00(0.06) \cdot 10^{-14}$
$B_s \to K^+ \mu\nu$	$4.6(0.4) \cdot 10^{-17}$ [417]	$7.9(2.2) \cdot 10^{-17}$

Table 9: Measurements and SM predictions for the semileptonic decays into pseudoscalar mesons. The SM predictions are computed using Eq. (6.23) with the form factors listed in Tab. 6.

Semileptonic meson decays

Tab. 9 lists the measurements and SM predictions for the branching ratios of the semileptonic decays into pseudoscalar mesons, while Tab. 10 lists the measurements and SM predictions for the decays into vector mesons.

Decay	Γ_{exp} [GeV]	Γ_{SM} [GeV]
$D^0 \to K^{*+} e\nu$	$3.45(0.26) \cdot 10^{-14}$ [18]	$3.13(0.33) \cdot 10^{-14}$
$D^0 \to K^{*+} \mu\nu$	$3.0(0.4) \cdot 10^{-14}$ [18]	$3.09(0.33) \cdot 10^{-14}$
$D^0 \to \rho^+ e\nu$	$2.41(0.19) \cdot 10^{-15}$ [18]	$2.81(0.39) \cdot 10^{-15}$
$D^0 \to \rho^+ \mu\nu$	$2.17(0.21) \cdot 10^{-15}$ [18]	$2.78(0.38) \cdot 10^{-15}$
$D^+ \to \bar{K}^* e\nu$	$3.44(0.07) \cdot 10^{-14}$ [18]	$3.15(0.33) \cdot 10^{-14}$
$D^+ \to \bar{K}^* \mu\nu$	$3.36(0.10) \cdot 10^{-14}$ [18]	$3.11(0.33) \cdot 10^{-14}$
$D^+ \to \rho^0 e\nu$	$1.21(0.06) \cdot 10^{-15}$ [18]	$1.43(0.20) \cdot 10^{-15}$
$D^+ \to \rho^0 \mu\nu$	$1.53(0.25) \cdot 10^{-15}$ [18]	$1.42(0.19) \cdot 10^{-15}$
$D^+ \to \omega e\nu$	$1.08(0.07) \cdot 10^{-15}$ [18]	$1.21(0.17) \cdot 10^{-15}$
$D^+ \to \omega \mu\nu$	$1.13(0.13) \cdot 10^{-15}$ [18]	$1.20(0.16) \cdot 10^{-15}$
$D_s^+ \to \phi e\nu$	$3.14(0.21) \cdot 10^{-14}$ [18]	$3.21(0.58) \cdot 10^{-14}$
$D_s^+ \to \phi \mu\nu$	$2.94(0.15) \cdot 10^{-14}$ [18]	$3.18(0.57) \cdot 10^{-14}$
$D_s^+ \to K^* e\nu$	$2.8(0.4) \cdot 10^{-15}$ [18]	$3.06(0.52) \cdot 10^{-15}$
$B^0 \to D^{*+} e\nu$	$2.13(0.10) \cdot 10^{-14}$ [418]	$2.48(0.56) \cdot 10^{-14}$
$B^0 \to D^{*+} \mu\nu$	$2.14(0.10) \cdot 10^{-14}$ [418]	$2.47(0.56) \cdot 10^{-14}$
$B^0 \to D^{*+} \tau\nu$	$6.3(0.4) \cdot 10^{-15}$ [418]	$6.4(1.7) \cdot 10^{-15}$
$B^0 \to \rho \ell\nu$	$1.06(0.14) \cdot 10^{-16}$ [18]	$9.7(2.9) \cdot 10^{-17}$
$B^+ \to \rho \ell\nu$	$6.3(0.4) \cdot 10^{-17}$ [18]	$9.7(2.9) \cdot 10^{-17}$
$B^+ \to D^* \ell\nu$	$2.24(0.11) \cdot 10^{-14}$ [18]	$2.48(0.56) \cdot 10^{-14}$
$B^+ \to D^* \tau\nu$	$7.6(0.8) \cdot 10^{-15}$ [18]	$6.4(1.7) \cdot 10^{-15}$
$B_s \to D_s^* \mu\nu$	$2.25(0.22) \cdot 10^{-14}$ [416]	$2.02(0.41) \cdot 10^{-14}$

Table 10: Measurements and SM predictions for the semileptonic decays into vector mesons. The SM predictions are computed using Eq. (6.25) with the form factors listed in Tab. 6.

F Credible Intervals and Auxiliary Plots

In this appendix, we present auxiliary results from the global fits, including the 90% credible intervals for the Wilson coefficients and the lower limits on $\Lambda/\sqrt{C}$ for each lepton flavor combination, as well as additional plots that illustrate the posterior distributions of the Wilson coefficients and the predictions of dineutrino decay rates.

Lepton-Flavor Specific Credible Intervals

We show the lepton-flavor specific 90% credible intervals and lower bounds on $\Lambda/\sqrt{C}$ for the Wilson coefficients obtained in the global fits in Tabs. 11–26 for the different classes of Wilson coefficients. The tables are organized by the lepton flavor combinations, with each row corresponding to a specific lepton pair or combination. The columns list the Wilson coefficients and their respective credible intervals or reaches on $\Lambda/\sqrt{C}$.

90% CI	$\tilde{C}^{(1)}_{\varphi l}$	$\tilde{C}^{(3)}_{\varphi l}$	$\tilde{C}_{\varphi e}$
ee	$[-0.087, 5.2] \cdot 10^{-3}$	$[-2.1, 0.72] \cdot 10^{-3}$	$[-1.6, 5.8] \cdot 10^{-3}$
$\mu\mu$	$[-3.7, 7.5] \cdot 10^{-3}$	$[-0.57, 2.1] \cdot 10^{-3}$	$[-3.9, 8.8] \cdot 10^{-3}$
$\tau\tau$	$[-0.41, 1.4] \cdot 10^{-2}$	$[-0.88, 3.3] \cdot 10^{-3}$	$[-1.1, 1.0] \cdot 10^{-2}$
$e\mu$	$[-2.1, 4.3] \cdot 10^{-3}$	$[-4.0, 2.0] \cdot 10^{-3}$	$[-6.7, 6.8] \cdot 10^{-5}$
$e\tau$	$[-3.0, 2.3] \cdot 10^{-2}$	$[-2.1, 2.8] \cdot 10^{-2}$	$[-8.6, 8.6] \cdot 10^{-4}$
$\mu\tau$	$[-2.5, 3.3] \cdot 10^{-2}$	$[-3.1, 2.4] \cdot 10^{-2}$	$[-7.6, 7.6] \cdot 10^{-4}$
LU	$[0.0085, 2.7] \cdot 10^{-3}$	$[-1.2, 0.97] \cdot 10^{-3}$	$[-0.49, 3.9] \cdot 10^{-3}$
LD	$[-2.2, 2.7] \cdot 10^{-4}$	$[-2.0, 2.6] \cdot 10^{-4}$	$[-2.0, 1.3] \cdot 10^{-4}$

Table 11: 90% credible intervals (CI) for the leptonic Higgs-current coefficients.

$\Lambda/\sqrt{C}$/TeV	$\tilde{C}_{\varphi l}^{(1)}$	$\tilde{C}_{\varphi l}^{(3)}$	$\tilde{C}_{\varphi e}$
ee	3.4	5.3	3.2
$\mu\mu$	2.8	5.4	2.6
$\tau\tau$	2.1	4.3	2.3
$e\mu$	3.8	3.9	30
$e\tau$	1.4	1.5	8.4
$\mu\tau$	1.4	1.4	8.9
LU	4.7	7.2	3.9
LD	15	15	17

Table 12: Lower limit on $\Lambda/\sqrt{C}$ in TeV for the leptonic Higgs-current coefficients at 90% credible level.

90% CI	$\tilde{C}_{\varphi q}^{(1)}$	$\tilde{C}_{\varphi q}^{(3)}$	$\tilde{C}_{\varphi u}$	$\tilde{C}_{\varphi d}$
ee	$[-3.2, 4.8] \cdot 10^{-3}$	$[-3.0, 0.65] \cdot 10^{-3}$	$[-0.66, 1.0] \cdot 10^{-2}$	$[-1.6, -0.23] \cdot 10^{-2}$
$\mu\mu$	$[-4.1, 4.2] \cdot 10^{-3}$	$[-1.0, 2.0] \cdot 10^{-3}$	$[-4.3, 9.5] \cdot 10^{-3}$	$[-1.3, -0.21] \cdot 10^{-2}$
$\tau\tau$	$[-2.7, 4.0] \cdot 10^{-3}$	$[-1.5, 1.5] \cdot 10^{-3}$	$[-0.34, 1.0] \cdot 10^{-2}$	$[-1.4, -0.28] \cdot 10^{-2}$
$e\mu$	$[-2.9, 4.1] \cdot 10^{-3}$	$[-1.7, 0.97] \cdot 10^{-3}$	$[-4.3, 9.2] \cdot 10^{-3}$	$[-1.3, -0.21] \cdot 10^{-2}$
$e\tau$	$[-2.9, 4.4] \cdot 10^{-3}$	$[-2.8, 0.55] \cdot 10^{-3}$	$[-4.2, 9.3] \cdot 10^{-3}$	$[-1.4, -0.22] \cdot 10^{-2}$
$\mu\tau$	$[-3.2, 3.6] \cdot 10^{-3}$	$[-1.1, 1.5] \cdot 10^{-3}$	$[-4.6, 9.0] \cdot 10^{-3}$	$[-1.3, -0.18] \cdot 10^{-2}$
LU	$[-3.0, 4.8] \cdot 10^{-3}$	$[-1.1, 1.3] \cdot 10^{-3}$	$[-6.2, 8.8] \cdot 10^{-3}$	$[-1.5, -0.29] \cdot 10^{-2}$
LD	$[-2.9, 3.0] \cdot 10^{-3}$	$[-1.6, 3.1] \cdot 10^{-3}$	$[-5.5, 8.3] \cdot 10^{-3}$	$[-1.3, -0.07] \cdot 10^{-2}$

Table 13: 90% credible intervals (CI) for the quark Higgs-current coefficients.

$\Lambda/\sqrt{C}$/TeV	$\tilde{C}_{\varphi q}^{(1)}$	$\tilde{C}_{\varphi q}^{(3)}$	$\tilde{C}_{\varphi u}$	$\tilde{C}_{\varphi d}$
ee	3.5	4.5	2.4	1.9
$\mu\mu$	3.8	5.5	2.5	2.1
$\tau\tau$	3.9	6.4	2.4	2.1
$e\mu$	3.9	5.9	2.6	2.1
$e\tau$	3.7	4.6	2.6	2.1
$\mu\tau$	4.1	6.3	2.6	2.2
LU	3.5	6.7	2.6	2.0
LD	4.5	4.4	2.7	2.2

Table 14: Lower limits on $\Lambda/\sqrt{C}$ in TeV for the quark Higgs-current coefficients at 90% credible level.

90% CI	$\tilde{C}_{ll}$	$\tilde{C}_{ee}$	$\tilde{C}_{le}$
ee	$[-0.011, 0.2]$	$[-0.23, 0.13]$	$[-0.24, 0.076]$
$\mu\mu$	$[-7.7, 8.0] \cdot 10^{-2}$	$[-0.31, 0.56]$	$[-0.85, 1.0]$
$\tau\tau$	$[-0.049, 0.32]$	$[-0.68, 1.6]$	$[-2.1, 3.1]$
$e\mu$ $(ijji)$	$[0.0078, 0.11]$		$[-0.55, 0.52]$
$e\mu$ $(ijij)$	$[-0.31, 0.33]$		$[-0.59, 0.54]$
$e\tau$ $(ijji)$	$[0.015, 0.16]$		$[-0.74, 0.71]$
$e\tau$ $(ijij)$	$[-0.39, 0.41]$		$[-0.75, 0.67]$
$\mu\tau$ $(ijji)$	$[0.0097, 0.14]$		$[-0.65, 0.69]$
$\mu\tau$ $(ijij)$	$[-0.35, 0.36]$		$[-0.68, 0.65]$
LU	$[-0.85, 2.7] \cdot 10^{-2}$	$[-7.9, 0.3] \cdot 10^{-2}$	$[-2.6, 0.4] \cdot 10^{-2}$
LD	$[-3.9, 6.3] \cdot 10^{-5}$	$[-4.5, 2.7] \cdot 10^{-5}$	$[-9.3, 5.7] \cdot 10^{-5}$

Table 15: 90% credible intervals (CI) for the four-lepton coefficients. In the LFV fits, the flavor combinations $ijji$ and $ijij$ are treated as independent degrees of freedom. The coefficient $\tilde{C}_{ee}$ is not constrained in the LFV fits, so that no credible intervals are shown for these cases.

$\Lambda/\sqrt{C}$	$\tilde{C}_{ll}$	$\tilde{C}_{ee}$	$\tilde{C}_{le}$
ee	0.55	0.51	0.50
$\mu\mu$	0.87	0.33	0.24
$\tau\tau$	0.44	0.20	0.14
$e\mu$ $(ijji)$	0.76		0.33
$e\mu$ $(ijij)$	0.43		0.32
$e\tau$ $(ijji)$	0.62		0.29
$e\tau$ $(ijij)$	0.39		0.29
$\mu\tau$ $(ijji)$	0.65		0.30
$\mu\tau$ $(ijij)$	0.41		0.30
LU	1.3	0.83	1.5
LD	31	37	26

Table 16: 90% credible level lower limits on $\Lambda/\sqrt{C}$ in TeV for the four-lepton coefficients. The flavor combinations $ijji$ and $ijij$ are treated as independent degrees of freedom in the LFV fits. The coefficient $\tilde{C}_{ee}$ is not constrained in the LFV fits, so that no lower limits are shown for these cases.

90% CI	$\tilde{C}_{eB}$	$\tilde{C}_{eW}$
ee	$[-3.5, 3.5] \cdot 10^{-3}$	$[-2.4, 2.4] \cdot 10^{-2}$
$\mu\mu$	$[-4.1, 4.2] \cdot 10^{-3}$	$[-2.9, 2.9] \cdot 10^{-2}$
$\tau\tau$	$[-0.85, 0.77]$	$[-0.2, 0.18]$
$e\mu$	$[-0.37, 0.37]$	$[-0.11, 0.11]$
μe	$[-0.36, 0.35]$	$[-0.11, 0.11]$
$e\tau$	$[-0.51, 0.5]$	$[-0.15, 0.15]$
τe	$[-0.51, 0.5]$	$[-0.15, 0.15]$
$\mu\tau$	$[-0.4, 0.38]$	$[-0.11, 0.12]$
$\tau\mu$	$[-0.45, 0.45]$	$[-0.13, 0.13]$
LU	$[-5.4, 5.5] \cdot 10^{-5}$	$[-2.4, 2.4] \cdot 10^{-2}$
LD	$[-5.9, 0.1] \cdot 10^{-8}$	$[-1.7, 1.7] \cdot 10^{-4}$

Table 17: 90% credible intervals (CI) for the leptonic dipole coefficients. Note that the flavor combinations ij and ji are independent degrees of freedom as the dipole operators are not Hermitian.

$\Lambda/\sqrt{C}$/TeV	$\tilde{C}_{eB}$	$\tilde{C}_{eW}$
ee	4.1	1.6
$\mu\mu$	3.8	1.4
$\tau\tau$	0.27	0.55
$e\mu$	0.41	0.76
μe	0.40	0.74
$e\tau$	0.35	0.64
τe	0.34	0.63
$\mu\tau$	0.37	0.68
$\tau\mu$	0.39	0.71
LU	33	1.6
LD	$1.0 \cdot 10^3$	19

Table 18: 90% credible level lower limits on $\Lambda/\sqrt{C}$ in TeV for the leptonic dipole coefficients. The flavor combinations ij and ji are treated as independent degrees of freedom as the dipole operators are not Hermitian.

90% CI	$\tilde{C}_{uB}$	$\tilde{C}_{uW}$	$\tilde{C}_{uG}$
ee	$[0.0076, 2.2] \cdot 10^{-2}$	$[-6.8, 2.0] \cdot 10^{-4}$	$[-1.2, 0.073] \cdot 10^{-3}$
$\mu\mu$	$[0.0077, 2.2] \cdot 10^{-2}$	$[-6.8, 2.0] \cdot 10^{-4}$	$[-1.2, 0.076] \cdot 10^{-3}$
$\tau\tau$	$[-0.021, 2.3] \cdot 10^{-2}$	$[-7.1, 2.2] \cdot 10^{-4}$	$[-1.3, 0.14] \cdot 10^{-3}$
$e\mu$	$[0.015, 2.2] \cdot 10^{-2}$	$[-6.7, 2.0] \cdot 10^{-4}$	$[-1.2, 0.063] \cdot 10^{-3}$
$e\tau$	$[0.017, 2.2] \cdot 10^{-2}$	$[-6.8, 2.0] \cdot 10^{-4}$	$[-1.2, 0.063] \cdot 10^{-3}$
$\mu\tau$	$[0.0081, 2.2] \cdot 10^{-2}$	$[-6.7, 2.0] \cdot 10^{-4}$	$[-1.2, 0.07] \cdot 10^{-3}$
LU	$[0.015, 2.2] \cdot 10^{-2}$	$[-6.7, 2.0] \cdot 10^{-4}$	$[-1.2, 0.061] \cdot 10^{-3}$
LD	$[0.013, 2.2] \cdot 10^{-2}$	$[-6.6, 2.1] \cdot 10^{-4}$	$[-1.2, 0.066] \cdot 10^{-3}$

Table 19: 90% credible intervals (CI) for the quark dipole coefficients.

$\Lambda/\sqrt{C}$/TeV	$\tilde{C}_{uB}$	$\tilde{C}_{uW}$	$\tilde{C}_{uG}$
ee	1.7	9.5	7.1
$\mu\mu$	1.7	9.5	7.1
$\tau\tau$	1.6	9.2	6.8
$e\mu$	1.7	9.5	7.1
$e\tau$	1.7	9.4	7.1
$\mu\tau$	1.7	9.5	7.1
LU	1.7	9.5	7.1
LD	1.7	9.6	7.1

Table 20: 90% credible level lower limits on $\Lambda/\sqrt{C}$ in TeV for the quark dipole coefficients.

90% CI	$\tilde{C}^{(1)}_{lequ}$	$\tilde{C}^{(3)}_{lequ}$
ee	$[-0.14, 0.15]$	$[-2.7, 2.6] \cdot 10^{-2}$
$\mu\mu$	$[-0.22, 0.2]$	$[-3.1, 3.2] \cdot 10^{-2}$
$\tau\tau$	$[-110.0, 114.0]$	$[-6.6, 5.9]$
$e\mu$	$[-190.0, 193.0]$	$[-3.1, 3.1]$
μe	$[-190.0, 189.0]$	$[-3.0, 3.0]$
$e\tau$	$[-49.0, 57.0]$	$[-3.9, 3.8]$
τe	$[-48.0, 49.0]$	$[-3.8, 3.7]$
$\mu\tau$	$[-33.0, 60.0]$	$[-3.1, 2.9]$
$\tau\mu$	$[-45.0, 44.0]$	$[-3.4, 3.4]$
LU	$[-0.1, 0.1]$	$[-3.8, -2.0] \cdot 10^{-6}$
LD	$[-5.2, 6.8] \cdot 10^{-3}$	$[-2.7, 2.1] \cdot 10^{-5}$

Table 21: 90% credible intervals (CI) for the scalar and tensor four-fermion coefficients. Note that the lepton flavor combinations ij and ji are independent degrees of freedom as the four-fermion operators are not Hermitian.

$\Lambda/\sqrt{C}$/TeV	$\tilde{C}^{(1)}_{lequ}$	$\tilde{C}^{(3)}_{lequ}$
ee	0.65	1.5
$\mu\mu$	0.53	1.4
$\tau\tau$	$2.3 \cdot 10^{-2}$	$9.6 \cdot 10^{-2}$
$e\mu$	$1.8 \cdot 10^{-2}$	0.14
μe	$1.8 \cdot 10^{-2}$	0.14
$e\tau$	$3.5 \cdot 10^{-2}$	0.13
τe	$3.3 \cdot 10^{-2}$	0.12
$\mu\tau$	$3.7 \cdot 10^{-2}$	0.13
$\tau\mu$	$3.2 \cdot 10^{-2}$	0.14
LU	0.76	$1.3 \cdot 10^{2}$
LD	3.0	47

Table 22: 90% lower limits on $\Lambda/\sqrt{C}$ in TeV for the scalar and tensor four-fermion coefficients. The lepton flavor combinations ij and ji are treated as independent degrees of freedom as the four-fermion operators are not Hermitian.

90% CI	$\tilde{C}^{(1)}_{lq}$	$\tilde{C}^{(3)}_{lq}$	$\tilde{C}_{qe}$
ee	$[-1.2, 1.2] \cdot 10^{-3}$	$[-0.4, 1.4] \cdot 10^{-3}$	$[-0.99, 1.7] \cdot 10^{-3}$
$\mu\mu$	$[-0.63, 1.5] \cdot 10^{-3}$	$[-0.92, 1.0] \cdot 10^{-3}$	$[-1.9, 1.4] \cdot 10^{-3}$
$\tau\tau$	$[-3.4, 2.8] \cdot 10^{-3}$	$[-1.3, 2.2] \cdot 10^{-3}$	$[-7.1, 1.5] \cdot 10^{-3}$
$e\mu$	$[-2.7, 3.6] \cdot 10^{-4}$	$[0.28, 3.7] \cdot 10^{-4}$	$[-3.1, 3.0] \cdot 10^{-4}$
$e\tau$	$[-3.5, 4.2] \cdot 10^{-4}$	$[-0.26, 4.8] \cdot 10^{-4}$	$[-4.0, 4.1] \cdot 10^{-4}$
$\mu\tau$	$[-3.4, 4.0] \cdot 10^{-4}$	$[0.65, 4.4] \cdot 10^{-4}$	$[-3.9, 4.0] \cdot 10^{-4}$
LU	$[-4.6, 5.5] \cdot 10^{-4}$	$[-2.4, 3.0] \cdot 10^{-4}$	$[-4.9, 8.5] \cdot 10^{-4}$
LD	$[-1.4, 1.3] \cdot 10^{-4}$	$[-0.73, 6.2] \cdot 10^{-5}$	$[-1.5, 1.6] \cdot 10^{-4}$

Table 23: 90% credible intervals (CI) for the semileptonic four-fermion coefficients with two left-handed quark doublets.

$\Lambda/\sqrt{C}$/TeV	$\tilde{C}_{lq}^{(1)}$	$\tilde{C}_{lq}^{(3)}$	$\tilde{C}_{qe}$
ee	7.1	6.7	5.9
$\mu\mu$	6.4	7.7	5.6
$\tau\tau$	4.2	5.2	2.9
$e\mu$	13	13	14
$e\tau$	12	11	12
$\mu\tau$	12	12	12
LU	11	14	8.4
LD	21	31	19

Table 24: 90% lower limits on $\Lambda/\sqrt{C}$ in TeV for the semileptonic four-fermion coefficients with two left-handed quark doublets.

	$\tilde{C}_{lu}$	$\tilde{C}_{ld}$	$\tilde{C}_{eu}$	$\tilde{C}_{ed}$
ee	$[-2.5, 1.6] \cdot 10^{-3}$	$[-2.1, 2.5] \cdot 10^{-3}$	$[-1.5, 4.2] \cdot 10^{-3}$	$[-3.3, 1.8] \cdot 10^{-3}$
$\mu\mu$	$[-3.2, 5.2] \cdot 10^{-3}$	$[-2.9, 1.9] \cdot 10^{-3}$	$[-7.6, 5.1] \cdot 10^{-3}$	$[-2.9, 3.9] \cdot 10^{-3}$
$\tau\tau$	$[-1.4, 0.96] \cdot 10^{-2}$	$[-5.5, 7.4] \cdot 10^{-3}$	$[-2.6, 0.42] \cdot 10^{-2}$	$[-0.27, 1.4] \cdot 10^{-2}$
$e\mu$	$[-4.8, 4.8] \cdot 10^{-4}$	$[-5.4, 5.4] \cdot 10^{-4}$	$[-2.7, 2.8] \cdot 10^{-4}$	$[-4.7, 4.7] \cdot 10^{-4}$
$e\tau$	$[-5.8, 6.7] \cdot 10^{-4}$	$[-5.1, 4.1] \cdot 10^{-4}$	$[-5.5, 5.4] \cdot 10^{-4}$	$[-4.6, 4.5] \cdot 10^{-4}$
$\mu\tau$	$[-5.4, 6.3] \cdot 10^{-4}$	$[-4.9, 3.8] \cdot 10^{-4}$	$[-5.2, 5.0] \cdot 10^{-4}$	$[-4.3, 4.3] \cdot 10^{-4}$
LU	$[-1.0, 1.7] \cdot 10^{-3}$	$[-1.8, 1.4] \cdot 10^{-3}$	$[0.43, 3.2] \cdot 10^{-3}$	$[-2.7, 0.57] \cdot 10^{-3}$
LD	$[-2.7, 3.6] \cdot 10^{-4}$	$[-2.4, 2.4] \cdot 10^{-4}$	$[-2.7, 2.8] \cdot 10^{-4}$	$[-2.6, 2.4] \cdot 10^{-4}$

Table 25: 90% credible intervals for the semileptonic four-fermion coefficients including two right-handed quark singlets.

$\Lambda/\sqrt{C}$/TeV	$\tilde{C}_{lu}$	$\tilde{C}_{ld}$	$\tilde{C}_{eu}$	$\tilde{C}_{ed}$
ee	4.9	4.9	3.8	4.3
$\mu\mu$	3.4	4.6	2.8	3.9
$\tau\tau$	2.1	2.9	1.5	2.1
$e\mu$	11	11	15	11
$e\tau$	9.5	11	11	11
$\mu\tau$	9.8	11	11	12
LU	6.1	5.8	4.3	4.7
LD	13	16	15	15

Table 26: 90% lower limits on $\Lambda/\sqrt{C}$ in TeV for the semileptonic four-fermion coefficients including two right-handed quark singlets.

Auxiliary Plots for MFV Ratios

Here, we present the auxiliary plots for the ratios of the MFV coefficients for operators with left-handed quark doublets, r_L^i. Fig. 1 show the distributions of the ratios for the Higgs-current coefficients, while Fig. 2 shows the distributions for the semileptonic four-fermion coefficients.

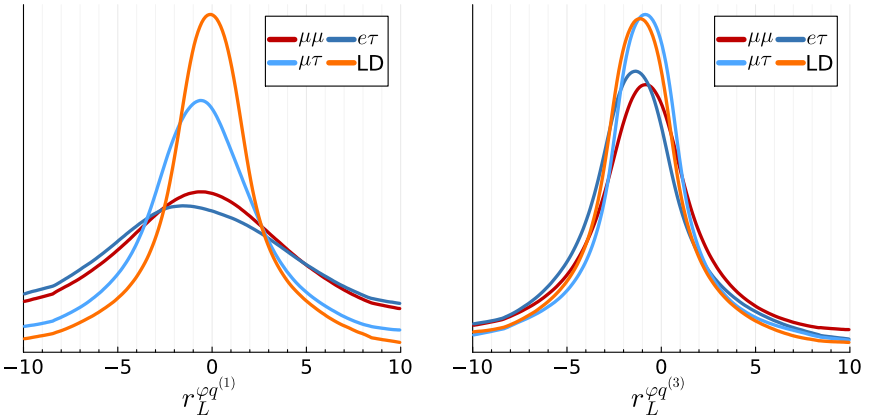

Figure 1: Posterior distributions for the MFV ratio $r_L^{\varphi q^{(1)}}$ (left) and $r_L^{\varphi q^{(3)}}$ (right) for the $\mu\mu$, $e\tau$, $\mu\tau$ and LD lepton-flavor scenarios.

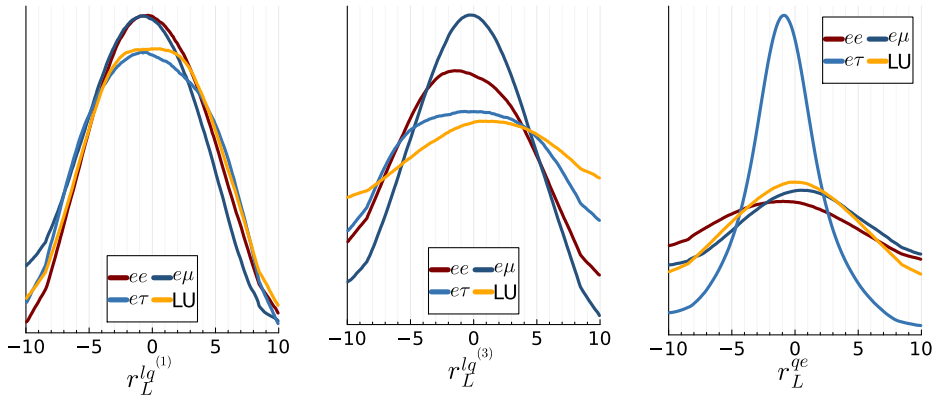

Figure 2: Posterior distributions for the MFV ratio $r_L^{lq^{(1)}}$ (left), $r_L^{lq^{(3)}}$ (center) and r_L^{qe} (right) for the ee, $e\mu$, $e\tau$ and LU lepton-flavor scenarios.

Auxiliary Plots for Dineutrino Predictions

Fig. 3 shows the predictions of the $B^+ \to M\nu\bar{\nu}$ decays obtained using the posterior of the LU fit. We show our predictions in blue, the SM predictions without SMEFT effects in orange, the current

experimental bounds in red and the projected sensitivities of the Belle II experiment [397] in purple.

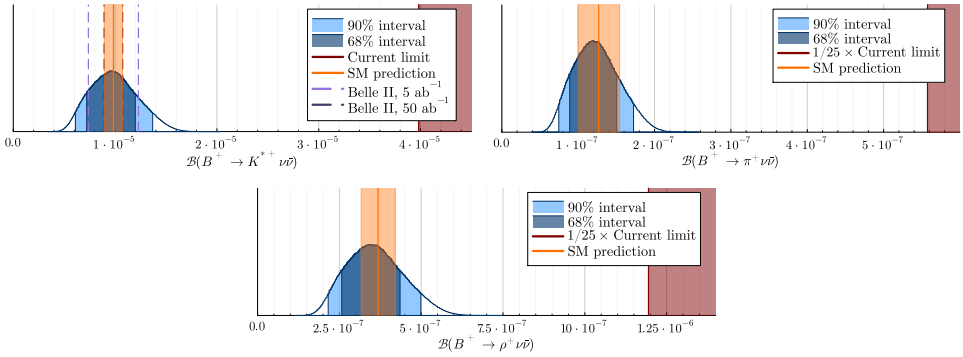

Figure 3: Predictions for the short-distance contributions to the dineutrino decays $B^+ \to K^{*+}\nu\bar{\nu}$ (top left), $B^+ \to \pi^+\nu\bar{\nu}$ (top right) and $B^+ \to \rho^+\nu\bar{\nu}$ (bottom) based on the LU fit. Colored bands indicate the 68% and 90% credible intervals; the orange band denotes the 1σ SM prediction. Red lines represent current experimental 90% CL bounds, while dashed purple lines show projected sensitivities of the Belle II experiment [397]. There are additional long-distance contributions from $B^+ \to \tau^+(\to P^+\bar{\nu})\nu$ [353, 398] that are not included here.

Bibliography

[1] Cornelius Grunwald et al. “More synergies from beauty, top, Z and Drell-Yan measurements in SMEFT”. In: *JHEP* 11 (2023), p. 110. DOI: 10.1007/JHEP11(2023)110. arXiv: 2304.12837 [hep-ph].

[2] Gudrun Hiller, Lara Nollen, and Daniel Wendler. “Total Drell-Yan in the flavorful SMEFT”. In: (Feb. 2025). arXiv: 2502.12250 [hep-ph].

[3] Cornelius Grunwald et al. “Beyond Universality: Global Fits of lepton-flavour-specific SMEFT Operators”. Manuscript in preparation. 2025.

[4] Cornelius Grunwald et al. “Synergies of Drell-Yan, top and beauty in global SMEFT fits”. In: *15th International Workshop on Top Quark Physics*. Nov. 2022. arXiv: 2211.12261 [hep-ph].

[5] Cornelius Grunwald et al. “Synergies of Drell-Yan, beauty, top, and Z observables in MFV-SMEFT”. In: *PoS* FPCP2023 (July 2023), p. 058. DOI: 10.22323/1.445.0058. arXiv: 2307.06150 [hep-ph].

[6] Cornelius Grunwald et al. “Predicting $B(B \to K^{(*)}\nu\bar{\nu})$ within the MFV-SMEFT using B, Top, Z and Drell-Yan data”. In: *PoS* EPS-HEP2023 (2024), p. 298. DOI: 10.22323/1.449.0298.

[7] Gudrun Hiller, Lara Nollen, and Daniel Wendler. “Teaming up MET plus jet with Drell-Yan in the SMEFT”. In: *PoS* DISCRETE2024 (2025), p. 002. DOI: 10.22323/1.481.0002. arXiv: 2503.13638 [hep-ph].

[8] Paul A. M. Dirac. “Quantum theory of emission and absorption of radiation”. In: *Proc. Roy. Soc. Lond. A* 114 (1927), p. 243. DOI: 10.1098/rspa.1927.0039.

[9] Julian S. Schwinger. “On Quantum electrodynamics and the magnetic moment of the electron”. In: *Phys. Rev.* 73 (1948), pp. 416–417. DOI: 10.1103/PhysRev.73.416.

[10] R. P. Feynman. “Space - time approach to quantum electrodynamics”. In: *Phys. Rev.* 76 (1949). Ed. by L. M. Brown, pp. 769–789. DOI: 10.1103/PhysRev.76.769.

[11] F. J. Dyson. “The S matrix in quantum electrodynamics”. In: *Phys. Rev.* 75 (1949), pp. 1736–1755. DOI: 10.1103/PhysRev.75.1736.

[12] Georges Aad et al. “Observation of a new particle in the search for the Standard Model Higgs boson with the ATLAS detector at the LHC”. In: *Phys. Lett. B* 716 (2012), pp. 1–29. DOI: 10.1016/j.physletb.2012.08.020. arXiv: 1207.7214 [hep-ex].

[13] Serguei Chatrchyan et al. “Observation of a New Boson at a Mass of 125 GeV with the CMS Experiment at the LHC”. In: *Phys. Lett. B* 716 (2012), pp. 30–61. DOI: 10.1016/j.physletb.2012.08.021. arXiv: 1207.7235 [hep-ex].

[14] S. L. Glashow. “Partial Symmetries of Weak Interactions”. In: *Nucl. Phys.* 22 (1961), pp. 579–588. DOI: 10.1016/0029-5582(61)90469-2.

[15] Steven Weinberg. “A Model of Leptons”. In: *Phys. Rev. Lett.* 19 (1967), pp. 1264–1266. DOI: 10.1103/PhysRevLett.19.1264.

[16] Abdus Salam. “Weak and Electromagnetic Interactions”. In: *Conf. Proc. C* 680519 (1968), pp. 367–377. DOI: 10.1142/9789812795915_0034.

[17] S. Schael et al. “Precision electroweak measurements on the Z resonance”. In: *Phys. Rept.* 427 (2006), pp. 257–454. DOI: 10.1016/j.physrep.2005.12.006. arXiv: hep-ex/0509008.

[18] S. Navas et al. “Review of particle physics”. In: *Phys. Rev. D* 110.3 (2024), p. 030001. DOI: 10.1103/PhysRevD.110.030001.

[19] “LHC Machine”. In: *JINST* 3 (2008). Ed. by Lyndon Evans and Philip Bryant, S08001. DOI: 10.1088/1748-0221/3/08/S08001.

[20] John R. Ellis et al. “Indirect sensitivities to the scale of supersymmetry”. In: *JHEP* 02 (2005), p. 013. DOI: 10.1088/1126-6708/2005/02/013. arXiv: hep-ph/0411216.

[21] Gino Isidori, Yosef Nir, and Gilad Perez. “Flavor Physics Constraints for Physics Beyond the Standard Model”. In: *Ann. Rev. Nucl. Part. Sci.* 60 (2010), p. 355. DOI: 10.1146/annurev.nucl.012809.104534. arXiv: 1002.0900 [hep-ph].

[22] Guido Altarelli and Martin W. Grunewald. “Precision electroweak tests of the standard model”. In: *Phys. Rept.* 403-404 (2004), pp. 189–201. DOI: 10.1016/j.physrep.2004.08.013. arXiv: hep-ph/0404165.

[23] W. Buchmuller and D. Wyler. “Effective Lagrangian Analysis of New Interactions and Flavor Conservation”. In: *Nucl. Phys. B* 268 (1986), pp. 621–653. DOI: 10.1016/0550-3213(86)90262-2.

[24] John Ellis et al. “Updated Global SMEFT Fit to Higgs, Diboson and Electroweak Data”. In: *JHEP* 06 (2018), p. 146. DOI: 10.1007/JHEP06(2018)146. arXiv: 1803.03252 [hep-ph].

[25] Stefan Alte, Matthias König, and William Shepherd. “Consistent Searches for SMEFT Effects in Non-Resonant Dijet Events”. In: *JHEP* 01 (2018), p. 094. DOI: 10.1007/JHEP01(2018)094. arXiv: 1711.07484 [hep-ph].

[26] D. Barducci et al. “Interpreting top-quark LHC measurements in the standard-model effective field theory”. In: (Feb. 2018). Ed. by Juan Antonio Aguilar-Saavedra et al. arXiv: 1802.07237 [hep-ph].

[27] Simone Alioli et al. “NLO QCD corrections to SM-EFT dilepton and electroweak Higgs boson production, matched to parton shower in POWHEG”. In: *JHEP* 08 (2018), p. 205. DOI: 10.1007/JHEP08(2018)205. arXiv: 1804.07407 [hep-ph].

[28] Luca Silvestrini and Mauro Valli. “Model-independent Bounds on the Standard Model Effective Theory from Flavour Physics”. In: *Phys. Lett. B* 799 (2019), p. 135062. DOI: 10.1016/j.physletb.2019.135062. arXiv: 1812.10913 [hep-ph].

[29] Nathan P. Hartland et al. “A Monte Carlo global analysis of the Standard Model Effective Field Theory: the top quark sector”. In: *JHEP* 04 (2019), p. 100. DOI: 10.1007/JHEP04(2019)100. arXiv: 1901.05965 [hep-ph].

[30] Ilaria Brivio et al. “O new physics, where art thou? A global search in the top sector”. In: *JHEP* 02 (2020), p. 131. DOI: 10.1007/JHEP02(2020)131. arXiv: 1910.03606 [hep-ph].

[31] John Ellis et al. “Top, Higgs, Diboson and Electroweak Fit to the Standard Model Effective Field Theory”. In: *JHEP* 04 (2021), p. 279. DOI: 10.1007/JHEP04(2021)279. arXiv: 2012.02779 [hep-ph].

[32] Jacob J. Ethier et al. “Combined SMEFT interpretation of Higgs, diboson, and top quark data from the LHC”. In: *JHEP* 11 (2021), p. 089. DOI: 10.1007/JHEP11(2021)089. arXiv: 2105.00006 [hep-ph].

[33] Riccardo Bartocci, Anke Biekötter, and Tobias Hurth. "Renormalisation group evolution effects on global SMEFT analyses". In: (Dec. 2024). arXiv: 2412.09674 [hep-ph].

[34] Marco Farina et al. "Energy helps accuracy: electroweak precision tests at hadron colliders". In: *Phys. Lett. B* 772 (2017), pp. 210–215. DOI: 10.1016/j.physletb.2017.06.043. arXiv: 1609.08157 [hep-ph].

[35] Javier Fuentes-Martin et al. "Charm physics confronts high-p_T lepton tails". In: *JHEP* 11 (2020), p. 080. DOI: 10.1007/JHEP11(2020)080. arXiv: 2003.12421 [hep-ph].

[36] Stefan Bißmann et al. "Top and Beauty synergies in SMEFT-fits at present and future colliders". In: *JHEP* 06 (2021), p. 010. DOI: 10.1007/JHEP06(2021)010. arXiv: 2012.10456 [hep-ph].

[37] Sebastian Bruggisser et al. "The Flavor of UV Physics". In: *JHEP* 05 (2021), p. 257. DOI: 10.1007/JHEP05(2021)257. arXiv: 2101.07273 [hep-ph].

[38] Sebastian Bruggisser, Danny van Dyk, and Susanne Westhoff. "Resolving the flavor structure in the MFV-SMEFT". In: *JHEP* 02 (2023), p. 225. DOI: 10.1007/JHEP02(2023)225. arXiv: 2212.02532 [hep-ph].

[39] Admir Greljo et al. "Rare b decays meet high-mass Drell-Yan". In: *JHEP* 05 (2023), p. 087. DOI: 10.1007/JHEP05(2023)087. arXiv: 2212.10497 [hep-ph].

[40] Luca Mantani and Veronica Sanz. "Probing the flavour-blind SMEFT: EFT validity and the interplay of energy scales". In: (Mar. 2025). arXiv: 2503.02935 [hep-ph].

[41] G. D'Ambrosio et al. "Minimal flavor violation: An Effective field theory approach". In: *Nucl. Phys. B* 645 (2002), pp. 155–187. DOI: 10.1016/S0550-3213(02)00836-2. arXiv: hep-ph/0207036.

[42] Roel Aaij et al. "Measurement of CP-Averaged Observables in the $B^0 \to K^{*0}\mu^+\mu^-$ Decay". In: *Phys. Rev. Lett.* 125.1 (2020), p. 011802. DOI: 10.1103/PhysRevLett.125.011802. arXiv: 2003.04831 [hep-ex].

[43] D. P. Aguillard et al. "Measurement of the Positive Muon Anomalous Magnetic Moment to 0.20 ppm". In: *Phys. Rev. Lett.* 131.16 (2023), p. 161802. DOI: 10.1103/PhysRevLett.131.161802. arXiv: 2308.06230 [hep-ex].

[44] R. Aaij et al. "Test of lepton universality in $b \to s\ell^+\ell^-$ decays". In: *Phys. Rev. Lett.* 131.5 (2023), p. 051803. DOI: 10.1103/PhysRevLett.131.051803. arXiv: 2212.09152 [hep-ex].

[45] R. Aaij et al. "Measurement of lepton universality parameters in $B^+ \to K^+\ell^+\ell^-$ and $B^0 \to K^{*0}\ell^+\ell^-$ decays". In: *Phys. Rev. D* 108.3 (2023), p. 032002. DOI: 10.1103/PhysRevD.108.032002. arXiv: 2212.09153 [hep-ex].

[46] Michael E. Peskin and Daniel V. Schroeder. *An Introduction to quantum field theory*. Reading, USA: Addison-Wesley, 1995. DOI: 10.1201/9780429503559.

[47] Steven Weinberg. *The Quantum theory of fields. Vol. 1: Foundations*. Cambridge University Press, June 2005. DOI: 10.1017/CBO9781139644167.

[48] Steven Weinberg. *The quantum theory of fields. Vol. 2: Modern applications*. Cambridge University Press, Aug. 2013. DOI: 10.1017/CBO9781139644174.

[49] Matthew D. Schwartz. *Quantum Field Theory and the Standard Model*. Cambridge University Press, Mar. 2014.

[50] H. Fritzsch, Murray Gell-Mann, and H. Leutwyler. "Advantages of the Color Octet Gluon Picture". In: *Phys. Lett. B* 47 (1973), pp. 365–368. DOI: 10.1016/0370-2693(73)90625-4.

[51] David J. Gross and Frank Wilczek. “Ultraviolet Behavior of Nonabelian Gauge Theories”. In: *Phys. Rev. Lett.* 30 (1973). Ed. by J. C. Taylor, pp. 1343–1346. DOI: 10.1103/PhysRevLett.30.1343.

[52] H. David Politzer. “Reliable Perturbative Results for Strong Interactions?” In: *Phys. Rev. Lett.* 30 (1973). Ed. by J. C. Taylor, pp. 1346–1349. DOI: 10.1103/PhysRevLett.30.1346.

[53] William J. Marciano and Heinz Pagels. “Quantum Chromodynamics: A Review”. In: *Phys. Rept.* 36 (1978), p. 137. DOI: 10.1016/0370-1573(78)90208-9.

[54] W. Pauli. “Über den Zusammenhang des Abschlusses der Elektronengruppen im Atom mit der Komplexstruktur der Spektren”. In: *Z. Phys.* 31.1 (1925), pp. 765–783. DOI: 10.1007/BF02980631.

[55] R. P. Feynman and Murray Gell-Mann. “Theory of Fermi interaction”. In: *Phys. Rev.* 109 (1958). Ed. by L. M. Brown, pp. 193–198. DOI: 10.1103/PhysRev.109.193.

[56] E. C. G. Sudarshan and R. e. Marshak. “Chirality invariance and the universal Fermi interaction”. In: *Phys. Rev.* 109 (1958), pp. 1860–1860. DOI: 10.1103/PhysRev.109.1860.2.

[57] M. Gell-Mann. “Isotopic Spin and New Unstable Particles”. In: *Phys. Rev.* 92 (1953), pp. 833–834. DOI: 10.1103/PhysRev.92.833.

[58] Murray Gell-Mann. “Symmetries of baryons and mesons”. In: *Phys. Rev.* 125 (1962), pp. 1067–1084. DOI: 10.1103/PhysRev.125.1067.

[59] F. Englert and R. Brout. “Broken Symmetry and the Mass of Gauge Vector Mesons”. In: *Phys. Rev. Lett.* 13 (1964). Ed. by J. C. Taylor, pp. 321–323. DOI: 10.1103/PhysRevLett.13.321.

[60] Peter W. Higgs. “Broken symmetries, massless particles and gauge fields”. In: *Phys. Lett.* 12 (1964), pp. 132–133. DOI: 10.1016/0031-9163(64)91136-9.

[61] Peter W. Higgs. “Broken Symmetries and the Masses of Gauge Bosons”. In: *Phys. Rev. Lett.* 13 (1964). Ed. by J. C. Taylor, pp. 508–509. DOI: 10.1103/PhysRevLett.13.508.

[62] G. S. Guralnik, C. R. Hagen, and T. W. B. Kibble. “Global Conservation Laws and Massless Particles”. In: *Phys. Rev. Lett.* 13 (1964). Ed. by J. C. Taylor, pp. 585–587. DOI: 10.1103/PhysRevLett.13.585.

[63] Peter W. Higgs. “Spontaneous Symmetry Breakdown without Massless Bosons”. In: *Phys. Rev.* 145 (1966), pp. 1156–1163. DOI: 10.1103/PhysRev.145.1156.

[64] Hideki Yukawa. “On the Interaction of Elementary Particles I”. In: *Proc. Phys. Math. Soc. Jap.* 17 (1935), pp. 48–57. DOI: 10.1143/PTPS.1.1.

[65] Nicola Cabibbo. “Unitary Symmetry and Leptonic Decays”. In: *Phys. Rev. Lett.* 10 (1963), pp. 531–533. DOI: 10.1103/PhysRevLett.10.531.

[66] Makoto Kobayashi and Toshihide Maskawa. “CP Violation in the Renormalizable Theory of Weak Interaction”. In: *Prog. Theor. Phys.* 49 (1973), pp. 652–657. DOI: 10.1143/PTP.49.652.

[67] B. Pontecorvo. “Mesonium and anti-mesonium”. In: *Sov. Phys. JETP* 6 (1957), p. 429.

[68] B. Pontecorvo. “Neutrino Experiments and the Problem of Conservation of Leptonic Charge”. In: *Zh. Eksp. Teor. Fiz.* 53 (1967), pp. 1717–1725.

[69] Ziro Maki, Masami Nakagawa, and Shoichi Sakata. “Remarks on the unified model of elementary particles”. In: *Prog. Theor. Phys.* 28 (1962), pp. 870–880. DOI: 10.1143/PTP.28.870.

[70] Ettore Majorana. “Teoria simmetrica dell’elettrone e del positrone”. In: *Nuovo Cim.* 14 (1937), pp. 171–184. DOI: 10.1007/BF02961314.

[71] Lincoln Wolfenstein. “Parametrization of the Kobayashi-Maskawa Matrix”. In: *Phys. Rev. Lett.* 51 (1983), p. 1945. DOI: 10.1103/PhysRevLett.51.1945.

[72] Y. Fukuda et al. “Evidence for oscillation of atmospheric neutrinos”. In: *Phys. Rev. Lett.* 81 (1998), pp. 1562–1567. DOI: 10.1103/PhysRevLett.81.1562. arXiv: hep-ex/9807003.

[73] S. L. Glashow, J. Iliopoulos, and L. Maiani. “Weak Interactions with Lepton-Hadron Symmetry”. In: *Phys. Rev. D* 2 (1970), pp. 1285–1292. DOI: 10.1103/PhysRevD.2.1285.

[74] C. G. Bollini and J. J. Giambiagi. “Dimensional Renormalization: The Number of Dimensions as a Regularizing Parameter”. In: *Nuovo Cim. B* 12 (1972), pp. 20–26. DOI: 10.1007/BF02895558.

[75] Gerard ’t Hooft and M. J. G. Veltman. “Regularization and Renormalization of Gauge Fields”. In: *Nucl. Phys. B* 44 (1972), pp. 189–213. DOI: 10.1016/0550-3213(72)90279-9.

[76] L. D. Landau and I. Ya. Pomeranchuk. “On point interactions in quantum electrodynamics”. In: *Dokl. Akad. Nauk SSSR* 102.3 (1955), pp. 489–492. DOI: 10.1016/B978-0-08-010586-4.50091-2.

[77] Gerard ’t Hooft. “A Planar Diagram Theory for Strong Interactions”. In: *Nucl. Phys. B* 72 (1974). Ed. by J. C. Taylor, p. 461. DOI: 10.1016/0550-3213(74)90154-0.

[78] Kenneth G. Wilson. “Confinement of Quarks”. In: *Phys. Rev. D* 10 (1974). Ed. by J. C. Taylor, pp. 2445–2459. DOI: 10.1103/PhysRevD.10.2445.

[79] P. A. Baikov, K. G. Chetyrkin, and J. H. Kühn. “Five-Loop Running of the QCD coupling constant”. In: *Phys. Rev. Lett.* 118.8 (2017), p. 082002. DOI: 10.1103/PhysRevLett.118.082002. arXiv: 1606.08659 [hep-ph].

[80] F. Herzog et al. “The five-loop beta function of Yang-Mills theory with fermions”. In: *JHEP* 02 (2017), p. 090. DOI: 10.1007/JHEP02(2017)090. arXiv: 1701.01404 [hep-ph].

[81] R. P. Feynman. “Quantum theory of gravitation”. In: *Acta Phys. Polon.* 24 (1963). Ed. by Jong-Ping Hsu and D. Fine, pp. 697–722.

[82] Gerard ’t Hooft and M. J. G. Veltman. “One loop divergencies in the theory of gravitation”. In: *Ann. Inst. H. Poincare A Phys. Theor.* 20 (1974), pp. 69–94.

[83] Steven Weinberg. “ULTRAVIOLET DIVERGENCES IN QUANTUM THEORIES OF GRAVITATION”. In: *General Relativity: An Einstein Centenary Survey*. 1980, pp. 790–831.

[84] Peter Minkowski. “$\mu \to e\gamma$ at a Rate of One Out of 10^9 Muon Decays?” In: *Phys. Lett. B* 67 (1977), pp. 421–428. DOI: 10.1016/0370-2693(77)90435-X.

[85] Tsutomu Yanagida. “Horizontal Symmetry and Masses of Neutrinos”. In: *Prog. Theor. Phys.* 64 (1980), p. 1103. DOI: 10.1143/PTP.64.1103.

[86] Rabindra N. Mohapatra and Goran Senjanovic. “Neutrino Mass and Spontaneous Parity Nonconservation”. In: *Phys. Rev. Lett.* 44 (1980), p. 912. DOI: 10.1103/PhysRevLett.44.912.

[87] Murray Gell-Mann, Pierre Ramond, and Richard Slansky. “Complex Spinors and Unified Theories”. In: *Conf. Proc. C* 790927 (1979), pp. 315–321. arXiv: 1306.4669 [hep-th].

[88] A. Zee. “A Theory of Lepton Number Violation, Neutrino Majorana Mass, and Oscillation”. In: *Phys. Lett. B* 93 (1980). [Erratum: Phys.Lett.B 95, 461 (1980)], p. 389. DOI: 10.1016/0370-2693(80)90349-4.

[89] K. S. Babu. “Model of ’Calculable’ Majorana Neutrino Masses”. In: *Phys. Lett. B* 203 (1988), pp. 132–136. DOI: 10.1016/0370-2693(88)91584-5.

[90] F. Zwicky. “Die Rotverschiebung von extragalaktischen Nebeln”. In: *Helv. Phys. Acta* 6 (1933), pp. 110–127. DOI: 10.1007/s10714-008-0707-4.

[91] Vera C. Rubin and W. Kent Ford Jr. “Rotation of the Andromeda Nebula from a Spectroscopic Survey of Emission Regions”. In: *Astrophys. J.* 159 (1970), pp. 379–403. DOI: 10.1086/150317.

[92] Douglas Clowe et al. “A direct empirical proof of the existence of dark matter”. In: *Astrophys. J. Lett.* 648 (2006), pp. L109–L113. DOI: 10.1086/508162. arXiv: astro-ph/0608407.

[93] Adam G. Riess et al. “Observational evidence from supernovae for an accelerating universe and a cosmological constant”. In: *Astron. J.* 116 (1998), pp. 1009–1038. DOI: 10.1086/300499. arXiv: astro-ph/9805201.

[94] S. Perlmutter et al. “Measurements of Ω and Λ from 42 High Redshift Supernovae”. In: *Astrophys. J.* 517 (1999), pp. 565–586. DOI: 10.1086/307221. arXiv: astro-ph/9812133.

[95] N. Aghanim et al. “Planck 2018 results. VI. Cosmological parameters”. In: *Astron. Astrophys.* 641 (2020). [Erratum: Astron.Astrophys. 652, C4 (2021)], A6. DOI: 10.1051/0004-6361/201833910. arXiv: 1807.06209 [astro-ph.CO].

[96] J. Wess and B. Zumino. “A Lagrangian Model Invariant Under Supergauge Transformations”. In: *Phys. Lett. B* 49 (1974), p. 52. DOI: 10.1016/0370-2693(74)90578-4.

[97] J. Wess and B. Zumino. “Supergauge Transformations in Four-Dimensions”. In: *Nucl. Phys. B* 70 (1974). Ed. by A. Salam and E. Sezgin, pp. 39–50. DOI: 10.1016/0550-3213(74)90355-1.

[98] Abdus Salam and J. A. Strathdee. “On Superfields and Fermi-Bose Symmetry”. In: *Phys. Rev. D* 11 (1975), pp. 1521–1535. DOI: 10.1103/PhysRevD.11.1521.

[99] Pierre Fayet. “Supersymmetry and Weak, Electromagnetic and Strong Interactions”. In: *Phys. Lett. B* 64 (1976), p. 159. DOI: 10.1016/0370-2693(76)90319-1.

[100] Th. Kaluza. “Zum Unitätsproblem der Physik”. In: *Sitzungsber. Preuss. Akad. Wiss. Berlin (Math. Phys.)* 1921 (1921), pp. 966–972. DOI: 10.1142/S0218271818700017. arXiv: 1803.08616 [physics.hist-ph].

[101] Oskar Klein. “Quantum Theory and Five-Dimensional Theory of Relativity. (In German and English)”. In: *Z. Phys.* 37 (1926). Ed. by J. C. Taylor, pp. 895–906. DOI: 10.1007/BF01397481.

[102] Nima Arkani-Hamed, Savas Dimopoulos, and G. R. Dvali. “The Hierarchy problem and new dimensions at a millimeter”. In: *Phys. Lett. B* 429 (1998), pp. 263–272. DOI: 10.1016/S0370-2693(98)00466-3. arXiv: hep-ph/9803315.

[103] Ignatios Antoniadis et al. “New dimensions at a millimeter to a Fermi and superstrings at a TeV”. In: *Phys. Lett. B* 436 (1998), pp. 257–263. DOI: 10.1016/S0370-2693(98)00860-0. arXiv: hep-ph/9804398.

[104] Lisa Randall and Raman Sundrum. “A Large mass hierarchy from a small extra dimension”. In: *Phys. Rev. Lett.* 83 (1999), pp. 3370–3373. DOI: 10.1103/PhysRevLett.83.3370. arXiv: hep-ph/9905221.

[105] Lisa Randall and Raman Sundrum. "An Alternative to compactification". In: *Phys. Rev. Lett.* 83 (1999), pp. 4690–4693. DOI: 10.1103/PhysRevLett.83.4690. arXiv: hep-th/9906064.

[106] R. D. Peccei and Helen R. Quinn. "CP Conservation in the Presence of Instantons". In: *Phys. Rev. Lett.* 38 (1977), pp. 1440–1443. DOI: 10.1103/PhysRevLett.38.1440.

[107] R. D. Peccei and Helen R. Quinn. "Constraints Imposed by CP Conservation in the Presence of Instantons". In: *Phys. Rev. D* 16 (1977), pp. 1791–1797. DOI: 10.1103/PhysRevD.16.1791.

[108] Steven Weinberg. "A New Light Boson?" In: *Phys. Rev. Lett.* 40 (1978), pp. 223–226. DOI: 10.1103/PhysRevLett.40.223.

[109] Frank Wilczek. "Problem of Strong P and T Invariance in the Presence of Instantons". In: *Phys. Rev. Lett.* 40 (1978), pp. 279–282. DOI: 10.1103/PhysRevLett.40.279.

[110] A. D. Sakharov. "Violation of CP Invariance, C asymmetry, and baryon asymmetry of the universe". In: *Pisma Zh. Eksp. Teor. Fiz.* 5 (1967), pp. 32–35. DOI: 10.1070/PU1991v034n05ABEH002497.

[111] David B. Kaplan and Howard Georgi. "SU(2) x U(1) Breaking by Vacuum Misalignment". In: *Phys. Lett. B* 136 (1984), pp. 183–186. DOI: 10.1016/0370-2693(84)91177-8.

[112] David B. Kaplan, Howard Georgi, and Savas Dimopoulos. "Composite Higgs Scalars". In: *Phys. Lett. B* 136 (1984), pp. 187–190. DOI: 10.1016/0370-2693(84)91178-X.

[113] Roberto Contino. "The Higgs as a Composite Nambu-Goldstone Boson". In: *Theoretical Advanced Study Institute in Elementary Particle Physics: Physics of the Large and the Small*. 2011, pp. 235–306. DOI: 10.1142/9789814327183_0005. arXiv: 1005.4269 [hep-ph].

[114] Nima Arkani-Hamed, Andrew G. Cohen, and Howard Georgi. "Electroweak symmetry breaking from dimensional deconstruction". In: *Phys. Lett. B* 513 (2001), pp. 232–240. DOI: 10.1016/S0370-2693(01)00741-9. arXiv: hep-ph/0105239.

[115] N. Arkani-Hamed et al. "The Littlest Higgs". In: *JHEP* 07 (2002), p. 034. DOI: 10.1088/1126-6708/2002/07/034. arXiv: hep-ph/0206021.

[116] Leonard Susskind. "Dynamics of Spontaneous Symmetry Breaking in the Weinberg-Salam Theory". In: *Phys. Rev. D* 20 (1979), pp. 2619–2625. DOI: 10.1103/PhysRevD.20.2619.

[117] C. D. Froggatt and Holger Bech Nielsen. "Hierarchy of Quark Masses, Cabibbo Angles and CP Violation". In: *Nucl. Phys. B* 147 (1979), pp. 277–298. DOI: 10.1016/0550-3213(79)90316-X.

[118] H. Georgi and S. L. Glashow. "Unity of All Elementary Particle Forces". In: *Phys. Rev. Lett.* 32 (1974), pp. 438–441. DOI: 10.1103/PhysRevLett.32.438.

[119] Jogesh C. Pati and Abdus Salam. "Lepton Number as the Fourth Color". In: *Phys. Rev. D* 10 (1974). [Erratum: Phys.Rev.D 11, 703–703 (1975)], pp. 275–289. DOI: 10.1103/PhysRevD.10.275.

[120] H. Georgi, Helen R. Quinn, and Steven Weinberg. "Hierarchy of Interactions in Unified Gauge Theories". In: *Phys. Rev. Lett.* 33 (1974), pp. 451–454. DOI: 10.1103/PhysRevLett.33.451.

[121] A. Abada et al. "FCC Physics Opportunities: Future Circular Collider Conceptual Design Report Volume 1". In: *Eur. Phys. J. C* 79.6 (2019), p. 474. DOI: 10.1140/epjc/s10052-019-6904-3.

[122] A. Abada et al. “FCC-ee: The Lepton Collider: Future Circular Collider Conceptual Design Report Volume 2”. In: *Eur. Phys. J. ST* 228.2 (2019), pp. 261–623. DOI: 10.1140/epjst/e2019-900045-4.

[123] M. Benedikt et al. “Future Circular Collider Feasibility Study Report: Volume 1, Physics, Experiments, Detectors”. In: (Apr. 2025). DOI: 10.17181/CERN.9DKX.TDH9. arXiv: 2505.00272 [hep-ex].

[124] M. Benedikt et al. “Future Circular Collider Feasibility Study Report: Volume 2, Accelerators, Technical Infrastructure and Safety”. In: (Apr. 2025). DOI: 10.17181/CERN.EBAY.7W4X. arXiv: 2505.00274 [physics.acc-ph].

[125] M. Benedikt et al. “Future Circular Collider Feasibility Study Report: Volume 3, Civil Engineering, Implementation and Sustainability”. In: (Mar. 2025). DOI: 10.17181/CERN.I26X.V4VF. arXiv: 2505.00273 [physics.acc-ph].

[126] A. Abada et al. “FCC-hh: The Hadron Collider: Future Circular Collider Conceptual Design Report Volume 3”. In: *Eur. Phys. J. ST* 228.4 (2019), pp. 755–1107. DOI: 10.1140/epjst/e2019-900087-0.

[127] M. Benedikt et al. “Future Circular Hadron Collider FCC-hh: Overview and Status”. In: (Mar. 2022). arXiv: 2203.07804 [physics.acc-ph].

[128] “A Multi-TeV Linear Collider Based on CLIC Technology: CLIC Conceptual Design Report”. In: (Oct. 2012). Ed. by M Aicheler et al. DOI: 10.5170/CERN-2012-007.

[129] T. K. Charles et al. “The Compact Linear Collider (CLIC) - 2018 Summary Report”. In: 2/2018 (Dec. 2018). Ed. by P. N. Burrows et al. DOI: 10.23731/CYRM-2018-002. arXiv: 1812.06018 [physics.acc-ph].

[130] J. de Blas et al. “The CLIC Potential for New Physics”. In: 3/2018 (Dec. 2018). DOI: 10.23731/CYRM-2018-003. arXiv: 1812.02093 [hep-ph].

[131] “The Compact Linear Collider (CLIC) - Project Implementation Plan”. In: 4/2018 (Dec. 2018). Ed. by M. Aicheler et al. DOI: 10.23731/CYRM-2018-004. arXiv: 1903.08655 [physics.acc-ph].

[132] Elizabeth E. Jenkins, Aneesh V. Manohar, and Peter Stoffer. “Low-Energy Effective Field Theory below the Electroweak Scale: Operators and Matching”. In: *JHEP* 03 (2018). [Erratum: JHEP 12, 043 (2023)], p. 016. DOI: 10.1007/JHEP03(2018)016. arXiv: 1709.04486 [hep-ph].

[133] Thomas Appelquist and J. Carazzone. “Infrared Singularities and Massive Fields”. In: *Phys. Rev. D* 11 (1975), p. 2856. DOI: 10.1103/PhysRevD.11.2856.

[134] Kenneth G. Wilson. “Nonlagrangian models of current algebra”. In: *Phys. Rev.* 179 (1969), pp. 1499–1512. DOI: 10.1103/PhysRev.179.1499.

[135] E. Fermi. “An attempt of a theory of beta radiation. 1.” In: *Z. Phys.* 88 (1934), pp. 161–177. DOI: 10.1007/BF01351864.

[136] C. S. Wu et al. “Experimental Test of Parity Conservation in β Decay”. In: *Phys. Rev.* 105 (1957), pp. 1413–1414. DOI: 10.1103/PhysRev.105.1413.

[137] Ilaria Brivio and Michael Trott. “The Standard Model as an Effective Field Theory”. In: *Phys. Rept.* 793 (2019), pp. 1–98. DOI: 10.1016/j.physrep.2018.11.002. arXiv: 1706.08945 [hep-ph].

[138] Kaustubh Agashe, Roberto Contino, and Alex Pomarol. “The Minimal composite Higgs model”. In: *Nucl. Phys. B* 719 (2005), pp. 165–187. DOI: 10.1016/j.nuclphysb.2005.04.035. arXiv: hep-ph/0412089.

[139] Giuliano Panico and Andrea Wulzer. *The Composite Nambu-Goldstone Higgs*. Vol. 913. Springer, 2016. DOI: 10.1007/978-3-319-22617-0. arXiv: 1506.01961 [hep-ph].

[140] R. Alonso et al. "The Effective Chiral Lagrangian for a Light Dynamical "Higgs Particle"". In: *Phys. Lett. B* 722 (2013). [Erratum: Phys.Lett.B 726, 926 (2013)], pp. 330–335. DOI: 10.1016/j.physletb.2013.04.037. arXiv: 1212.3305 [hep-ph].

[141] Gerhard Buchalla, Oscar Catà, and Claudius Krause. "Complete Electroweak Chiral Lagrangian with a Light Higgs at NLO". In: *Nucl. Phys. B* 880 (2014). [Erratum: Nucl.Phys.B 913, 475–478 (2016)], pp. 552–573. DOI: 10.1016/j.nuclphysb.2014.01.018. arXiv: 1307.5017 [hep-ph].

[142] Armen Tumasyan et al. "A portrait of the Higgs boson by the CMS experiment ten years after the discovery." In: *Nature* 607.7917 (2022). [Erratum: Nature 623, (2023)], pp. 60–68. DOI: 10.1038/s41586-022-04892-x. arXiv: 2207.00043 [hep-ex].

[143] Georges Aad et al. "Characterising the Higgs boson with ATLAS data from Run 2 of the LHC". In: *Phys. Rept.* 11 (2024), p. 001. DOI: 10.1016/j.physrep.2024.11.001. arXiv: 2404.05498 [hep-ex].

[144] Javier Fuentes-Martin, Jorge Portoles, and Pedro Ruiz-Femenia. "Integrating out heavy particles with functional methods: a simplified framework". In: *JHEP* 09 (2016), p. 156. DOI: 10.1007/JHEP09(2016)156. arXiv: 1607.02142 [hep-ph].

[145] Adrian Carmona et al. "Matchmakereft: automated tree-level and one-loop matching". In: *SciPost Phys.* 12.6 (2022), p. 198. DOI: 10.21468/SciPostPhys.12.6.198. arXiv: 2112.10787 [hep-ph].

[146] Javier Fuentes-Martín et al. "A proof of concept for matchete: an automated tool for matching effective theories". In: *Eur. Phys. J. C* 83.7 (2023), p. 662. DOI: 10.1140/epjc/s10052-023-11726-1. arXiv: 2212.04510 [hep-ph].

[147] Stefano De Angelis and Gauthier Durieux. "EFT matching from analyticity and unitarity". In: *SciPost Phys.* 16 (2024), p. 071. DOI: 10.21468/SciPostPhys.16.3.071. arXiv: 2308.00035 [hep-ph].

[148] Jaco ter Hoeve et al. "The automation of SMEFT-assisted constraints on UV-complete models". In: *JHEP* 01 (2024), p. 179. DOI: 10.1007/JHEP01(2024)179. arXiv: 2309.04523 [hep-ph].

[149] Mikael Chala et al. "Efficient on-shell matching". In: (Nov. 2024). arXiv: 2411.12798 [hep-ph].

[150] Florian Bonnet et al. "Systematic study of the d=5 Weinberg operator at one-loop order". In: *JHEP* 07 (2012), p. 153. DOI: 10.1007/JHEP07(2012)153. arXiv: 1204.5862 [hep-ph].

[151] Benjamin Fuks et al. "Probing the Weinberg operator at colliders". In: *Phys. Rev. D* 103.11 (2021), p. 115014. DOI: 10.1103/PhysRevD.103.115014. arXiv: 2012.09882 [hep-ph].

[152] Andreas Helset and Andrew Kobach. "Baryon Number, Lepton Number, and Operator Dimension in the SMEFT with Flavor Symmetries". In: *Phys. Lett. B* 800 (2020), p. 135132. DOI: 10.1016/j.physletb.2019.135132. arXiv: 1909.05853 [hep-ph].

[153] Kåre Fridell et al. "Probing lepton number violation: a comprehensive survey of dimension-7 SMEFT". In: *JHEP* 05 (2024), p. 154. DOI: 10.1007/JHEP05(2024)154. arXiv: 2306.08709 [hep-ph].

[154] Arnau Bas Beneito I et al. “An EFT approach to baryon number violation: lower limits on the new physics scale and correlations between nucleon decay modes”. In: *JHEP* 07 (2024), p. 004. DOI: 10.1007/JHEP07(2024)004. arXiv: 2312.13361 [hep-ph].

[155] Hector Gisbert, Antonio Rodríguez-Sánchez, and Luiz Vale Silva. “Baryon number violation with top quark operators in the SMEFT”. In: (Aug. 2024). arXiv: 2409.00218 [hep-ph].

[156] Landon Lehman. “Extending the Standard Model Effective Field Theory with the Complete Set of Dimension-7 Operators”. In: *Phys. Rev. D* 90.12 (2014), p. 125023. DOI: 10.1103/PhysRevD.90.125023. arXiv: 1410.4193 [hep-ph].

[157] Landon Lehman and Adam Martin. “Low-derivative operators of the Standard Model effective field theory via Hilbert series methods”. In: *JHEP* 02 (2016), p. 081. DOI: 10.1007/JHEP02(2016)081. arXiv: 1510.00372 [hep-ph].

[158] Brian Henning et al. “2, 84, 30, 993, 560, 15456, 11962, 261485, ...: Higher dimension operators in the SM EFT”. In: *JHEP* 08 (2017). [Erratum: JHEP 09, 019 (2019)], p. 016. DOI: 10.1007/JHEP08(2017)016. arXiv: 1512.03433 [hep-ph].

[159] Christopher W. Murphy. “Dimension-8 operators in the Standard Model Effective Field Theory”. In: *JHEP* 10 (2020), p. 174. DOI: 10.1007/JHEP10(2020)174. arXiv: 2005.00059 [hep-ph].

[160] Simone Alioli et al. “Theoretical developments in the SMEFT at dimension-8 and beyond”. In: *Snowmass 2021*. Mar. 2022. arXiv: 2203.06771 [hep-ph].

[161] Radja Boughezal, Yingsheng Huang, and Frank Petriello. “Exploring the SMEFT at dimension eight with Drell-Yan transverse momentum measurements”. In: *Phys. Rev. D* 106.3 (2022), p. 036020. DOI: 10.1103/PhysRevD.106.036020. arXiv: 2207.01703 [hep-ph].

[162] Lukas Allwicher et al. “Drell-Yan tails beyond the Standard Model”. In: *JHEP* 03 (2023), p. 064. DOI: 10.1007/JHEP03(2023)064. arXiv: 2207.10714 [hep-ph].

[163] Tyler Corbett et al. “Impact of dimension-eight SMEFT operators in the electroweak precision observables and triple gauge couplings analysis in universal SMEFT”. In: *Phys. Rev. D* 107.11 (2023), p. 115013. DOI: 10.1103/PhysRevD.107.115013. arXiv: 2304.03305 [hep-ph].

[164] Yi Liao, Xiao-Dong Ma, and Hao-Lin Wang. “Probing dimension-8 SMEFT operators through neutral meson mixing”. In: *JHEP* 03 (2025), p. 133. DOI: 10.1007/JHEP03(2025)133. arXiv: 2409.10305 [hep-ph].

[165] Sally Dawson, Samuel Homiller, and Matthew Sullivan. “Impact of dimension-eight SMEFT contributions: A case study”. In: *Phys. Rev. D* 104.11 (2021), p. 115013. DOI: 10.1103/PhysRevD.104.115013. arXiv: 2110.06929 [hep-ph].

[166] Sally Dawson et al. “Role of dimension-eight operators in an EFT for the 2HDM”. In: *Phys. Rev. D* 106.5 (2022), p. 055012. DOI: 10.1103/PhysRevD.106.055012. arXiv: 2205.01561 [hep-ph].

[167] Céline Degrande and Hao-Lin Li. “Impact of dimension-8 SMEFT operators on diboson productions”. In: *JHEP* 06 (2023), p. 149. DOI: 10.1007/JHEP06(2023)149. arXiv: 2303.10493 [hep-ph].

[168] John Ellis, Ken Mimasu, and Francesca Zampedri. “Dimension-8 SMEFT analysis of minimal scalar field extensions of the Standard Model”. In: *JHEP* 10 (2023), p. 051. DOI: 10.1007/JHEP10(2023)051. arXiv: 2304.06663 [hep-ph].

[169] B. Grzadkowski et al. “Dimension-Six Terms in the Standard Model Lagrangian”. In: *JHEP* 10 (2010), p. 085. DOI: 10.1007/JHEP10(2010)085. arXiv: 1008.4884 [hep-ph].

[170] G. F. Giudice et al. “The Strongly-Interacting Light Higgs”. In: *JHEP* 06 (2007), p. 045. DOI: 10.1088/1126-6708/2007/06/045. arXiv: hep-ph/0703164.

[171] Roberto Contino et al. “Effective Lagrangian for a light Higgs-like scalar”. In: *JHEP* 07 (2013), p. 035. DOI: 10.1007/JHEP07(2013)035. arXiv: 1303.3876 [hep-ph].

[172] Kaoru Hagiwara et al. “Low-energy effects of new interactions in the electroweak boson sector”. In: *Phys. Rev. D* 48 (1993), pp. 2182–2203. DOI: 10.1103/PhysRevD.48.2182.

[173] Elizabeth E. Jenkins, Aneesh V. Manohar, and Michael Trott. “Renormalization Group Evolution of the Standard Model Dimension Six Operators I: Formalism and lambda Dependence”. In: *JHEP* 10 (2013), p. 087. DOI: 10.1007/JHEP10(2013)087. arXiv: 1308.2627 [hep-ph].

[174] Elizabeth E. Jenkins, Aneesh V. Manohar, and Michael Trott. “Renormalization Group Evolution of the Standard Model Dimension Six Operators II: Yukawa Dependence”. In: *JHEP* 01 (2014), p. 035. DOI: 10.1007/JHEP01(2014)035. arXiv: 1310.4838 [hep-ph].

[175] Rodrigo Alonso et al. “Renormalization Group Evolution of the Standard Model Dimension Six Operators III: Gauge Coupling Dependence and Phenomenology”. In: *JHEP* 04 (2014), p. 159. DOI: 10.1007/JHEP04(2014)159. arXiv: 1312.2014 [hep-ph].

[176] Jason Aebischer, Jacky Kumar, and David M. Straub. “Wilson: a Python package for the running and matching of Wilson coefficients above and below the electroweak scale”. In: *Eur. Phys. J. C* 78.12 (2018), p. 1026. DOI: 10.1140/epjc/s10052-018-6492-7. arXiv: 1804.05033 [hep-ph].

[177] Laure Berthier and Michael Trott. “Towards consistent Electroweak Precision Data constraints in the SMEFT”. In: *JHEP* 05 (2015), p. 024. DOI: 10.1007/JHEP05(2015)024. arXiv: 1502.02570 [hep-ph].

[178] Laure Berthier and Michael Trott. “Consistent constraints on the Standard Model Effective Field Theory”. In: *JHEP* 02 (2016), p. 069. DOI: 10.1007/JHEP02(2016)069. arXiv: 1508.05060 [hep-ph].

[179] Ilaria Brivio and Michael Trott. “Scheming in the SMEFT... and a reparameterization invariance!” In: *JHEP* 07 (2017). [Addendum: JHEP 05, 136 (2018)], p. 148. DOI: 10.1007/JHEP07(2017)148. arXiv: 1701.06424 [hep-ph].

[180] Ilaria Brivio, Yun Jiang, and Michael Trott. “The SMEFTsim package, theory and tools”. In: *JHEP* 12 (2017), p. 070. DOI: 10.1007/JHEP12(2017)070. arXiv: 1709.06492 [hep-ph].

[181] Anke Biekötter et al. “Electroweak input schemes and universal corrections in SMEFT”. In: *JHEP* 07 (2023), p. 115. DOI: 10.1007/JHEP07(2023)115. arXiv: 2305.03763 [hep-ph].

[182] Sébastien Descotes-Genon et al. “The CKM parameters in the SMEFT”. In: *JHEP* 05 (2019), p. 172. DOI: 10.1007/JHEP05(2019)172. arXiv: 1812.08163 [hep-ph].

[183] Admir Greljo, Ajdin Palavrić, and Anders Eller Thomsen. “Adding Flavor to the SMEFT”. In: *JHEP* 10 (2022), p. 010. DOI: 10.1007/JHEP10(2022)005. arXiv: 2203.09561 [hep-ph].

[184] Tobias Hurth, Sophie Renner, and William Shepherd. “Matching for FCNC effects in the flavour-symmetric SMEFT”. In: *JHEP* 06 (2019), p. 029. DOI: 10.1007/JHEP06(2019)029. arXiv: 1903.00500 [hep-ph].

[185] Darius A. Faroughy et al. “Flavour symmetries in the SMEFT”. In: *JHEP* 08 (2020), p. 166. DOI: 10.1007/JHEP08(2020)166. arXiv: 2005.05366 [hep-ph].

[186] Admir Greljo, Ajdin Palavrić, and Aleks Smolkovič. “Leading directions in the SMEFT: Renormalization effects”. In: *Phys. Rev. D* 109.7 (2024), p. 075033. DOI: 10.1103/PhysRevD.109.075033. arXiv: 2312.09179 [hep-ph].

[187] Lukas Allwicher et al. “Probing third-generation New Physics with $K\to\pi\nu\nu^{-}$ and $B\to K(*)\nu\nu^{-}$”. In: *Phys. Lett. B* 861 (2025), p. 139295. DOI: 10.1016/j.physletb.2025.139295. arXiv: 2410.21444 [hep-ph].

[188] Rafael Aoude et al. “The impact of flavour data on global fits of the MFV SMEFT”. In: *JHEP* 12 (2020), p. 113. DOI: 10.1007/JHEP12(2020)113. arXiv: 2003.05432 [hep-ph].

[189] Riccardo Bartocci, Anke Biekötter, and Tobias Hurth. “A global analysis of the SMEFT under the minimal MFV assumption”. In: *JHEP* 05 (2024), p. 074. DOI: 10.1007/JHEP05(2024)074. arXiv: 2311.04963 [hep-ph].

[190] Arthur Cayley. “A memoir on the theory of matrices”. In: *Philosophical transactions of the Royal Society of London* 148 (2009), pp. 17–37.

[191] William Rowan Hamilton. *Lectures on Quaternions*. eng. London: Hodges and Smith, 1853. URL: http://eudml.org/doc/203375.

[192] W. Buchmuller, R. Ruckl, and D. Wyler. “Leptoquarks in Lepton - Quark Collisions”. In: *Phys. Lett. B* 191 (1987). [Erratum: Phys.Lett.B 448, 320–320 (1999)], pp. 442–448. DOI: 10.1016/0370-2693(87)90637-X.

[193] X. G. He et al. “NEW Z-prime PHENOMENOLOGY”. In: *Phys. Rev. D* 43 (1991), pp. 22–24. DOI: 10.1103/PhysRevD.43.R22.

[194] Wouter Dekens and Peter Stoffer. “Low-energy effective field theory below the electroweak scale: matching at one loop”. In: *JHEP* 10 (2019). [Erratum: JHEP 11, 148 (2022)], p. 197. DOI: 10.1007/JHEP10(2019)197. arXiv: 1908.05295 [hep-ph].

[195] Elizabeth E. Jenkins, Aneesh V. Manohar, and Peter Stoffer. “Low-Energy Effective Field Theory below the Electroweak Scale: Anomalous Dimensions”. In: *JHEP* 01 (2018). [Erratum: JHEP 12, 042 (2023)], p. 084. DOI: 10.1007/JHEP01(2018)084. arXiv: 1711.05270 [hep-ph].

[196] G. Cowan. *Statistical data analysis*. 1998.

[197] E. T. Jaynes. *Probability Theory: The Logic of Science*. CUP, 2003.

[198] Frederick James. *Statistical methods in experimental physics*. 2006.

[199] Thomas Bayes Rev. “An essay toward solving a problem in the doctrine of chances”. In: *Phil. Trans. Roy. Soc. Lond.* 53 (1764), pp. 370–418. DOI: 10.1098/rstl.1763.0053.

[200] Giulio D’Agostini. *Bayesian Reasoning in Data Analysis: A Critical Introduction*. Singapore: World Scientific, 2003. DOI: 10.1142/5262. URL: https://cds.cern.ch/record/642515.

[201] Tyler Corbett et al. “Drell-Yan production in universal theories beyond dimension-six SMEFT”. In: (Mar. 2025). arXiv: 2503.19962 [hep-ph].

[202] Admir Greljo et al. “Parton distributions in the SMEFT from high-energy Drell-Yan tails”. In: *JHEP* 07 (2021), p. 122. DOI: 10.1007/JHEP07(2021)122. arXiv: 2104.02723 [hep-ph].

[203] Hesham El Faham et al. “Single top production in association with a WZ pair at the LHC in the SMEFT”. In: *JHEP* 01 (2022), p. 100. DOI: 10.1007/JHEP01(2022)100. arXiv: 2111.03080 [hep-ph].

[204] Rafael Aoude et al. “Quantum SMEFT tomography: Top quark pair production at the LHC”. In: *Phys. Rev. D* 106.5 (2022), p. 055007. DOI: 10.1103/PhysRevD.106.055007. arXiv: 2203.05619 [hep-ph].

[205] Fabio Maltoni, Giuseppe Ventura, and Eleni Vryonidou. “Impact of SMEFT renormalisation group running on Higgs production at the LHC”. In: *JHEP* 12 (2024), p. 183. DOI: 10.1007/JHEP12(2024)183. arXiv: 2406.06670 [hep-ph].

[206] Alexander Basan et al. “Measuring the top energy asymmetry at the LHC: QCD and SMEFT interpretations”. In: *JHEP* 03 (2020), p. 184. DOI: 10.1007/JHEP03(2020)184. arXiv: 2001.07225 [hep-ph].

[207] Tommaso Giani, Giacomo Magni, and Juan Rojo. “SMEFiT: a flexible toolbox for global interpretations of particle physics data with effective field theories”. In: *Eur. Phys. J. C* 83.5 (2023), p. 393. DOI: 10.1140/epjc/s10052-023-11534-7. arXiv: 2302.06660 [hep-ph].

[208] Eugenia Celada et al. “Mapping the SMEFT at high-energy colliders: from LEP and the (HL-)LHC to the FCC-ee”. In: *JHEP* 09 (2024), p. 091. DOI: 10.1007/JHEP09(2024)091. arXiv: 2404.12809 [hep-ph].

[209] J. De Blas et al. “HEPfit: a code for the combination of indirect and direct constraints on high energy physics models”. In: *Eur. Phys. J. C* 80.5 (2020), p. 456. DOI: 10.1140/epjc/s10052-020-7904-z. arXiv: 1910.14012 [hep-ph].

[210] J. de Blas et al. “Global analysis of electroweak data in the Standard Model”. In: *Phys. Rev. D* 106.3 (2022), p. 033003. DOI: 10.1103/PhysRevD.106.033003. arXiv: 2112.07274 [hep-ph].

[211] Ilaria Brivio et al. “To profile or to marginalize - A SMEFT case study”. In: *SciPost Phys.* 16.1 (2024), p. 035. DOI: 10.21468/SciPostPhys.16.1.035. arXiv: 2208.08454 [hep-ph].

[212] Nuno Castro et al. “EFTfitter—A tool for interpreting measurements in the context of effective field theories”. In: *Eur. Phys. J. C* 76.8 (2016), p. 432. DOI: 10.1140/epjc/s10052-016-4280-9. arXiv: 1605.05585 [hep-ex].

[213] Allen Caldwell, Daniel Kollar, and Kevin Kroninger. “BAT: The Bayesian Analysis Toolkit”. In: *Comput. Phys. Commun.* 180 (2009), pp. 2197–2209. DOI: 10.1016/j.cpc.2009.06.026. arXiv: 0808.2552 [physics.data-an].

[214] Oliver Schulz et al. “BAT.jl: A Julia-Based Tool for Bayesian Inference”. In: *SN Comput. Sci.* 2.3 (2021), pp. 1–17. DOI: 10.1007/s42979-021-00626-4. arXiv: 2008.03132 [stat.CO].

[215] Stefan Bißmann et al. “Correlating uncertainties in global analyses within SMEFT matters”. In: *Phys. Rev. D* 102 (2020), p. 115019. DOI: 10.1103/PhysRevD.102.115019. arXiv: 1912.06090 [hep-ph].

[216] Johannes Buchner. “UltraNest – a robust, general purpose Bayesian inference engine”. In: (Jan. 2021). arXiv: 2101.09604 [stat.CO].

[217] Matti Vihola. “Robust adaptive Metropolis algorithm with coerced acceptance rate”. In: *Statistics and Computing* 22.5 (Sept. 2012), pp. 997–1008. ISSN: 0960-3174. DOI: 10.1007/s11222-011-9269-5. URL: https://doi.org/10.1007/s11222-011-9269-5.

[218] Georges Aad et al. “Search for the charged-lepton-flavor-violating decay $Z \to e\mu$ in pp collisions at $\sqrt{s} = 13$ TeV with the ATLAS detector”. In: *Phys. Rev. D* 108 (2023), p. 032015. DOI: 10.1103/PhysRevD.108.032015. arXiv: 2204.10783 [hep-ex].

[219] Georges Aad et al. “Search for lepton-flavor-violation in Z-boson decays with τ-leptons with the ATLAS detector”. In: *Phys. Rev. Lett.* 127 (2022), p. 271801. DOI: 10.1103/PhysRevLett.127.271801. arXiv: 2105.12491 [hep-ex].

[220] Armen Tumasyan et al. “Precision measurement of the W boson decay branching fractions in proton-proton collisions at $\sqrt{s} = 13$ TeV”. In: *Phys. Rev. D* 105.7 (2022), p. 072008. DOI: 10.1103/PhysRevD.105.072008. arXiv: 2201.07861 [hep-ex].

[221] J. Abdallah et al. “Measurement and interpretation of fermion-pair production at LEP energies above the Z resonance”. In: *Eur. Phys. J. C* 45 (2006), pp. 589–632. DOI: 10.1140/epjc/s2005-02461-0. arXiv: hep-ex/0512012.

[222] Wolfram Research Inc. *Mathematica, Version 14.2*. Champaign, IL, 2024. URL: https://www.wolfram.com/mathematica.

[223] R. Mertig, M. Bohm, and Ansgar Denner. “FEYN CALC: Computer algebraic calculation of Feynman amplitudes”. In: *Comput. Phys. Commun.* 64 (1991), pp. 345–359. DOI: 10.1016/0010-4655(91)90130-D.

[224] Vladyslav Shtabovenko, Rolf Mertig, and Frederik Orellana. “New Developments in FeynCalc 9.0”. In: *Comput. Phys. Commun.* 207 (2016), pp. 432–444. DOI: 10.1016/j.cpc.2016.06.008. arXiv: 1601.01167 [hep-ph].

[225] Vladyslav Shtabovenko, Rolf Mertig, and Frederik Orellana. “FeynCalc 9.3: New features and improvements”. In: *Comput. Phys. Commun.* 256 (2020), p. 107478. DOI: 10.1016/j.cpc.2020.107478. arXiv: 2001.04407 [hep-ph].

[226] Vladyslav Shtabovenko, Rolf Mertig, and Frederik Orellana. “FeynCalc 10: Do multiloop integrals dream of computer codes?” In: *Comput. Phys. Commun.* 306 (2025), p. 109357. DOI: 10.1016/j.cpc.2024.109357. arXiv: 2312.14089 [hep-ph].

[227] A. Dedes et al. “SmeftFR v3 – Feynman rules generator for the Standard Model Effective Field Theory”. In: *Comput. Phys. Commun.* 294 (2024), p. 108943. DOI: 10.1016/j.cpc.2023.108943. arXiv: 2302.01353 [hep-ph].

[228] Albert M Sirunyan et al. “Search for resonant and nonresonant new phenomena in high-mass dilepton final states at $\sqrt{s} = 13$ TeV”. In: *JHEP* 07 (2021), p. 208. DOI: 10.1007/JHEP07(2021)208. arXiv: 2103.02708 [hep-ex].

[229] Georges Aad et al. “Search for heavy Higgs bosons decaying into two tau leptons with the ATLAS detector using pp collisions at $\sqrt{s} = 13$ TeV”. In: *Phys. Rev. Lett.* 125.5 (2020), p. 051801. DOI: 10.1103/PhysRevLett.125.051801. arXiv: 2002.12223 [hep-ex].

[230] Georges Aad et al. “Search for lepton-flavour violation in high-mass dilepton final states using 139 fb^{-1} of pp collisions at $\sqrt{s} = 13$ TeV with the ATLAS detector”. In: *JHEP* 23 (2020), p. 082. DOI: 10.1007/JHEP10(2023)082. arXiv: 2307.08567 [hep-ex].

[231] Georges Aad et al. “Search for a heavy charged boson in events with a charged lepton and missing transverse momentum from pp collisions at $\sqrt{s} = 13$ TeV with the ATLAS detector”. In: *Phys. Rev. D* 100.5 (2019), p. 052013. DOI: 10.1103/PhysRevD.100.052013. arXiv: 1906.05609 [hep-ex].

[232] A. Tumasyan et al. “Search for new physics in the τ lepton plus missing transverse momentum final state in proton-proton collisions at $\sqrt{s} = 13$ TeV”. In: *JHEP* 09 (2023), p. 051. DOI: 10.1007/JHEP09(2023)051. arXiv: 2212.12604 [hep-ex].

[233] John C. Collins, Davison E. Soper, and George F. Sterman. "Factorization of Hard Processes in QCD". In: *Adv. Ser. Direct. High Energy Phys.* 5 (1989), pp. 1–91. DOI: 10.1142/9789814503266_0001. arXiv: hep-ph/0409313.

[234] John C. Collins, Davison E. Soper, and George F. Sterman. "Soft Gluons and Factorization". In: *Nucl. Phys. B* 308 (1988), pp. 833–856. DOI: 10.1016/0550-3213(88)90130-7.

[235] J. Alwall et al. "The automated computation of tree-level and next-to-leading order differential cross sections, and their matching to parton shower simulations". In: *JHEP* 07 (2014), p. 079. DOI: 10.1007/JHEP07(2014)079. arXiv: 1405.0301 [hep-ph].

[236] Ilaria Brivio. "SMEFTsim 3.0 — a practical guide". In: *JHEP* 04 (2021), p. 073. DOI: 10.1007/JHEP04(2021)073. arXiv: 2012.11343 [hep-ph].

[237] Neil D. Christensen and Claude Duhr. "FeynRules - Feynman rules made easy". In: *Comput. Phys. Commun.* 180 (2009), pp. 1614–1641. DOI: 10.1016/j.cpc.2009.02.018. arXiv: 0806.4194 [hep-ph].

[238] Adam Alloul et al. "FeynRules 2.0 - A complete toolbox for tree-level phenomenology". In: *Comput. Phys. Commun.* 185 (2014), pp. 2250–2300. DOI: 10.1016/j.cpc.2014.04.012. arXiv: 1310.1921 [hep-ph].

[239] Celine Degrande et al. "UFO - The Universal FeynRules Output". In: *Comput. Phys. Commun.* 183 (2012), pp. 1201–1214. DOI: 10.1016/j.cpc.2012.01.022. arXiv: 1108.2040 [hep-ph].

[240] J. Pumplin et al. "New generation of parton distributions with uncertainties from global QCD analysis". In: *JHEP* 07 (2002), p. 012. DOI: 10.1088/1126-6708/2002/07/012. arXiv: hep-ph/0201195.

[241] A. D. Martin et al. "Parton distributions for the LHC". In: *Eur. Phys. J. C* 63 (2009), pp. 189–285. DOI: 10.1140/epjc/s10052-009-1072-5. arXiv: 0901.0002 [hep-ph].

[242] Emanuele R. Nocera et al. "A first unbiased global determination of polarized PDFs and their uncertainties". In: *Nucl. Phys. B* 887 (2014), pp. 276–308. DOI: 10.1016/j.nuclphysb.2014.08.008. arXiv: 1406.5539 [hep-ph].

[243] Richard D. Ball et al. "Parton distributions for the LHC Run II". In: *JHEP* 04 (2015), p. 040. DOI: 10.1007/JHEP04(2015)040. arXiv: 1410.8849 [hep-ph].

[244] S. Alekhin et al. "Parton distribution functions, α_s, and heavy-quark masses for LHC Run II". In: *Phys. Rev. D* 96.1 (2017), p. 014011. DOI: 10.1103/PhysRevD.96.014011. arXiv: 1701.05838 [hep-ph].

[245] Richard D. Ball et al. "Parton distributions from high-precision collider data". In: *Eur. Phys. J. C* 77.10 (2017), p. 663. DOI: 10.1140/epjc/s10052-017-5199-5. arXiv: 1706.00428 [hep-ph].

[246] Tie-Jiun Hou et al. "New CTEQ global analysis of quantum chromodynamics with high-precision data from the LHC". In: *Phys. Rev. D* 103.1 (2021), p. 014013. DOI: 10.1103/PhysRevD.103.014013. arXiv: 1912.10053 [hep-ph].

[247] S. Bailey et al. "Parton distributions from LHC, HERA, Tevatron and fixed target data: MSHT20 PDFs". In: *Eur. Phys. J. C* 81.4 (2021), p. 341. DOI: 10.1140/epjc/s10052-021-09057-0. arXiv: 2012.04684 [hep-ph].

[248] Richard D. Ball et al. "The path to proton structure at 1% accuracy". In: *Eur. Phys. J. C* 82.5 (2022), p. 428. DOI: 10.1140/epjc/s10052-022-10328-7. arXiv: 2109.02653 [hep-ph].

[249] Juan Cruz-Martinez et al. “LO, NLO, and NNLO parton distributions for LHC event generators”. In: *JHEP* 09 (2024), p. 088. DOI: 10.1007/JHEP09(2024)088. arXiv: 2406.12961 [hep-ph].

[250] Andy Buckley et al. “LHAPDF6: parton density access in the LHC precision era”. In: *Eur. Phys. J. C* 75 (2015), p. 132. DOI: 10.1140/epjc/s10052-015-3318-8. arXiv: 1412.7420 [hep-ph].

[251] Christian Bierlich et al. “A comprehensive guide to the physics and usage of PYTHIA 8.3”. In: *SciPost Phys. Codeb.* 2022 (2022), p. 8. DOI: 10.21468/SciPostPhysCodeb.8. arXiv: 2203.11601 [hep-ph].

[252] Vardan Khachatryan et al. “Event generator tunes obtained from underlying event and multiparton scattering measurements”. In: *Eur. Phys. J. C* 76.3 (2016), p. 155. DOI: 10.1140/epjc/s10052-016-3988-x. arXiv: 1512.00815 [hep-ex].

[253] “ATLAS Pythia 8 tunes to 7 TeV data”. In: (Nov. 2014).

[254] J. de Favereau et al. “DELPHES 3, A modular framework for fast simulation of a generic collider experiment”. In: *JHEP* 02 (2014), p. 057. DOI: 10.1007/JHEP02(2014)057. arXiv: 1307.6346 [hep-ex].

[255] R. Brun and F. Rademakers. “ROOT: An object oriented data analysis framework”. In: *Nucl. Instrum. Meth. A* 389 (1997). Ed. by M. Werlen and D. Perret-Gallix, pp. 81–86. DOI: 10.1016/S0168-9002(97)00048-X.

[256] Eric Conte, Benjamin Fuks, and Guillaume Serret. “MadAnalysis 5, A User-Friendly Framework for Collider Phenomenology”. In: *Comput. Phys. Commun.* 184 (2013), pp. 222–256. DOI: 10.1016/j.cpc.2012.09.009. arXiv: 1206.1599 [hep-ph].

[257] Darius A. Faroughy, Admir Greljo, and Jernej F. Kamenik. “Confronting lepton flavor universality violation in B decays with high-p_T tau lepton searches at LHC”. In: *Phys. Lett. B* 764 (2017), pp. 126–134. DOI: 10.1016/j.physletb.2016.11.011. arXiv: 1609.07138 [hep-ph].

[258] Benoît Assi and Adam Martin. “Energy-enhanced dimension eight SMEFT effects in VBF Higgs production”. In: *JHEP* 02 (2025), p. 029. DOI: 10.1007/JHEP02(2025)029. arXiv: 2410.21563 [hep-ph].

[259] Benoît Assi and Adam Martin. “Energy-Enhanced Expansion of the Standard Model Effective Field Theory”. In: (Apr. 2025). arXiv: 2504.10617 [hep-ph].

[260] Gudrun Hiller and Daniel Wendler. “Missing energy plus jet in the SMEFT”. In: *JHEP* 09 (2024), p. 009. DOI: 10.1007/JHEP09(2024)009. arXiv: 2403.17063 [hep-ph].

[261] Víctor Bresó-Pla, Adam Falkowski, and Martín González-Alonso. “A_{FB} in the SMEFT: precision Z physics at the LHC”. In: *JHEP* 08 (2021), p. 021. DOI: 10.1007/JHEP08(2021)021. arXiv: 2103.12074 [hep-ph].

[262] J. Abdallah et al. “Measurement of the W pair production cross-section and W branching ratios in e+ e- collisions at s**(1/2) = 161-GeV to 209-GeV”. In: *Eur. Phys. J. C* 34 (2004), pp. 127–144. DOI: 10.1140/epjc/s2004-01709-5. arXiv: hep-ex/0403042.

[263] A. Heister et al. “Measurement of W-pair production in e+ e- collisions at centre-of-mass energies from 183-GeV to 209-GeV”. In: *Eur. Phys. J. C* 38 (2004), pp. 147–160. DOI: 10.1140/epjc/s2004-02048-3.

[264] P. Achard et al. “Measurement of the cross section of W-boson pair production at LEP”. In: *Phys. Lett. B* 600 (2004), pp. 22–40. DOI: 10.1016/j.physletb.2004.08.060. arXiv: hep-ex/0409016.

[265] G. Abbiendi et al. “Measurement of the e+ e- —> W+ W- cross section and W decay branching fractions at LEP”. In: *Eur. Phys. J. C* 52 (2007), pp. 767–785. DOI: 10.1140/epjc/s10052-007-0442-0. arXiv: 0708.1311 [hep-ex].

[266] F. Abe et al. “A Measurement of the production and muonic decay rate of W and Z bosons in $p\bar{p}$ collisions at $\sqrt{s} = 1.8$ TeV”. In: *Phys. Rev. Lett.* 69 (1992), pp. 28–32. DOI: 10.1103/PhysRevLett.69.28.

[267] B. Abbott et al. “Measurement of W and Z boson production cross sections”. In: *Phys. Rev. D* 60 (1999), p. 052003. DOI: 10.1103/PhysRevD.60.052003. arXiv: hep-ex/9901040.

[268] David Albert et al. “Decays of Intermediate Vector Bosons, Radiative Corrections and QCD Jets”. In: *Nucl. Phys. B* 166 (1980), pp. 460–492. DOI: 10.1016/0550-3213(80)90208-4.

[269] Ansgar Denner. “Techniques for calculation of electroweak radiative corrections at the one loop level and results for W physics at LEP-200”. In: *Fortsch. Phys.* 41 (1993), pp. 307–420. DOI: 10.1002/prop.2190410402. arXiv: 0709.1075 [hep-ph].

[270] Lukas Allwicher et al. “HighPT: A tool for high-p_T Drell-Yan tails beyond the standard model”. In: *Comput. Phys. Commun.* 289 (2023), p. 108749. DOI: 10.1016/j.cpc.2023.108749. arXiv: 2207.10756 [hep-ph].

[271] Radja Boughezal, Yingsheng Huang, and Frank Petriello. “Impact of high invariant-mass Drell-Yan forward-backward asymmetry measurements on SMEFT fits”. In: *Phys. Rev. D* 108.7 (2023), p. 076008. DOI: 10.1103/PhysRevD.108.076008. arXiv: 2303.08257 [hep-ph].

[272] Hamed Abdolmaleki et al. “Exploring SMEFT couplings using the forward–backward asymmetry in neutral current Drell–Yan production at the LHC”. In: *Eur. Phys. J. C* 84.12 (2024), p. 1277. DOI: 10.1140/epjc/s10052-024-13480-4. arXiv: 2310.19638 [hep-ph].

[273] Lukas Allwicher et al. “On the EFT validity for Drell–Yan tails at the LHC”. In: *Eur. Phys. J. C* 85.4 (2025), p. 463. DOI: 10.1140/epjc/s10052-025-14171-4. arXiv: 2412.14162 [hep-ph].

[274] Claude Duhr, Falko Dulat, and Bernhard Mistlberger. “Drell-Yan Cross Section to Third Order in the Strong Coupling Constant”. In: *Phys. Rev. Lett.* 125.17 (2020), p. 172001. DOI: 10.1103/PhysRevLett.125.172001. arXiv: 2001.07717 [hep-ph].

[275] Zahari Kassabov et al. “The top quark legacy of the LHC Run II for PDF and SMEFT analyses”. In: *JHEP* 05 (2023), p. 205. DOI: 10.1007/JHEP05(2023)205. arXiv: 2303.06159 [hep-ph].

[276] M. Jezabek and Johann H. Kuhn. “QCD Corrections to Semileptonic Decays of Heavy Quarks”. In: *Nucl. Phys. B* 314 (1989), pp. 1–6. DOI: 10.1016/0550-3213(89)90108-9.

[277] Georges Aad et al. “Measurement of the polarisation of W bosons produced in top-quark decays using dilepton events at s=13 TeV with the ATLAS experiment”. In: *Phys. Lett. B* 843 (2023), p. 137829. DOI: 10.1016/j.physletb.2023.137829. arXiv: 2209.14903 [hep-ex].

[278] Long Chen et al. “Top-Quark Decay at Next-to-Next-to-Next-to-Leading Order in QCD”. In: (Sept. 2023). arXiv: 2309.01937 [hep-ph].

[279] Armen Tumasyan et al. "Measurement of differential $t\bar{t}$ production cross sections in the full kinematic range using lepton+jets events from proton-proton collisions at $\sqrt{s}$ = 13 TeV". In: *Phys. Rev. D* 104.9 (2021), p. 092013. DOI: 10.1103/PhysRevD.104.092013. arXiv: 2108.02803 [hep-ex].

[280] Georges Aad et al. "Measurements of the inclusive and differential production cross sections of a top-quark–antiquark pair in association with a Z boson at $\sqrt{s} = 13$ TeV with the ATLAS detector". In: *Eur. Phys. J. C* 81.8 (2021), p. 737. DOI: 10.1140/epjc/s10052-021-09439-4. arXiv: 2103.12603 [hep-ex].

[281] Georges Aad et al. "Measurement of the total and differential cross-sections of $t\bar{t}W$ production in pp collisions at $\sqrt{s}$ = 13 TeV with the ATLAS detector". In: *JHEP* 05 (2024), p. 131. DOI: 10.1007/JHEP05(2024)131. arXiv: 2401.05299 [hep-ex].

[282] Georges Aad et al. "Measurements of inclusive and differential cross-sections of combined $t\bar{t}\gamma$ and $tW\gamma$ production in the eμ channel at 13 TeV with the ATLAS detector". In: *JHEP* 09 (2020), p. 049. DOI: 10.1007/JHEP09(2020)049. arXiv: 2007.06946 [hep-ex].

[283] Georges Aad et al. "Measurement of the associated production of a top-antitop-quark pair and a Higgs boson decaying into a $b\bar{b}$ pair in pp collisions at $\sqrt{s} = 13$ TeV using the ATLAS detector at the LHC". In: *Eur. Phys. J. C* 85.2 (2025), p. 210. DOI: 10.1140/epjc/s10052-025-13740-x. arXiv: 2407.10904 [hep-ex].

[284] Alessandro Broggio et al. "Top-quark pair hadroproduction in association with a heavy boson at NLO+NNLL including EW corrections". In: *JHEP* 08 (2019), p. 039. DOI: 10.1007/JHEP08(2019)039. arXiv: 1907.04343 [hep-ph].

[285] G. Bevilacqua et al. "Hard Photons in Hadroproduction of Top Quarks with Realistic Final States". In: *JHEP* 10 (2018), p. 158. DOI: 10.1007/JHEP10(2018)158. arXiv: 1803.09916 [hep-ph].

[286] Luca Buonocore et al. "Precise Predictions for the Associated Production of a W Boson with a Top-Antitop Quark Pair at the LHC". In: *Phys. Rev. Lett.* 131.23 (2023), p. 231901. DOI: 10.1103/PhysRevLett.131.231901. arXiv: 2306.16311 [hep-ph].

[287] Stefano Catani et al. "Higgs Boson Production in Association with a Top-Antitop Quark Pair in Next-to-Next-to-Leading Order QCD". In: *Phys. Rev. Lett.* 130.11 (2023), p. 111902. DOI: 10.1103/PhysRevLett.130.111902. arXiv: 2210.07846 [hep-ph].

[288] Aram Hayrapetyan et al. "Search for physics beyond the standard model in top quark production with additional leptons in the context of effective field theory". In: *JHEP* 12 (2023), p. 068. DOI: 10.1007/JHEP12(2023)068. arXiv: 2307.15761 [hep-ex].

[289] Georges Aad et al. "Measurement of high-mass $t\bar{t}\ell^+\ell^-$ production and lepton flavour universality-inspired effective field theory interpretations at $\sqrt{s} = 13$ TeV with the ATLAS detector". In: (Apr. 2025). arXiv: 2504.05919 [hep-ex].

[290] T. Aoyama et al. "The anomalous magnetic moment of the muon in the Standard Model". In: *Phys. Rept.* 887 (2020), pp. 1–166. DOI: 10.1016/j.physrep.2020.07.006. arXiv: 2006.04822 [hep-ph].

[291] Tatsumi Aoyama, Toichiro Kinoshita, and Makiko Nio. "Theory of the Anomalous Magnetic Moment of the Electron". In: *Atoms* 7.1 (2019), p. 28. DOI: 10.3390/atoms7010028.

[292] R. Aliberti et al. "The anomalous magnetic moment of the muon in the Standard Model: an update". In: (May 2025). arXiv: 2505.21476 [hep-ph].

[293] Georges Aad et al. “Observation of the $\gamma\gamma \to \tau\tau$ Process in Pb+Pb Collisions and Constraints on the τ-Lepton Anomalous Magnetic Moment with the ATLAS Detector”. In: *Phys. Rev. Lett.* 131.15 (2023), p. 151802. DOI: 10.1103/PhysRevLett.131.151802. arXiv: 2204.13478 [hep-ex].

[294] S. Eidelman and M. Passera. “Theory of the tau lepton anomalous magnetic moment”. In: *Mod. Phys. Lett. A* 22 (2007), pp. 159–179. DOI: 10.1142/S0217732307022694. arXiv: hep-ph/0701260.

[295] K. Afanaciev et al. “New limit on the μ+->e+γ decay with the MEG II experiment”. In: (Apr. 2025). arXiv: 2504.15711 [hep-ex].

[296] Bernard Aubert et al. “Searches for Lepton Flavor Violation in the Decays tau+- —> e+- gamma and tau+- —> mu+- gamma”. In: *Phys. Rev. Lett.* 104 (2010), p. 021802. DOI: 10.1103/PhysRevLett.104.021802. arXiv: 0908.2381 [hep-ex].

[297] A. Abdesselam et al. “Search for lepton-flavor-violating tau-lepton decays to $\ell\gamma$ at Belle”. In: *JHEP* 10 (2021), p. 19. DOI: 10.1007/JHEP10(2021)019. arXiv: 2103.12994 [hep-ex].

[298] Andreas Crivellin, Saereh Najjari, and Janusz Rosiek. “Lepton Flavor Violation in the Standard Model with general Dimension-Six Operators”. In: *JHEP* 04 (2014), p. 167. DOI: 10.1007/JHEP04(2014)167. arXiv: 1312.0634 [hep-ph].

[299] Md Isha Ali et al. “SMEFT analysis of charged lepton flavor violating B-meson decays”. In: *Phys. Rev. D* 109.7 (2024), p. 075028. DOI: 10.1103/PhysRevD.109.075028. arXiv: 2312.05071 [hep-ph].

[300] I. Plakias and O. Sumensari. “Lepton flavor violation in semileptonic observables”. In: *Phys. Rev. D* 110.3 (2024), p. 035016. DOI: 10.1103/PhysRevD.110.035016. arXiv: 2312.14070 [hep-ph].

[301] U. Bellgardt et al. “Search for the Decay $\mu^+ \to e^+e^+e^-$”. In: *Nucl. Phys. B* 299 (1988), pp. 1–6. DOI: 10.1016/0550-3213(88)90462-2.

[302] K. Hayasaka et al. “Search for Lepton Flavor Violating Tau Decays into Three Leptons with 719 Million Produced Tau+Tau- Pairs”. In: *Phys. Lett. B* 687 (2010), pp. 139–143. DOI: 10.1016/j.physletb.2010.03.037. arXiv: 1001.3221 [hep-ex].

[303] N. Tsuzuki et al. “Search for lepton-flavor-violating τ decays into a lepton and a vector meson using the full Belle data sample”. In: *JHEP* 06 (2023), p. 118. DOI: 10.1007/JHEP06(2023)118. arXiv: 2301.03768 [hep-ex].

[304] Y. Miyazaki et al. “Search for lepton flavor violating tau- decays into l- eta, l- eta-prime and l- pi0”. In: *Phys. Lett. B* 648 (2007), pp. 341–350. DOI: 10.1016/j.physletb.2007.03.027. arXiv: hep-ex/0703009.

[305] Bernard Aubert et al. “Search for Lepton Flavor Violating Decays $\tau^\pm \to \ell^\pm\pi^0$, $\ell^\pm\eta$, $\ell^\pm\eta'$”. In: *Phys. Rev. Lett.* 98 (2007), p. 061803. DOI: 10.1103/PhysRevLett.98.061803. arXiv: hep-ex/0610067.

[306] W. J. Marciano and A. Sirlin. “Electroweak Radiative Corrections to tau Decay”. In: *Phys. Rev. Lett.* 61 (1988), pp. 1815–1818. DOI: 10.1103/PhysRevLett.61.1815.

[307] Swagato Banerjee et al. “Averages of b-hadron, c-hadron, and τ-lepton properties as of 2023”. In: (Nov. 2024). arXiv: 2411.18639 [hep-ex].

[308] Jens Erler. “Electroweak radiative corrections to semileptonic tau decays”. In: *Rev. Mex. Fis.* 50 (2004), pp. 200–202. arXiv: hep-ph/0211345.

[309] Andrzej J. Buras, Matthias Jamin, and Peter H. Weisz. "Leading and Next-to-leading QCD Corrections to ϵ Parameter and $B^0 - \bar{B}^0$ Mixing in the Presence of a Heavy Top Quark". In: *Nucl. Phys. B* 347 (1990), pp. 491–536. DOI: 10.1016/0550-3213(90)90373-L.

[310] F. Gabbiani et al. "A Complete analysis of FCNC and CP constraints in general SUSY extensions of the standard model". In: *Nucl. Phys. B* 477 (1996), pp. 321–352. DOI: 10.1016/0550-3213(96)00390-2. arXiv: hep-ph/9604387.

[311] Jonathan A. Bagger, Konstantin T. Matchev, and Ren-Jie Zhang. "QCD corrections to flavor changing neutral currents in the supersymmetric standard model". In: *Phys. Lett. B* 412 (1997), pp. 77–85. DOI: 10.1016/S0370-2693(97)00920-9. arXiv: hep-ph/9707225.

[312] Damir Bečirević, Olcyr Sumensari, and Renata Zukanovich Funchal. "Lepton flavor violation in exclusive $b \to s$ decays". In: *Eur. Phys. J. C* 76.3 (2016), p. 134. DOI: 10.1140/epjc/s10052-016-3985-0. arXiv: 1602.00881 [hep-ph].

[313] Roel Aaij et al. "Search for the Rare Decays $B_s^0 \to e^+e^-$ and $B^0 \to e^+e^-$". In: *Phys. Rev. Lett.* 124.21 (2020), p. 211802. DOI: 10.1103/PhysRevLett.124.211802. arXiv: 2003.03999 [hep-ex].

[314] Armen Tumasyan et al. "Measurement of the $B_S^0 \to \mu^+\mu^-$ decay properties and search for the $B^0 \to \mu^+\mu^-$ decay in proton-proton collisions at $\sqrt{s} = 13$ TeV". In: *Phys. Lett. B* 842 (2023), p. 137955. DOI: 10.1016/j.physletb.2023.137955. arXiv: 2212.10311 [hep-ex].

[315] Roel Aaij et al. "Search for the decays $B_s^0 \to \tau^+\tau^-$ and $B^0 \to \tau^+\tau^-$". In: *Phys. Rev. Lett.* 118.25 (2017), p. 251802. DOI: 10.1103/PhysRevLett.118.251802. arXiv: 1703.02508 [hep-ex].

[316] Eduardo Cortina Gil et al. "Search for Lepton Number and Flavor Violation in K^+ and π^0 Decays". In: *Phys. Rev. Lett.* 127.13 (2021), p. 131802. DOI: 10.1103/PhysRevLett.127.131802. arXiv: 2105.06759 [hep-ex].

[317] D. B. White et al. "Search for the decays eta —> mu e and eta —> e+ e-". In: *Phys. Rev. D* 53 (1996), pp. 6658–6661. DOI: 10.1103/PhysRevD.53.6658.

[318] Roy A. Briere et al. "Rare decays of the eta-prime". In: *Phys. Rev. Lett.* 84 (2000), pp. 26–30. DOI: 10.1103/PhysRevLett.84.26. arXiv: hep-ex/9907046.

[319] D. Ambrose et al. "New limit on muon and electron lepton number violation from K0(L) —> mu+- e-+ decay". In: *Phys. Rev. Lett.* 81 (1998), pp. 5734–5737. DOI: 10.1103/PhysRevLett.81.5734. arXiv: hep-ex/9811038.

[320] Roel Aaij et al. "Search for the lepton-flavour violating decays $B_{(s)}^0 \to e^\pm\mu^\mp$". In: *JHEP* 03 (2018), p. 078. DOI: 10.1007/JHEP03(2018)078. arXiv: 1710.04111 [hep-ex].

[321] H. Atmacan et al. "Search for $B^0 \to \tau^\pm\ell^\mp$ ($\ell = e, \mu$) with a hadronic tagging method at Belle". In: *Phys. Rev. D* 104.9 (2021), p. L091105. DOI: 10.1103/PhysRevD.104.L091105. arXiv: 2108.11649 [hep-ex].

[322] L. Nayak et al. "Search for $B_s^0 \to \ell^\mp\tau^\pm$ with the Semi-leptonic Tagging Method at Belle". In: *JHEP* 08 (2023), p. 178. DOI: 10.1007/JHEP08(2023)178. arXiv: 2301.10989 [hep-ex].

[323] Roel Aaij et al. "Search for the lepton-flavour-violating decays $B_s^0 \to \tau^\pm\mu^\mp$ and $B^0 \to \tau^\pm\mu^\mp$". In: *Phys. Rev. Lett.* 123.21 (2019), p. 211801. DOI: 10.1103/PhysRevLett.123.211801. arXiv: 1905.06614 [hep-ex].

[324] B. I. Eisenstein et al. “Precision Measurement of B(D+ —> mu+ nu) and the Pseudoscalar Decay Constant f(D+)”. In: *Phys. Rev. D* 78 (2008), p. 052003. DOI: 10.1103/PhysRevD.78.052003. arXiv: 0806.2112 [hep-ex].

[325] A. Zupanc et al. “Measurements of branching fractions of leptonic and hadronic D_s^+ meson decays and extraction of the D_s^+ meson decay constant”. In: *JHEP* 09 (2013), p. 139. DOI: 10.1007/JHEP09(2013)139. arXiv: 1307.6240 [hep-ex].

[326] N. Satoyama et al. “A Search for the rare leptonic decays B+ —> mu+ nu(mu) and B+ —> e+ nu(nu)”. In: *Phys. Lett. B* 647 (2007), pp. 67–73. DOI: 10.1016/j.physletb.2007.01.068. arXiv: hep-ex/0611045.

[327] M. T. Prim et al. “Search for $B^+ \to \mu^+ \nu_\mu$ and $B^+ \to \mu^+ N$ with inclusive tagging”. In: *Phys. Rev. D* 101.3 (2020), p. 032007. DOI: 10.1103/PhysRevD.101.032007. arXiv: 1911.03186 [hep-ex].

[328] Lorenzo Calibbi et al. “Indirect constraints on lepton-flavor-violating quarkonium decays”. In: *Phys. Rev. D* 106.11 (2022), p. 115039. DOI: 10.1103/PhysRevD.106.115039. arXiv: 2207.10913 [hep-ph].

[329] M. N. Achasov et al. “Search for Lepton Flavor Violation Process $e^+e^- \to e\mu$ in the Energy Region $\sqrt{s} = 984 - 1060MeV$ and$\phi \to e\mu$ Decay”. In: *Phys. Rev. D* 81 (2010), p. 057102. DOI: 10.1103/PhysRevD.81.057102. arXiv: 0911.1232 [hep-ex].

[330] M. Ablikim et al. “Search for the Lepton Flavor Violation Process $J/\psi \to e\mu$ at BESIII”. In: *Phys. Rev. D* 87 (2013), p. 112007. DOI: 10.1103/PhysRevD.87.112007. arXiv: 1304.3205 [hep-ex].

[331] Medina Ablikim et al. “Search for the charged lepton flavor violating decay $J/\psi \to e\tau$”. In: *Phys. Rev. D* 103.11 (2021), p. 112007. DOI: 10.1103/PhysRevD.103.112007. arXiv: 2103.11540 [hep-ex].

[332] M. Ablikim et al. “Search for the lepton flavor violation processes J / psi —> mu tau and e tau”. In: *Phys. Lett. B* 598 (2004), pp. 172–177. DOI: 10.1016/j.physletb.2004.08.005. arXiv: hep-ex/0406018.

[333] S. Patra et al. “Search for charged lepton flavor violating decays of $\Upsilon(1S)$”. In: *JHEP* 05 (2022), p. 095. DOI: 10.1007/JHEP05(2022)095. arXiv: 2201.09620 [hep-ex].

[334] M. Ablikim et al. “Search for invisible decays of ω and ϕ with J/ψ data at BESIII”. In: *Phys. Rev. D* 98.3 (2018), p. 032001. DOI: 10.1103/PhysRevD.98.032001. arXiv: 1805.05613 [hep-ex].

[335] J. P. Lees et al. “Search for $B \to K^{(*)}\nu\overline{\nu}$ and invisible quarkonium decays”. In: *Phys. Rev. D* 87.11 (2013), p. 112005. DOI: 10.1103/PhysRevD.87.112005. arXiv: 1303.7465 [hep-ex].

[336] Bernard Aubert et al. “A Search for Invisible Decays of the Upsilon(1S)”. In: *Phys. Rev. Lett.* 103 (2009), p. 251801. DOI: 10.1103/PhysRevLett.103.251801. arXiv: 0908.2840 [hep-ex].

[337] Claude Bourrely, Irinel Caprini, and Laurent Lellouch. “Model-independent description of B —> pi l nu decays and a determination of |V(ub)|”. In: *Phys. Rev. D* 79 (2009). [Erratum: Phys.Rev.D 82, 099902 (2010)], p. 013008. DOI: 10.1103/PhysRevD.82.099902. arXiv: 0807.2722 [hep-ph].

[338] Aoife Bharucha, David M. Straub, and Roman Zwicky. “$B \to V\ell^+\ell^-$ in the Standard Model from light-cone sum rules”. In: *JHEP* 08 (2016), p. 098. DOI: 10.1007/JHEP08(2016)098. arXiv: 1503.05534 [hep-ph].

[339] Y. Aoki et al. “FLAG Review 2024”. In: (Nov. 2024). arXiv: 2411.04268 [hep-lat].

[340] A. Sirlin. “Large m(W), m(Z) Behavior of the O(alpha) Corrections to Semileptonic Processes Mediated by W”. In: *Nucl. Phys. B* 196 (1982), pp. 83–92. DOI: 10.1016/0550-3213(82)90303-0.

[341] J. G. Korner et al. “A Detailed Analysis of D, $D(s)$ and B Meson Transition Form-factors and the Determination of $V(cb)$”. In: *Z. Phys. C* 48 (1990), pp. 663–672. DOI: 10.1007/BF01614702.

[342] Yue-Liang Wu, Ming Zhong, and Ya-Bing Zuo. “B(s), D(s) —> pi, K, eta, rho, K*, omega, phi Transition Form Factors and Decay Rates with Extraction of the CKM parameters |V(ub)|, |V(cs)|, |V(cd)|”. In: *Int. J. Mod. Phys. A* 21 (2006), pp. 6125–6172. DOI: 10.1142/S0217751X06033209. arXiv: hep-ph/0604007.

[343] Wolfgang Altmannshofer et al. “Symmetries and Asymmetries of $B \to K^* \mu^+ \mu^-$ Decays in the Standard Model and Beyond”. In: *JHEP* 01 (2009), p. 019. DOI: 10.1088/1126-6708/2009/01/019. arXiv: 0811.1214 [hep-ph].

[344] Joaquim Matias et al. “Complete Anatomy of $\bar{B}_d - > \bar{K}^{*0}(- > K\pi)l^+l^-$ and its angular distribution”. In: *JHEP* 04 (2012), p. 104. DOI: 10.1007/JHEP04(2012)104. arXiv: 1202.4266 [hep-ph].

[345] Sebastien Descotes-Genon et al. “Optimizing the basis of $B \to K^* ll$ observables in the full kinematic range”. In: *JHEP* 05 (2013), p. 137. DOI: 10.1007/JHEP05(2013)137. arXiv: 1303.5794 [hep-ph].

[346] David M. Straub. “flavio: a Python package for flavour and precision phenomenology in the Standard Model and beyond”. In: (Oct. 2018). arXiv: 1810.08132 [hep-ph].

[347] J. P. Lees et al. “Search for the rare decays $B ß \pi \ell^+ \ell^-$ and $B^0 ß \eta \ell^+ \ell^-$”. In: *Phys. Rev. D* 88.3 (2013), p. 032012. DOI: 10.1103/PhysRevD.88.032012. arXiv: 1303.6010 [hep-ex].

[348] Nakul R. Soni et al. “Rare $b \to d$ decays in covariant confined quark model”. In: *Eur. Phys. J. A* 58.3 (2022), p. 39. DOI: 10.1140/epja/s10050-022-00685-y. arXiv: 2008.07202 [hep-ph].

[349] J. -T. Wei et al. “Search for B —> pi l+ l- Decays at Belle”. In: *Phys. Rev. D* 78 (2008), p. 011101. DOI: 10.1103/PhysRevD.78.011101. arXiv: 0804.3656 [hep-ex].

[350] Roel Aaij et al. “First measurement of the differential branching fraction and CP asymmetry of the $B^\pm \to \pi^\pm \mu^+ \mu^-$ decay”. In: *JHEP* 10 (2015), p. 034. DOI: 10.1007/JHEP10(2015)034. arXiv: 1509.00414 [hep-ex].

[351] Jon A. Bailey et al. “$B \to \pi \ell \ell$ form factors for new-physics searches from lattice QCD”. In: *Phys. Rev. Lett.* 115.15 (2015), p. 152002. DOI: 10.1103/PhysRevLett.115.152002. arXiv: 1507.01618 [hep-ph].

[352] Rigo Bause et al. “Model-independent analysis of $b \to d$ processes”. In: *Eur. Phys. J. C* 83.5 (2023), p. 419. DOI: 10.1140/epjc/s10052-023-11586-9. arXiv: 2209.04457 [hep-ph].

[353] W. G. Parrott, C. Bouchard, and C. T. H. Davies. “Standard Model predictions for B→Kℓ+ℓ-, B→Kℓ1-ℓ2+ and B→K$\nu\nu^-$ using form factors from Nf=2+1+1 lattice QCD”. In: *Phys. Rev. D* 107.1 (2023). [Erratum: Phys.Rev.D 107, 119903 (2023)], p. 014511. DOI: 10.1103/PhysRevD.107.014511. arXiv: 2207.13371 [hep-ph].

[354] R. Aaij et al. “Differential branching fractions and isospin asymmetries of $B \to K^{(*)} \mu^+ \mu^-$ decays”. In: *JHEP* 06 (2014), p. 133. DOI: 10.1007/JHEP06(2014)133. arXiv: 1403.8044 [hep-ex].

[355] Nico Gubernari et al. “Improved theory predictions and global analysis of exclusive $b \to s\mu^+\mu^-$ processes”. In: *JHEP* 09 (2022), p. 133. DOI: 10.1007/JHEP09(2022)133. arXiv: 2206.03797 [hep-ph].

[356] J. P. Lees et al. “Search for $B^+ \to K^+\tau^+\tau^-$ at the BaBar experiment”. In: *Phys. Rev. Lett.* 118.3 (2017), p. 031802. DOI: 10.1103/PhysRevLett.118.031802. arXiv: 1605.09637 [hep-ex].

[357] Roel Aaij et al. “Angular analysis of $B^0 \to K^{*0}e^+e^-$ decays”. In: (Feb. 2025). arXiv: 2502.10291 [hep-ex].

[358] Marcel Algueró et al. “To (b)e or not to (b)e: no electrons at LHCb”. In: *Eur. Phys. J. C* 83.7 (2023), p. 648. DOI: 10.1140/epjc/s10052-023-11824-0. arXiv: 2304.07330 [hep-ph].

[359] I. Adachi et al. “Search for $B^0 \to K^{*0}\tau^+\tau^-$ decays at the Belle II experiment”. In: (Apr. 2025). arXiv: 2504.10042 [hep-ex].

[360] Roel Aaij et al. “Angular Analysis of the $B^+ \to K^{*+}\mu^+\mu^-$ Decay”. In: *Phys. Rev. Lett.* 126.16 (2021), p. 161802. DOI: 10.1103/PhysRevLett.126.161802. arXiv: 2012.13241 [hep-ex].

[361] Roel Aaij et al. “Angular analysis of the decay $B_s^0 \to \phi e^+e^-$”. In: (Apr. 2025). arXiv: 2504.06346 [hep-ex].

[362] Roel Aaij et al. “Angular analysis of the rare decay $B_s^0 \to \phi\mu^+\mu^-$”. In: *JHEP* 11 (2021), p. 043. DOI: 10.1007/JHEP11(2021)043. arXiv: 2107.13428 [hep-ex].

[363] Roel Aaij et al. “Evidence for the decay $B_S^0 \to \overline{K}^{*0}\mu^+\mu^-$”. In: *JHEP* 07 (2018), p. 020. DOI: 10.1007/JHEP07(2018)020. arXiv: 1804.07167 [hep-ex].

[364] Bharti Kindra and Namit Mahajan. “Predictions of angular observables for $\bar{B}_s \to K^*\ell\ell$ and $\bar{B} \to \rho\ell\ell$ in the standard model”. In: *Phys. Rev. D* 98.9 (2018), p. 094012. DOI: 10.1103/PhysRevD.98.094012. arXiv: 1803.05876 [hep-ph].

[365] Bernard Aubert et al. “Search for the rare decay $B \to \pi l^+ l^-$”. In: *Phys. Rev. Lett.* 99 (2007), p. 051801. DOI: 10.1103/PhysRevLett.99.051801. arXiv: hep-ex/0703018.

[366] S. Choudhury et al. “Test of lepton flavor universality and search for lepton flavor violation in $B \to K\ell\ell$ decays”. In: *JHEP* 03 (2021), p. 105. DOI: 10.1007/JHEP03(2021)105. arXiv: 1908.01848 [hep-ex].

[367] J. P. Lees et al. “A search for the decay modes $B^{+-} \to h^{+-}\tau^{+-}l$”. In: *Phys. Rev. D* 86 (2012), p. 012004. DOI: 10.1103/PhysRevD.86.012004. arXiv: 1204.2852 [hep-ex].

[368] Bernard Aubert et al. “Measurements of branching fractions, rate asymmetries, and angular distributions in the rare decays $B \to K\ell^+\ell^-$ and $B \to K^*\ell^+\ell^-$”. In: *Phys. Rev. D* 73 (2006), p. 092001. DOI: 10.1103/PhysRevD.73.092001. arXiv: hep-ex/0604007.

[369] Roel Aaij et al. “Search for the lepton-flavour violating decays $B^0 \to K^{*0}\mu^\pm e^\mp$ and $B_s^0 \to \phi\mu^\pm e^\mp$”. In: *JHEP* 06 (2023), p. 073. DOI: 10.1007/JHEP06(2023)073. arXiv: 2207.04005 [hep-ex].

[370] I. Adachi et al. “Search for lepton flavor-violating decay modes $B^0 \to K^{*0}\tau^\pm\ell^\mp$ ($\ell = e, \mu$) with hadronic B-tagging at Belle and Belle II”. In: (May 2025). arXiv: 2505.08418 [hep-ex].

[371] R. Aaij et al. “Search for the lepton-flavour violating decays $B^0 \to K^{*0}\tau^\pm\mu^\mp$”. In: *JHEP* 06 (2023), p. 143. DOI: 10.1007/JHEP06(2023)143. arXiv: 2209.09846 [hep-ex].

[372] I. Adachi et al. “Evidence for $B^+ \to K^+\nu\bar{\nu}$ decays”. In: *Phys. Rev. D* 109.11 (2024), p. 112006. DOI: 10.1103/PhysRevD.109.112006. arXiv: 2311.14647 [hep-ex].

[373] M. Ablikim et al. “Search for the decay $D^0 \to \pi^0 \nu\bar{\nu}$”. In: *Phys. Rev. D* 105.7 (2022), p. L071102. DOI: 10.1103/PhysRevD.105.L071102. arXiv: 2112.14236 [hep-ex].

[374] Andrzej J. Buras, Julia Harz, and Martin A. Mojahed. “Disentangling new physics in $K \to \pi\nu\bar{\nu}$ and $B \to K\,(K^*)\,\nu\bar{\nu}$ observables”. In: *JHEP* 10 (2024), p. 087. DOI: 10.1007/JHEP10(2024)087. arXiv: 2405.06742 [hep-ph].

[375] S. Rosauro-Alcaraz and L. P. S. Leal. “Disentangling left and right-handed neutrino effects in $B \to K^{(*)}\nu\nu$”. In: *Eur. Phys. J. C* 84.8 (2024), p. 795. DOI: 10.1140/epjc/s10052-024-13104-x. arXiv: 2404.17440 [hep-ph].

[376] Damir Bečirević et al. “Right-handed interactions in puzzling B-decays”. In: *Phys. Lett. B* 861 (2025), p. 139285. DOI: 10.1016/j.physletb.2025.139285. arXiv: 2410.23257 [hep-ph].

[377] Feng-Zhi Chen, Qiaoyi Wen, and Fanrong Xu. “Correlating $B \to K^{(*)}\nu\bar{\nu}$ and flavor anomalies in SMEFT”. In: *Eur. Phys. J. C* 84 (2024), p. 1012. DOI: 10.1140/epjc/s10052-024-13425-x. arXiv: 2401.11552 [hep-ph].

[378] Lukas Allwicher et al. “Understanding the first measurement of B(B$\to$K$\nu\nu^-$)”. In: *Phys. Lett. B* 848 (2024), p. 138411. DOI: 10.1016/j.physletb.2023.138411. arXiv: 2309.02246 [hep-ph].

[379] Zeren Simon Wang, Herbert K. Dreiner, and Julian Y. Günther. “The decay $B \to K+\nu+\bar{\nu}$ at Belle II and a massless bino in R-parity-violating supersymmetry”. In: *Eur. Phys. J. C* 85.1 (2025), p. 66. DOI: 10.1140/epjc/s10052-025-13745-6. arXiv: 2309.03727 [hep-ph].

[380] Chandan Hati et al. “QCD axion, color-mediated neutrino masses, and B+$\to$K++Emiss anomaly”. In: *Phys. Rev. D* 111.1 (2025), p. 015038. DOI: 10.1103/PhysRevD.111.015038. arXiv: 2408.00060 [hep-ph].

[381] Wolfgang Altmannshofer and Shibasis Roy. “Joint explanation of the B$\to\pi$K puzzle and the B$\to$K$\nu\nu^-$ excess”. In: *Phys. Rev. D* 111.7 (2025), p. 075029. DOI: 10.1103/PhysRevD.111.075029. arXiv: 2411.06592 [hep-ph].

[382] Quan-Yi Hu. “Are the new particles heavy or light in $b \to sE_{\text{miss}}$?” In: *Eur. Phys. J. C* 85.5 (2025), p. 556. DOI: 10.1140/epjc/s10052-025-14290-y. arXiv: 2412.19084 [hep-ph].

[383] Lorenzo Calibbi et al. “Is Dark Matter the origin of the $B \to K\nu\bar{\nu}$ excess at Belle II?” In: (Feb. 2025). arXiv: 2502.04900 [hep-ph].

[384] Patrick D. Bolton et al. “Impact of new invisible particles on $B \to K^{(*)}E_{\text{miss}}$ observables”. In: (Mar. 2025). arXiv: 2503.19025 [hep-ph].

[385] Chuan-Hung Chen, Cheng-Wei Chiang, and Leon M. G. de la Vega. “Leptoquark-mediated Dirac neutrino mass and its impact on $B \to K\nu\bar{\nu}$ and $K \to \pi\nu\bar{\nu}$ decays”. In: (Mar. 2025). arXiv: 2503.22431 [hep-ph].

[386] Tobias Felkl, Sze Lok Li, and Michael A. Schmidt. “A tale of invisibility: constraints on new physics in b $\to s\nu\nu$”. In: *JHEP* 12 (2021), p. 118. DOI: 10.1007/JHEP12(2021)118. arXiv: 2111.04327 [hep-ph].

[387] Christoph Bobeth et al. “Patterns of Flavour Violation in Models with Vector-Like Quarks”. In: *JHEP* 04 (2017), p. 079. DOI: 10.1007/JHEP04(2017)079. arXiv: 1609.04783 [hep-ph].

[388] G. D’Ambrosio et al. “Anatomy of kaon decays and prospects for lepton flavour universality violation”. In: *JHEP* 09 (2022), p. 148. DOI: 10.1007/JHEP09(2022)148. arXiv: 2206.14748 [hep-ph].

[389] J. Grygier et al. “Search for $B \to h\nu\bar{\nu}$ decays with semileptonic tagging at Belle”. In: *Phys. Rev. D* 96.9 (2017). [Addendum: Phys.Rev.D 97, 099902 (2018)], p. 091101. DOI: 10.1103/PhysRevD.96.091101. arXiv: 1702.03224 [hep-ex].

[390] W. Adam et al. “Study of rare b decays with the DELPHI detector at LEP”. In: *Z. Phys. C* 72 (1996), pp. 207–220. DOI: 10.1007/s002880050238.

[391] Jean Pierre Delahaye et al. “Muon Colliders”. In: (Jan. 2019). arXiv: 1901.06150 [physics.acc-ph].

[392] Carlotta Accettura et al. “Towards a muon collider”. In: *Eur. Phys. J. C* 83.9 (2023). [Erratum: Eur.Phys.J.C 84, 36 (2024)], p. 864. DOI: 10.1140/epjc/s10052-023-11889-x. arXiv: 2303.08533 [physics.acc-ph].

[393] Admir Greljo, Hector Tiblom, and Alessandro Valenti. “New Physics Through Flavor Tagging at FCC-ee”. In: (Nov. 2024). arXiv: 2411.02485 [hep-ph].

[394] “Prospects in BSM physics at FCC”. In: (Mar. 2025). Ed. by P. Azzi et al. DOI: 10.17181/69m03-zzb95.

[395] J. Charles et al. “CP violation and the CKM matrix: Assessing the impact of the asymmetric B factories”. In: *Eur. Phys. J. C* 41.1 (2005), pp. 1–131. DOI: 10.1140/epjc/s2005-02169-1. arXiv: hep-ph/0406184.

[396] Luiz Vale Silva. “2023 update of the extraction of the CKM matrix elements”. In: *12th International Workshop on the CKM Unitarity Triangle*. May 2024. arXiv: 2405.08046 [hep-ph].

[397] W. Altmannshofer et al. “The Belle II Physics Book”. In: *PTEP* 2019.12 (2019). Ed. by E. Kou and P. Urquijo. [Erratum: PTEP 2020, 029201 (2020)], p. 123C01. DOI: 10.1093/ptep/ptz106. arXiv: 1808.10567 [hep-ex].

[398] Rigo Bause et al. “Interplay of dineutrino modes with semileptonic rare B-decays”. In: *JHEP* 12 (2021), p. 061. DOI: 10.1007/JHEP12(2021)061. arXiv: 2109.01675 [hep-ph].

[399] Elie Hammou et al. “Hide and seek: how PDFs can conceal new physics”. In: *JHEP* 11 (2023), p. 090. DOI: 10.1007/JHEP11(2023)090. arXiv: 2307.10370 [hep-ph].

[400] Mark N. Costantini et al. “SIMUnet: an open-source tool for simultaneous global fits of EFT Wilson coefficients and PDFs”. In: *Eur. Phys. J. C* 84.8 (2024), p. 805. DOI: 10.1140/epjc/s10052-024-13079-9. arXiv: 2402.03308 [hep-ph].

[401] Aleksandr Azatov et al. “New physics in b $\to$ s$\mu\mu$: FCC-hh or a muon collider?” In: *JHEP* 10 (2022), p. 149. DOI: 10.1007/JHEP10(2022)149. arXiv: 2205.13552 [hep-ph].

[402] R. J. Dowdall et al. “Neutral B-meson mixing from full lattice QCD at the physical point”. In: *Phys. Rev. D* 100.9 (2019), p. 094508. DOI: 10.1103/PhysRevD.100.094508. arXiv: 1907.01025 [hep-lat].

[403] Gerhard Buchalla, Andrzej J. Buras, and Markus E. Lautenbacher. “Weak decays beyond leading logarithms”. In: *Rev. Mod. Phys.* 68 (1996), pp. 1125–1144. DOI: 10.1103/RevModPhys.68.1125. arXiv: hep-ph/9512380.

[404] Martin Beneke and Matthias Neubert. “Flavor singlet B decay amplitudes in QCD factorization”. In: *Nucl. Phys. B* 651 (2003), pp. 225–248. DOI: 10.1016/S0550-3213(02)01091-X. arXiv: hep-ph/0210085.

[405] Vladimir M. Braun et al. “The ρ-meson light-cone distribution amplitudes from lattice QCD”. In: *JHEP* 04 (2017), p. 082. DOI: 10.1007/JHEP04(2017)082. arXiv: 1612.02955 [hep-lat].

[406] Ying Chen et al. “Charmed and ϕ meson decay constants from 2+1-flavor lattice QCD”. In: *Chin. Phys. C* 45.2 (2021), p. 023109. DOI: 10.1088/1674-1137/abcd8f. arXiv: 2008.05208 [hep-lat].

[407] M. S. Bhagwat and P. Maris. “Vector meson form factors and their quark-mass dependence”. In: *Phys. Rev. C* 77 (2008), p. 025203. DOI: 10.1103/PhysRevC.77.025203. arXiv: nucl-th/0612069.

[408] Damir Bečirević et al. “Lattice QCD and QCD sum rule determination of the decay constants of η_c, J/ψ and h_c states”. In: *Nucl. Phys. B* 883 (2014), pp. 306–327. DOI: 10.1016/j.nuclphysb.2014.03.024. arXiv: 1312.2858 [hep-ph].

[409] B. Colquhoun et al. “Υ and Υ' Leptonic Widths, a_μ^b and m_b from full lattice QCD”. In: *Phys. Rev. D* 91.7 (2015), p. 074514. DOI: 10.1103/PhysRevD.91.074514. arXiv: 1408.5768 [hep-lat].

[410] C. Glenn Boyd, Benjamin Grinstein, and Richard F. Lebed. “Constraints on form-factors for exclusive semileptonic heavy to light meson decays”. In: *Phys. Rev. Lett.* 74 (1995), pp. 4603–4606. DOI: 10.1103/PhysRevLett.74.4603. arXiv: hep-ph/9412324.

[411] Alexei Bazavov et al. “D-meson semileptonic decays to pseudoscalars from four-flavor lattice QCD”. In: *Phys. Rev. D* 107.9 (2023), p. 094516. DOI: 10.1103/PhysRevD.107.094516. arXiv: 2212.12648 [hep-lat].

[412] Gunnar S. Bali et al. “$D_s \to \eta, \eta'$ semileptonic decay form factors with disconnected quark loop contributions”. In: *Phys. Rev. D* 91.1 (2015), p. 014503. DOI: 10.1103/PhysRevD.91.014503. arXiv: 1406.5449 [hep-lat].

[413] E. McLean et al. “$B_s \to D_s \ell\nu$ Form Factors for the full q^2 range from Lattice QCD with non-perturbatively normalized currents”. In: *Phys. Rev. D* 101.7 (2020), p. 074513. DOI: 10.1103/PhysRevD.101.074513. arXiv: 1906.00701 [hep-lat].

[414] Nico Gubernari, Ahmet Kokulu, and Danny van Dyk. “$B \to P$ and $B \to V$ Form Factors from B-Meson Light-Cone Sum Rules beyond Leading Twist”. In: *JHEP* 01 (2019), p. 150. DOI: 10.1007/JHEP01(2019)150. arXiv: 1811.00983 [hep-ph].

[415] R. Glattauer et al. “Measurement of the decay $B \to D\ell\nu_\ell$ in fully reconstructed events and determination of the Cabibbo-Kobayashi-Maskawa matrix element $|V_{cb}|$”. In: *Phys. Rev. D* 93.3 (2016), p. 032006. DOI: 10.1103/PhysRevD.93.032006. arXiv: 1510.03657 [hep-ex].

[416] Roel Aaij et al. “Measurement of $|V_{cb}|$ with $B_s^0 \to D_s^{(*)-}\mu^+\nu_\mu$ decays”. In: *Phys. Rev. D* 101.7 (2020), p. 072004. DOI: 10.1103/PhysRevD.101.072004. arXiv: 2001.03225 [hep-ex].

[417] R. Aaij et al. “First observation of the decay $B_s^0 \to K^-\mu^+\nu_\mu$ and Measurement of $|V_{ub}|/|V_{cb}|$”. In: *Phys. Rev. Lett.* 126.8 (2021), p. 081804. DOI: 10.1103/PhysRevLett.126.081804. arXiv: 2012.05143 [hep-ex].

[418] I. Adachi et al. “Determination of |Vcb| using B¯0→D*+ℓ−ν¯ℓ decays with Belle II”. In: *Phys. Rev. D* 108.9 (2023), p. 092013. DOI: 10.1103/PhysRevD.108.092013. arXiv: 2310.01170 [hep-ex].

Glossary

BSM	Beyond the Standard Model
CKM	Cabibbo-Kobayashi-Maskawa matrix
CLIC	Compact Linear Collider
DY	Drell-Yan
EFT	Effective Field Theory
EW	Electroweak
EWSB	Electroweak Symmetry Breaking
FCC	Future Circular Collider
FCNC	Flavor-Changing Neutral Current
GIM	Glashow-Iliopoulos-Maiani mechanism
HISZ	Hagiwara-Ishihara-Szalapski-Zeppenfeld
HE-LHC	High-Energy Large Hadron Collider
HL-LHC	High-Luminosity Large Hadron Collider
IR	Infrared
LD	Lepton Flavor Democratic
LEFT	Low-Energy Effective Field Theory
LEP	Large Electron-Positron Collider
LFC	Lepton-Flavor Conserving
LFV	Lepton-Flavor Violation
LHC	Large Hadron Collider
LU	Lepton Flavor Universal
MFV	Minimal Flavor Violation
MLE	Maximum Likelihood Estimation
NP	New Physics
PDF	Parton Distribution Function
PMNS	Pontecorvo-Maki-Nakagawa-Sakata matrix
QCD	Quantum Chromodynamics
QED	Quantum Electrodynamics
RGE	Renormalization Group Equation
SILH	Strongly Interacting Light Higgs
SLC	Stanford Linear Collider
SM	Standard Model
SMEFT	Standard Model Effective Field Theory
UV	Ultraviolet
VEV	Vacuum Expectation Value

Acknowledgments

First and foremost, I would like to thank my advisor, Prof. Dr. Gudrun Hiller, for making all of this possible. I am deeply thankful for her continuous encouragement, patience, and support throughout my doctoral studies. She has been a wonderful mentor, giving me the freedom to explore my ideas, challenging me to push my boundaries, and offering me countless opportunities to grow as a researcher and as a person. Her support and the trust she placed in me have been invaluable, and I have learned so much from her expertise and dedication to science.

My heartfelt thanks also go to the Studienstiftung des deutschen Volkes, for their generous support and for providing me with the incredible opportunity to study the topic I love the most. I am so grateful for all the inspiring people I have met through the Studienstiftung, for the unforgettable experiences, and for the continuous encouragement and guidance I have received.

I would further like to thank Prof. Dr. Emanuel Stamou for his continuous support, for always offering his assistance, and for lending an open ear whenever needed. I am likewise very grateful to Prof. Dr. Kevin Kröninger for his consistently kind and supportive attitude during our collaboration, which I greatly appreciated.

Moreover, special thanks are due to Dr. Cornelius Grunwald for patiently addressing my numerous questions and helping me with my countless bugs and coding issues. I am also deeply grateful to Dr. Stefan Bißmann for his early support, helpful insights, and all the knowledge he shared with me.

Of course, I have immense gratitude for my family and friends, for their unwavering support and love throughout this journey. For my mother, who has always stood by me, believed in me, and provided so much encouragement. For my sister, whose kindness, compassion, and friendship have become an invaluable part of my life. For my father and my grandmother Gisela, whose support has allowed me to pursue my dreams and aspirations.

To my partner, Rene, I cannot express enough gratitude. He has been my rock and my greatest supporter during these years, always offering reassurance, patience, and unconditional support in every moment, being there for me through the ups and downs of this time. He has been a constant source of strength, and I am incredibly grateful to have him by my side.

I also want to give a special acknowledgment to Peter Furlan, whose encouragement and kindness during my undergraduate studies have made a big difference for me. He has given me more support, inspiration and confidence than he likely realizes, and I doubt I would be where I am today without him.

Finally, I want to thank everyone at the department from the bottom of my heart for creating such an amazing and unforgettable time. Special appreciation goes to my office mates, Daniel Wendler and Kai Sieja, who have always brightened my days and shared the joys as well as the challenges of PhD studies with me. I am enormously grateful to all my colleagues and friends at TIII/TIV for sharing countless laughs, celebrations and invaluable memories with me.